
**The distribution of dark
matter and stellar orbits in
nine Coma early-type galaxies
derived from their stellar
kinematics**

Jens Thomas



München 2006

**The distribution of dark
matter and stellar orbits in
nine Coma early-type galaxies
derived from their stellar
kinematics**

Jens Thomas

Dissertation
an der Fakultät für Physik
der Ludwig-Maximilians-Universität
München

vorgelegt von
Jens Thomas
aus Essen

München, den 05.04.2006

Erstgutachter: Prof. Dr. Ralf Bender
Zweitgutachter: Prof. Dr. Ortwin Gerhard
Tag der mündlichen Prüfung: 27.10.2006

Contents

Zusammenfassung	xv
1 Introduction	1
1.1 General motivation	1
1.2 Dynamical modelling of early-type galaxies	4
1.3 The orbit superposition technique	7
1.4 State of affairs	9
1.5 Aims and structure of the thesis	12
2 Mapping distribution functions by orbit superpositions	15
2.1 Introduction	15
2.2 The orbit library	17
2.2.1 Spatial and velocity binning	18
2.2.2 Orbital properties	18
2.2.3 Choice of orbits	19
2.2.4 Use of the library	22
2.3 Orbital weights and phase-space densities	22
2.3.1 Phase-space densities of orbits	23
2.3.2 Orbital weights from DFs	23
2.4 Orbital phase volumes	24
2.5 Mapping distribution functions onto the library	28
2.5.1 Spherical γ -models	29
2.5.2 Flattened Plummer model	32
2.5.3 Changing the spatial coverage of the library	34
2.5.4 Changing the number of orbits in the library	36
2.6 Fitting the library	36
2.6.1 Maximum entropy technique	36
2.6.2 The smoothing parameter α	38
2.7 Reconstructing distribution functions from fitted libraries	38
2.7.1 Hernquist model	39
2.7.2 Flattened Plummer model	42
2.8 Summary	44

3	Regularisation and orbit models for NGC 4807	47
3.1	Introduction	47
3.2	NGC 4807: model input	49
3.2.1	Photometric data	49
3.2.2	Deprojection	49
3.2.3	Kinematic data	51
3.3	Orbit superposition models	53
3.3.1	Basic grids	53
3.3.2	Luminous and dark mass distributions	53
3.3.3	Orbit collection	55
3.3.4	Orbit superposition	55
3.3.5	Comparing model with data kinematics	56
3.4	Regularisation	57
3.4.1	Motivation	57
3.4.2	Regularisation from isotropic rotator models	58
3.5	Recovering isotropic rotator models	64
3.5.1	Mass-to-light ratio Υ and inclination i	64
3.5.2	Internal kinematics	65
3.5.3	Mass distribution	66
3.6	Dark matter in NGC 4807	70
3.7	Stellar motions in NGC 4807	75
3.8	Phase-space structure of NGC 4807	76
3.9	Summary and Discussion	83
3.9.1	Regularised orbit models	83
3.9.2	Luminous and dark matter in NGC 4807	84
3.9.3	Comparing the kinematics: χ^2_{GH} versus χ^2_{LOSVD}	85
3.9.4	The outer parts of NGC 4807	88
3.9.5	Internal stellar kinematics of NGC 4807	91
4	The coma sample and its modelling: general survey	93
4.1	Summary of observations	93
4.2	Modelling setup and regularisation	95
4.3	Notes on individual galaxies	96
4.4	Confidence levels	108
5	Mass composition of Coma ellipticals	111
5.1	Outline	111
5.2	Evidence against constant mass-to-light ratios	111
5.3	Crosscheck with stellar populations	113
5.3.1	Independent stellar mass-to-light ratios	114
5.3.2	Stellar population gradients	115
5.3.3	Projection effects	118
5.3.4	Discussion	120
5.3.5	Conclusions	125
5.4	Spatial distribution of luminous and dark matter	127
5.4.1	Circular velocity curves	127

5.4.2	Mass-density profiles	128
5.4.3	Dark matter fractions	131
5.5	Uncertainties in the mass decomposition	132
5.5.1	Central dark matter	132
5.5.2	Radially increasing stellar mass-to-light ratios	132
5.6	Regularisation	135
5.7	Dark matter distribution functions	136
5.8	Summary	140
6	Dynamical structure of Coma ellipticals	143
6.1	Outline	143
6.2	Flattening and anisotropy	143
6.2.1	Galaxy fits	144
6.2.2	Maximum entropy models	146
6.3	Local dynamical structure around the poles	147
6.3.1	Velocity anisotropies	147
6.3.2	Anisotropy and H_4	149
6.3.3	The local distribution function	150
6.4	The bulk of stars at intermediate latitudes	153
6.5	Local dynamical structure around the equatorial plane	154
6.5.1	Velocity anisotropy	154
6.5.2	The local distribution function	155
6.5.3	The vertical structure	159
6.6	Discussion of the dynamical structure	165
6.7	Regularisation	169
6.8	Summary	170
7	Scaling relations	177
7.1	Outline	177
7.2	Stellar mass-to-light ratios	177
7.3	Orbital anisotropy	180
7.4	Fundamental plane	183
7.5	Tully-Fisher relation of ellipticals	187
7.6	Centre-halo relation	189
7.7	Dark matter scaling relations	190
7.7.1	Halo scaling relations	191
7.7.2	Central dark matter	196
7.8	Summary	198
8	Summary and conclusions	201
A	The sensitivity of Υ_{dyn} on the central photometric resolution	207
B	The centre of GMP0144/NGC4957	209
C	Orbital shape parameters	213

D The average local distribution function	217
E The triple nucleus of M31	219
Danksagung	249

List of Figures

2.1	Surface of Section in a flattened Hernquist potential	20
2.2	Example of a Voronoi tessellated surface of section	26
2.3	Distribution of orbital energies and angular momenta in a library	28
2.4	Isotropic Hernquist model mapped by an orbit superposition	30
2.5	Anisotropic Hernquist model mapped by an orbit superposition	31
2.6	Plummer model mapped by an orbit superposition	33
2.7	DF-mapping with orbit libraries of different spatial extension	35
2.8	DF-mapping with different number of orbits	37
2.9	Isotropic Hernquist model fitted by an orbit library	40
2.10	Reconstructed DF of isotropic Hernquist model	41
2.11	Accuracy of the reconstructed isotropic Hernquist DF	42
2.12	Anisotropic Hernquist model fitted by an orbit library	43
2.13	Plummer model fitted by an orbit library	45
2.14	Accuracy of the reconstructed Plummer DF	46
3.1	Photometric data and deprojections of NGC 4807	50
3.2	Deprojections of NGC 4807, viewed edge-on	52
3.3	Smooth reconstruction of an isotropic rotator model	59
3.4	Overfitted reconstruction of an isotropic rotator model	60
3.5	Model-kinematics along not observed position angles	61
3.6	Accuracy of reconstructed velocity moments	63
3.7	Reconstruction of mass-to-light ratio and inclination	65
3.8	Reconstruction of internal velocity moments	67
3.9	Recovery of the mass decomposition of a test model	68
3.10	Recovery of dark halo parameters of a test model	69
3.11	The stellar mass-to-light ratio Υ of NGC 4807	71
3.12	Projected kinematics of edge-on models of NGC 4807	72
3.13	The mass structure of NGC 4807	73
3.14	The dark halo parameters of NGC 4807	74
3.15	Luminous and dark matter profiles in models of NGC 4807	76
3.16	Projected kinematics of an $i = 50^\circ$ model of NGC 4807	77
3.17	Internal velocity moments in the best-fitting model of NGC 4807	78
3.18	Confidence intervals for the velocity moments of NGC 4807	79
3.19	Internal kinematics of the $i = 50^\circ$ model of NGC 4807	80

3.20	Phase-density versus energy in the bestfit model of NGC 4807 . . .	81
3.21	Phase-density versus ϑ_{\max} and $L_z/L_{z,\text{circ}}$ for NGC 4807	82
3.22	Stellar populations versus dynamical models for NGC 4807	86
3.23	Reconstruction of a test model from $\min(\hat{\chi}_{\text{LOSVD}}^2)$	87
3.24	Halo structure of NGC 4807 from $\min(\hat{\chi}_{\text{LOSVD}}^2)$	89
3.25	The keel in the DF of NGC4807 and its projected kinematics . . .	90
4.1	Photometry and kinematics of NGC 4827 against models	99
4.2	Photometry and kinematics of NGC 4860 against models	100
4.3	Photometry and kinematics of NGC 4952 against models	101
4.4	Photometry and kinematics of NGC 4869 against models	102
4.5	Photometry and kinematics of NGC 4931 against models	103
4.6	Photometry and kinematics of IC 3947 against models	104
4.7	Photometry and kinematics of NGC 4926 against models	105
4.8	Photometry and kinematics of NGC 4957 against models	106
4.9	Photometry and kinematics of NGC 4807 against models	107
4.10	χ_{GH}^2 and minor-axis rotation	109
5.1	Confidence levels of luminous mass-to-light ratios	112
5.2	Dynamical versus stellar population Υ -profiles: Kroupa-IMF . . .	113
5.3	Dynamical versus stellar population Υ -profiles: Salpeter-IMF . . .	115
5.4	Stellar population ages in the Coma sample	116
5.5	H β -measurements for the Coma sample	117
5.6	Projection effects related to spatially varying Υ_* -profiles	121
5.7	Averaged Υ : Kroupa-IMF	123
5.8	Averaged Υ : Salpeter-IMF	124
5.9	Dynamical Υ_{dyn} and trends with stellar populations	126
5.10	Survey of circular velocity curves	128
5.11	Normalised circular velocity curves	129
5.12	Survey of mass-density profiles	130
5.13	Survey of dark-matter fractions	131
5.14	Dark-matter fractions in maximum-halo models	133
5.15	Mass-density profiles in maximum-halo models	134
5.16	Stellar populations and the local M/L	135
5.17	Effect of regularisation on Υ_{dyn}	136
5.18	Effect of regularisation on circular velocity curves	137
5.19	Dark matter fraction versus regularisation parameter α	138
5.20	Survey of dark-matter distribution functions	139
6.1	Mean anisotropy and intrinsic flattening: Coma galaxies	145
6.2	Mean anisotropy and intrinsic flattening: maximum entropy . . .	146
6.3	Survey of minor-axis meridional velocity anisotropies	148
6.4	Survey of minor-axis azimuthal velocity anisotropies	149
6.5	Minor-axis anisotropy- H_4 relation	150
6.6	Average polar distribution function and anisotropy	151
6.7	Differential DF: polar axis	153

6.8	Average local distribution function at intermediate latitudes . . .	155
6.9	Differential DF at intermediate latitudes	156
6.10	Survey of major-axis velocity anisotropies	157
6.11	Survey of major-axis velocity anisotropies	158
6.12	Average local DF around the equatorial plane	160
6.13	Differential DF around the equatorial plane	161
6.14	Local anisotropy versus H_4 : major axis	162
6.15	Average local DF around the equatorial plane and H_3	163
6.16	Vertical structure of the orbit distributions in Coma galaxies . . .	164
6.17	Comparison of equatorial and polar orbit distributions	166
6.18	Minor-axis meridional anisotropy versus regularisation α	170
6.19	Minor-axis azimuthal anisotropy versus regularisation α	171
6.20	Minor-axis anisotropy- H_4 relation at different α	172
6.21	Major-axis meridional anisotropy versus regularisation α	173
6.22	Major-axis azimuthal anisotropy versus regularisation α	174
6.23	Histogram of orbital weights	175
7.1	Scaling of Υ_{dyn} with M_* in different samples	178
7.2	Scaling of M/L with M_* in different samples	180
7.3	Average anisotropies: COMA versus ROUND	182
7.4	Average anisotropies: COMA, NUKER and ROUND	183
7.5	Virial scaling relation for Coma galaxies	185
7.6	Tully-Fisher relation of early-type galaxies	188
7.7	The baryonic Tully-Fisher relation	189
7.8	Central velocity dispersion versus circular velocity	190
7.9	Dark halo parameter scalings	192
7.10	The transition radius from luminous to dark matter dominance .	193
7.11	Correlation between halo core radius and halo velocity	194
7.12	Halo velocity scaling relation	195
7.13	Central dark matter scaling relations	196
A.1	The effect of seeing on the bestfit Υ_{dyn} for GMP5975	208
B.1	Central kinematics in GMP0144	210
B.2	Central isophotal twist in GMP0144	211
B.3	Central spatial coverage of GMP0144 with kinematic observations	212
C.1	Mean orbital radii and binding energy	214
C.2	Survey of orbits in the bestfit potential of GMP5975	216
D.1	Average local DF versus individual orbital phase-densities	218

List of Tables

3.1	Results of simulations to determine the optimal regularisation . . .	62
4.1	Summary of photometric data	94
4.2	Summary of kinematic data.	94
4.3	Summary of bestfit models.	96
7.1	Linear fits of $\log \Upsilon_{\text{dyn}}$ versus $\log M_*$	179
7.2	Linear fits of $\log M/L$ versus $\log M_*$	179
7.3	Tully-Fisher relation fit parameters	187
7.4	Centre-halo relation fit parameters	191

Zusammenfassung

Elliptische Galaxien sind homogene, von alten Sternen dominierte dynamische Systeme, die sich heute in einem Zustand annähernden Gleichgewichts befinden. Ihre Entstehung liegt zeitlich weit zurück und ihr jetziger Zustand lässt nur noch indirekte Rückschlüsse auf den genauen Zeitpunkt und die Art ihrer Entstehung zu. Moderne Theorien zur Strukturbildung im Universum sagen vorher, dass alle massereicheren Galaxien von Halos aus dunkler Materie umgeben sind. Die zentrale Dichte der dunklen Materie stellt sich dabei als ein indirektes Mass für die Entstehungsepoche der Galaxien heraus. Hinweise auf den Entstehungsprozess – die Literatur kennt im wesentlichen den Kollaps einer protogalaktischen Gaswolke oder die Verschmelzung mehrerer Vorläufergalaxien – ergeben sich aus der Verteilung der Sternbahnen in elliptischen Galaxien. Sowohl die Verteilung der Masse als auch die der Sternbahnen sind schwierig aus Beobachtungen zu bestimmen, weil elliptische Galaxien dreidimensionale Objekte sind und man nicht von vornherein weiß unter welchem Blickwinkel man sie beobachtet. Außerdem bilden ihre Sterne ein stossfreies dynamisches System, das beliebige Grade von Anisotropie annehmen kann.

Seit etwa Anfang der 90er Jahre stehen mit den Messungen von projizierten Geschwindigkeitsprofilen Beobachtungsdaten zur Verfügung, die eine Rekonstruktion des genauen dynamischen Aufbaus einzelner Objekte zulassen. Erst seit etwa fünf Jahren hat die Entwicklung dynamischer Modelle ein vergleichbares Niveau erreicht, so dass es jetzt möglich ist, zumindest die volle Bandbreite achsensymmetrischer Modelle mit Beobachtungen einzelner Galaxien zu vergleichen. Die vorliegende Arbeit ist die erste Studie einer Stichprobe von mehreren Objekten mit achsensymmetrischen Modellen. Ähnlich umfangreiche Arbeiten waren bisher auf die Anwendung sphärisch-symmetrischer Modelle beschränkt, in denen weder Rotation noch Inklinationseffekte berücksichtigt werden können.

Die Datenanalyse der vorliegenden Arbeit basiert auf der sog. Schwarzschild-Methode. Dabei wird zunächst aus Galaxienbildern das Gravitationspotential der sichtbaren Materie berechnet. Anschließend wird eine Bibliothek mit tausenden Sternbahnen angelegt, aus deren Überlagerung dann ein Modell konstruiert wird. Falls nötig, wird dunkle Materie hinzugefügt bis Modell und Daten im Rahmen der Messfehler übereinstimmen. Diese Methode wird im Rahmen der Arbeit weiterentwickelt: Eine gleichmässige Verteilung von invarianten Kurven einzelner Orbits in geeignet gewählten Poincaré-Schnitten wird als Kriterium für eine zuverlässige Berücksichtigung aller Bahntypen eingeführt.

Ein Verfahren wird implementiert, das ebenfalls Poincaré-Schnitte verwendet, um die Phasenvolumina einzelner Orbits und damit die Phasenraumverteilungsfunktion von Galaxien zu berechnen. Monte-Carlo Simulationen zeigen, dass mit optimierter Regularisierung sowohl interne Geschwindigkeiten als auch die Massenstruktur mit einer Genauigkeit von etwa 15 Prozent aus den vorliegenden Daten rekonstruiert werden können.

Die untersuchten elliptischen Galaxien haben näherungsweise konstante Kreisgeschwindigkeiten außerhalb ihrer Zentren, ähnlich wie Spiralgalaxien. Die Halo Skalenradien einiger Ellipsen sind allerdings um einen Faktor zehn kleiner als die in gleichhellen Spiralen. Mit den flachen Rotationskurven sind 10 bis 50 Prozent dunkler Materie innerhalb des Effektivradius verknüpft. Die zentrale Dichte der dunklen Materie ist in Ellipsen um einen Faktor ≈ 25 höher als in Spiralgalaxien, was eine Entstehungsrotverschiebung von $z \approx 4$ impliziert. Soweit bestätigen die Modelle aus dieser Arbeit Resultate früherer Arbeiten mit sphärisch symmetrischen Modellen.

In den Coma Galaxien mit den ältesten stellaren Populationen sind entweder – im Vergleich zu jüngeren Galaxien – mehr Sterne geringer Masse gebildet worden oder aber die dunkle Materie in diesen Galaxien folgt einer ähnlichen radialen Verteilung, wie die leuchtende Materie.

Die Ergebnisse der Arbeit bestätigen kürzlich erschienene Arbeiten, nach denen elliptische Galaxien im grossen und ganzen eine homologe dynamische Familie bilden. Die verbleibende Streuung um entsprechende, aus dem Virialsatz ableitbare, globale Skalenrelationen sind auf eine systematische Verknüpfung des Drehimpulses mit der Leuchtkraftverteilung zurückzuführen. Der Ursprung dieser Relation ist noch unklar, aber ihr Vorhandensein erlaubt die Streuung in den Skalenrelationen um ein Drittel zu reduzieren. Dadurch könnte es in Zukunft möglich sein, die Entfernung einzelner Ellipsen mit grosser Genauigkeit aus ihrer Kinematik abzuleiten.

Die Abflachung der untersuchten Galaxien kommt durch eine relative Unterhäufigkeit von Sternen auf Bahnen, die den Äquator mit hoher vertikaler Geschwindigkeit durchkreuzen, zustande. Eine solche Verteilung von Sternen maximiert ihre Entropie im Phasenraum, wodurch elliptische Galaxien zu einem hohen Grade dynamisch relaxiert scheinen.

Allerdings offenbart eine genaue Untersuchung der Sternverteilung im Phasenraum eine reichhaltige Feinstruktur. Ein Objekt besteht aus der Überlagerung einer dünnen, rotierenden Scheibe und eines strukturlosen Sphäroids. In anderen Galaxien zeigt sich eine starke Asymmetrie zwischen rotierenden und gegenrotierenden Sternen in ihren Außenbezirken, gekoppelt mit relativ niedrigen stellaren Altern. Beides deutet daraufhin, dass die Sterne in diesen Regionen erst vor relativ kurzer Zeit zur Galaxie hinzugekommen sind. Über den beobachteten radialen Bereich zeigt keine Galaxie die typische Struktur nach einem Kollaps. Die Vielfalt der dynamischen Eigenschaften spricht eher für das Verschmelzungsszenario mit seiner natürlichen Variation an Ausgangskonfigurationen und -objekten.

Chapter 1

Introduction

The present work is aimed to analyse a sample of nine early-type galaxies in the Coma cluster with respect to their dynamical structure and mass composition. The motivation for the project, an outline of the applied method and of the thesis' structure are the subject of this chapter.

1.1 General motivation

Elliptical galaxies are among the brightest galactic objects in the universe. They owe their names from a globally smooth, elliptical light distribution on the sky and are preferentially found in environments densely populated with other galaxies, such as the inner parts of galaxy clusters. In contrast to spiral galaxies, they are genuinely three dimensional objects and their dominant structural component is the system of their stars. In further contrast to spirals, massive ellipticals are basically old and enriched in α -elements with galaxies in high density environments being older than their field counterparts. At lower masses indications for occasional juvenescence become more frequent (Thomas, Maraston, Bender & Mendes de Oliveira 2005). From the centre outwards ellipticals get bluer, mostly caused by decreasing stellar metallicity (Mehlert et al. 2003). Stellar mass-to-light ratios Υ_* are radially constant to first order. Regarded as a class, ellipticals obey several scaling relations. For example, more luminous ellipticals are redder (Faber 1973), which in contrast to individual galaxy gradients, reflects a gradual increase of stellar ages with luminosity. The overall smooth and featureless light distributions suggest ellipticals to rest in a state of approximate dynamical equilibrium. In fact, effective radius, effective surface brightness and central velocity dispersion of ellipticals are tightly related to form the so-called fundamental plane (FP; Faber et al. 1987; Djorgovski & Davies 1987; Dressler et al. 1987). Although such a relation generally follows from virial equilibrium, the observed FP is tilted with respect to the relation expected for a family of homologous objects. Indeed, ellipticals exhibit a gradual structural change with luminosity. Fainter objects have more centrally concentrated light profiles than

brighter ones (Caon, Capaccioli & d’Onofrio 1993; Graham, Trujillo & Caon 2001). This is only one aspect of a deeper dichotomy: fainter ($M_B > -20.5$) ellipticals are radio and X-ray quiet, disk-shaped and have steep central power-law density profiles. In contrast, their luminous counterparts are boxy, X-ray and radio loud and exhibit shallow central cores (Bender 1988a; Bender et al. 1989). Comparison with simple isotropic rotator models let to the conjecture that the fainter branch of ellipticals is flattened by rotation, while the brighter branch is intrinsically anisotropic (Bender 1988a; Bender et al. 1989). Most ellipticals are consistent with axial symmetry, but preferentially in more luminous ones rotational symmetry is sometimes broken, implied by isophotal twists (e.g. Bertola & Galletta 1979) and/or minor-axis rotation (Jedrzejewski & Schechter 1989). Substructure occurs in form of photometrically and/or kinematically decoupled central cores (Efstathiou, Ellis & Carter 1982; Bender 1988b; Franx & Illingworth 1988) or inner, metal-enriched stellar disks (Bender & Surma 1992; Scorza & Bender 1995; Morelli et al. 2004). In many nearby ellipticals central supermassive black holes have been detected. Their masses are closely linked to the velocity dispersion and mass, respectively, of the surrounding galaxy (Magorrian et al. 1998; Gebhardt et al. 2000b; Ferrarese & Merritt 2000).

Origin and structure. The origin of elliptical galaxies is an open issue since a long time. For comparison, spiral galaxies exhibit an extended star formation history hinting at a relatively quiescent, temporally extended gradual growth. Thus, their evolutionary history (in very rough terms) can be seen as an extrapolation of their present status to the past. The latter, in turn, is observationally relatively easy accessible. The case of ellipticals is different. Their very morphology (as mentioned above) points at a long-lived state of evolutionary passive dynamical equilibrium. In line with high stellar population ages and relatively short star formation time scales (implied by the α -enrichment) this suggests a distinct formation episode far back in time. To understand their origin, one must therefore either search for potential progenitors at high redshift or, alternatively, scan their present day structure for characteristic relics of their formation epoch.

Dynamical structure. One potential formation channel is the monolithic collapse scenario, after which ellipticals formed by the collapse of a single protogalactic gas cloud (Eggen, Lynden-Bell & Sandage 1962; Larson 1974). Investigations of the dynamical implications of this scenario in form of computer simulations following the collapse of a stellar systems from cold initial conditions have revealed density profiles similar to those of real ellipticals (van Albada 1982). Moreover, they recovered a characteristic fingerprint of the initial collapse in the orbital structure of its end product: a gradual change from central isotropy to strong outer radial anisotropy (van Albada 1982).

Another possible formation scenario of ellipticals is by merging (e.g. Toomre & Toomre 1972). Observational evidence for merging comes from ongoing galaxy collisions structurally evolving towards ellipticals (e.g. Schweizer 1982).

The merger hypothesis has been the subject of extensive computer simulations. Compared to the characteristic structure of a monolithic collapse, mergers can produce a rich diversity of dynamical systems. Specifically, dependencies of the orbital structure on progenitor properties (Hernquist 1992, 1993), on the merging geometry (Weil & Hernquist 1996; Dubinski 1998) and on the mass ratio of the progenitors (Naab & Burkert 2003; Jesseit, Naab & Burkert 2005) have been elaborated.

It follows that the internal dynamical structure is a key to understand the formation and evolutionary history of elliptical galaxies.

Mass structure. Similarly interesting is the mass distribution in ellipticals and especially the question whether these galaxies carry dark matter halos. Numerous studies of gas and/or stellar kinematics in spiral and dwarf galaxies, of their satellite dynamics, of the dynamics of galaxies in clusters, of the gas distributions and gravitational lensing signals in clusters and of the cosmic web of structures give compelling evidence for the presence of dark matter on all cosmic scales. Moreover, dark matter has become a necessary ingredient in current galaxy formation theories. It is required to assist the growth of structures, since the homogeneity of the cosmic microwave background radiation sets upper limits on the initial fluctuations of baryonic matter. These are too small to grow to present day cosmic structures. By postulating that these fluctuations exhibit only the tip of an iceberg, that they are embedded in larger fluctuations of an invisible dark medium the so-called cold dark matter theory has been very successful in explaining the large scale structure of the universe. A crucial point of this theory is its prediction that essentially every galaxy should be located in a dark matter halo, also elliptical galaxies. Beyond the question of the very presence of dark matter in ellipticals, its actual radial distribution contains important information about their formation time. This, because the (assumed) collisionless nature of dark matter particles gives rise to a close relationship between the concentration of a halo and its major-assembly epoch (Navarro, Frenk & White 1996; Jing & Suto 2000; Wechsler et al. 2002). Thus, knowing the mass distribution in ellipticals, especially their dark matter distribution, is important to (1) verify basic predictions of current galaxy formation theories and (2) to constrain the formation epoch of elliptical galaxies.

Modelling approaches. The diversity of methods to study the mass distribution of ellipticals is relatively large. Occasionally, ellipticals harbour extended gas disks that can be used as direct tracers of the gravitational potential. However, such cases are rare and so far only a handful of objects have been investigated (Bertola et al. 1993; Oosterloo et al. 2002). More promising is the analysis of hot gas halos in the X-ray regime, but this channel is restricted to the most luminous galaxies (Loewenstein & White 1999; Fukazawa et al. 2006). Rarely, ellipticals are part of strong lensing configurations, putting tight constraints on their mass profile over a limited radial range (around the distorted images). As regarding gas disks only a handful of cases is known and the in-

volved systems are at intermediate redshifts (Keeton 2001; Treu & Koopmans 2004). Galaxy-galaxy lensing allows to study the properties of galaxy halos far out, but only in a statistical manner, individual objects cannot be studied (e.g. Brainerd, Blandford & Smail 1996).

In the past, most extensive use has been made of stellar kinematics. Compared to all other mentioned methods it has the great advantage not only to constrain the mass distribution but at the same time also the dynamical configuration. As it has been outlined above, both contain important clues on the formation and evolution of elliptical galaxies. Stellar dynamical studies divide into two branches. Most studies so far are based on integrated stellar absorption line kinematics. The difficulty here is that the absorption-line shape, carrying the relevant information about the kinematics of the stars, becomes difficult to measure in the outer faint parts of ellipticals. To circumvent the related problems, discrete kinematical tracers such as planetary nebulae (PNe) and globular clusters have gained more and more interest recently.

As will be outlined in the following, our present knowledge about the internal structure of elliptical galaxies is still rare, both in terms of the orbital composition and in terms of the radial mass distribution.

1.2 Dynamical modelling of early-type galaxies

The analysis of stellar kinematics in elliptical galaxies rises several problems. For comparison, the rotation profile $v_{\text{circ}}(r)$ of cold atomic hydrogen disks in spirals can be more or less directly interpreted in terms of the radial mass distribution

$$v_{\text{circ}}^2 \propto \frac{M(r)}{r}. \quad (1.1)$$

Crucial for this simplicity is that (1) the internal v_{circ} can be inferred from the observed projected line-of-sight velocity. For flat disks this is ensured, because the inclination angle i of the disk is uniquely related to its apparent ellipticity and the intrinsic v_{circ} follows directly from the observed rotation velocity and i . Likewise important for gas disks is that (2) the internal energy resides completely in circular motions. None of these two critical conditions holds for the stars in ellipticals. The internal flattening of the stellar distribution in an elliptical galaxy is not known a priori. Instead, it is a degenerate function of apparent ellipticity and inclination i . Regarded as a class, deprojection of the ellipticity distribution has revealed that fainter ($M_B > -20.5$) ellipticals are mostly oblate axisymmetric with short to long axis ratio around $b/a = 0.83$, while brighter ones are generally rounder (Tremblay & Merritt 1996). The flattening of an individual object, however, is not directly given and, consequently, the internal energy distribution cannot be directly derived from its observed projections. The only way to proceed is to probe the whole range of imaginable intrinsic stellar configurations and projection angles with respect to the observations in each single case. This defines an ambitious program.

The general description of a system of stars is given by its phase-space distribution function (DF) f , defined such that

$$f(\vec{r}, \vec{v}, t) d^3r d^3v \quad (1.2)$$

is the stellar light at time t , in the infinitesimal phase-space element around (\vec{r}, \vec{v}) . It determines all relevant properties of the system. For example, the surface brightness μ and line-of-sight-velocity-distribution (LOSVD) \mathcal{L} at time t and (projected) position (x_p, y_p) follow as

$$\mu(x_p, y_p, t) = \int f(\vec{r}_p, \vec{v}, t) d^3v dz \quad (1.3)$$

and

$$\mathcal{L}(x_p, y_p, v_p, t) = \int f(\vec{r}_p, \vec{v}_p, t) dv_x dv_y dz, \quad (1.4)$$

with $\vec{r}_p = (x_p, y_p, z)$ and $\vec{v}_p = (v_x, v_y, v_p)$. Since the collisional relaxation time in galaxy-sized objects is generally larger than the age of the universe, the temporal behaviour of the DF is governed by the incompressibility of its phase-space flow, expressed in the collisionless Boltzmann equation

$$\frac{df}{dt} \equiv \frac{\partial f}{\partial t} + \vec{v} \cdot \nabla_r f - \nabla \Phi \cdot \nabla_v f = 0. \quad (1.5)$$

If the system is not explicitly time-dependent (which is assumed in the following) equation (1.5) reduces to

$$\frac{df}{dt} = \vec{v} \cdot \nabla_r f - \nabla \Phi \cdot \nabla_v f = 0. \quad (1.6)$$

All forces acting on the system are subsumed in the potential Φ . To be considered are the gravity of stars and dark matter (DM)

$$\Phi = \Phi_\nu + \Phi_{\text{DM}}, \quad (1.7)$$

where stellar self-gravity is related to the DF via

$$\nu = \int f(\vec{r}, \vec{v}, t) d^3v, \quad (1.8)$$

Poisson's equation

$$\Delta \Phi_\nu = -4\pi G \Upsilon_* \nu \quad (1.9)$$

and the actual stellar mass-to-light ratio Υ_* (which may vary with phase-space position).

The only further constraint on the form of f comes from its assumed stationarity. In this case Jeans theorem ensures that f depends on the phase-space coordinates only through isolating integrals of motion (Lynden-Bell 1962b). Let these be denoted $I_j(\vec{r}, \vec{v})$, $1 \leq j \leq n$, then

$$f = f(I_1, \dots, I_n) \quad (1.10)$$

and the distribution function of ellipticals is constant along individual orbits. Several methods have been proposed to reconstruct the DF from observations via equations (1.3) and (1.4).

In parameterised models a certain form for the DF is presumed and the best-fit model is chosen among the range of parameters. Fully general models seek a non-parametrical reconstruction of the DF. An intermediate case is the basis-function ansatz, where the weights of (several tens of) prototypical basis functions in a linear superposition are derived from observations. Parameterised models and basis function models require explicit knowledge of all relevant integrals to specify the DF (or the basis functions, respectively). Spherical potentials with the two classical integrals E (energy) and L (total angular momentum) provide a semi-analytic framework. Most axisymmetric potentials, however, admit not only the two classical integrals E and L_z (angular momentum along the symmetry axis) but an additional non-classical integral of motion, the so-called third integral I_3 (e.g. Contopoulos 1963). The latter is only in restricted subclasses of potentials known in terms of elementary functions. Likewise, in most triaxial potentials the energy E is the only explicitly given integral. One has tried to overcome the lack of explicit knowledge about all relevant integrals by (1) resorting on moments of the DF (Jeans approach); by (2) restriction to subclasses of DFs that vary only with respect to known integrals; by (3) the use of approximate integrals; by (4) restriction to special (separable) potentials, where all integrals are given explicitly.

Jeans models are physically questionable because the predicted dynamical configuration is not ensured to correspond to an everywhere positive stellar density. Models of the second kind (2) have been extensively used in the axisymmetric case by assuming $f = f(E, L_z)$ (so-called two-integral, or 2I, models). If compared to observations of real ellipticals, such 2I-models fail to match the major and minor-axis data simultaneously (van der Marel 1991; Bender, Saglia & Gerhard 1994; Cretton & van den Bosch 1998; Emsellem, Dejonghe & Bacon 1999). The third integral in axisymmetric potentials has been approximated by integrals of fitted Staeckel potentials (de Zeeuw & Lynden-Bell 1985) or by perturbations of the angular momentum (Gerhard & Saha 1991), leading to models of the third kind (3). Concerning the fourth class, especially triaxial symmetry has been explored in terms of Staeckel potentials, but these imply unrealistically extended central cores.

Two fully general non-parametric methods do not suffer from the integral issue. The made-to-measure method consists of fitting an arbitrary N -body system to a given set of constraints (Syer & Tremaine 1996) and is even independent from the stationarity assumption. It has yet only been applied to the Galaxy, however (Bissantz, Debattista & Gerhard 2004). Another fully general method, the orbit superposition technique (Schwarzschild 1979), makes literal use of the fact that f according to equation (1.10) is constant along individual orbits. The DF is constructed as a superposition of individual orbital DFs, whose properties are derived from integrating orbits. It is used for this work and detailed in the following.

1.3 The orbit superposition technique

According to equation (1.10) the DF is constant along individual orbits

$$f(I_1, \dots, I_n) = \int f(I'_1, \dots, I'_n) \delta(I_1 - I'_1) \dots \delta(I_n - I'_n) dI'_1 \dots dI'_n \quad (1.11)$$

and, thus, can be approximated as the superposition of a finite number of single orbit distribution functions

$$f \approx \sum_i f_i \delta(I_1 - I_{1,i}) \dots \delta(I_n - I_{n,i}), \quad (1.12)$$

where f_i is the phase-density along the orbit corresponding to the set of integrals $\{I_{1,i}, \dots, I_{n,i}\}$.

Any property K of the stellar system is related to the DF f by a phase-space projection

$$K = \int f \mathcal{K} dV \quad (1.13)$$

with an appropriate integral kernel \mathcal{K} (dV denotes the six-dimensional volume-element in phase-space). For example,

$$\mathcal{K}_\mu(\vec{r}, \vec{v}) \equiv \begin{cases} 1 & : x = x_p, y = y_p \\ 0 & : \text{otherwise} \end{cases} \quad (1.14)$$

and

$$\mathcal{K}_\mathcal{L}(\vec{r}, \vec{v}) \equiv \begin{cases} 1 & : x = x_p, y = y_p, v_z = v_p \\ 0 & : \text{otherwise} \end{cases} \quad (1.15)$$

in equations (1.3) and (1.4), respectively. The discretisation in equation (1.12) implies that

$$K \approx \sum_i f_i \int \delta(I_1 - I_{1,i}) \dots \delta(I_n - I_{n,i}) \mathcal{K} dV \equiv \sum_i f_i \int_i \mathcal{K} dV. \quad (1.16)$$

The subscript i in the second integration indicates that the integral is restricted to the region in phase-space covered by orbit i . The quadrature

$$K'_i \equiv \int_i \mathcal{K} dV \quad (1.17)$$

can be evaluated conveniently via the time-averages theorem, stating that the fractional time dt/T an orbit spends in a phase-volume dV equals the fraction of dV with respect to the whole orbital phase volume¹ V , in suggestive notation

$$\frac{dV}{V} = \frac{dt}{T}. \quad (1.18)$$

¹Strictly speaking this only holds for regular, non-resonant orbits. In potentials of interest here, the fraction of chaotic or resonant orbits is below one percent usually.

Accordingly, if $\psi_i : \mathcal{R} \rightarrow \mathcal{P}$ describes the parameter curve of orbit i in phase-space \mathcal{P} , then equation (1.17) becomes

$$K'_i = V_i \int \mathcal{K} \circ \psi_i \frac{dt}{T}, \quad (1.19)$$

with V_i being the phase-volume represented by orbit i . In practice, orbits are integrated numerically with finite time-steps Δt and equation (1.19) is approximated by

$$K'_i \approx V_i \sum_j \mathcal{K} \circ \psi_i(t_i^j) \frac{\Delta t_i^j}{T_i}, \quad (1.20)$$

where

$$T_i \equiv \sum_j \Delta t_i^j \quad (1.21)$$

is the total integration time of orbit i and

$$t_i^j \equiv \sum_{k < j} \Delta t_i^k. \quad (1.22)$$

Defining

$$K_i \equiv \sum_j \mathcal{K} \circ \psi_i(t_i^j) \frac{\Delta t_i^j}{T_i} \quad (1.23)$$

equation (1.16) finally reads

$$K \approx \sum_i (f_i \times V_i) K_i. \quad (1.24)$$

Noteworthy, by employing the time-averages theorem the distribution function shows up in the calculation of K only as the product

$$w_i \equiv f_i \times V_i, \quad (1.25)$$

which is the total amount of light carried by orbit i and is usually called the *weight* or *occupation number*, respectively, of the orbit. Hence, modelling galaxy observations does not require computation of orbital phase-volumes.

Orbit modelling has some essential advantages. First, via the time-averages theorem (1.18) K_i can easily be calculated with any desired accuracy during the integration of orbit i . The overall accuracy of the galaxy model then only depends on the phase-space coverage with orbits. Moreover, in the orbit representation the integrals of motion enter only implicitly via orbital initial conditions. Thus, the orbit superposition method is especially promising in systems, where not all integrals of motion are known. Two limitations have to be regarded in practice: (1) If resonances become frequent the orbit superposition method in general is still valid (ensured by the Jeans theorem), but the Schwarzschild method in a stricter sense – employing equation (1.18) to project orbits in the

space of observables – is no longer applicable. A typical example is the Keplerian character of the force field in the direct vicinity of a point source (black hole) where all orbits are closed. (2) Orbits must be integrated over the whole phase-space region they have access to. Chaotic orbits can reveal a quasi-regular behaviour in a subpart of their phase-space manifold over long periods. If such fragments of orbits are treated as regular orbits, the model is no longer stationary in a rigorous sense. To maintain full stationarity such suborbital building blocks need to be combined to superorbits (Merritt & Valluri 1996; Häfner et al. 2000).

The Schwarzschild method was originally developed to investigate dynamical equilibrium configurations in triaxial potentials (Schwarzschild 1979) and subsequently used to explore the dynamical effects of central density cusps on the orbital structure and existence of stationary configurations (Schwarzschild 1982; Miralda-Escudé & Schwarzschild 1989; Schwarzschild 1993; Merritt & Fridman 1996; Merritt & Valluri 1996). Other early applications were the survey of dynamical properties of scale free potentials (Richstone 1980, 1982, 1984; Levison & Richstone 1984a) and exemplary studies of real galaxies (Levison & Richstone 1984b; Katz & Richstone 1985). Only recently, the focus of research shifted towards modelling real galaxies extensively. Present implementations cover spherical symmetry (Richstone & Tremaine 1984; Rix et al. 1997; Romanowsky et al. 2003) axial symmetry (Cretton et al. 1999; Gebhardt et al. 2000a; Häfner et al. 2000; Valluri, Merritt & Emsellem 2004; Cappellari et al. 2006) and triaxial symmetry (Zhao 1996; van den Bosch et al. 2005).

1.4 State of affairs

Orbit modelling. Although the orbit modelling technique is about 20 years old, still some issues have not been addressed thoroughly. As pointed out earlier, the integrals of motion do not enter the modelling explicitly. However, to achieve a representative phase-space coverage with orbits the phase-space structure related to a given potential has to be known to some degree. The latter, closing the circle, is imprinted in the integrals of motion the potential admits. The resolution of phase-space sampling provided by a given orbit library can in any case be checked in two ways.

Firstly, if the integrals are known somehow, then the orbit collection can be mapped onto integral space and the related grid can be evaluated. Ideally, the orbit sampling should be adapted to the behaviour of the system the model is aimed to represent. For example, where the DF is expected to vary strongly, like around the transition from a disk to a bulge in a two-component system, orbits should be sampled densely. When modelling real galaxies, neither the integrals nor the expected DF are given. If only one integral is unknown (for example I_3 in the axisymmetric case), then surfaces of section (SOS) can be used to examine the orbit sampling, since they can be matched to separate orbits according to the unknown integral (cf. Sec. 2.2.3). None of the presently implemented orbit sampling strategies for axisymmetric potentials (reviewed in

Sec. 2.2.3) has been examined as just described.

A second method to probe the sufficiency of the orbit sampling is to practically reconstruct synthetic template DFs. This can be done by either deriving mock observations from a DF and studying the match of a fitted orbit model with the input DF. Alternatively, the amount of light carried by each orbit with respect to the input DF can be calculated (via equation 1.25) and the properties of the orbit superposition based on these weights can be compared to direct phase-space integrations. This approach has also not yet followed fully, mainly because the mapping from orbit libraries to phase-space and vice versa requires knowledge of the orbital phase-volumes (cf. equation 1.25). Since these are not necessarily required for modelling real galaxies (as mentioned above), they have been paid little attention to. Besides enabling a rigorous check of the orbit sampling, knowledge of the phase-volumes is essential to analyse the dynamical structure of galaxy models. For example, two orbits with equal phase-densities can have different weights just because one occupies a much larger phase-volume than the other. On the other hand, even if an orbit has a lower weight than another, it may represent an over-density in a certain phase-space region that reveals a distinct kinematical component.

Another issue is that when using Schwarzschild models to reconstruct real galaxies one is usually faced with the situation that the number of orbits in the models (e.g. the number of adjustable parameters) is much larger than the number of data constraints. As a consequence, the models tend to overfit the data in the sense that they match individual data points better than implied by the measurement errors. Ideally, one would like to consider only those models that fit the data within a reasonable range of χ^2 -levels and to ignore all others. This requires, however, knowing all models that fit within some χ^2 limits, which is practically impossible. Instead of exploring the whole manifold of these solutions, one forces the models in practice to fulfil additional structural constraints on top of the observational ones. Several expressions have been developed for these constraints, such as minimising second derivatives of the DF, maximising the entropy of the DF, minimising gradients of orbital weights and so on – all related to theoretical considerations about the smoothness of the DF in phase-space (cf. Sec. 3.1). Regardless of this diversity, all regularisation methods have in common that the relative importance of both sets of constraints is controlled by a single regularisation parameter. It follows a one-to-one relation between the weight of structural constraints and the goodness of fit, as putting more weight on the data constraints will inevitably lead to a lower χ^2 and vice versa. Although this is what one practically wants, it has the undesired consequence to bias the so derived models, because at each value of the regularisation parameter (or, equivalently, at each χ^2) no more than one member of the full manifold of models fitting at the actual χ^2 -level is picked up. Note, that the occurrence of this bias is *independent* of the specific choice of the regularisation parameter, unless the solution manifold shrinks approximately to a single point. What actually varies as a function of this parameter is the direction into which the bias works. By construction, one usually knows this direction when the weight on the structural constraints is large, but one does not know its direction when the

weight is mostly on the data constraints. In the latter case, it depends strongly on the (irreproducible) noise in the data.

The way to implement regularisation is to simulate observations from realistic synthetic model galaxies and to investigate systematically which smoothing yields the best match of fitted orbit superpositions with the input model. This has not yet been carried out in the general axisymmetric case, but only for two-integral approximations (Cretton et al. 1999; Krajnović et al. 2005).

Galaxy modelling. Early dark matter studies considered as kinematical input to dynamical models only the mean rotation v and dispersion σ (e.g. Katz & Richstone 1985; Saglia, Bertin & Stiavelli 1992). By a now well understood mass-anisotropy degeneracy, these data alone are insufficient to reconstruct the orbital state of a galaxy and/or its mass distribution (Binney & Mamon 1982). Observance of the full LOSVD allows to reconstruct the DF, given the potential is known (Dejonghe & Merritt 1992) and to put constraints on both the DF and the potential, if the latter is not known in advance (Merritt & Saha 1993; Gerhard 1993). Due to signal-to-noise limitations, the LOSVD is usually decomposed into a Gauss-Hermite series and the first four coefficients – rotation v , dispersion σ , asymmetric and symmetric deviations of a pure Gaussian H_3 and H_4 – are used in models (Gerhard 1993; van der Marel & Franx 1993).

Various dynamical studies have revealed that elliptical galaxy kinematical data inside the half-light radius r_{eff} can be well reproduced under the assumption of a constant mass-to-light ratio M/L . This is generally taken as evidence for dark matter being negligible in the inner regions of elliptical galaxies. Only very recently LOSVDs farther out have become available to probe for the presence of dark matter. Most studies with such extended data have the character of case studies though. They have been carried out with restriction to spherical potentials for NGC2434 (orbit models; Rix et al. 1997), NGC6703 (basis functions; Gerhard et al. 1998), NGC1399 (basis functions; Saglia et al. 2000) and NGC3258 (basis functions; de Bruyne et al. 2004) and with axisymmetric models for NGC3115 (Staeckel fits, basis functions; Emsellem, Dejonghe & Bacon 1999), NGC1700 (same method; Statler, Dejonghe & Smecker-Hane 1999) and NGC2320 (orbit models; Cretton, Rix & de Zeeuw 2000). Two larger samples, both comprising roughly 20 apparently round, non-rotating objects, have been analysed in the spherical approximation based on basis functions (Kronawitter et al. 2000) or parameterised models with constant anisotropy (Magorrian & Ballantyne 2001). These models predict dark matter fractions between 20 and 50 percent inside r_{eff} . However, in the only galaxy studied with general axisymmetric models, NGC2320, the case for DM is ambiguous and models with constant M/L fit as well. Three objects have been declared to lack of any dark matter on the basis of PNe kinematics (diversity of spherical models; Romanowsky et al. 2003).

The dark matter fractions derived in all but the last mentioned studies agree with results from other methods. The analysis of cold gas kinematics has revealed roughly constant rotation curves as in spiral galaxies with the implied

evidence for dark matter (Bertola et al. 1993; Oosterloo et al. 2002). Likewise halo gas temperatures and densities conclude that dark matter makes about 20 percent of mass inside the half-light radius r_{eff} and up to 40-80 percent at $5 - 6 r_{\text{eff}}$ (Loewenstein & White 1999; Fukazawa et al. 2006). Dark matter fractions from lensing studies are similar (Keeton 2001; Treu & Koopmans 2004).

Taking these results together, evidence for the ubiquitous presence of dark matter in ellipticals grows steadily. However, its radial distribution, especially in those regions ($\lesssim 2 r_{\text{eff}}$) that carry crucial information about their formation epoch, is still largely unknown. Only stellar dynamical studies can resolve these, but only one object has been addressed allowing for axial symmetry. All other studies rely on spherical approximations.

Concerning the dynamical structure of ellipticals, the situation is even more heterogeneous. Apart from the very centre, spherical models mostly predict radial anisotropy (Rix et al. 1997; Gerhard et al. 1998; Kronawitter et al. 2000; Magorrian & Ballantyne 2001; Houghton et al. 2006). Allowing for axial symmetry yields a variety of internal structure. Radial anisotropy has been found in NGC1600 (basis functions, approximate I_3 ; Matthias & Gerhard 1999), NGC2320 (orbit models; Cretton, Rix & de Zeeuw 2000), NGC3379 (orbit models; Gebhardt et al. 2000a) and M32 (orbit models; Verolme et al. 2002). Tangential anisotropy occurred in NGC4697 (Staeckel fits; Dejonghe et al. 1996), NGC3115 (Staeckel fits; Emsellem, Dejonghe & Bacon 1999), NGC1700 (Staeckel fits; Statler, Dejonghe & Smecker-Hane 1999), IC1459 (orbit models; Cappellari et al. 2002), the twelve ellipticals of the Nuker team (orbit models; Gebhardt et al. 2003) and NGC3377 (orbit models; Copin, Cretton & Emsellem 2004).

Most of the above studies are based on data inside r_{eff} and dark matter has been neglected completely (e.g. a constant M/L has been assumed). This is questionable in view of the evidence for increasing M/L beyond r_{eff} . Even if models are only fit to observations further in, some of the orbits that contribute to the inner kinematics, especially in radially anisotropic systems, are shaped during their visits of outer regions inhabited by dark matter. The results of studies not taking into account dark matter need therefore confirmation in a more general modelling context. The same holds for spherical models as well, in which inclination effects and rotation are ignored.

Concluding, due to the lack of any study of a sizeable sample of galaxies with extended data and sufficiently general models, our knowledge of both, the mass distribution and the dynamical structure of ellipticals, is still poor and tentative.

1.5 Aims and structure of the thesis

The present work is aimed to improve on this situation regarding our present poor knowledge about the dynamical structure and mass composition of elliptical galaxies. It advances previous work in the following points:

- It provides the first analysis of a sample of generic, flattened ellipticals

with LOSVDs along the minor and the major axis reaching out to $\approx 3 r_{\text{eff}}$, suitable to probe for the distribution of dark matter and the dynamical structure over a wide radial range.

- Fully general orbit models are applied that allow to probe (1) the flattening of the galaxies, (2) possible substructure in form of disks and (3) inclination effects.
- The orbit modelling technique is advanced to yield (1) a representative phase-space coverage with orbits, (2) to optimise regularisation and (3) to derive for the first time the phase-space distribution function of early-type galaxies in axial symmetry. So far, the applied code is the only tested for its accuracy to reconstruct synthetic distribution functions.

The thesis is structured as follows. The specific implementation of the orbit modelling method used in this work is based on a program originally developed by the Nuker team to recover black-hole masses in the centres of galaxies (Richstone & Tremaine 1984; Gebhardt et al. 2000a). The advanced implementation developed for the investigation of dark matter halos is the subject of Chap. 2. The treatment of regularisation and a pilot study of one sample galaxy follow in Chap. 3. Both, Chaps. 2 and 3 are replica of papers published during this work (Thomas et al. 2004, 2005). Chap. 4 introduces the analysis of the Coma sample by a survey of the individual galaxies and their models. In Chaps. 5 and 6 the mass distribution and dynamical structure are discussed in detail. Scaling relations and comparison with other works are the subject of Chap. 7. A short thesis summary and concluding remarks are combined in Chap. 8.

A few technical issues are separately addressed in the four Apps. A-D. The effects of seeing on the dynamical modelling is the topic of App. A. Observational evidence for central non-axisymmetry in GMP0144/NGC4957 is exposed in App. B. In App. C the parameterisation of orbital shapes used in this work is introduced. The calculation of radial phase-density profiles from orbit distributions is the content of App. D.

Finally, in App. E the paper Bender et al. (2005) on the nuclear structure of M31 is reproduced. The orbit models used in this publication were calculated during the course of this work.

Chapter 2

Mapping stationary axisymmetric phase-space distribution functions by orbit libraries

2.1 Introduction

Since the pioneering work of Schwarzschild (1979) orbit superposition techniques have become an important tool in the dynamical modelling of spheroidal stellar systems. Stationary distribution functions (DFs) of such systems are subject to Jeans' theorem and hence depend on the phase-space coordinates only via the integrals of motion. In the axisymmetric case these integrals are energy E , angular momentum along the axis of symmetry L_z , and, for most potentials, an additional, non-classical “third integral” I_3 . Because any set of integrals of motion essentially represents an orbit and, conversely, any orbit can be represented by a set of integrals of motion, the DF can be approximated by the sum of single-orbit DFs, with the only adjustable parameters being the total amount of light carried by each orbit. The main task that remains to describe hot stellar systems adequately is to find an appropriate set of orbits.

Orbit superposition techniques have been used to model spheroidal stellar systems in various symmetries (e.g. Rix et al. 1997; Romanowsky & Kochanek 2001; van der Marel et al. 1998; Cretton et al. 1999; Cappellari et al. 2002; Verolme et al. 2002; Gebhardt et al. 2003; van de Ven et al. 2003), with the goal of determining dynamical parameters such as central black hole mass, internal velocity anisotropy or global mass-to-light ratio. An orbit library tracing the phase-space structure of a trial potential is fitted to observed photometry and kinematics, to decide whether or not it gives a valid model of the corresponding galaxy.

In the spherical case there exists a well-known mass-anisotropy degeneracy permitting in general convincing fits to the projected velocity dispersion σ , even if the trial potential differs from the true one (Binney & Mamon 1982). With complete knowledge of the full line-of-sight velocity distributions (LOSVDs), however, it is possible to reconstruct the DF, given the potential is known (Dejonghe & Merritt 1992). Furthermore, even for the realistic case where the potential is not known in advance, Merritt & Saha (1993) and Gerhard (1993) have shown how the information contained in the LOSVDs can constrain both the potential and the DF.

Likewise, in the axisymmetric case, Dehnen & Gerhard (1993) have calculated realistic smooth DFs and have shown that a similarly close relationship exists between the potential and internal kinematics on the one hand and the projected kinematics on the other. However, fits of axisymmetric libraries still pose some additional unanswered questions. Recently, Valluri, Merritt & Emsellem (2004) discussed the indeterminacy of the reconstruction of the potential in general axisymmetric systems from two- or three-dimensional data sets by studying the shape of the χ^2 -contours describing the quality of the orbital fit. Cretton & Emsellem (2004) argued that, even in the case of a mathematically non-degenerate $f(E, L_z)$ -system, an artificial degeneracy occurs, caused by the discreteness of the orbit library. They emphasised the role of appropriate smoothing, but did not provide a definite solution. Richstone et al. (2004) critically analysed their arguments and emphasised that both high quality comprehensive data sets and orbit libraries are needed to achieve a reliable modelling of axisymmetric systems.

In view of this discussion concerning orbit-based dynamical models it seems worthwhile to step back and investigate how well orbit libraries represent the phase-space structure of a given dynamical system. This includes an examination of the choice of orbits, which in the generic axisymmetric case is difficult, since part of the phase-space structure is unknown due to our ignorance about I_3 . Central to such an analysis are the orbital phase volumes, which accomplish the transformation from the relative contributions of individual orbits to the library, the so called orbital occupation numbers or orbital weights, into phase-space densities (and vice versa). The availability of such phase volumes offers several applications:

- (i) Accurate phase volumes allow the calculation of internal and projected properties such as density and velocity profiles, line-of-sight velocity distributions (LOSVDs) etc. of general axisymmetric DFs $f(E, L_z, I_3)$ via orbit libraries. Besides the possibility of systematically studying the structure of general axisymmetric systems, these profiles provide a direct check on the choice of orbits through a comparison with the profiles calculated from directly integrating the DFs.
- (ii) From any fitted library one can reconstruct the corresponding DF via the phase volumes, and thus reconstruct the DF from any observed early-type galaxy in the axisymmetric approximation.

- (iii) If the library is fitted to some reference data constructed from a DF, then
 - (ii) allows an investigation of how closely the fit matches the input DF, and thus an effective regularisation scheme can be implemented, permitting real (noisy) data sets to be fitted.

Vandervoort (1984) touched on the problem by establishing the transformation from cells of integrals to the corresponding phase-space volumes. However, the resulting relations are only suitable for explicitly known integrals, for example for single orbits only in the rare case in which all integrals are known. For components integrated about the unknown integrals they have been applied by, for example, Rix et al. (1997), Cretton et al. (1999) and Verolme & de Zeeuw (2002).

The aim of this paper is to introduce a general implementation for the calculation of individual orbital phase volumes in any axisymmetric potential, and, by following applications (i) and (iii) to prove that our libraries accurately map given dynamical systems. This directly supports our setup of the library and sets the basis for our project to recover the dynamical structure and mass composition of a sample of flattened early-type galaxies in the Coma cluster. In a subsequent paper we will focus on the question of how much smoothing has to be applied in order to obtain an optimal estimate of the dynamical system underlying a given set of noisy and spatially incomplete observational data. The full analysis of the data set (Mehlert et al. 2000; Wegner et al. 2002) will be addressed in a future publication.

The paper is organised as follows. In Section 2.2 we define all quantities related to the library used in the subsequent Sections and describe our orbit sampling. Section 2.3 outlines the relation between orbital weights and orbital phase-space densities. Section 2.4 contains a description of our implementation to calculate individual orbital phase-space volumes. In a first application, we calculate internal and projected properties of given DFs using orbit libraries in Section 2.5. Section 2.6 we discuss how the library is fitted to given data sets, and in Section 2.7 we reconstruct reference DFs from their projected kinematics. Finally, in Section 2.8 we summarise the results.

2.2 The orbit library

Our method of setting up the orbit libraries used for the dynamical modelling is based on the procedure presented in Richstone et al. (in preparation). There, the reader finds a description of the basic properties of the program. In this section we define quantities that are used later on in this paper.

In the following we assume that the luminosity density ν is known. In an analysis of real data it has to be obtained by deprojection of the measured photometry. With the stellar mass-to-light ratio $\Gamma = M/L$, the mass density ρ_l of the luminous material follows from ν as $\rho_l = \Gamma \nu$.

The total mass density ρ possibly includes a dark component ρ_{DM} and reads

$$\rho = \rho(\Gamma, r_c, v_c) = \Gamma \nu + \rho_{\text{DM}}. \quad (2.1)$$

Once the mass-profile is fixed, the potential Φ follows by integrating Poisson’s equation. With Φ known, a large set of orbits is calculated, sampling homogeneously the phase-space connected with Φ .

2.2.1 Spatial and velocity binning

As described in Richstone et al. (in preparation) we divide the meridional plane into bins, equally spaced in $\sin \vartheta^1$, linear in r near the inner boundary r_{\min} of the library, and logarithmic at the outer boundary r_{\max} . (If not stated otherwise, we use $N_r = 20$ radial bins, $N_\vartheta = 5$ angular bins.) For the projection of the library we use the same binning as for the meridional plane. Every spatial bin in the plane of the sky is subdivided into N_{vel} bins linearly spaced in projected velocity between $-v_{\max}$ and v_{\max} , leading to a bin size for the LOSVDs of

$$\Delta v_{\text{LOSVD}} = 2 \frac{v_{\max}}{N_{\text{vel}}}. \quad (2.2)$$

Even if the potential is spherical, our spatial binning tags an axis of symmetry. Later, when referring to a “minor-axis” we always mean the axis $\vartheta = 90^\circ$ of the library.

2.2.2 Orbital properties

Luminosity. The normalised contribution of orbit i to the luminosity in spatial bin $1 \leq j \leq N_r \times N_\vartheta$, dL_i^j , equals the fraction of time the orbit spends in bin j . Let Δt_i^k denote the k th time-step in the integration of orbit i , so that

$$t_i^k \equiv \sum_{h \leq k} \Delta t_i^h \quad (2.3)$$

is the total time elapsed until time-step k , and

$$\mathcal{J}^j \equiv \{k : (r(t_i^k), \vartheta(t_i^k)) \in \text{bin}(j)\} \quad (2.4)$$

contains all time-steps during which orbit i is located in spatial bin j . Accordingly, we can write

$$dL_i^j = \sum_{k \in \mathcal{J}^j} \frac{\Delta t_i^k}{T_i}, \quad (2.5)$$

with $T_i \equiv \sum \Delta t_i^k$ being the total integration time of orbit i .

Given the orbit’s weight w_i to the whole library – the integrated luminosity along the orbit – the total luminosity of the library in spatial bin j reads

$$dL^j = \sum_i w_i dL_i^j. \quad (2.6)$$

¹Throughout the paper, we use spherical coordinates (r, ϑ, φ) , with $\vartheta = 0^\circ$ corresponding to the equatorial plane. If not stated otherwise, we use superscripts or subscripts h, i, j, k as indices, l, m, n as exponents.

Internal velocity moments. To obtain the internal velocity moments $\langle v_r^l v_\vartheta^m v_\varphi^n \rangle$ of the orbit library, we store for each orbit i and each time step Δt_i^k the product of velocities $v_r^l v_\vartheta^m v_\varphi^n$ and fractional time $\Delta t_i^k / T_i$. All contributions in spatial bin j are summed to yield

$$\langle v_r^l v_\vartheta^m v_\varphi^n \rangle_i^j \equiv \sum_{k \in \mathcal{J}^j} v_r^l v_\vartheta^m v_\varphi^n \frac{\Delta t_i^k}{T_i}. \quad (2.7)$$

Thus for the whole library the velocity moments in spatial bin j follow as

$$\langle v_r^l v_\vartheta^m v_\varphi^n \rangle^j = \frac{1}{dL^j} \sum_i w_i \langle v_r^l v_\vartheta^m v_\varphi^n \rangle_i^j. \quad (2.8)$$

Projected kinematics. For the projected kinematics of the library we record the normalised contribution to the kinematics LOSVD_i^{jk} at projected position j and projected velocity $1 \leq k \leq N_{\text{vel}}$ for every orbit. Again, for the whole library the LOSVD reads

$$\text{LOSVD}^{jk} = \sum_i w_i \text{LOSVD}_i^{jk}. \quad (2.9)$$

By fitting a Gauss-Hermite series to the LOSVD_i^{jk} we obtain the Gauss-Hermite parameters (Gerhard 1993; van der Marel & Franx 1993),

$$\text{GHP}^{jk} = \{\gamma^{jk}, v^{jk}, \sigma^{jk}, H_3^{jk}, H_4^{jk}\}, \quad (2.10)$$

of the LOSVD.

2.2.3 Choice of orbits

To obtain a reliable representation of phase-space it is important that any allowed combination of the integrals of motion (E, L_z, I_3) is represented to some degree of approximation by an orbit in the library. The absence of some orbit family in the library might cause certain dynamical configurations to be misleadingly emphasised in the final fit.

Sampling E and L_z . Richstone et al. (in preparation) adjust the orbit sampling in (E, L_z) -space according to their spatial binning. From the requirement that every pair of grid bins $r_i \leq r_j$ in the equatorial plane should be connected by at least one equatorial orbit with $r_{\text{peri}} = r_i$ and $r_{\text{apo}} = r_j$ they derive a unique grid of orbital energies E and z-angular momenta L_z . We experimented with doubling the number of pericentres and/or apocentres per radial bin, but found, that the above-described method yields a sufficiently dense sampling of the (E, L_z) -plane.

Sampling I_3 . It is common practice in the various existing Schwarzschild codes to sample I_3 by dropping orbits at given energy E and angular momentum L_z from the zero-velocity-curve [ZVC, defined by $E = L_z^2/(2r^2 \cos^2 \vartheta) + \Phi(r, \vartheta)$]. Richstone et al. (in preparation) use the intersections of the angular rays of the meridional grid with the ZVC as starting points. This sampling ensures that each sequence of orbits with common E and L_z contains at least one orbit that is roughly confined to the region between the equatorial plane and each angular ray of the meridional grid.

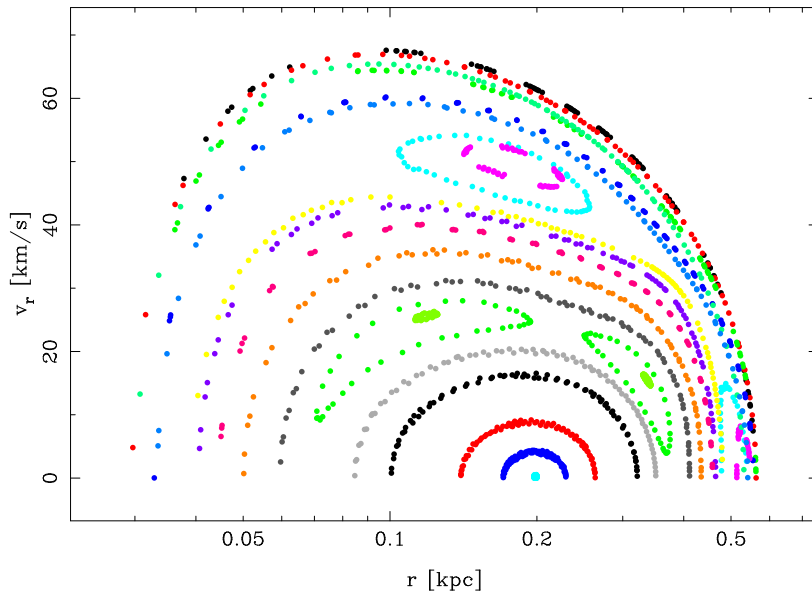


Figure 2.1: Example of a surface of section for a flattened Hernquist model (details in the text). All orbits have been integrated for $N_{\text{SOS}} = 80$ intersections with the SOS.

If we consider only those potentials symmetrical about the equatorial plane with $d\Phi/dz > 0$, then every orbit eventually crosses the equatorial plane and leaves a footprint in the surface of section (SOS) given by the radii r and radial velocities v_r of the upward equatorial crossings. Orbits respecting a third integral show up in the SOS as nested invariant curves, sometimes with embedded resonances (e.g. Binney & Tremaine 1987). Fig. 2.1 shows an example of a SOS. The dots mark representative points of invariant curves obtained by numerically following orbits with common E and L_z in a flattened Hernquist potential with total mass $M = 10^{11}M_{\odot}$, scaling radius $r_s = 10$ kpc and a flattening of $q = 0.5$ (see Sect. 2.5.1 below for further details).

The SOS encompasses all available orbital shapes, and a representative sampling of orbits should result in the SOSs being homogeneously filled with orbital imprints. Unfortunately, we are not aware of any simple relationship between

the drop-point of an orbit on the ZVC and its corresponding appearance in the SOS, as long as I_3 is not known explicitly. In order to guarantee a representative collection of orbits in any potential, we sample the orbits as follows.

In a first step we drop orbits from the (outer) intersections of the angular rays of our spatial grid with the ZVC as described in Richstone et al. (in preparation). Then, for any pair (E, L_z) included in the library we choose N_L radii r_l , $1 \leq l \leq N_L$ equally spaced in $\log(r)$ on the equatorial plane between r_{peri} and r_{apo} of the equatorial radial orbit with energy E and angular momentum L_z . We start with the smallest of these radii r_l and launch an orbit i from the equatorial plane with the maximal radial velocity

$$v_{r,i} = \sqrt{2[E - \Phi(r_l)] - \frac{L_z^2}{r_l^2}} \equiv v_{\text{max}}(E, L_z, r_l). \quad (2.11)$$

For the subsequent orbits i' we step-wise decrease $v_{r,i'}$ by $\Delta v_{r,i'}$ (see equation 2.13 below) until we reach $v_{r,i'} = 0$ and pass over to the next radius r_{l+1} .

With (E, L_z) and $(r_l, v_{r,i})$ fixed, the orbital $v_{\vartheta,i}$ is determined by

$$v_{\vartheta,i}(E, L_z, r_l, v_{r,i}) = \sqrt{2[E - \Phi(r_l)] - v_{r,i}^2 - \frac{L_z^2}{r_l^2}}. \quad (2.12)$$

When $v_{r,i} = 0$, then $v_{\vartheta,i}(E, L_z, r_l, v_{r,i}) = v_{\text{max}}(E, L_z, r_l)$. For each velocity pair we launch an orbit from the equatorial plane at the actual r_l with the actual velocities $v_{r,i}$ and $v_{\vartheta,i}$. This procedure is repeated for each of the N_L radii. If, at a specific launch position, we find an imprint in the SOS of a previously integrated orbit that differs from the current launch position by less than 10 per cent in radius and radial velocity, we regard this part of the SOS as already sampled and discard the orbit.

The velocity step-size $\Delta v_{r,i}$ is set as

$$\Delta v_{r,i} = \min \{ \Delta v_{\text{LOSVD}}, \xi v_{m,i-1} \}, \quad (2.13)$$

where Δv_{LOSVD} is the width of the LOSVD bins (cf. equation 2.2), and

$$v_{m,i} = \max_{1 \leq s \leq N_{\text{SOS}}} \{ v_i^s : (r_i^s, v_i^s) \in \text{SOS} \}. \quad (2.14)$$

Here SOS denotes the set of the N_{SOS} orbital imprints in the SOS and i is the index of the actual orbit. We usually take $\xi = 1/3.5$. From trying different values for N_L we found that $N_L = 30$ was sufficient to yield a dense filling of the SOS with approximately one invariant curve crossing the r -axis of the SOS in each of the equatorial meridional grid bins.

The velocity step-size is largest for the radial orbits and gradually decreases when the SOS is filled with orbits (note that $v_{m,i-1}$ is the maximum of the radial velocities in the SOS of the ‘‘precursor’’ orbit $i - 1$). For the shell orbits, the step-size becomes smallest. The adjustment of the step-size in each step ensures that we sample the more radial orbits with a resolution that corresponds at least

to the width of the LOSVD bins and that the sampling is refined for the shell orbits. The shell orbits have a large ϑ -motion and need to be included in the library to avoid a radially biased collection of orbits.

After the above sampling, we measure the maximum f_s of all $r_{\min,i}/r_{\max,i}$, with

$$r_{\min,i} = \min_{1 \leq s \leq N_{\text{SOS}}} \{r_i^s : (r_i^s, v_i^s) \in \text{SOS}\} \quad (2.15)$$

and $r_{\max,i}$ defined analogously. To ensure that the sequence contains all orbits up to (approximately) the thin-shell orbit, we complete the library if necessary by launching orbits from the equatorial plane with $v_r = 0$ at

$$r = \frac{3r_{\min,i'} + r_{\max,i'}}{4}, \quad (2.16)$$

where $f_s = r_{\min,i'}/r_{\max,i'}$, until $f_s > 0.9$.

Fig. 2.1 illustrates for a flattened Hernquist potential the dense coverage of the SOS with invariant curves after all orbits are integrated.

2.2.4 Use of the library

If the relative contribution of each orbit to the whole library, the orbital weight w_i , is specified, then according to equations (2.6), (2.8) and (2.9) the library provides a specific model including the LOSVDs, internal density distribution, internal velocity moments and so on of this particular orbit superposition.

If the library is constructed to test whether or not a given trial mass distribution leads to a consistent model of an observed galaxy, then the model and in particular the LOSVDs have to be compared with the observations. If the comparison turns out not to yield a satisfactory fit, then either the weights can be recalculated (see Section 2.6 for details) or the actual mass distribution has to be rejected. If, on the other hand, the fit shows that the actual set of weights seems to be a valid model of the galaxy, then one can reconstruct the internal velocity structure and DF from the w_i .

Conversely, if one has a DF at hand and wants to calculate, for example, its projected kinematics without going through the appropriate integrals, one can assign the orbital weights according to the DF (see Section 2.5) without any fitting procedure and analyse the output of the library. This can be useful in systematic studies of the projected properties of stationary axisymmetric distribution functions depending on all three integrals (E, L_z, I_3).

In the following we will make use of both applications with the goal of investigating the accuracy of our orbit libraries.

2.3 Orbital weights and phase-space densities

In order to reconstruct the DF from the library or to calculate spatial profiles of internal or projected properties of some given DF, it is necessary to convert orbital weights into phase-space densities and vice versa. This section summarises

the connection between orbital weights and orbital phase-space densities under the regime of Jeans' theorem.

2.3.1 Phase-space densities of orbits

Consider a system in which the orbits respect n integrals of motion I_1, \dots, I_n . Because the phase-space density of stationary systems is constant along individual orbits (Jeans' theorem), the phase-space density along orbit i is given as the orbital weight w_i divided by the phase-space volume V_i . More formally, let \mathcal{I} denote the n -dimensional set of orbital integrals (I_1, \dots, I_n) , let \mathcal{V} denote the 6-dimensional phase-space, $\mathcal{P}(\mathcal{V})$ its power set, and let $\xi : \mathcal{I} \rightarrow \mathcal{P}(\mathcal{V})$ map a n -tuple of orbital integrals $(I_1, \dots, I_n) \in \mathcal{I}$ onto the hypersurface $\xi(I_1, \dots, I_n) \subseteq \mathcal{V}$ in phase-space covered by the corresponding orbit,

$$\xi(I_1, \dots, I_n) \equiv \{p \in \mathcal{V} : I_1(p) = I_1, \dots, I_n(p) = I_n\}. \quad (2.17)$$

With $\mathcal{U}_i \subseteq \mathcal{I}$ being the small cell in integral space represented by the orbit i ,

$$\begin{aligned} \mathcal{U}_i \equiv \{ & (I_1, \dots, I_n) \in \mathcal{I} : I_1 \in [I_{1,i} - \Delta I_{1,i}, I_{1,i} + \Delta I_{1,i}], \\ & \dots, I_n \in [I_{n,i} - \Delta I_{n,i}, I_{n,i} + \Delta I_{n,i}] \} \end{aligned} \quad (2.18)$$

we define the characteristic function

$$\chi_i \equiv \begin{cases} 1 & : (r, \vartheta, \varphi, v_r, v_\vartheta, v_\varphi) \in \mathcal{O}_i \\ 0 & : (r, \vartheta, \varphi, v_r, v_\vartheta, v_\varphi) \notin \mathcal{O}_i \end{cases} \quad (2.19)$$

of the image set

$$\mathcal{O}_i \equiv \bigcup_{\mathcal{W} \in \xi(\mathcal{U}_i)} \mathcal{W} \quad (2.20)$$

of \mathcal{U}_i in phase-space. The volume of the phase-space region represented by orbit i then follows as

$$V_i = \int \chi_i d^3r d^3v \quad (2.21)$$

and accordingly the phase-space density along the orbit reads

$$f_i \equiv \frac{w_i}{V_i}. \quad (2.22)$$

2.3.2 Orbital weights from DFs

If we reverse the application of equation (2.22), and assign the orbital weights according to some given DF f ,

$$w_i = f_i V_i, \quad (2.23)$$

with $f_i \equiv f(I_{1,i}, \dots, I_{n,i})$ now being the DF f evaluated at the orbit's position in integral space, then the DF f_{lib} of the entire library, which consists of the combined contributions of all orbits

$$f_{\text{lib}} = \sum_i f_i \chi_i, \quad (2.24)$$

will be the mapped version of f onto the library. Equation (2.23) together with equations (2.6), (2.8) and (2.9) can be used to calculate the LOSVDs, internal velocity profiles and density distribution of any axisymmetric DF with known potential.

2.4 Orbital phase volumes

Two degrees of freedom. Binney, Gerhard & Hut (1985) have shown that, for autonomous Hamiltonian systems with two degrees of freedom the phase volume of any orbit can be derived from the SOS by integrating the times between successive orbital visits of the SOS:

$$V \approx \Delta E \int_{\text{SOS}} T(r, v_r) dr dv_r, \quad (2.25)$$

where $T(r, v_r)$ is the time the orbit needs from (r, v_r) to the next intersection with the SOS, and ΔE defines a small but finite cell around the orbit's actual energy E characterising the hypersurface in phase space represented by the orbit.

Axisymmetric case. Richstone et al. (in preparation) carry over this result to axisymmetric systems and approximate the phase volumes as

$$V \approx \Delta L_z \Delta E \int_{\text{SOS}} T(r, v_r) dr dv_r. \quad (2.26)$$

Here ΔL_z and ΔE stand for the range of energies and angular momenta represented by the orbit under consideration. Equation (2.26) is valid whether the orbit is regular or chaotic.

Calculating the SOS-integral. In what follows we describe our novel implementation of equation (2.26) which improves on the method of Richstone et al. (in preparation) to deliver higher precision phase-space volumes.

For all orbits in a sequence with common energy E and angular momentum L_z we obtain a representative sample \mathcal{S} of the SOS by storing N_{sos} imprints of each orbit in the SOS given by the radial positions and velocities² at the times $t_i^{k(s)}$ of the orbital equatorial crossings:

$$\mathcal{S} \equiv \left\{ (r_i^s, v_i^s) : r_i^s \equiv r(t_i^{k(s)}), v_i^s \equiv |v_r(t_i^{k(s)})|, \right. \\ \left. E_i = E, L_{z,i} = L_z, 1 \leq s \leq N_{\text{sos}} \right\}. \quad (2.27)$$

Typically, we integrate each orbit up to $N_{\text{sos}} = 80$ intersections with the SOS and choose $N'_{\text{sos}} = 60$ points for the calculation of the phase volumes randomly out of the whole set of intersections. We also store the time intervals

$$t(r_i^s, v_i^s) \equiv t_i^{k(s+1)} - t_i^{k(s)} \quad (2.28)$$

²To reduce the computational effort we take the absolute value of the radial velocities, thereby exploiting the symmetry of the SOS with respect to the r -axis in our application.

between two successive intersections.

Inspection of Fig. 2.1 shows that only a tessellation approach can be used to numerically integrate equation (2.26) in the general case, including regular, resonant and chaotic orbits. To this end we decided to perform a Voronoi tessellation of \mathcal{S} using the software of Shewchuk (1996). This tessellation uniquely allocates a polygon to each element of \mathcal{S} . The edges of the polygon are located on the perpendicular bisections of pairs containing the element under consideration and one of its neighbours, and are equidistant to the actual pair and a third element. For almost all elements the polygons are closed and encompass an area containing the actual element and all points that are closer to it than to any other element. The areas enclosed by the polygons completely cover the space between the elements and therefore characterise the fractional area inside the SOS occupied by each orbit.

Fig. 2.2 shows the same SOS as Fig. 2.1. The open circles represent r and v_r at the orbital equatorial crossings. The thin lines around these circles mark the Voronoi cells allocated to the elements of \mathcal{S} and the solid dots show boundary points (see below).

With ΔA_i^s denoting the surface area inside the polygon around $(r_i^s, v_i^s) \in \mathcal{S}$, the integral expression in the phase volume of orbit i (cf. equation 2.26) can be approximated³ as

$$\int_{\text{SOS}} T(r, v_r) dr dv_r \approx \sum_s t(r_i^s, v_i^s) \Delta A_i^s. \quad (2.29)$$

At the boundary of the distribution of sampled points, there may not be enough neighbours around a given element of \mathcal{S} to close its polygon. In order to ensure that every Voronoi polygon is closed and confined to an area enclosed by the ZVC of the SOS (given by v_r of equation 2.11) we construct an envelope around the distribution of sampled orbital intersections. In Fig. 2.2 the points of the envelope are marked by the solid dots. They are constructed as follows.

The first step is to determine the maximum \hat{v}_0 of radial velocities in \mathcal{S} :

$$\hat{v}_0 \equiv \max \{v_r : (r, v_r) \in \mathcal{S}\}. \quad (2.30)$$

To ensure that no Voronoi cell exceeds below the axis $v_r = 0$, all imprints in the SOS with $v_i^s \leq \epsilon \hat{v}_0$ are mirrored about the axis $v_r = 0$ (typically $\epsilon = 0.1$). For the rest of the SOS we construct an envelope in an iterative loop starting from

$$(\hat{r}_0, \hat{v}_0) \equiv (r, v_r) \in \mathcal{S}, v_r = \hat{v}_0. \quad (2.31)$$

In each iteration $n + 1$ we search for $(\hat{r}_{n+1}, \hat{v}_{n+1}) \in \mathcal{S}$ obeying

$$\hat{v}_{n+1} = \max \{v_r : (r, v_r) \in \mathcal{S}, r > \hat{r}_n\}. \quad (2.32)$$

³Note that the Poincaré map of the SOS onto itself is area-preserving, and ΔA_i^s should be independent of s . The Voronoi tessellation, however, yields only approximately constant ΔA_i^s . Nevertheless, as Section 2.5 shows, the resulting phase volumes are of high accuracy.

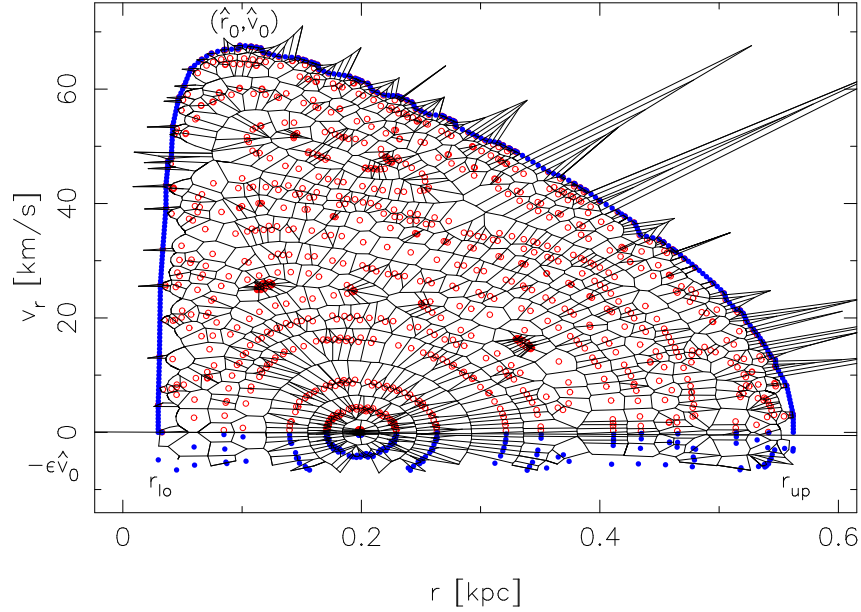


Figure 2.2: A Voronoi tessellation of the SOS of Fig. 2.1. Open circles mark individual intersections of orbits with the SOS; solid dots are points added to make the Voronoi cells well behaved at the boundaries.

The envelope consists of points densely sampled from the line segment connecting (r'_n, v'_n) and (r'_{n+1}, v'_{n+1}) , where the prime indicates that the coordinates are slightly shifted outwards, i.e. $r'_n = (1 + \delta)\hat{r}_n$ and $v'_n = (1 + \delta)\hat{v}_n$, with a typical value of $\delta = 0.01$. The loop eventually stops after N iterations at $\hat{r}_N = r_{\text{up}}$ and is followed by an analogous procedure running from \hat{r}_0 to r_{lo} to complete the envelope along the left part of the SOS. The points on the envelope are used as additional seeds for the Voronoi tessellation.

As Fig. 2.2 shows, the apposition of the boundary points as described above ensures that all orbital Voronoi cells are closed and confined to an area roughly bounded by the outermost invariant curve of the SOS. The definition of the boundary is purely geometrical and is insensitive to numerical uncertainties in the orbit integration. The spiky cells along the upper boundary belong to seeds of the envelope and do not affect the calculation of the orbital phase volumes.

The Voronoi tessellation used to approximate the integral expression in equation (2.26) via equation (2.29) defines a robust method to calculate the relative phase volume of any orbit inside a particular sequence of orbits with common E and L_z , including resonances and chaotic orbits. The areas assigned to the individual orbital imprints in the SOS completely fill the area below the ZVC of the SOS. Thus, a cruder sampling of the SOS is compensated by larger individual orbital phase volumes. In the limit of an infinitely dense sampling, the assigned “phase-space weights” obtained by the tessellation approach single-orbit phase

volumes.

Calculating $\Delta E \Delta L_z$. For a complete determination of the phase volumes we also need the relative contribution of a whole sequence of orbits with common (E, L_z) as compared with other sequences with different energies and angular momenta. These are described by the factors $\Delta L_z \Delta E$ of the orbital phase volumes (cf. equation 2.26). They are in fact equal for all orbits in the same sequence and need to be calculated only once for each sequence.

Fig. 2.3 shows an example of the (E, L_z) -plane of a typical library. The dots show the grid of sampled orbital energies and angular momenta. Each dot represents a sequence of orbits with common E and L_z but different I_3 . To calculate $\Delta L_z \Delta E$ for a particular sequence, we construct a quadrangle around the sequence's (E, L_z) and estimate the product $\Delta L_z \Delta E$ as the surface area enclosed by this quadrangle. The thin lines in Fig. 2.3 show the boundaries of these quadrangles, which are constructed as follows.

As described in Section 2.2.1, the grid in (E, L_z) -space is derived from the requirement, that for every pair $r_i < r_j$ of equatorial grid bins, the library contains at least one equatorial orbit with $r_{\text{peri}} = r_i$ and $r_{\text{apo}} = r_j$. Consider now a sequence of orbits with $(E_{\text{seq}}, L_{z,\text{seq}})$ and corresponding $r_{\text{peri,seq}}$ and $r_{\text{apo,seq}}$ of the equatorial orbit. In (E, L_z) -space all sequences inside the boundary of the sampled area are surrounded by four other sequences having both their pericentre and their apocentre in adjacent spatial bins. Let $r_{\text{peri},j}$ and $r_{\text{apo},j}$, $1 \leq j \leq 4$, denote the corresponding pericentres and apocentres of the equatorial orbits of these sequences. We construct a quadrangle around the sequence $(E_{\text{seq}}, L_{z,\text{seq}})$ by connecting the energies and angular momenta of four fictitious orbit sequences characterised by the pericentre $\hat{r}_{\text{peri},j}$ and apocentre $\hat{r}_{\text{apo},j}$ of their equatorial orbits:

$$\hat{r}_{\text{peri},j} = \frac{1}{2}(r_{\text{peri},j} + r_{\text{peri,seq}}) \quad (2.33)$$

and

$$\hat{r}_{\text{apo},j} = \frac{1}{2}(r_{\text{apo},j} + r_{\text{apo,seq}}). \quad (2.34)$$

The sequences with the largest apocentres and the smallest pericentres are surrounded by less than four sequences having both their pericentre and their apocentre in adjacent spatial bins. For these sequences we calculate the edges of the quadrangle as if there were further sequences around, whose energies and angular momenta follow from our spatial grid at smaller radii than r_{min} and larger radii than r_{max} .

Sequences with $r_{\text{peri,seq}} \approx r_{\text{apo,seq}}$ (lying on the upper boundary of the sampled area in Fig. 2.3 and usually containing only one, approximately circular, orbit) are also not surrounded by four sequences as described above. For these sequences we take the $(E_{\text{seq}}, L_{z,\text{seq}})$ of the actual sequence as the upper right edge of the quadrangle.

As can be seen in Fig. 2.3 the quadrangles around the sequences' energies and angular momenta completely cover the sampled part of the allowed area in

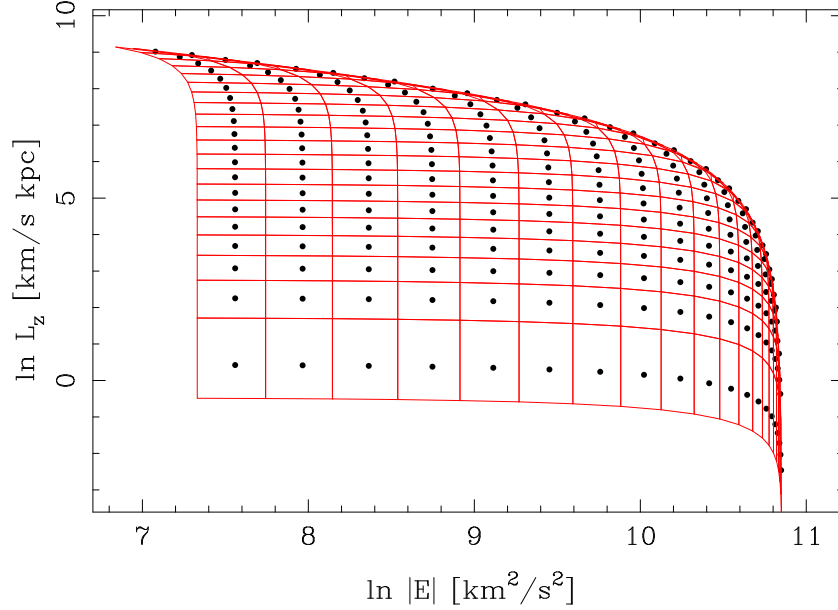


Figure 2.3: Typical distribution of sampled energies E and angular momenta L_z of an orbit library. The thin red lines show the boundaries of small cells assigned to each sequence. Their surface area is taken to estimate $\Delta E \Delta L_z$. The potential equals that of Figs. 2.1 and 2.2.

(E, L_z) -space below the curve $L_z(E) = L_{z,\text{circ}}$. They give a reasonable measure of the fractional area in (E, L_z) -space, occupied by each orbit sequence.

2.5 Mapping distribution functions onto the library

In this section we describe how to use the phase volumes from the previous Section to calculate internal and projected properties of stationary DFs using an orbit library. To this end, starting with a density profile ρ and a stationary distribution function f_ρ connected to ρ via $\rho = \int f_\rho d^3v$, a library is constructed as described in Section 2.2. Instead of fitting the library to the kinematics of f_ρ ,

$$\text{LOSVD}_f(v_{\text{los}}) = \frac{1}{\rho} \int f_\rho d^2v_\perp, \quad (2.35)$$

we *assign* an appropriate weight to each orbit such that the superposition of all orbits represents f_ρ (see Section 2.3.2 above). We then compare the internal density distribution ρ_{lib} and the anisotropy profile β_{lib} , as well as the projected kinematics GHP_{lib} , obtained from the library with the same properties ρ , β and GHP calculated directly from the DF (see Sections 2.5.1 and 2.5.2). Thereby

we can check to what accuracy the orbit library reproduces a *given* dynamical system.

2.5.1 Spherical γ -models

As a first reference case, we explore spherical γ -models.

Properties of the input model. The stellar body of the reference model is constructed from γ -models (Dehnen 1993) with density

$$\rho_\gamma(r) = \frac{M}{4\pi} \frac{r_s(3-\gamma)}{r^\gamma(r_s+r)^{4-\gamma}}. \quad (2.36)$$

These models approximate the de Vaucouleurs law of ellipticals quite well for $\gamma \in [1, 2]$. The DF is assumed to be of the Osipkov-Merritt type $f_{\text{OM}} = f_{\text{OM}}(E - L^2/2r_a^2)$ (Osipkov 1979; Merritt 1985a,b). The corresponding systems are isotropic inside the anisotropy radius r_a , at $r \ll r_a$, and radially anisotropic at $r \gg r_a$:

$$\beta \equiv 1 - \frac{\sigma_\theta^2 + \sigma_\phi^2}{2\sigma_r^2} = \frac{r^2}{r^2 + r_a^2}. \quad (2.37)$$

We tested various combinations of the parameters (γ, r_s, r_a) . However, since the conclusions drawn from the comparisons do not depend strongly on γ , the following contains only a discussion of the results for the Hernquist model ($\gamma = 1$), where the DF can be written in terms of elementary functions and reads (Hernquist 1990)

$$f(E, L) \propto \frac{1}{8(1-q^2)^{5/2}} - 3 \arcsin q + (1-2q^2) \left[q\sqrt{1-q^2}(8q^4 - 8q^2 - 3) + \frac{r_s^2}{r_a^2} q \right] \quad (2.38)$$

with $q = \sqrt{r_s(E - L^2/2r_a^2)/GM}$.

Comparison of model and library. Fig. 2.4 shows the GHPs, density and anisotropy profiles of a library with $\approx 2 \times 8800$ orbits, extending from $\approx 5 \times 10^{-4} r_s$ to $\approx 28 r_s$. For this library we used a closed meshed sampling containing two different pericentres for each radial bin. The weights for the orbits were directly derived from equation (2.23) and the Hernquist DF of equation (2.38) with $r_s = 10.5 \text{ kpc}$, a total mass of $M = 7.5 \times 10^{11} M_\odot$, and $r_a = \infty$ (isotropic model). The big dots show the expected kinematics, density and anisotropy of the Hernquist model. The GHPs were obtained by first calculating the LOSVDs at the position of the corresponding spatial bin from the DF using the method described in Carollo, de Zeeuw & van der Marel (1995) and then fitting a Gauss-Hermite (GH) series to the LOSVDs. For the density distribution and anisotropy we used equations (2.36) and (2.37), respectively.

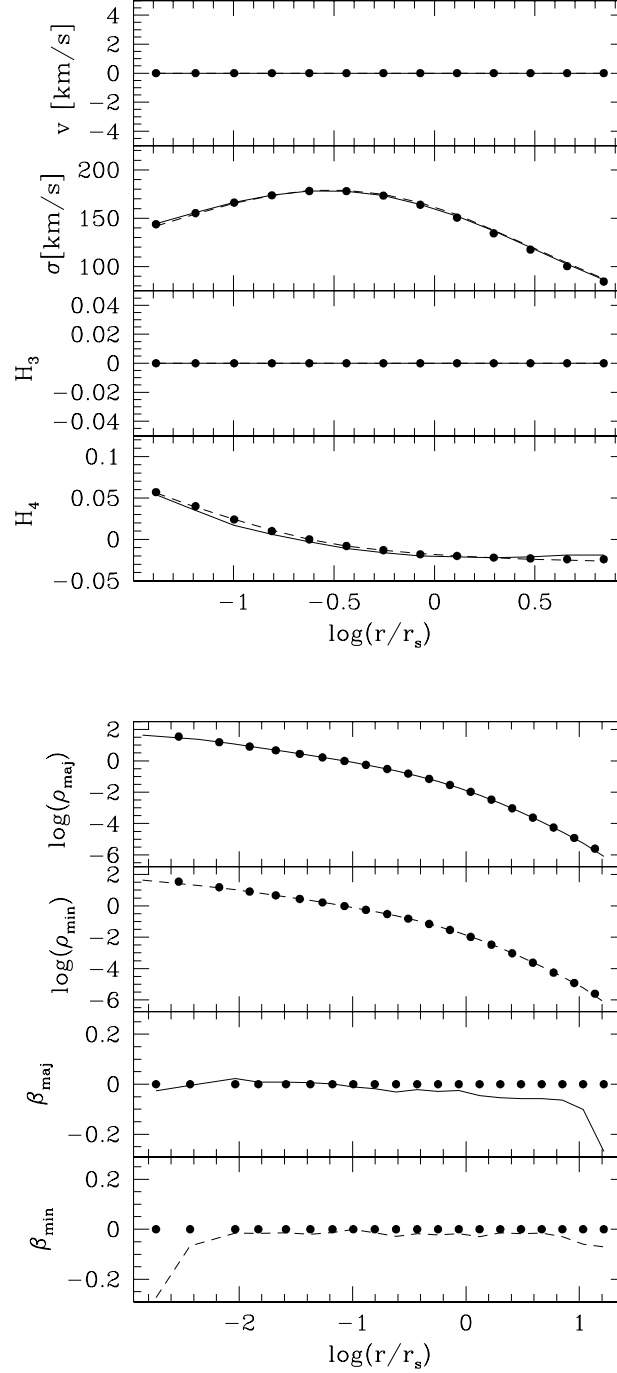
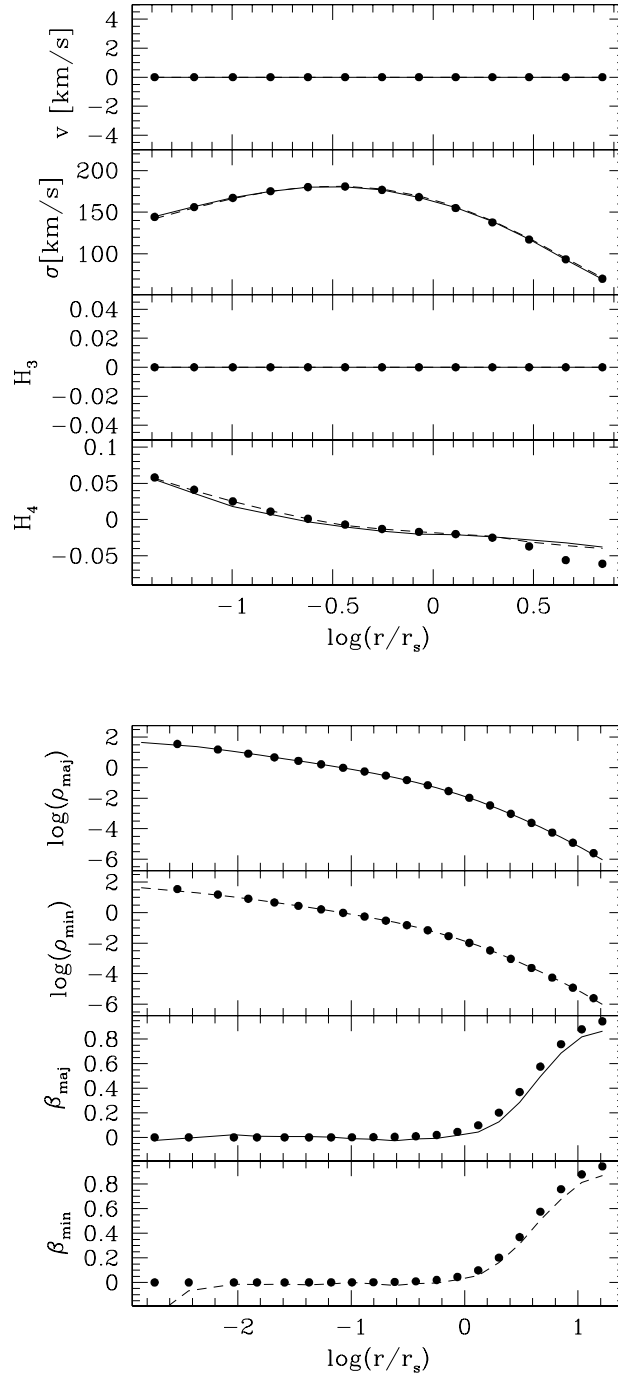


Figure 2.4: Comparison of a Hernquist model (big dots) and a library with weights directly derived from the spherical, isotropic Hernquist DF (lines). The upper panel shows the projected kinematics along the major axis (solid line) and minor axis (dashed line). The lower panel shows the density distribution (upper two rows, $[\rho] = M_{\odot}/\text{pc}^3$) and the anisotropy parameter (lower two rows) for the minor and major axis, respectively.

Figure 2.5: As Fig. 2.4, but for an anisotropic Hernquist model with $r_a = 4 r_s$.

As the figure shows, the library is able to reproduce the GHP and internal density distribution of the model to a high degree of accuracy. The mean fractional difference in σ is below $\Delta\sigma < 1$ per cent and the mean difference in H_4 is below $\Delta H_4 < 0.01$. The largest deviations between model and library occur in the anisotropy profile with $\text{rms}(\beta) = 0.06$ (taken over a whole angular ray). The individual differences, however, are smaller than $\Delta\beta = 0.1$ over almost the whole spatial range covered by the library. Near the inner and outer boundaries of the library the orbit sampling becomes incomplete, with mostly radial orbits coming either from outside the outer boundary or from inside the inner boundary are missing. Consequently, the anisotropy of the library is lower than in the isotropic reference model.

Fig. 2.5 is as Fig. 2.4, but for an anisotropic Hernquist model with $r_a = 4 r_s$. It confirms the results from the isotropic model. The offset in the H_4 -profiles at large radii is due to errors in the GH fit. At these radii the resolution of our LOSVD-bins is too low to give reliable GHPs. However, the match of the individual LOSVDs itself is as good as at smaller radii.

Again the largest deviations show up in the β -profiles, with a mean $\text{rms}(\beta_{\text{hern}} - \beta_{\text{lib}}) = 0.03$. As in the isotropic case the differences between model and library increase when approaching the edges of the library, where the radial velocity dispersion of the library is systematically lower than expected.

2.5.2 Flattened Plummer model

We now go one step further and use a *flattened* test object, namely the flattened Plummer model of Lynden-Bell (1962a) (normalised such that in the spherical limit M defines the total mass of the model):

$$\rho_{\text{pl}}(r, \vartheta) = \frac{M\lambda^{-9/4}}{4\pi} [(3a^2 - 2b^2)(r^2 + a^2)^2 + (4a^2 - b^2)b^2r^2 \cos^2(\vartheta)], \quad (2.39)$$

$\lambda = (r^2 + a^2)^2 - 2b^2r^2 \cos^2(\vartheta)$. The parameters a and b describe the extension of the core and the flattening. The part of the distribution function that is even in L_z is

$$f_{\text{pl}}(E, L_z) = \frac{\sqrt{2}}{4\pi^{3/2}} \left[\frac{\Gamma(6)}{\Gamma(\frac{9}{2})} D E^{\frac{7}{2}} + \frac{\Gamma(10)}{\Gamma(\frac{15}{2})} C L_z^2 E^{\frac{13}{2}} \right], \quad (2.40)$$

$C \propto (3a^2 - 2b^2)$ and $D \propto 5b^2(2a^2 - b^2)$. The Plummer models do not rotate as long as the uneven part of f_{pl} vanishes and prograde and retrograde orbits exactly balance each other.

Comparison of model and library. Fig. 2.6 shows a flattened Plummer model with $a = 5.0$ kpc, $b = a/2$ and $M = 7.5 \times 10^{11} M_\odot$ (big dots) and profiles obtained from a library with $\approx 2 \times 4400$ orbits, extending from $\approx 10^{-3} a$ to $\approx 20 a$ (solid and dashed lines as in Figs. 2.4 and 2.5). The weights were derived

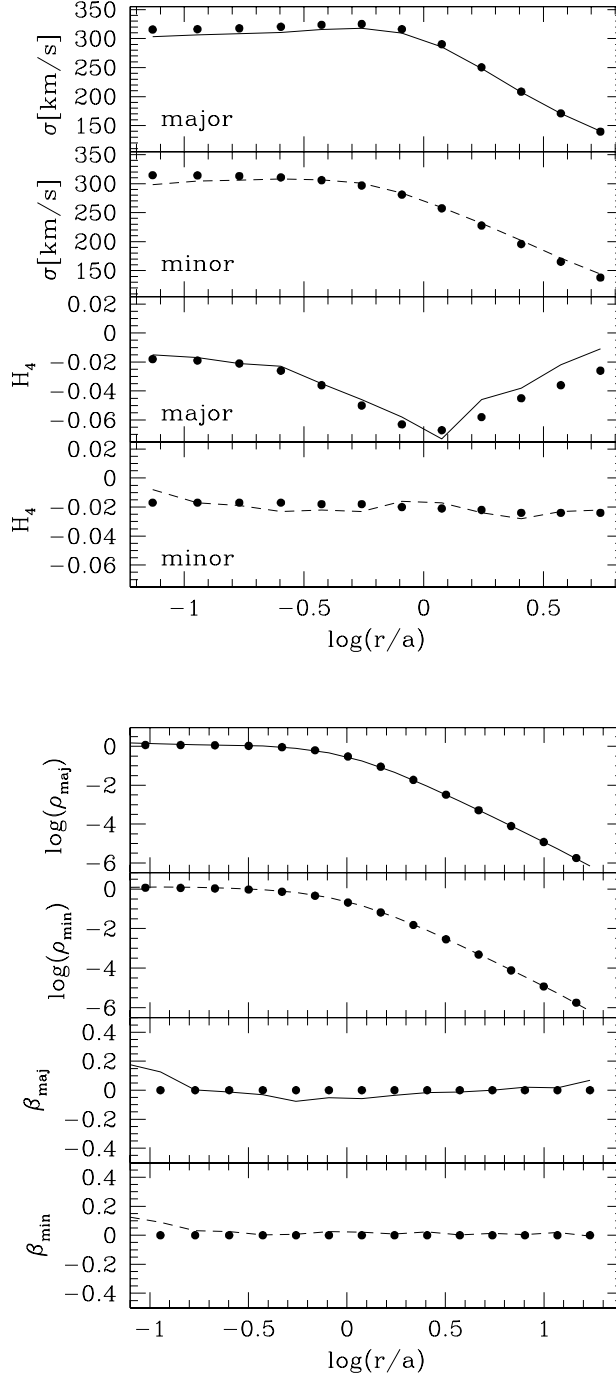


Figure 2.6: Comparison of a flattened Plummer model (big dots) and a library with weights directly derived from the DF (lines). Upper panel: projected kinematics along the major axis (solid lines) and minor axis (dashed lines). Only moments independent from the uneven part of the DF are shown. Lower panel: density distribution (upper two rows, $[\rho] = M_{\odot} \text{pc}^{-3}$) and the anisotropy parameter (lower two rows) for the two axes.

from f_{pl} via equation (2.23). The kinematics along the major and the minor axis have been calculated from higher order Jeans equations (Magorrian & Binney 1994). Before the GH parameters were determined, the projected moments were integrated along a 3.6-arcsec wide major-axis slit and a 2.0-arcsec wide minor-axis slit. (Note that for the axisymmetric case we take $\beta = 1 - \sigma_{\vartheta}^2/\sigma_r^2$.)

As in the spherical case, the Gauss-Hermite parameters of the projected kinematics are reproduced to better than a few percent. Deviations in the outer parts of the H_4 -profile stem from the GH-fit and are not seen in the LOSVDs. The density distribution is also well reproduced down to $\approx a/10$, and the anisotropy parameter is $|\beta| < 0.1$ from the outer edge of the library down to $\approx a/10$.

2.5.3 Changing the spatial coverage of the library

The library only discretely represents a finite part of the available phase space. To check how this affects the accuracy of the calculation of phase-space integrals of a given DF with the library, we did the profile comparisons described in Sections 2.5.1 and 2.5.2 for libraries with different spatial extents and for different resolutions in the space of orbital integrals.

The upper panel of Fig. 2.7 shows σ and H_4 along the major and the minor axis for the isotropic Hernquist model (big dots). The four lines show the outcome of four libraries with different spatial coverages. For the solid line $r_{\text{min}} = 2.5 \times 10^{-4}$, $r_{\text{max}} = 10$ (in units of the effective radius); for the dotted line $r_{\text{min}} = 2.5 \times 10^{-3}$, $r_{\text{max}} = 10$; for the short dashed line $r_{\text{min}} = 2.5 \times 10^{-4}$, $r_{\text{max}} = 5$; and for the long dashed line $r_{\text{min}} = 2.5 \times 10^{-3}$, $r_{\text{max}} = 5$.

As expected, the less extended libraries fail to reproduce the innermost or outermost data points. In the vicinity of the equatorial plane (along the major axis and at the central parts of the minor axis), the library becomes dominated by azimuthal motion when approaching r_{min} or r_{max} , since orbits coming from further outside or inside are missing. Consequently, the LOSVDs are too flat (H_4 too small) as compared with the expectations (see for example the outermost parts of the dashed lines of the libraries with small r_{max} along the major axis, and the innermost parts of the long-dashed and dotted lines of the libraries with large r_{min} in the minor-axis H_4 -profile).

The effect can also be seen in the internal dynamical structure, which is illustrated in the lower panel of Fig. 2.7, where the anisotropy of the library with respect to φ and to ϑ is plotted:

$$\beta_{\varphi} \equiv 1 - \frac{\sigma_{\varphi}^2}{\sigma_r^2}, \quad \beta_{\vartheta} \equiv 1 - \frac{\sigma_{\vartheta}^2}{\sigma_r^2}. \quad (2.41)$$

Near the centre $\beta_{\varphi} < 0$ along the major and minor axes, confirming the dominance of φ -motion brought about by the dominance of orbits having their inner turning points there and consequently rotating rapidly around the axis of symmetry. The effect is less pronounced at the outer points of the major axis, where the effective potential of the meridional-plane motion is less dominated by the L_z -term.

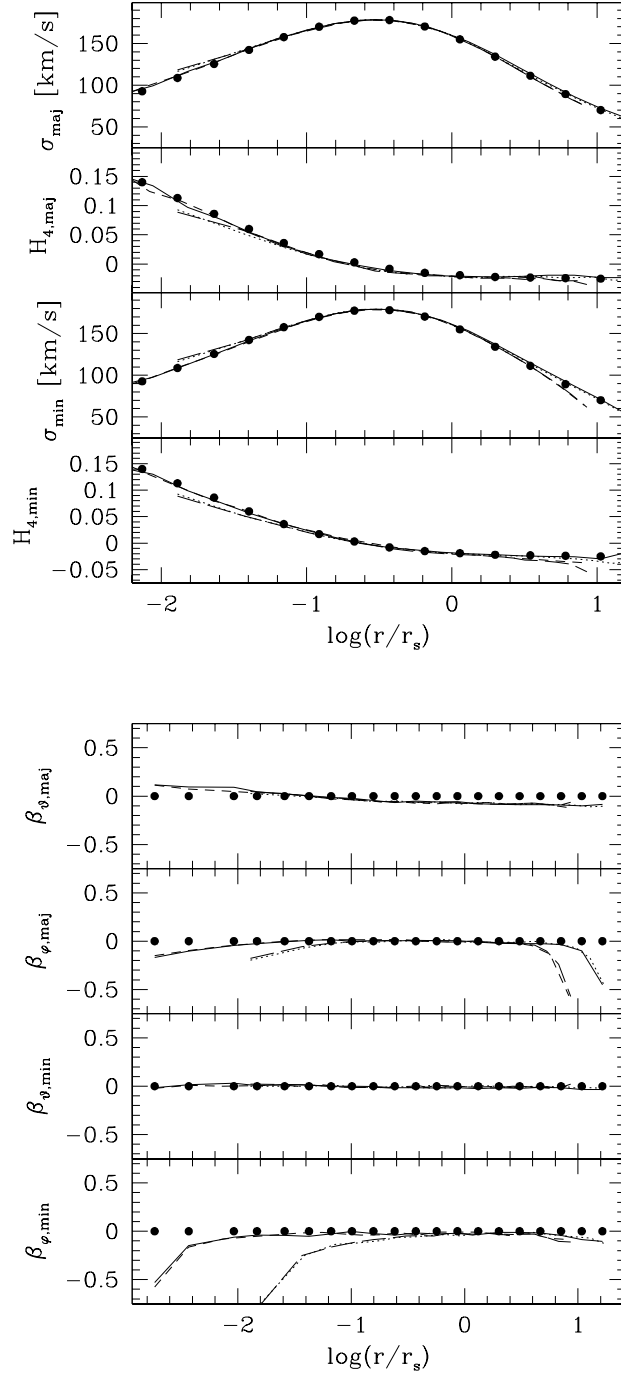


Figure 2.7: σ and H_4 (upper panel) and anisotropy (lower panel) along the major and minor axes for the isotropic Hernquist model (big dots) and four libraries with different spatial extension ($r_{\text{min}}/r_{\text{eff}}, r_{\text{max}}/r_{\text{eff}}$): ($2.5 \times 10^{-4}, 10$) solid line; ($2.5 \times 10^{-3}, 10$) dotted line; ($2.5 \times 10^{-4}, 5$) short dashed line; ($2.5 \times 10^{-3}, 5$) long dashed line.

The β_ϑ -profiles lack boundary effects because they are independent from the (E, L_z) -sampling and simply reflect the degree to which the SOSs are filled with orbital invariant curves.

Along the minor axis the agreement of library and model in projected σ is quite good. Near the centre the library's σ is enhanced because the orbits have their pericentre there.

2.5.4 Changing the number of orbits in the library

Fig. 2.8 shows the same comparison as Fig. 2.7, but for libraries in which we have omitted every second r_{peri} , resulting in only $\approx 2 \times 4700$ orbits per library. The overall appearance of Fig. 2.8 is quite similar to that of Fig. 2.7, but there are some minor differences. First, the scatter in the GHPs has increased slightly; however, the match of predictions and library is still on a level of a few percent.

The most striking difference is the increase of radial relative to azimuthal motion near the centre of the library. This probably reflects the fact that the pericentres of the orbit sequences are located at the inner edge of each radial bin. Therefore the most radial orbits, which contribute also significantly to v_ϕ near their turning points, move through the whole bin before turning around and thus raise the radial velocity dispersion. This effect is strongest in the centre, since our binning there becomes relatively large compared with the variation of the potential. The balance between radial and meridional motion is not affected by this resolution effect, because the sampling *inside* each sequence (in the SOS) is independent from the (E, L_z) -grid, and thus independent from the resolution of the sampled pericentres and apocentres.

2.6 Fitting the library

So far we have not tackled the problem of finding the orbital weights w_i according to some given kinematical constraints. This section contains a brief description of our use of the maximum entropy technique of Richstone & Tremaine (1988) to fit the library to some LOSVDs.

2.6.1 Maximum entropy technique

Given a set of kinematic constraints, we seek the orbital weights that best fit the library to the constraints. These weights are derived from the maximisation of an entropy-like quantity (Richstone & Tremaine 1988)

$$\hat{S} \equiv S - \alpha\chi^2, \quad (2.42)$$

where

$$\chi^2 = \sum_{j,k} \left(\frac{\text{LOSVD}(\text{lib})^{jk} - \text{LOSVD}(\text{data})^{jk}}{\Delta\text{LOSVD}(\text{data})^{jk}} \right)^2 \quad (2.43)$$

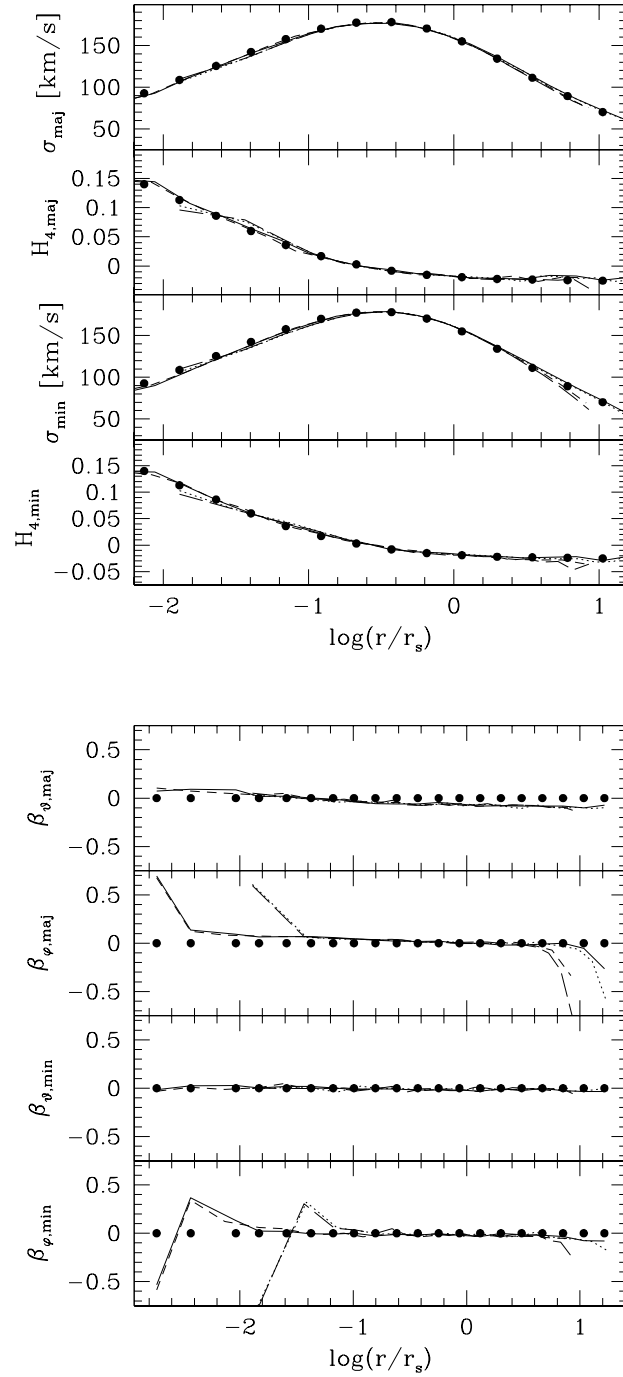


Figure 2.8: Same profiles as in Fig. 2.7, but the libraries have been set up with a coarser sampling with roughly half the number of orbits as compared with Fig. 2.7.

gives the departure between the predicted kinematics of the library LOSVD(lib) (cf. equation 2.9) and the data kinematics LOSVD(data). Note that the luminosity density ν is not fitted, but used as a boundary condition (see Richstone et al. in preparation for details). S is an approximation to the usual Boltzmann-entropy:

$$S \equiv \int f_{\text{lib}} \ln(f_{\text{lib}}) d^3r d^3v = \sum_i w_i \ln\left(\frac{w_i}{V_i}\right). \quad (2.44)$$

In the absence of any other condition, the maximisation of S forces the weights w_i to be proportional to the phase volumes V_i . This fact can be used to bias the library towards any set of predefined weights. If, for example, we substitute the phase volumes in equation (2.44) by $V_i \rightarrow f_i V_i$, then

$$S \rightarrow S' = \sum_i w_i \ln\left(\frac{w_i}{f_i V_i}\right), \quad (2.45)$$

and the maximisation of S' yields weights w_i proportional to $f_i V_i$. According to equation (2.23) the factors f_i can be chosen to bias the library towards any given DF f . The Boltzmann entropy corresponds to the case of equal a priori probabilities $f_i = f_j$ in phase space.

2.6.2 The smoothing parameter α

The smoothing parameter α controls the influence of the entropy S on the fitted weights. If α is small, the maximum of \hat{S} is less affected by χ^2 and the library gives a poor fit to the data. Consequently, it will not represent the true structure of the object to which it is fitted. If, on the other hand, α is large, the maximum of \hat{S} is largely determined by the minimum of χ^2 . In this case the library fits the noise in the data. The DF of the library is then highly unsmooth and again does not represent the true DF of the corresponding object.

The problem of how much smoothing has to be applied in order to obtain an optimal estimate of the true underlying DF for a given set of observational data with specific errors and spatial sampling will be the subject of a forthcoming paper. Here, we focus on illustrating the accuracy of our method to setup the orbit libraries. In the following, we will always choose α such that the library yields the best match to the input DF.

2.7 Reconstructing distribution functions from fitted libraries

In this Section we use the DFs of Section 2.5, but instead of exploiting equation (2.23) to *assign* the orbital weights and to compare spatial profiles of the library and the original DF, we now fit the library to the DF as follows. First, we calculate the density profile and GHPs connected with the DF:

$$\rho = \int f d^3v \quad (2.46)$$

and

$$\text{LOSVD}_f(v_{los}) = \frac{1}{\rho} \int f \, d^2v_{\perp} \quad (2.47)$$

where the GHPs are obtained from the LOSVDs as described in Section 2.5.1. We compose a library as described in Section 2.2 and fit it to the GHPs via the maximum entropy technique of Section 2.6. Finally, we compare the orbital weights $w_i(\alpha)$ resulting from the fit with those expected from the DF via equation (2.23). By showing that the fitted weights approximate the input DF over a large region in phase space, we justify the decision that we can use the degree to which the library approximates the DF as a criterion to determine the optimal amount of smoothing, a fact that we will exploit in a subsequent paper in more detail.

In order to find the best fit weights that minimise the χ^2 of Eq.(2.43), we derived error bars for the LOSVDs by first assigning error bars to the GHPs and then determining LOSVD errors by means of Monte Carlo simulations. The error for σ was chosen to increase linearly with r from 2 per cent at the innermost data point to 10 per cent at the outermost data point. For H_3 and H_4 the errors increase from 0.01 to 0.05. The definition of the errors is somewhat arbitrary since we do not add noise to the data points, but they are roughly comparable with real data error bars. Since $v = 0$ in the models, the error for v is set to $\Delta v = 2 \text{ km s}^{-1}$. A detailed investigation of the influence of realistic errors on the accuracy of the reconstructed internal properties of a fitted library will be presented in a forthcoming paper.

2.7.1 Hernquist model

Fig. 2.9 shows a comparison of characteristic properties of a library fitted to the kinematics corresponding to the dots in the upper panel and the original DF. The definition of the lines and dots as well as the input DF are the same as for Fig. 2.4, and the fit was obtained with $\alpha = 0.0046$. As expected, the match to the kinematics and the internal density profile is excellent after the fit. The anisotropy is smaller than $|\beta| < 0.1$ over a spatial region greatly exceeding the area where the LOSVDs were fitted. Only near the very centre does the minor-axis β -profile drop significantly because of the lack of radial orbits coming from inside the inner boundary of the library (cf. Section 2.5).

Fig. 2.10 shows the DF reconstructed from the fitted weights via equation (2.22) (dots) together with the input DF (thick line). Each dot represents the phase-space density along one single orbit, and the densities are scaled according to $\sum w_i = \sum V_i = 1$. Over a region covering 90 per cent of the library's mass, the rms difference between the Hernquist DF and the orbital phase-space densities is 12.1 per cent. The remaining departures between model and fit are mostly due to boundary effects arising from the discrete and finite nature of the library.

Fig. 2.11 shows the fractional differences of input model and library as a function of orbital energy E and angular momentum L_z . For each dot, the contributions of individual orbits with common E and L_z have been integrated.

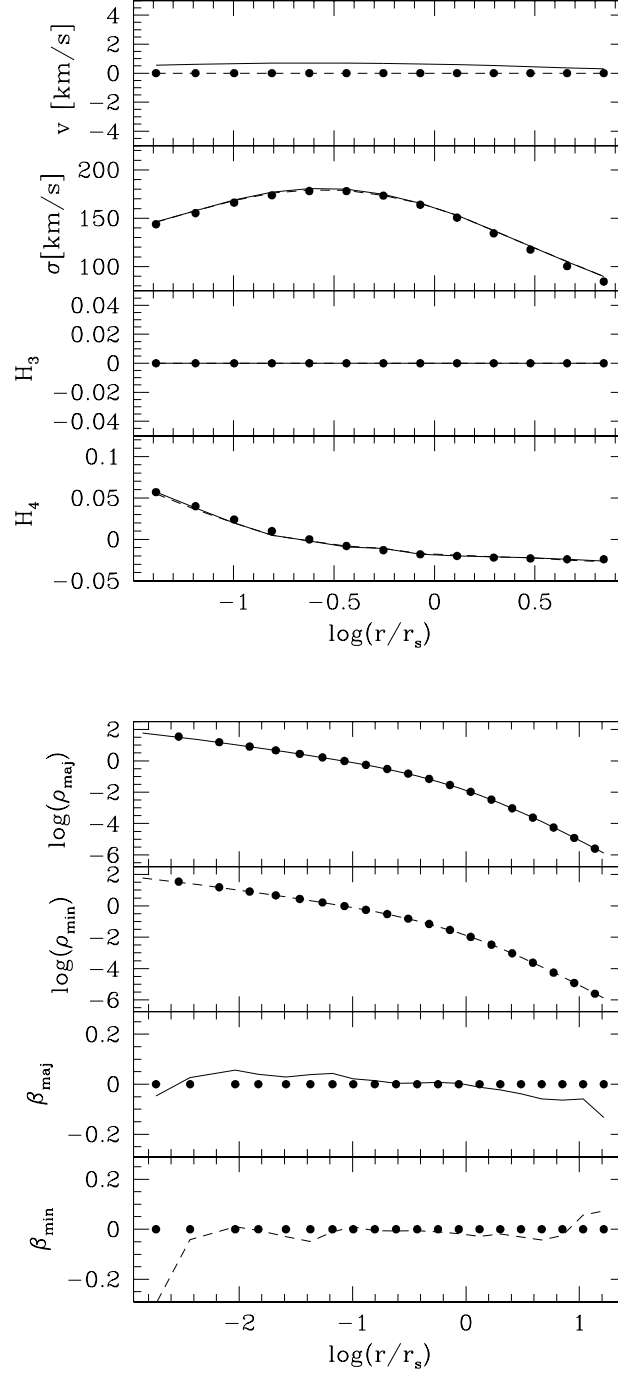


Figure 2.9: Comparison of a library fitted to the LOSVDs of a spherical, isotropic Hernquist DF (lines) and the Hernquist model itself (big dots). The upper panel shows the projected kinematics along the major axis (solid line) and minor axis (dashed line). The lower panel shows the density distribution (upper two rows, $[\rho] = M_{\odot} \text{pc}^{-3}$) and the anisotropy parameter (lower two rows) for the two axes.

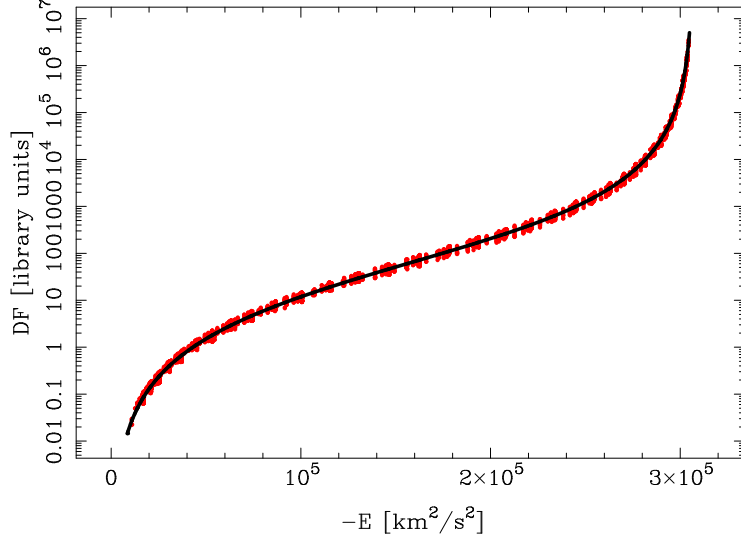


Figure 2.10: Comparison of the DF of a spherical Hernquist model (solid line, units defined in the text) with the phase-space densities obtained from a library fitted to GHPs along two perpendicular axes in the galaxy (details in the text). Each dot represents a single orbit. The rms between library and model is 12.1 per cent over a region covering 90 per cent of the library’s mass.

Larger dots correspond to larger differences between input DF and fitted library. From Fig. 2.11 it can be seen that the remaining deviations between library and input DF mostly stem from orbits lying at the boundary of the phase-space region covered by the library. Since the library only contains a finite number of all orbits, the fit to the kinematics with the density as a boundary condition enforces some redistribution of orbits as compared with the original DF. For example, at the outer boundary of the library ($E \approx 0$) the fitted orbital phase-space densities are too large as compared with the input DF. These orbits compensate the cut-off in energy and contain all the light that should have been distributed along even less bound orbits. For the same reason, the library fails to reproduce the Hernquist DF near the most bound orbits.

Fig. 2.12 shows the results when fitting the same library to the projected kinematics of the anisotropic Hernquist model with $r_a = 4r_s$, corresponding to the dots in the upper panel of the figure. Again, after the fit the library perfectly reproduces the internal density profile and the projected kinematics. The mismatch in the outer parts of the H_4 -profiles result from errors in the GHP fit (cf. Section 2.5.1). However, we do not fit the library to the GHP, but directly to the LOSVD. The β -profiles of the library follow the expected curves well inside the region covered by kinematical constraints. In the outer parts,

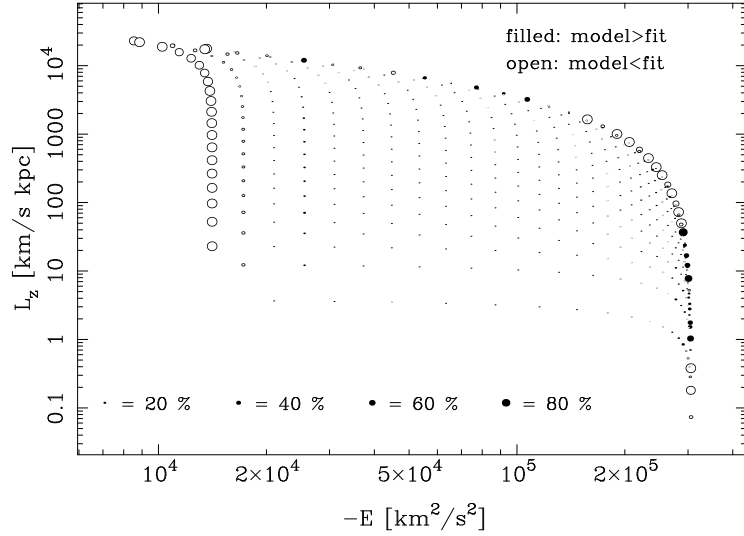


Figure 2.11: The fractional difference between a spherical Hernquist model and a fitted library as a function of orbital energy E and z -angular momentum L_z . Larger dots correspond to larger differences. For open dots the DF of the library overestimates the real DF, and for the solid dots it underestimates the DF.

however, they do not follow the input model to predominantly radial motion but turn back to an isotropic appearance. This is a reflection of the entropy maximisation used in the fit, which forces those parts of the library that are not constrained by data points to isotropy.

To confirm this effect of entropy maximisation, we refitted the library, but replaced the V_i in equation (2.44) by the weights of the anisotropic Hernquist DF following from equation (2.23). Since for the maximum entropy solution of equation (2.44) (without any other condition) the weights w_i are proportional to the values V_i , now being the weights of the anisotropic DF instead of the phase volumes, the fit is biased towards the anisotropic Hernquist model. The characteristics of the corresponding fit are displayed by the dotted lines in Fig. 2.12. The projected kinematics and internal density are indistinguishable from the maximum entropy fit, but now the anisotropy profile is in perfect agreement with the input model.

2.7.2 Flattened Plummer model

Fig. 2.13 shows the GHPs and internal density and anisotropy of the Plummer model with $b = a/2$ of Section 2.5.2, together with a fitted library containing $\approx 2 \times 4400$ orbits. The library was fitted to the LOSVDs corresponding to the

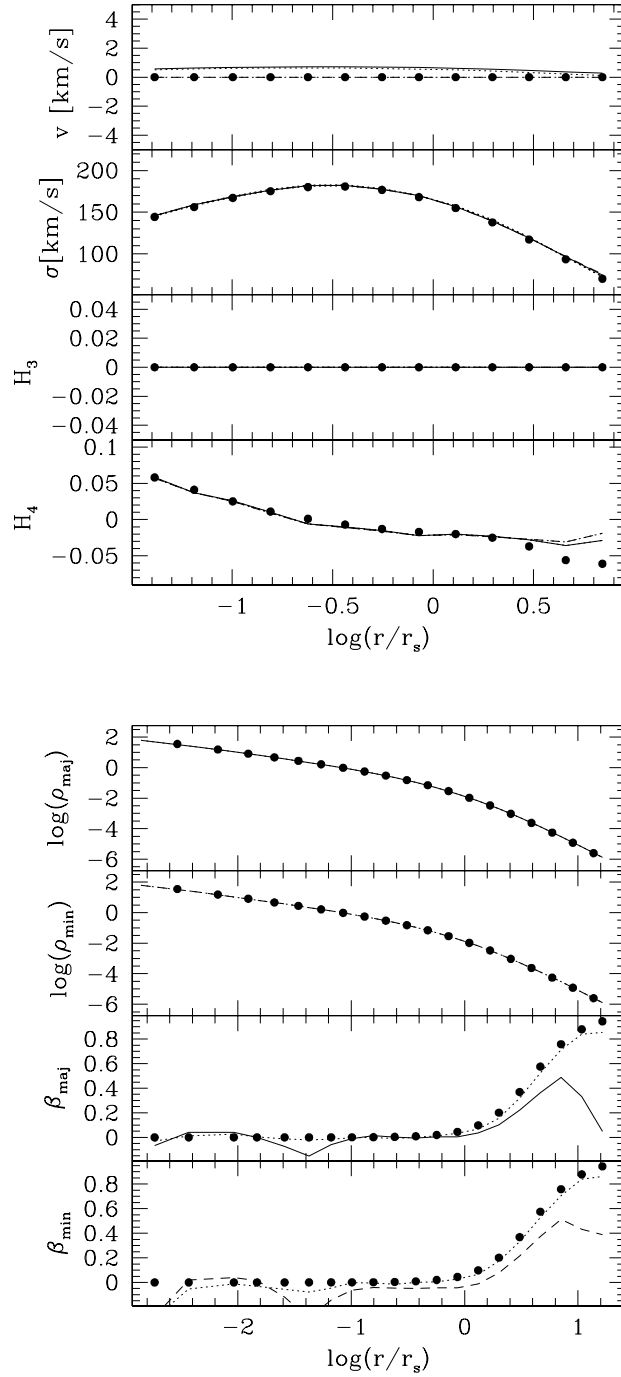


Figure 2.12: As Fig. 2.9, but for an anisotropic Hernquist model with $r_a = 4 r_s$. The dotted line shows the result of a fit with “biased weights” (see text for details).

dots of the upper panel of the figure with a smoothing parameter of $\alpha \approx 0.03$. The small deviations between the library's kinematics and the model in the upper panel of the figure are due to the low resolution in the GH fit and are not seen in the LOSVDs used for the fit. The anisotropy parameter is confined to $|\beta| < 0.1$ over all the region where the library is constrained by kinematic data.

The rms difference between the reconstructed DF and the input model is ≈ 15 per cent over a region covering 90 per cent of the library's mass. As Fig. 2.14 shows, differences between the model and library are confined to the boundaries of the sampled (E, L_z) -region of the phase space. As for the Hernquist model, the reason for these differences is the incomplete orbit sampling at the edges of the library.

2.8 Summary

We have presented a modified version of the Schwarzschild code of Richstone et al. (in preparation). The code involves a new orbit sampling at given energy E and angular momentum L_z and a new implementation for the calculation of the orbital phase volumes.

For our libraries we supplement the drop of orbits with common energy E and angular momentum L_z from the ZVC as described in Richstone et al. (in preparation) by scanning the SOS with a resolution that varies as the sampling progresses from the more radial to the more shell-type orbits. This sampling has been shown to completely fill the SOS connected with a pair (E, L_z) with orbital imprints.

A Voronoi tessellation of the SOSs of orbits with common E and L_z allows us to calculate the phase-space volumes of individual orbits in any axisymmetric potential. With the phase volumes we can convert the orbital weights describing the relative contribution of the orbits to the whole library into phase-space densities and vice versa. As a first application we use the densities to check our method of setting up the library in two different ways.

First, we calculate the spatial profiles of internal and projected properties of isotropic and anisotropic DFs of spherical γ -models as well as of the flattened Plummer model with the library. The density profiles, anisotropy profiles and projected kinematics of the library closely match those inferred directly from the corresponding DF. The errors in the higher-order GH parameters H_n , $\Delta H_n < 0.01$ for $n = 3, 4$, and the fractional error in the projected dispersion, $\Delta\sigma < 1$ per cent, are accurate on a level better than that of present-day observational errors. The largest deviations occur in the anisotropy profile, but are smaller than $\Delta\beta < 0.1$ at almost all positions in the library; however, they increase towards the edges of the spatial region that is covered by the orbits. This boundary effect is caused by the locally incomplete orbit sampling there. If in practical applications the libraries are constructed to extend beyond the area with observational constraints, these inaccuracies are negligible. Hence, our libraries fairly represent the phase-space structure of the models considered.

As a second application we *fitted* libraries to the GHPs of the same spherical

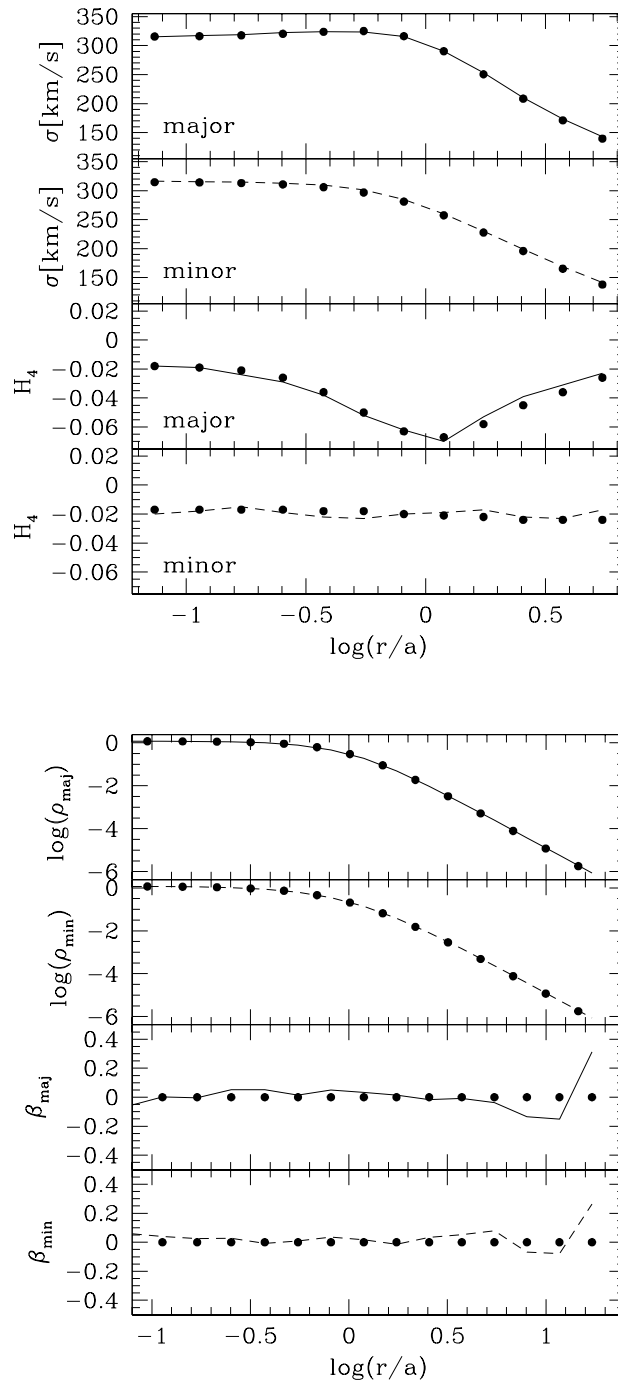


Figure 2.13: Comparison of a flattened Plummer model (big dots) and a fitted library (lines). The upper panel shows the projected kinematics along the major axis (solid lines) and minor axis (dashed lines). The lower panel shows internal moments along the minor and major axis, respectively (units as in Fig. 2.6).

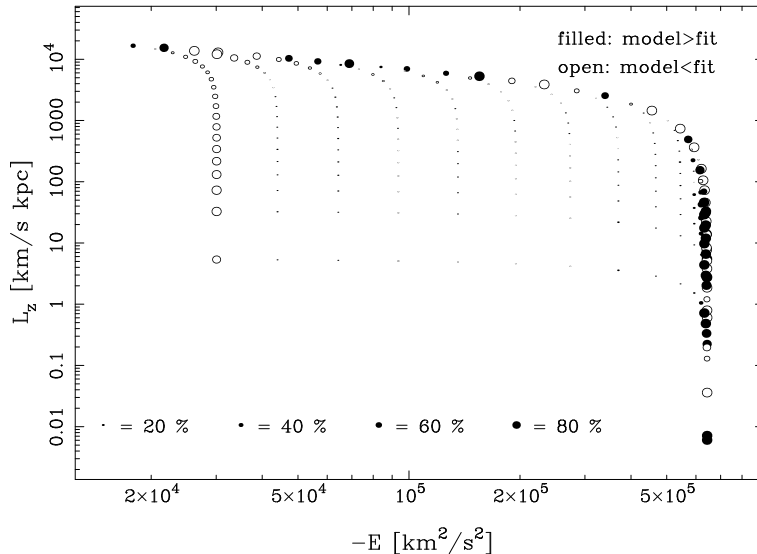


Figure 2.14: Deviations from the reconstructed DF of a fitted library and the Plummer DF of Fig. 2.13. Each dot represents one sequence of orbits with common E and L_z . For the open dots the DF of the library overestimates the real DF, and for the solid dots it underestimates it. Larger dots indicate larger differences.

γ -models and flattened Plummer models. The reconstructed DFs match the input DF with a rms of about 15 per cent over a region covering 90 per cent of the library's mass. The remaining deviations are mostly restricted to orbits at the boundary of the phase-space volume represented by the library. This is not unexpected since the library only discretely represents a finite subregion of the input system. Consequently some redistribution of orbits is necessary to compensate for orbits not included in the library.

We will investigate the influence of observational errors on the reconstructed DFs and of the amount of smoothing applied in the fit in a forthcoming publication. In a further step we will reconstruct the internal structure and mass composition of a sample of flattened early-type galaxies in the axisymmetric approximation.

Chapter 3

Regularised orbit models unveiling the stellar structure and dark matter halo of the Coma elliptical NGC 4807

3.1 Introduction

Interpreting the stellar kinematical data of ellipticals in terms of galaxy structural parameters requires knowing the gravitational potential as well as the distribution of stellar orbits, which – due to projection effects – is not directly given by observations. In equilibrium stellar systems, the phase-space distribution function (DF) describing the orbital state depends on phase-space coordinates only through the integrals of motion, admitted by the actual potential (Jeans theorem; e.g. Binney & Tremaine 1987).

In cases where integrals of motion can be expressed (or, approximated) in terms of elementary functions, the DF can be parametrised explicitly. Several round as well as a couple of flattened ellipticals have been modelled based on this approach (e.g. Dehnen & Gerhard 1994; Carollo et al. 1995; Qian et al. 1995; Dejonghe et al. 1996; Gerhard et al. 1998; Emsellem, Dejonghe & Bacon 1999; Matthias & Gerhard 1999; Statler, Dejonghe & Smecker-Hane 1999; Kronawitter et al. 2000; Saglia et al. 2000; Gerhard et al. 2001). On the other hand, the orbit superposition modelling technique of Schwarzschild provides fully general dynamical models for *any* axisymmetric or triaxial potential and has been successfully applied to a growing number of early-type galaxies (e.g. Rix et al. 1997; Cretton & van den Bosch 1998; Cretton, Rix & de Zeeuw 2000; Gebhardt

et al. 2000a; Cappellari et al. 2002; Verolme et al. 2002; Gebhardt et al. 2003; Romanowsky et al. 2003; Copin, Cretton & Emsellem 2004; Valluri, Merritt & Emsellem 2004; Krajnović et al. 2005).

Even if the number of dynamical models is steadily increasing, the only comprehensive investigation of elliptical galaxy DFs addressing the question of dark matter in these systems is still the basis-function based spherical modelling of 21 round galaxies by Kronawitter et al. (2000) and Gerhard et al. (2001). To extend the results found there and in the handful of studies of individual objects quoted above, we started a project aimed to probe a sample of *flattened* early-type galaxies in the Coma cluster, collecting major (Mehlert et al. 2000) and minor axis (Wegner et al. 2002) kinematical data. The goal is to investigate the dynamical structure and dark matter content of these galaxies.

Most present-day orbit superpositions, conceptionally based on the original implementation of Schwarzschild, do not automatically provide the entire phase-space DF, but only orbital occupation numbers or weights, respectively, characterising the total amount of light carried by each orbit. In principle, changing the orbit sampling strategy allows one to infer the DF from any orbit superposition (Häfner et al. 2000), but this approach has not yet been followed fully. To take advantage of both, the full generality of orbit superpositions and the availability of DFs, we extended the orbit superposition code of Richstone & Tremaine (1988) and Gebhardt et al. (2000a) to reconstruct phase-space DFs in the axisymmetric case (Thomas et al. 2004).

Recovering stellar DFs from photometric and kinematic observations – in particular the application of non-parametric methods like orbit superpositions – invokes regularisation in order to pick up smooth phase-space distributions (e.g. Richstone & Tremaine 1988; Merritt 1993). Different regularisation schemes have been applied in the context of orbit libraries, among them variants of minimising occupation number gradients in orbit space (Zhao 1996) and maximum entropy (Richstone & Tremaine 1988). The proper amount of regularisation has thereby commonly been adjusted to the data (e.g. Rix et al. 1997; Verolme et al. 2002; Richstone et al., in preparation).

One aim of this paper is to readdress the question of how much regularisation is needed to recover galaxy internal structural properties from observations with spatial sampling and noise typical for our sample of Coma galaxies. To this end we study observationally motivated reference models under realistic observational conditions and optimise regularisation with respect to the reconstruction of intrinsic input-model properties (see e.g. Gerhard et al. 1998; Cretton et al. 1999). By simulating and recovering reference galaxies we also determine to which degree the internal mass structure and orbital content are constrained by observational data in our sample. Furthermore χ^2 -statistics are measured to assign confidence intervals to real galaxy orbit superpositions.

To demonstrate the prospects of regularised orbit superpositions for our project we also present an application to one galaxy. We have chosen the faint giant E2 elliptical NGC 4807 ($M_B = -20.76$ for $H_0 = 69$ km/s/Mpc from Hyperleda) for the following reasons: (1) The galaxy has a prominent boxy photometric feature in the outer parts constraining its inclination. (2) Stel-

lar kinematic data reach out to $3 r_{\text{eff}}$ along the major axis probing its dark halo outside the galaxy main-body. (3) NGC 4807 lacks significant minor-axis rotation and isophotal twist and thus is an ideal target for axisymmetric modelling. (4) The galaxy is only mildly flattened and the dynamical models can be compared with earlier studies of similar galaxies done mostly in the spherical approximation.

The paper is organised as follows. Sec. 3.2 summarises the observations of NGC 4807, Sec. 3.3 outlines the orbit superposition technique. In Sec. 3.4 Monte-Carlo simulations performed to derive the optimal regularisation are described and the achieved accuracy of galaxy reconstructions follows in Sec. 3.5. Orbit models for NGC 4807 are presented in Secs. 3.6-3.8. The paper is closed with a combined summary and discussion of the results in Sec. 3.9.

3.2 NGC 4807: model input

In the following we assume a distance $d = 100$ Mpc to NGC 4807 (corresponding to $H_0 = 69$ km/s/Mpc) and take $r_{\text{eff}} = 6.7$ arcsec as its effective radius (Mehlert et al. 2000).

3.2.1 Photometric data

The photometric data are combined from two different sources. For the outer parts of NGC 4807 Kron-Cousins R_C band CCD photometry is drawn from Mehlert et al. (2000), consisting of profiles for the surface brightness μ_R , ellipticity ϵ and isophotal shape parameters a_4 and a_6 out to $\approx 5.5 r_{\text{eff}}$ (see Bender & Möllenhoff 1987 for a definition of a_n). A seeing of 2 arcsec during the observations causes the profiles to be unresolved in their central parts (at $d = 100$ Mpc one arcsec corresponds to 0.485 kpc). To increase the central resolution, the ground-based data are supplemented by corresponding profiles for μ_V , ϵ , a_4 and a_6 extracted from archival HST V band data (Principal Investigator: John Lucey; Proposal ID: 5997).

The two surface brightness profiles μ_R and μ_V are joined by shifting the HST V band according to the average $\langle \mu_R - \mu_V \rangle$ taken over the region $0.75 r_{\text{eff}} \leq R \leq 3 r_{\text{eff}}$, where both data sets overlap and seeing effects are negligible. The shift $\langle \mu_R - \mu_V \rangle$ is well defined with a rms of only 0.015 mag.

For the orbit models ground-based photometry is used outside $R \geq 3 r_{\text{eff}}$ and HST data inside $R < 3 r_{\text{eff}}$. Fig. 3.1 shows the combined μ_R , ϵ , a_4 and a_6 profiles applied for the modelling.

3.2.2 Deprojection

In the implementation of Schwarzschild's modelling technique used here, orbit models are not directly fitted to observed photometry. Instead, the deprojected luminosity density is used as a boundary condition for any orbit superposition (see Sec. 3.3.4).

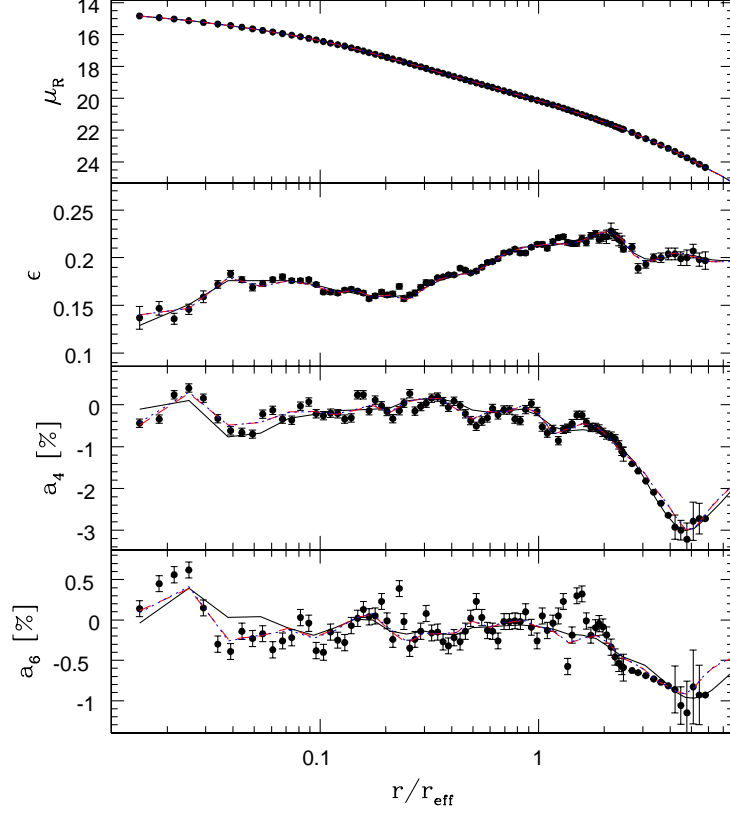


Figure 3.1: Photometric data for NGC 4807 (dots with error bars, from top to bottom: surface brightness μ_R , ellipticity ϵ , isophotal shape parameters a_4 and a_6) and three deprojections: edge-on deprojection (solid); $i = 50^\circ$ -deprojection (dashed); diskly $i = 50^\circ$ - deprojection (dotted).

Deprojection of axisymmetric galaxies is unique only for edge-on systems (inclination $i = 90^\circ$; Rybicki 1987). For any inclination $i < 90^\circ$ disk-like konusdensities can be added to the luminosity profile without affecting its projected appearance for any $i' < i$ (Gerhard & Binney 1996). From $i = 90^\circ$ to $i = 0^\circ$ the variety of different luminosity models projecting to the same galaxy image generally increases.

Deprojections for NGC 4807 are obtained with the program of Magorrian (1999). The code allows one to explore the full range of luminosity densities consistent with the photometric data by forcing the deprojection towards different internal shapes. For example, at any given inclination i the goodness of fit

of the deprojection can be penalised towards any degree of internal boxiness and diskiness, respectively. The deprojections are fitted without seeing-correction, since our joint photometry includes ground-based data only outside $R \geq 3 r_{\text{eff}}$, where seeing effects are negligible. Outside the last measured photometric data point ($R \geq 5.5 r_{\text{eff}}$), the photometry is extrapolated by a de Vaucouleurs profile fitted to the inner parts of the galaxy. The isophotes outside $R > 5.5 R_{\text{eff}}$ are assumed to be perfect ellipses with a constant flattening corresponding to the galaxy’s outermost measured ellipticity.

From the average flattening $\langle q \rangle = 0.8$ of NGC 4807 we expect an inclination angle $i > 38^\circ$. Lower viewing angles would require density distributions intrinsically flatter than E7, which are not observed. In Fig. 3.1 three representative deprojections are overplotted to the photometric data: the (unique) $i = 90^\circ$ -deprojection; a deprojection at $i = 50^\circ$ without any shape penalty; a disk $i = 50^\circ$ -deprojection. All three luminosity models are equally consistent with the data. The differences between the models are illustrated in Fig. 3.2, which displays the isophotal shape parameters and the corresponding isophotes of the deprojections as they appear viewed from edge-on. At this viewing angle internal density distortions show up the strongest.

As Fig. 3.2 reveals, both deprojections at $i = 50^\circ$ are heavily boxy around $R \approx 2 r_{\text{eff}}$ ($a_4 \approx -10$ per cent for the deprojection without shape preference and $a_4 \approx -8$ per cent for the disk deprojection). These distortions are a reflection of the drop in a_4 at $R > 3 r_{\text{eff}}$ in the data of NGC 4807. Projected density distortions progressively strengthen in deprojection from $i = 90^\circ$ to $i = 0^\circ$ and assuming $i = 50^\circ$ already causes a considerable amplification. Near the centre – where the observed isophotes are consistent with being purely elliptical – the disk deprojection appears smoother with on average larger a_4 , albeit lacking the strong a_4 -peak occurring in the deprojection without shape preference at $R = 0.05 r_{\text{eff}}$.

We have constructed orbit models for both, the $i = 90^\circ$ and the non-disk $i = 50^\circ$ deprojections, but the heavily distorted density distributions at $i = 50^\circ$ lead us to expect that we likely view NGC 4807 close to edge-on.

3.2.3 Kinematic data

The kinematic data are described in Mehlert et al. (2000) and Wegner et al. (2002). They consist of two long-slit spectra for the major and the minor axis, respectively. Profiles of lower order Gauss-Hermite coefficients γ_0 , v , σ , H_3 and H_4 (Gerhard 1993; van der Marel & Franx 1993) parameterising the line-of-sight velocity distribution (LOSVD) reach out to $3 r_{\text{eff}}$ along the major-axis and out to $0.6 r_{\text{eff}}$ along the minor-axis. Our orbit models are not directly fitted to the observed Gauss-Hermite parameters, but to binned LOSVDs. Therefore the Gauss-Hermite parameters are transformed into suitable LOSVDs as follows. First, the Gauss-Hermite series according to the observed γ_0 , v , σ , H_3 and H_4 is evaluated at 1000 values of line-of-sight velocity v_{los} , linearly spaced in the range $-4\sigma \leq v_{\text{los}} \leq 4\sigma$. At each of the sampled projected velocities error bars ΔLOSVD are assigned to the LOSVD from the errors in the corresponding

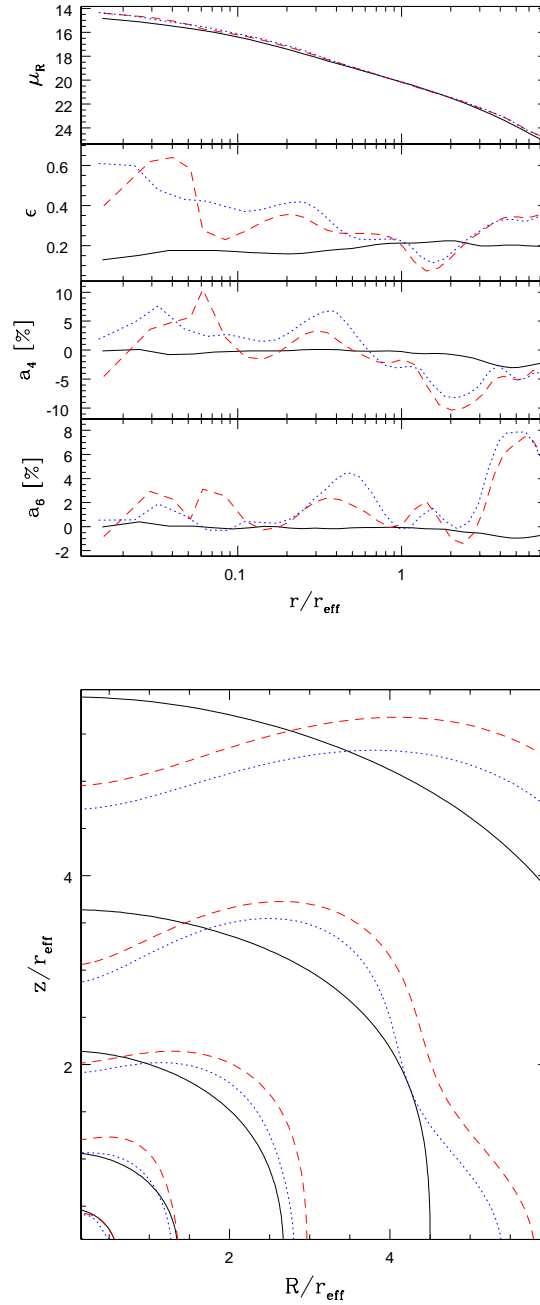


Figure 3.2: Projected appearance of the three deprojections shown in Fig. 3.1 when seen edge-on. The top panel shows isophotal shape parameters (cf. Fig. 3.1), the bottom panel displays the corresponding isophotes. Solid: $i = 90^\circ$ deprojection; dashed: $i = 50^\circ$ -deprojection; dotted: disk $i = 50^\circ$ -deprojection.

Gauss-Hermite parameters by means of Monte-Carlo simulations. The LOSVD is then binned appropriately for comparison with the orbit library (see Sec. 3.3.1 below).

For NGC 4807, the scatter in kinematical data from different sides of the galaxy is mostly negligible compared with the statistical errors in the data. Therefore, the orbit models are fitted to a symmetrized data set, derived by averaging the Gauss-Hermite parameters from each side. The largest scatter appears in the outermost major-axis H_4 -measurement. To infer the impact of its uncertainty on the reconstructed DF, we separately refitted the mass model that most closely matches the symmetrized data set, to the kinematics of the two different sides of NGC 4807. Both fits lead to similar models in terms of DF and internal kinematical structure, suggesting that the asymmetry in this single measurement does not largely affect our results.

3.3 Orbit superposition models

Our method of setting up orbit libraries to construct best fitting models is described in detail in Richstone et al. (in preparation) and in Thomas et al. (2004). Here, we only briefly outline some aspects of the method relevant to the present paper.

To recover the mass distribution of a given galaxy by orbit libraries, a grid of (parameterised) trial potentials is probed. In each trial potential (Sec. 3.3.2) a large set of orbits is calculated (Sec. 3.3.3) and an orbit superposition is constructed that best matches the observational constraints (Sec. 3.3.4). The best-fitting mass parameters with corresponding errors then follow from a χ^2 -analysis.

3.3.1 Basic grids

For comparison with observations the meridional plane of the orbit model as well as its projection onto the plane of the sky are divided into bins in radius r and polar angle ϑ . The grid in radius is logarithmic in the outer parts and becomes linear in the inner parts; the angular bins cover equal steps in $\sin \vartheta$ (see Richstone et al, in preparation, for details). For NGC 4807 the models are calculated in $N_r \times N_\vartheta = 200$ bins with $N_r = 20$ and $N_\vartheta = 10$. Each spatial bin of the model's sky-projection is subdivided into $N_{\text{vel}} = 15$ bins in projected velocity for the purpose of fitting the library to the observed kinematics.

3.3.2 Luminous and dark mass distributions

Luminous matter. We assume that the luminous mass of NGC 4807 is sufficiently characterised by a constant stellar mass-to-light ratio Υ (see also Sec. 3.9 and Fig. 3.22 for a verification of this assumption). The stellar mass density then reads $\Upsilon \nu$, where the luminosity density ν is taken from the deprojections of Sec. 3.2.2.

Dark matter. Modelling of spiral and dwarf galaxy rotation curves indicates shallow inner dark matter density distributions, i.e. logarithmic density slopes $\gamma \equiv d \ln(\rho_{\text{DM}})/d \ln(r) \approx 0$ (e.g. de Blok et al. 2001; Gentile et al. 2004). Flat dark matter density cores also fit to the kinematics of round ellipticals (Gerhard et al. 2001), although Rix et al. (1997) found steeper profiles consistent with observations of NGC 2434. Some optical or radio rotation curves also allow density slopes up to $\gamma \leq -1$, but they do not prefer steep profiles (Swaters et al. 2003).

Shallow dark matter density profiles conflict with predictions of (pure dark matter) cosmological N -body simulations. In the Λ CDM scenario, dark matter distributions with central density cusps around $-1.5 < \gamma < -1$ are found (e.g. Moore et al. 1999; Navarro et al. 2004). Similar steep profiles emerge in warm dark matter (Colin, Avila-Reese & Valenzuela 2000; Knebe et al. 2002), whereas self-interacting dark matter offers central $\gamma \approx 0$ (Davé et al. 2001).

To probe the whole diversity of theoretically and observationally motivated profiles we allow for two different dark matter distributions, one with central $\gamma = 0$, representative of shallow profiles and another with central $\gamma = -1$, representative of the steeper cases.

Cored profiles. A dark matter distribution that provides asymptotically flat circular velocity curves in combination with flat ($\gamma = 0$) inner density cores is given by the logarithmic potential (Binney & Tremaine 1987)

$$\Phi_{\text{LOG}}(R, z) = \frac{v_c^2}{2} \ln \left(r_c^2 + R^2 + \frac{z^2}{q^2} \right), \quad (3.1)$$

where $R = r \cos(\vartheta)$, $z = r \sin(\vartheta)$ are Cartesian coordinates in the meridional plane and $\vartheta = 0^\circ$ corresponds to the equator. The density distribution generating Φ_{LOG} reads (Binney & Tremaine 1987)

$$\rho_{\text{LOG}}(R, z) \propto v_c^2 \frac{(2q^2 + 1)r_c^2 + R^2 + 2(1 - \frac{1}{2q^2})z^2}{(r_c^2 + R^2 + z^2/q^2)^2 q^2} \quad (3.2)$$

and is positive everywhere for $q \in [1/\sqrt{2}, 1]$. The flattening of the density distribution (3.2) differs from that of the potential q . It is generally smaller and varies with radius. In the following, we will only consider cored profiles with $q = 1.0$ (spherical). Together with the assumption of a constant mass-to-light ratio Υ models with dark matter distributions according to equation (3.2) can be seen as analogues to maximum-disk models of spiral galaxies and have been called maximum-stellar-mass models (Gerhard et al. 1998).

Cuspy profiles. A representative cuspy mass distribution fitting simulated dark matter halos over a wide range of radii is the Navarro-Frenk-White (NFW) profile (Navarro, Frenk & White 1996)

$$\rho_{\text{NFW}}(r, r_s, c) \propto \frac{\delta_c}{(r/r_s)(1 + r/r_s)^2}, \quad (3.3)$$

with a central logarithmic density slope $\gamma = -1$. The parameter δ_c in equation (3.3) is related to a concentration parameter c via

$$\delta_c = \frac{200}{3} \frac{c^3}{\ln(1+c) - c/(1+c)}. \quad (3.4)$$

By the substitution $r \rightarrow r\sqrt{\cos^2(\vartheta) + \sin^2(\vartheta)/q^2}$ equation (3.3) provides halos with a constant flattening q .

In CDM cosmology the two parameters c and r_s turn out to be correlated in the sense that higher mass halos are less concentrated, with some scatter due to different mass assembly histories (Navarro, Frenk & White 1996; Jing & Suto 2000; Wechsler et al. 2002). The corresponding relation reads

$$r_s^3 \propto 10^{(A-\log c)/B} \left(200 \frac{4\pi}{3} c^3\right)^{-1}. \quad (3.5)$$

Here, we take $A = 1.05$ and $B = 0.15$ (Navarro, Frenk & White 1996; Rix et al. 1997), which – for the concentrations $5 < c < 25$ considered here – is equivalent to within 10 per cent to the relation given in Wechsler et al. (2002) for the now standard Λ CDM.

Total gravitating mass and potential. Luminous and dark matter components combine to the total mass density

$$\rho = \Upsilon \nu + \rho_{\text{DM}}, \quad (3.6)$$

with ρ_{DM} being either ρ_{LOG} or ρ_{NFW} . The potential Φ follows by integrating Poisson’s equation.

3.3.3 Orbit collection

Given Φ , a large set of orbits is calculated in order to sample the phase-space of the potential. Energies E and angular momenta L_z of the orbits are chosen to connect every pair of equatorial radial grid bins by at least one equatorial orbit. The surfaces of section (SOS) connected to pairs of (E, L_z) – here the upward orbital crossings with the equator – are densely filled with orbits of all available shapes (Thomas et al. 2004). A typical orbit library contains between 6500 and 9500 orbits for $L_z > 0$. Each orbit’s retrograde counterpart with $L_z < 0$ is included in the library by reversing the azimuthal velocities appropriately. In total a typical library then contains between 13000 to 19000 orbits.

3.3.4 Orbit superposition

Any superposition of a library’s orbits generates a model with a specific internal density distribution and specific projected kinematics that can be compared with the observations. The relative contribution of each orbit to the superposition –

the orbital weight w_i – represents the total amount of light carried by orbit i . To fit a library to a given dataset the maximum entropy technique of Richstone & Tremaine (1988) is applied by maximising

$$\hat{S} \equiv S - \alpha \chi_{\text{LOSVD}}^2, \quad (3.7)$$

where

$$\chi_{\text{LOSVD}}^2 \equiv \sum_{j=1}^{N_{\mathcal{L}}} \sum_{k=1}^{N_{\text{vel}}} \left(\frac{\mathcal{L}_{\text{mod}}^{jk} - \mathcal{L}_{\text{dat}}^{jk}}{\Delta \mathcal{L}_{\text{dat}}^{jk}} \right)^2 \quad (3.8)$$

quantifies the deviations between the model LOSVDs \mathcal{L}_{mod} and the observed LOSVDs \mathcal{L}_{dat} at $N_{\mathcal{L}}$ spatial positions j and in the N_{vel} bins of projected velocity k . By S , the Boltzmann entropy

$$S \equiv \int f \ln(f) \, d^3r \, d^3v = \sum_i w_i \ln \left(\frac{w_i}{V_i} \right) \quad (3.9)$$

of the library's DF f is denoted, V_i is the orbital phase-volume of orbit i , computed as in Thomas et al. (2004), and α is a regularisation parameter (see Sec. 3.4).

The decomposition of the library potential Φ into two components generated by the stellar and the dark matter mass distributions, respectively, is meaningful only if the final orbit model self-consistently generates the stellar contribution to the potential. Therefore, the luminosity density ν is used as a boundary condition for the maximisation of equation (3.7). This also guarantees a perfect match of the orbit model to the photometric observations.

3.3.5 Comparing model with data kinematics

Since our original data set for NGC 4807 consists of Gauss-Hermite parameters up to H_4 we will quote the deviations between model and data kinematics in terms of

$$\chi_{\text{GH}}^2 \equiv \sum_{j=1}^{N_{\mathcal{L}}} \left[\left(\frac{v_{\text{mod}}^j - v_{\text{dat}}^j}{\Delta v_{\text{dat}}^j} \right)^2 + \left(\frac{\sigma_{\text{mod}}^j - \sigma_{\text{dat}}^j}{\Delta \sigma_{\text{dat}}^j} \right)^2 + \left(\frac{H_{3,\text{mod}}^j - H_{3,\text{dat}}^j}{\Delta H_{3,\text{dat}}^j} \right)^2 + \left(\frac{H_{4,\text{mod}}^j - H_{4,\text{dat}}^j}{\Delta H_{4,\text{dat}}^j} \right)^2 \right]. \quad (3.10)$$

The sum in equation (3.10) over $N_{\mathcal{L}}$ LOSVDs contains $N_{\text{data}} \equiv 4 \times N_{\mathcal{L}}$ terms and the parameters v_{mod} , σ_{mod} , $H_{3,\text{mod}}$ and $H_{4,\text{mod}}$ are obtained from the corresponding LOSVDs of equation (3.8) by fitting a 4th-order Gauss-Hermite series¹.

¹The fifth parameter of the fit, the intensity γ_0 , is not included in equation (3.10) since we scale data as well as model LOSVDs to the same surface brightness before comparison. This does not automatically imply that the fitted intensities γ_0 of model and data LOSVDs are identical, but it largely affects their differences. Following the approach of Gerhard et al. (1998) we therefore omit γ_0 in χ_{GH}^2 .

Equation (3.10) can only be applied if the sampling of the LOSVD is sufficient to get reliable and unbiased estimates of the Gauss-Hermite parameters and it should be noticed that in the implementation of the orbit superposition method applied here (in contrast to the programs building up on the work of Rix et al. 1997 and Cretton et al. 1999) χ_{GH}^2 is not explicitly minimised. We discuss the effects of using equation (3.10) instead of equation (3.8) to derive confidence regions in Sec. 3.9.3.

3.4 Regularisation

The regularisation parameter α in equation (3.7) controls the relative importance of entropy maximisation and χ^2 -minimisation in the model. Basically, increasing α puts more weight on the χ^2 -minimisation in the orbit superposition and reduces the influence of S in equation (3.7). For data sets with relatively sparse spatial sampling as considered here, the freedom in the orbit superpositions allows to fit models to the noise in the data when applying $\alpha > 1$. Such orbit models show, however, large density depressions and contradict the traditional view of relaxed dynamical systems. On the other hand, models with lower α have smoother distribution functions in the sense that the adopted form for S tends to isotropize the orbital DF, thereby reducing its dependency on L_z and I_3 . Fitting orbit models to data sets with different spatial coverage and quality will likely change the effect of α on the final fit. Likewise, changing the functional form of S can be used to bias the models towards other than isotropic DFs (Thomas et al. 2004). The best choice for α and S has to be investigated case-by-case, depending on the galaxies under study and on the amount and form of information that is to be extracted from the observations.

3.4.1 Motivation

Figs. 3.3 and 3.4 exemplify the effects of regularisation in terms of two distribution functions reconstructed from fits of the same library for an edge-on isotropic rotator model of NGC 4807. The Gauss-Hermite profiles in the lower panels of the figures are derived from velocity moments obeying higher-order Jeans equations in the self-consistent potential of the deprojection (Magorrian & Binney 1994). Before calculating the Gauss-Hermite parameters the velocity moments are slit averaged and seeing convolved to simulate the observations of Sec. 3.2.3. Noise is added to v and σ according to the fractional errors of the observations and to H_3 and H_4 according to the absolute errors. The lower panels of Figs. 3.3 and 3.4, respectively, display the rotator kinematics along the major and minor axes, together with fits of an orbit library containing 2×6922 orbits. For Fig. 3.3 the fits were obtained at $\alpha = 0.02$ and for Fig. 3.4 at $\alpha = 6.73$. The distribution functions reconstructed from the two fits are plotted against orbital energy E in the upper panels of the figures. Each dot represents the phase-space density w_i/V_i along a single orbit, scaled according to $\sum w_i = \sum V_i = 1$ (Thomas et al. 2004). The more regularised fit in Fig. 3.3 yields $\chi_{\text{GH}}^2/N_{\text{data}} = 0.3$ ($N_{\text{data}} = 48$),

while for Fig. 3.4 the goodness of fit is $\chi_{\text{GH}}^2/N_{\text{data}} = 0.17$.

The DF at $\alpha = 6.73$ has density depressions of several orders of magnitude for orbits with roughly the same energy. Orbit models with such DFs are difficult to interpret as the result of relaxation processes like violent relaxation and others, occurring in the dynamical evolution of real galaxies (e.g. Lynden-Bell 1967). They often predict uncommon kinematics along position angles not covered by observational data. To illustrate this, the projected kinematics predicted along a diagonal axis (position angle $\vartheta = 45^\circ$) by the two DFs of Figs. 3.3 and 3.4 are plotted in Fig. 3.5. For comparison the (undisturbed) kinematics of the isotropic rotator model are also overplotted. The profiles of the almost non-regularised ($\alpha = 6.73$) fit show large point-to-point variations, which cannot easily be reconciled with the scatter in real observations. Also, the mean deviation between the non-regularised orbit superposition and the input isotropic rotator (IR) model are larger for the non-regularised one than for the regularised one, e.g. $\langle H_3^{\text{IR}} - H_3 \rangle = 0.06$ for $\alpha = 6.73$ compared with $\langle H_3^{\text{IR}} - H_3 \rangle = 0.02$ for $\alpha = 0.02$.

The above example demonstrates the importance of regularisation in the context of recovering internal dynamics of isotropic rotators from sparse data sets typical for our sample of Coma galaxies. For NGC 4807 we have determined the optimal amount of regularisation by means of Monte-Carlo simulations of several such isotropic rotator models (see Sec. 3.4.2 below).

The DFs of isotropic rotator models are of the form $f = f(E, L_z)$ and represent only a minority of all possible DFs, since they are constant along I_3 . The choice of such reference models for galaxies like NGC 4807 (fast rotating, faint giant ellipticals) is observationally motivated (Kormendy & Bender 1996) and further supported by the weak velocity anisotropy found in previous dynamical studies (e.g. Gerhard et al. 2001; see also Sec. 3.7 for the case of NGC 4807), implying only a mild dependence of the DF on I_3 . For more luminous ellipticals (shaped primarily by velocity anisotropy) or lenticulars embedded in roundish halos other reference models should be explored. We will turn to this in a future publication.

3.4.2 Regularisation from isotropic rotator models

The isotropic rotator models constructed to determine the optimal regularisation with respect to the analysis of NGC 4807's internal structure are based on the edge-on as well as the $i = 50^\circ$ deprojections. For numerical reasons, however, the models at $i = 50^\circ$ are forced to have isophotes close to pure ellipses by setting $a_4 \equiv a_6$ for the deprojection. Six models have been probed, three at each of the inclinations $i = 50, 90^\circ$: one self-consistent, one embedded in a LOG-halo and a third embedded in a NFW-halo. Kinematic profiles are calculated from higher order internal velocity moments (Magorrian & Binney 1994) following the procedure described in Sec. 3.4.1. Orbit libraries are fitted to the kinematic profiles and the internal velocity moments reconstructed from the fits are compared with the original input-moments for various values of α . The optimal balance between entropy maximisation and χ^2 -minimisation

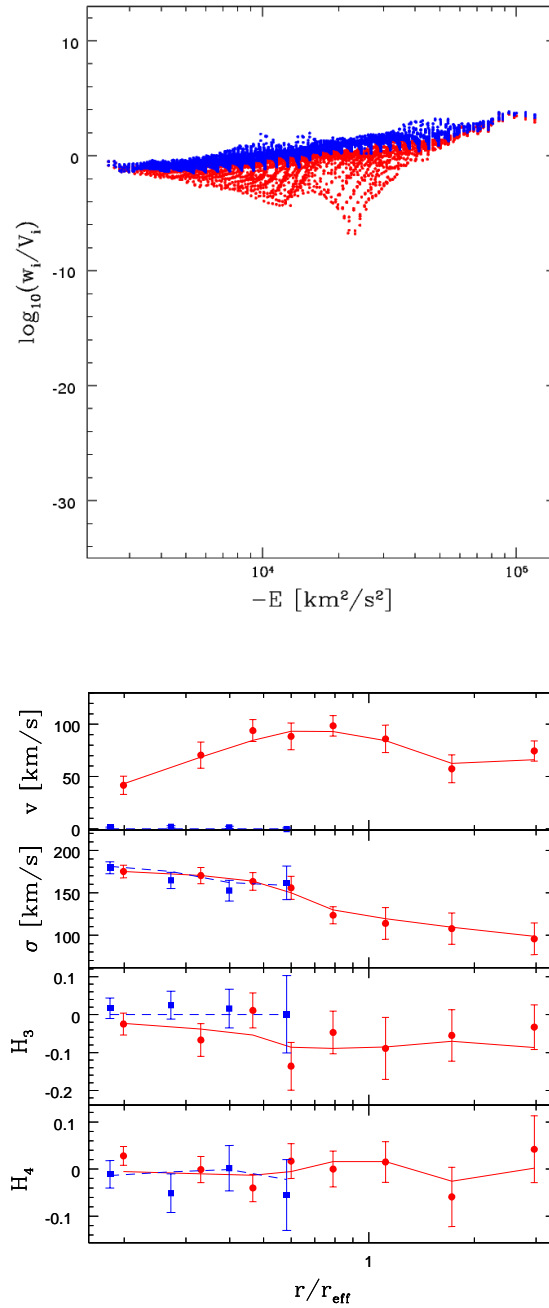


Figure 3.3: Reconstructed phase-space densities of individual orbits against energy (upper panel) for an isotropic rotator model of NGC 4807 (details in the text). For the underlying fit (lower panel; dots/squares: major/minor axis isotropic rotator model; solid/dashed lines: major/minor axis orbit model) a regularisation of $\alpha = 0.02$ is used.

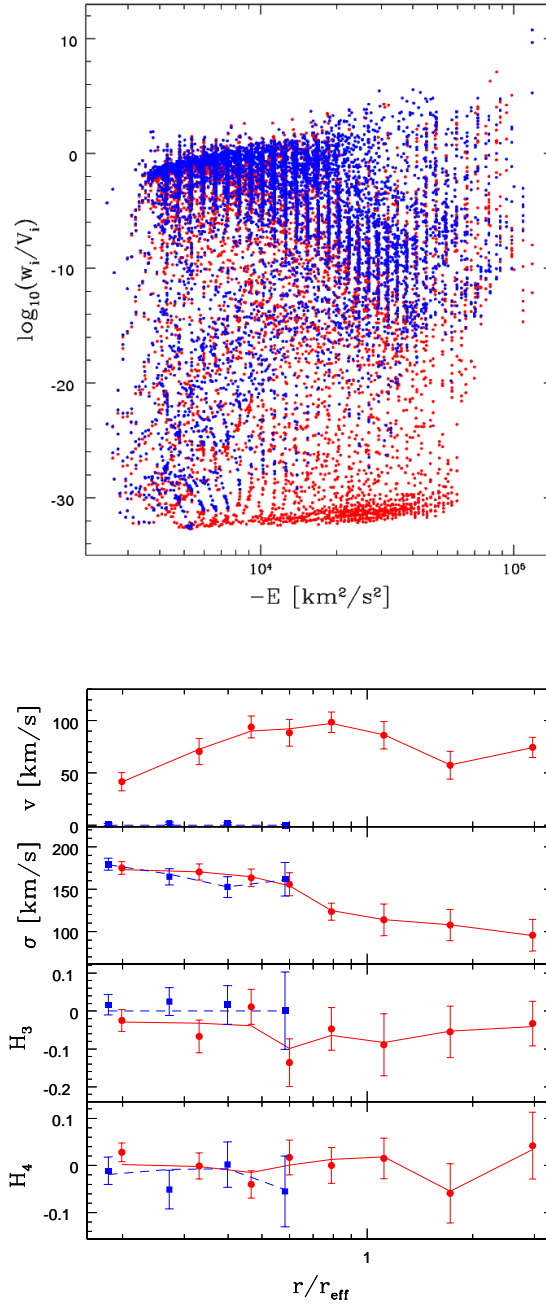


Figure 3.4: As Fig. 3.3, but for regularisation with $\alpha = 6.73$. Note that the lower boundary of phase-space densities in the upper panel is partly due to the program setting all orbital weights smaller than $w_i < w_{\text{min}} \equiv 10^{-37}$ equal to $w_i \equiv w_{\text{min}}$.

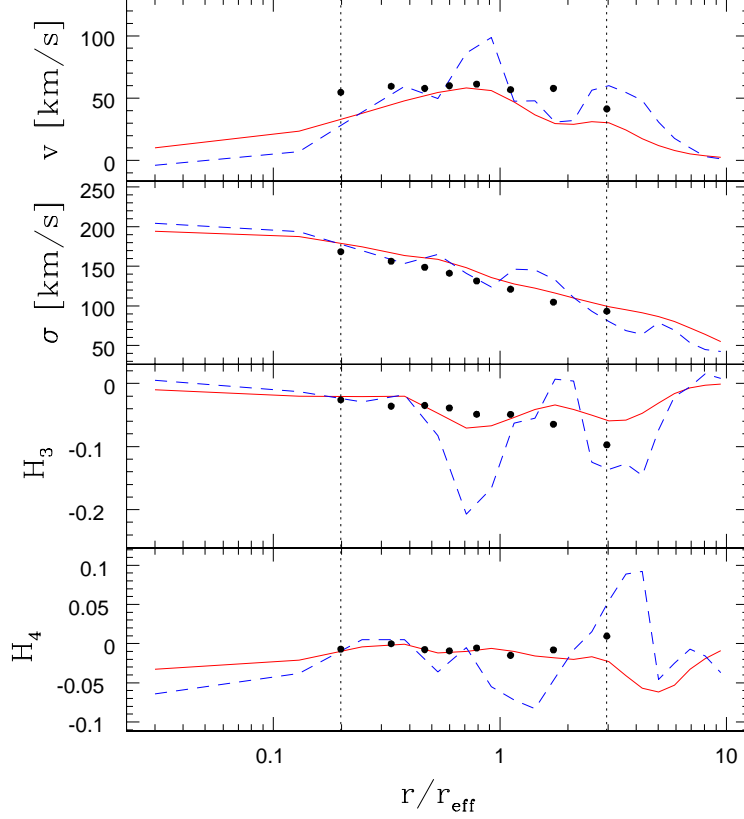


Figure 3.5: Projected kinematics of the two DFs of Figs. 3.3 and 3.4 along a diagonal axis with position angle $\vartheta = 45^\circ$. Solid lines: $\alpha = 0.02$ (\rightarrow Fig. 3.3); dashed lines: $\alpha = 6.73$ (\rightarrow Fig. 3.4); dots: kinematics of the isotropic rotator model. Note that the orbit superpositions were fitted to the model only along the major and minor axes.

is revealed where the reconstructed internal velocity moments are closest to the input model.

Fig. 3.6 shows the results for a self-consistent model based on the $i = 90^\circ$ -deprojection. The upper panel shows the rms difference $\Delta(\alpha)$ between original and reconstructed internal velocity moments (up to second order) as a function of the regularisation parameter α . The rms is evaluated between the innermost and outermost fitted data points, at all position angles ϑ , including intermediate ones, not covered by data points. The lower panel illustrates the goodness of fit $\chi_{\text{GH}}^2/N_{\text{data}}$. Solid lines correspond to the mean obtained by fitting orbit models

input model	α_0	$\Delta(\alpha_0)$	$\chi_{\text{GH}}^2(\alpha_0)$	N_{orbit}
$i = 90^\circ$, SC	0.0199	13.5 %	0.712	2×6922
$i = 90^\circ$, LOG	0.0166	12.7 %	0.719	2×8273
$i = 90^\circ$, NFW	0.0138	13.2 %	0.692	2×8469
$i = 50^\circ$, SC	0.0238	12.6 %	0.539	2×6697
$i = 50^\circ$, LOG	0.0166	13.8 %	0.826	2×8126
$i = 50^\circ$, NFW	0.0166	13.5 %	0.797	2×8324

Table 3.1: Summary of simulations aimed at optimising the regularisation parameter α . Columns from left to right: inclination of reference model; potential of reference model (SC = self-consistent, LOG = logarithmic spherical halo, NFW = spherical NFW-halo, details in the text); regularisation parameter α_0 that yields the best reconstruction of internal velocity moments; rms $\Delta(\alpha_0)$ between internal velocity moments of reference models and reconstructions achieved with $\alpha = \alpha_0$; goodness of fit $\chi_{\text{GH}}^2(\alpha_0)$; number of orbits N_{orbit} used for the modelling.

to 60 Monte-Carlo realisations of the simulated data. Shaded areas comprise the 68 per cent fraction of best reconstructions (upper panel) and 68 per cent fraction of best fitting solutions (lower panel), respectively.

The best results are obtained for $\alpha = 0.02$, when internal kinematics of the fits follow the input moments to an accuracy of about 15 per cent in the mean. Lower α yield less accurate reconstructions since the orbit superpositions do not fit the data enough (see χ_{GH}^2 in the lower panel). For larger α on the other hand, the rms $\Delta(\alpha)$ increases, because the library starts to fit the noise in the data.

On average, the orbit models at $\alpha = 0.02$ fit with $\chi_{\text{GH}}^2/N_{\text{data}} < 1$. A proper normalisation for χ_{GH}^2 is however hard to obtain, since we do not exactly know the number of free parameters in the library. For $\alpha = 0$ this number is zero, because χ^2 does not appear in equation (3.7) while for $\alpha \rightarrow \infty$ there are roughly as many free parameters as orbits in the library², because then S becomes negligible in equation (3.7). Thus, we do not try to calculate a reduced χ^2 .

Table 3.1 summarises the total of simulations done to fix α . The first column labels the three models investigated at each of the two inclinations $i = 50^\circ$ and $i = 90^\circ$ (SC: self-consistent models without halo; LOG: a dark halo with $r_c = 5$ kpc and $v_c = 265$ km/s according to equation (3.2) is added to the stars; NFW: dark halo profile like in equation (3.3) with $r_s = 10.0$ kpc, $c = 27.0$; for all models $\Upsilon = 3.0$). The halo models are constructed to produce a roughly flat circular velocity. In the second column of Table 3.1 the regularisation α_0 is quoted attaining the best reconstruction of the internal velocity moments, quantified in the third column as $\Delta(\alpha_0) = \min(\Delta(\alpha))$. The corresponding goodness of fit $\chi_{\text{GH}}^2(\alpha_0)$ is given in the fourth column of the table. The number of orbits in each of the fitted libraries is found in the last column.

²We have neglected the boundary condition related to ν . This is expected to reduce the number of free parameters, but is unlikely to break its dependency on α .

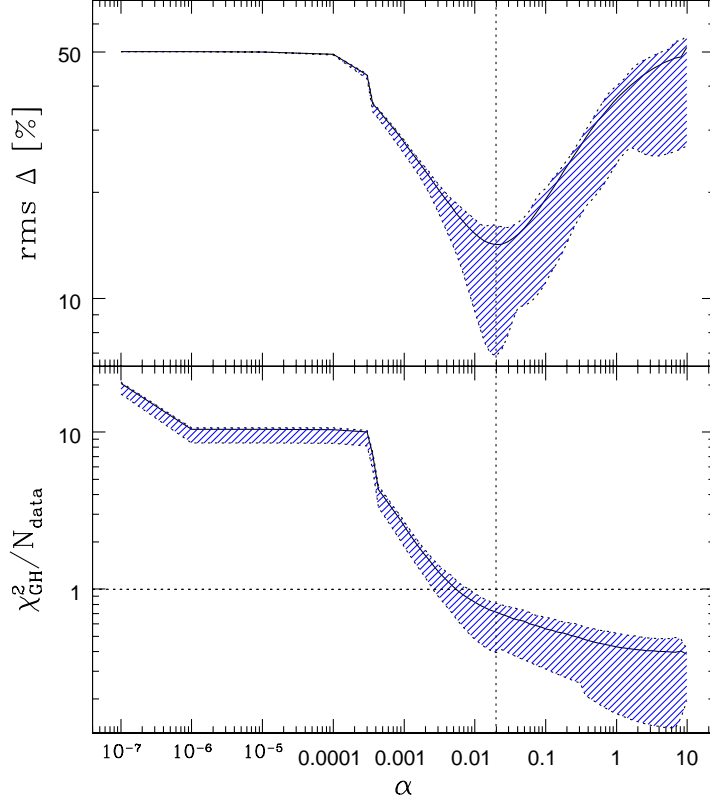


Figure 3.6: Match $\Delta(\alpha)$ of internal velocity moments and $\chi_{\text{GH}}^2/N_{\text{data}}$ of the Gauss-Hermite parameters as a function of the regularisation parameter α . Lines represent the mean over 60 fits to Monte-Carlo realisations of the isotropic rotator’s kinematic profiles; shaded regions encompass 68 per cent of the simulations closest to the corresponding minimum in $\Delta(\alpha)$ and $\chi_{\text{GH}}^2/N_{\text{data}}$, respectively.

On average, the six probed models yield $\langle\alpha_0\rangle = 0.0179 \pm 0.0035$. The low scatter seems to indicate that α_0 does not depend strongly on the potentials tested. In the implementation of the maximum entropy technique used here, α is increased iteratively in discrete steps (see Richstone et al., in preparation). For the models of NGC 4807 we apply $\alpha = 0.0199 \approx 0.02$, which is the closest larger neighbour of $\langle\alpha_0\rangle$ in these iterations.

In the remainder of the paper, by quoting 68 (90, 95) per cent confidence levels, we always refer to all orbit models whose $\chi_{\text{GH}}^2/N_{\text{data}}$ are below the corre-

sponding maximum χ^2 -level of the 68 (90, 95) per cent best-matching fits in the simulations. For these fits parameters like Υ , i , r_c , $v_c \dots$ are set equal to the true input values, but in the analysis of real galaxies they are varied. Strictly speaking then, the χ^2 -statistics from the simulations are not directly applicable to real galaxies. For example, to determine the correct statistics for the case where Υ , r_c and v_c are varied to find the best-fitting mass-model, about 10^2 orbital fits for each triple of (Υ, r_c, v_c) are necessary to yield the corresponding three dimensional χ^2 -distribution. Such simulations however cannot be performed in a reasonable amount of time with present-day computer power.

Probably, our confidence regions derived as described above overestimate the error budget. For example, in the simulations we find 68 per cent of all orbits within $\Delta\chi_{\text{GH}}^2/N_{\text{data}} = 0.38$ from the mean best-fit values. In contrast, applying classical $\Delta\chi^2$ -statistics for a two parameter fit, yields about 95 per cent confidence at the same $\Delta\chi_{\text{GH}}^2/N_{\text{data}} = 0.38$.

3.5 Recovering isotropic rotator models

The aim of this Section is to quantify in a practical sense to which degree a sparse data set like the one described in Sec. 3.2.3 constrains the internal kinematics and mass structure of a typical galaxy in our sample.

3.5.1 Mass-to-light ratio Υ and inclination i

First, we disregard the possible presence of a dark halo and try to recover the mass-to-light ratio and inclination of the self-consistent edge-on model in Table 3.1. Therefore, Fig. 3.7 resumes the results of fitting libraries with mass-to-light ratios in the range $2.0 \leq \Upsilon \leq 4.0$ and inclinations $i = 50, 70, 90^\circ$ to the kinematics of this isotropic rotator model. The goodness of fit $\chi_{\text{GH}}^2/N_{\text{data}}$ for each pair (Υ, i) is averaged over 10 Monte-Carlo realisations of the kinematic profiles and evaluated at two different regularisations. For the upper panel $\alpha = 0.02$ according to the simulations described in Sec. 3.4.2. Horizontal dotted lines in the plot correspond to 68, 90 and 95 per cent confidence levels as derived from the statistics of the simulations in Sec. 3.4.2.

One can read from the plot that the mass-to-light ratio is well recovered: the orbital fits reveal $\Upsilon = 3.0 \pm 0.5$, where the input model has $\Upsilon_{\text{IR}} = 3.0$. The minimum χ_{GH}^2 occurs at the true value independent of the assumed inclination. The latter is only weakly constrained. For $\Upsilon = 3.0$ an inclination of $i = 70^\circ$ results in nearly the same $\chi_{\text{GH}}^2/N_{\text{data}}$ as the fit with the input $i_{\text{IR}} = 90^\circ$. Even the orbit models with $i = 50^\circ$ can only be rejected with less than 90 per cent confidence.

For the lower panel the fits are evaluated at $\alpha = 0.44$ (this choice of α is motivated in Sec. 3.6). Although at this less restrictive regularisation the confidence intervals shrink as compared with $\alpha = 0.02$ the mass-to-light ratio is now less constrained, $\Upsilon = 3.0 \pm 1.0$. The same holds for the inclination: at

$\Upsilon = 3.0$ all three probed inclinations are now within the 68 per cent confidence interval.

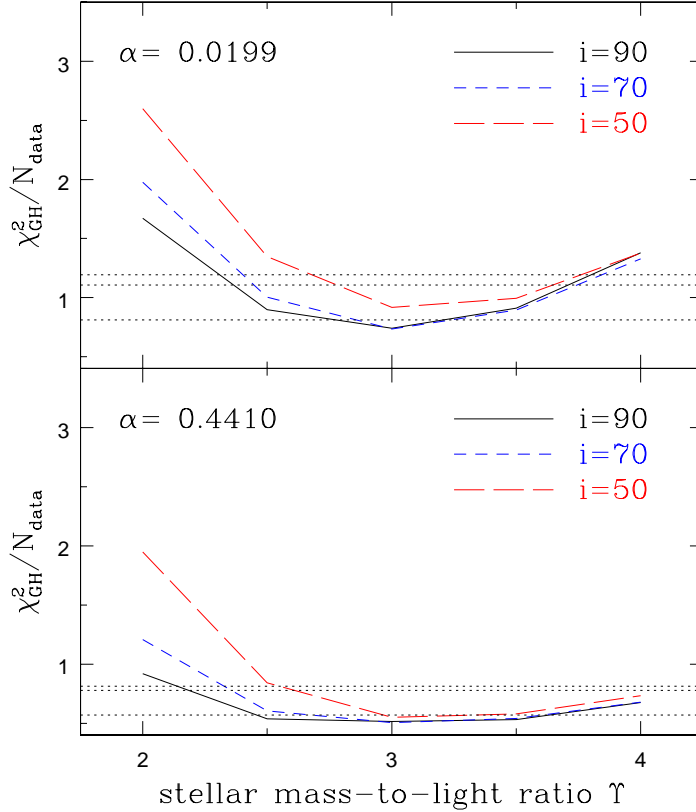


Figure 3.7: χ^2_{GH} per data point ($N_{\text{data}} = 48$) as function of stellar M/L for three different inclinations i . Top panel: with optimal smoothing, bottom panel: weak smoothing. The input 2I-model has $M/L = 3.0$ and is edge-on. Pointed horizontal lines in each panel represent the χ^2_{GH} values enclosing 68, 90 and 95 per cent of the Monte-Carlo simulations, respectively.

3.5.2 Internal kinematics

To give an impression about the ability to recover internal motions (assuming the potential is known) Fig. 3.8 compares internal velocity moments reconstructed from libraries fitted to the self-consistent edge-on isotropic rotator model of Sec. 3.4.1 with the corresponding moments of the input model. Solid lines portray the isotropic rotator model and points show the average reconstructed

moments from fits to 60 Monte-Carlo simulations of the kinematic profiles; error bars indicate 1σ deviations from the mean. For the reconstructions $\alpha = 0.02$ is used.

The three upper rows demonstrate that for the internal major axis the second order moments σ_R , σ_z and σ_φ are accurately reproduced by the fit over the region between the pointed vertical lines indicating the radii of the innermost and outermost kinematical points included in the fit. The fractional errors of σ_R and σ_φ are below 3 per cent and of σ_z are below 6 per cent. For the internal rotation velocity v_φ the fractional errors are larger than 10 per cent at some points. The match of the rotation velocity can be increased when going to larger α , but then the second order moments start to wiggle around the input moments and the overall match of reconstructed to original moments becomes worse. Fig. 3.8 is representative also for the remaining internal position angles of the libraries. It follows that most of the rms in Fig. 3.6 results from a mismatch in v_φ .

The last row shows a comparison of the anisotropy parameter $\beta_\vartheta = 1 - \sigma_\vartheta^2/\sigma_r^2$, which vanishes for isotropic rotator distribution functions $f = f(E, L_z)$. The reconstructions are consistent with $\beta_\vartheta = 0$ given the scatter caused by the noisy data. The small offset of $\Delta\beta_\vartheta = 0.05$ is due to a slight overestimation of the radial velocity dispersion and emphasises how sensitive β_ϑ responds to small inaccuracies in the velocity dispersions.

3.5.3 Mass distribution

The next step is to recover the structure of the isotropic rotator model in the second row of Table 3.1, where a logarithmic dark halo is present. To this end, we fitted libraries with different dark halos to pseudo data sets of the rotator model, keeping the stellar mass-to-light ratio constant. Fig. 3.9 combines the results of the simulations. It shows, from top to bottom, cumulative mass-to-light ratio $M(r)/L(r)$, circular velocity $v_{\text{circ}}(r)$ and dark matter fraction $M_{\text{DM}}(r)/M(r)$ as a function of radius. Vertical dotted lines mark the boundaries of the spatial region covered with kinematic data, thick lines display the input model. The shaded areas have been constructed by determining at each radius the minimum and maximum of M/L , v_{circ} and M_{DM}/M of all libraries within the 68 per cent confidence range derived from the simulations of Sec. 3.4.2. Libraries with LOG-halos as well as NFW-halos have been tried (see below) and for each library fits to 10 realisations of the isotropic rotator kinematics were averaged.

The figure demonstrates that in the region covered by the data the mass structure of the input model is well reproduced, with progressively larger scatter towards the outer edge of the data. The uncertainty of the mass-to-light ratio is $\Delta M/L \approx 1.0$ at $1 r_{\text{eff}}$, the circular velocity is accurate to 10 per cent at the same central distance. In the outer parts orbit superpositions with larger masses than the input model are better consistent with the data than smaller mass models. Nevertheless, the dark matter fraction is determined to $\Delta(M_{\text{DM}}/M) = 0.2$ even at the outermost data point.

The top panel of Fig. 3.10 displays 68, 90 and 95 per cent confidence intervals

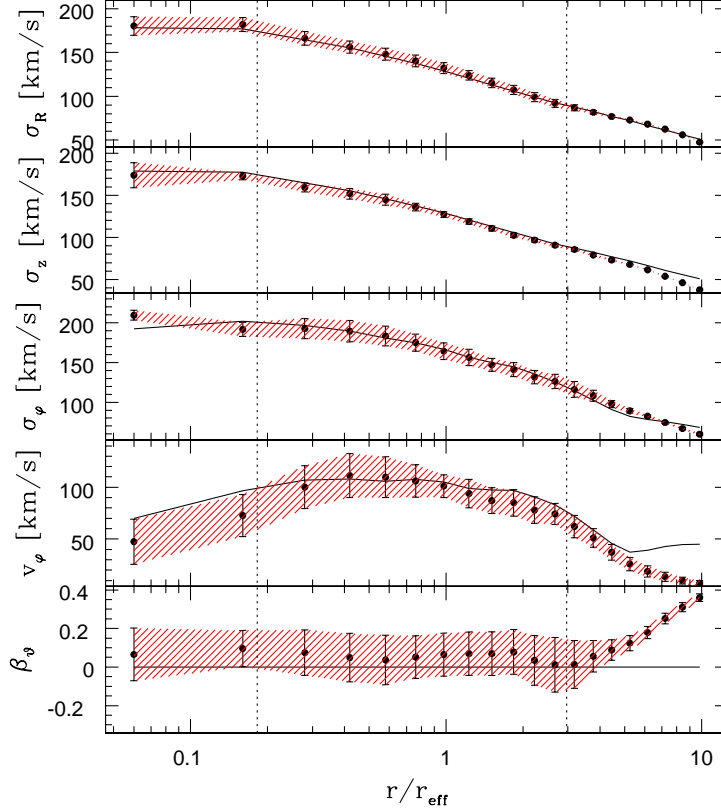


Figure 3.8: Internal velocity moments along the major axis of libraries fitted to the self-consistent edge-on isotropic rotator model of Sec. 3.4.1. Dots: mean from fits to 60 Monte-Carlo realisations of the kinematic data; shaded regions: 1σ deviation from the mean; solid lines: velocity moments of the input model; dotted lines: boundaries of the radial region included in the fit.

for the two parameters r_c and v_c of LOG-halos (cf. equation 3.2). Each dot marks a pair of (r_c, v_c) probed by fitting a library to 10 realisations of the pseudo-data as described above. The input model's dark halo parameters are marked by the asterisk, the circle designates the best-fitting orbit model.

As expected, the halo parameters are not well constrained. Although the best-fitting parameter pair is close to the input model, the 68 per cent confidence contour comprises a large set of libraries and remains open to the upper right edge of the plot. This follows from a degeneracy between the two parameters r_c and v_c (e.g. Gerhard et al. 1998). Increasing r_c and v_c appropriately puts

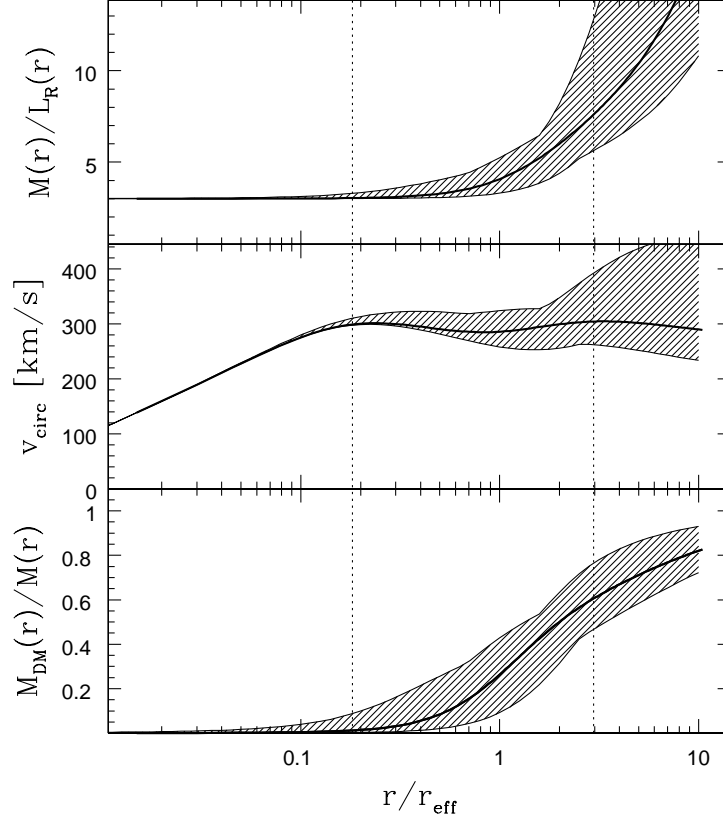


Figure 3.9: Accuracy of the mass reconstruction. Thick lines: the isotropic rotator model marked by the asterisk in Fig. 3.10; shaded areas: 68 per cent confidence regions of fits to pseudo data sets of the model. For each mass-model the goodness-of-fit is averaged over 10 fits to MC-realizations of pseudo-data.

more mass in the outer parts of the halos while rendering the regions covered by kinematics roughly unchanged. The increasing width of the shaded areas in the upper two panels of Fig. 3.9 is an illustration of this degeneracy.

We also fitted one parameter NFW-halos according to equation (3.5) to the same isotropic rotator model in order to examine whether these profiles can be excluded by the data set at hand. The lower panel of Fig. 3.10 displays the results in terms of $\chi_{\text{GH}}^2/N_{\text{data}}$ as a function of concentration index c . Horizontal dotted lines correspond to 68, 90 and 95 per cent confidence levels, the solid line shows fits with spherical halos ($q = 1.0$), while for the dashed line $q = 0.7$. Apparently, neither the halo flattening nor the central halo density slope are

constrained by the data, because both spherical as well as flattened NFW-halos exist that provide fits equally as good as the LOG-halos. These NFW-halos join smoothly to the mass-distribution recovered in Fig. 3.9 and mimic LOG-halos over the limited spatial region covered by kinematic data.

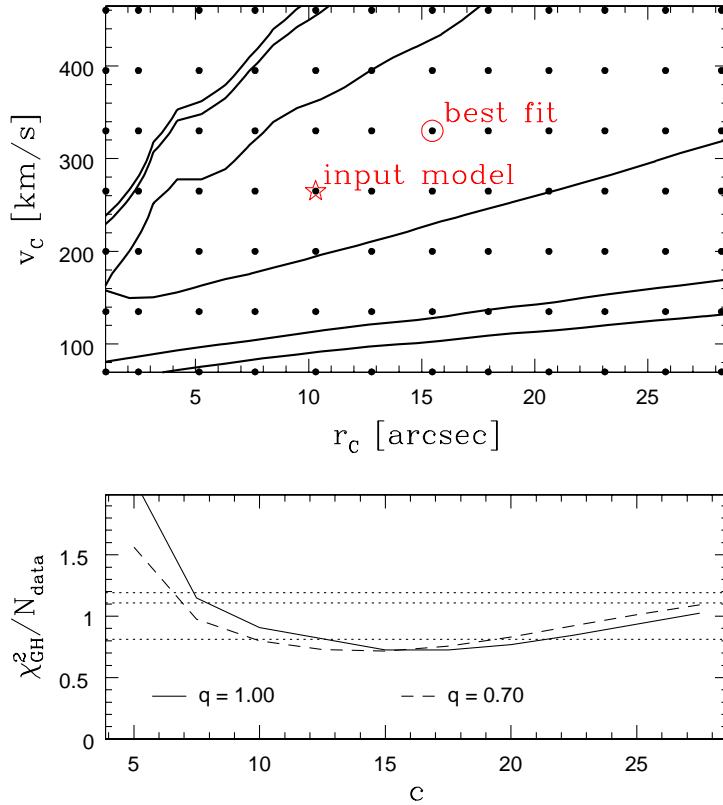


Figure 3.10: Recovering an isotropic rotator model’s dark halo: r_c and v_c of the input model model are marked by the asterisk in the top panel, the best-fit reconstruction is marked by the circle. Lines in the top panel display 68, 90 and 95 per cent confidence contours of the fits. The lower panel shows – for the same input model – χ^2 of NFW-type fits (solid/dashed: $q = 1.0/q = 0.7$); horizontal lines: 68, 90 and 95 per cent confidence levels. Each library has been fitted to 10 realisations of the input-model kinematics.

Fig. 3.10 suggests that it is not possible to discriminate between LOG and NFW halos insofar as they provide similar mass distributions over the spatial region sampled by kinematic data. More extended data sets are likely to reduce

this degeneracy, but will probably not completely remove it. On the other hand, as Fig. 3.9 reveals, the mass distribution and composition of the input model can be recovered well, independently of the specific parameterisation chosen to emulate it.

3.6 Dark matter in NGC 4807

Now, we turn to the analysis of the distribution of luminous and dark mass in NGC 4807. Fig. 3.11 shows the minimum $\chi_{\text{GH}}^2/N_{\text{data}}$ (scaled, see below) at each modelled stellar mass-to-light ratio $\Upsilon \in \{1.0, 2.0, 2.5, 3.0, 3.5, 4.0, 5.0\}$. Horizontal lines indicate the 68, 90 and 95 per cent confidence limits derived from the simulations of Sec. 3.4.2. For the upper panel $\alpha = 0.02$ is used and LOG-potentials with stellar mass-to-light ratios $2.5 \leq \Upsilon \leq 3.0$ fit best to the data. Projected kinematics of the best-fitting orbit model are plotted in the upper panel of Fig. 3.12 together with the data. The model is edge-on, has stellar $\Upsilon = 3.0$ and a spherical dark halo of LOG-type with core radius $r_c = 6.8$ kpc and asymptotic circular velocity $v_c = 300$ km/s. It fits the data very well with (unscaled) $\min(\chi_{\text{GH}}^2/N_{\text{data}}) = 0.17$, even too well when compared with the average $\langle \chi_{\text{GH}}^2/N_{\text{data}} \rangle = 0.71$ expected from the Monte-Carlo simulations. Since both, the scatter in the kinematic data from different sides of the galaxy (cf. Sec. 3.2.3) and the point-to-point variations in the profiles are smaller than the statistical error bars, the latter might be slightly overestimated. Hence, in the following all $\chi_{\text{GH}}^2/N_{\text{data}}$ are rescaled such that $\min(\chi_{\text{GH}}^2/N_{\text{data}}) = \langle \chi_{\text{GH}}^2/N_{\text{data}} \rangle$. The good match of model and data nevertheless reconfirms that NGC 4807 is consistent with axisymmetry.

Applying regularisation with $\alpha = 0.02$, self-consistent models (mass follows light) are ruled out by more than 95 per cent confidence (see thin solid line in the upper panel of Fig. 3.11). The best-fitting self-consistent model fits with (rescaled) $\chi_{\text{GH}}^2/N_{\text{data}} = 1.67$ and is compared with the data in the bottom panel of Fig. 3.12. It has $\Upsilon = 3.5$, larger than the best-fitting halo model, but fails to reach the measured rotation in the outer parts of the galaxy. A drop in the outer major axis H_3 -profile indicates that the model maintains the measured dispersion σ around the observed v partly by putting light on retrograde orbits. This causes the LOSVD to fall off too sharply at velocities larger than v and to develop a wing at negative velocities, resulting in the too negative H_3 . Lack of support for dispersion at large rotation velocities hints at mass missing in the outer parts of this model. Higher mass-to-light ratios, however, would strengthen the mismatch between the central regions of the model and the innermost (minor axis) velocity dispersions.

To push the self-consistent model to the same level of agreement with the data reached in the upper panel of Fig. 3.12, regularisation must be lowered to $\alpha = 0.45$. Although the best-fitting self-consistent model then gives a satisfactory fit in the sense of a reasonable $\chi_{\text{GH}}^2/N_{\text{data}}$, it is again ruled out by more than 95 per cent confidence when compared with the mean $\langle \chi_{\text{GH}}^2/N_{\text{data}} \rangle$ using the Monte-Carlo simulations. This, because halo models at $\alpha = 0.45$ still give

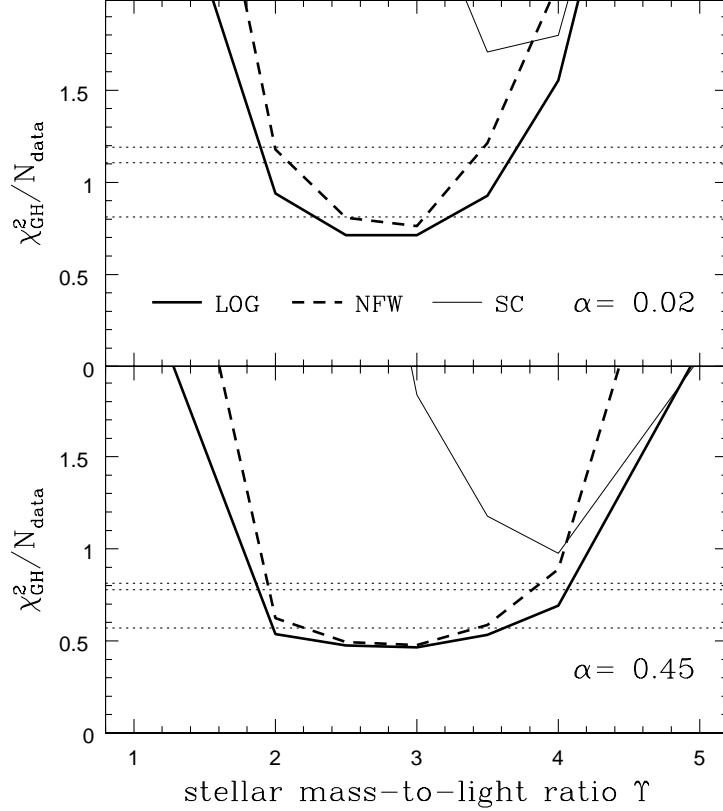


Figure 3.11: Deviations between the observed kinematics of NGC 4807 and the fitted libraries in terms of χ_{GH}^2 as a function of Υ . At each Υ the minimum $\min(\chi_{\text{GH}}^2)$ is plotted, separately for the case of LOG-halos (thick solid line), one-parameter NFW-halos (thick dashed) and for the self-consistent case (thin solid). For the top row the regularisation parameter is $\alpha = 0.02$, for the bottom row $\alpha = 0.45$.

significantly better fits to the data. The only effect of lower regularisation – as shown in the run of $\chi_{\text{GH}}^2/N_{\text{data}}$ versus Υ in the lower panel of Fig. 3.11 – is a slight broadening of the minimum region in $\chi_{\text{GH}}^2/N_{\text{data}}$ and, consequently, an expansion of the allowed range of mass-to-light ratios, yielding now $2.0 \leq \Upsilon \leq 3.5$ as compared with $2.5 \leq \Upsilon \leq 3.0$ at $\alpha = 0.02$. Concluding, NGC 4807 cannot be convincingly modelled with self-consistent orbit models, even at weak regularisation.

In Fig. 3.13 (from top to bottom) the 68 per cent confidence regions of cumulative mass-to-light ratio $M(r)/L_R(r)$, circular velocity v_{circ} and dark mat-

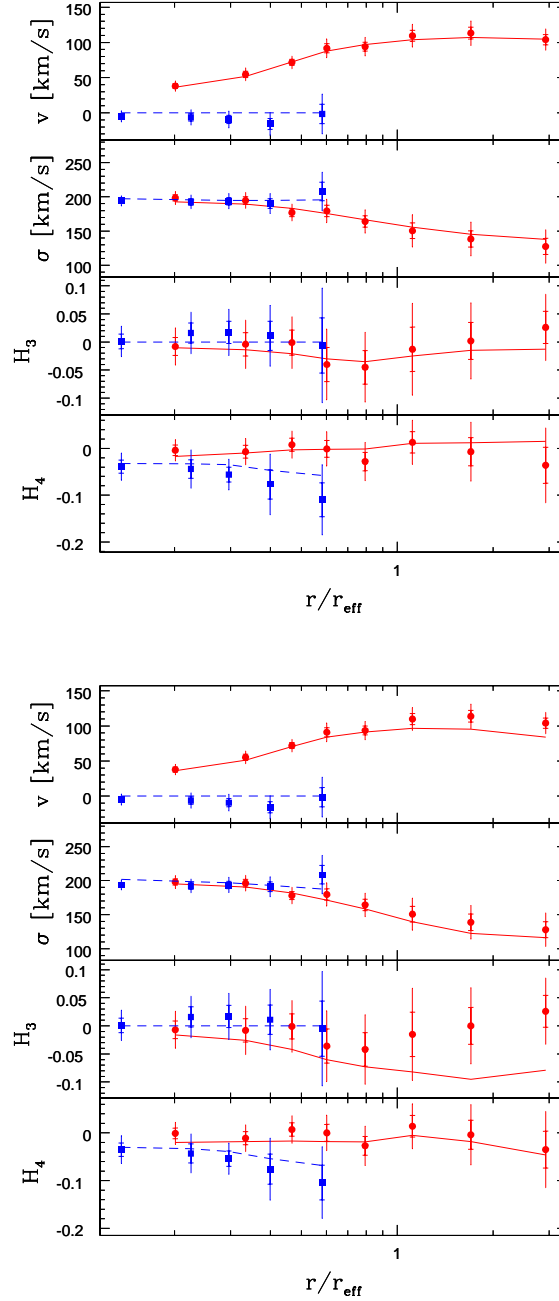


Figure 3.12: Comparison of NGC 4807 (dots: major axis kinematic data; squares: minor axis) with the overall best-fitting model (upper panel) and best-fitting self-consistent model (lower panel). Both orbit models are at $i = 90^\circ$. For each data point two error bars are given: the statistical error from the observational data (larger, without marks) and the error bar corresponding to the scaled χ_{GH}^2 (marks).

ter fraction $M_{\text{DM}}(r)/M(r)$ are shown (analogue to Fig. 3.9). Within $1 r_{\text{eff}}$ dark matter is negligible and the dynamical mass-to-light ratio equals the stellar one, $M(r)/L_R(r) = \Upsilon = 3.0$. Between $1 r_{\text{eff}}$ and $3 r_{\text{eff}}$ dark matter comes up from $M_{\text{DM}}/M = 0.21 \pm 0.14$ to $M_{\text{DM}}/M = 0.63 \pm 0.13$ and combines with the luminous matter to a roughly flat circular velocity curve with $v_{\text{circ}} = 280 \pm 30$ km/s at $1 r_{\text{eff}}$ and $v_{\text{circ}} = 318 \pm 48$ km/s at the last kinematic data point. In the same spatial region the total mass-to-light ratio rises from $M(r)/L_R(r) = 3.8 \pm 0.8$ to $M(r)/L_R(r) = 8.4 \pm 2.4$. Dark mass equals luminous mass at roughly two effective radii. Beyond the last kinematic data point, the models are not well constrained and the profiles start to diverge.

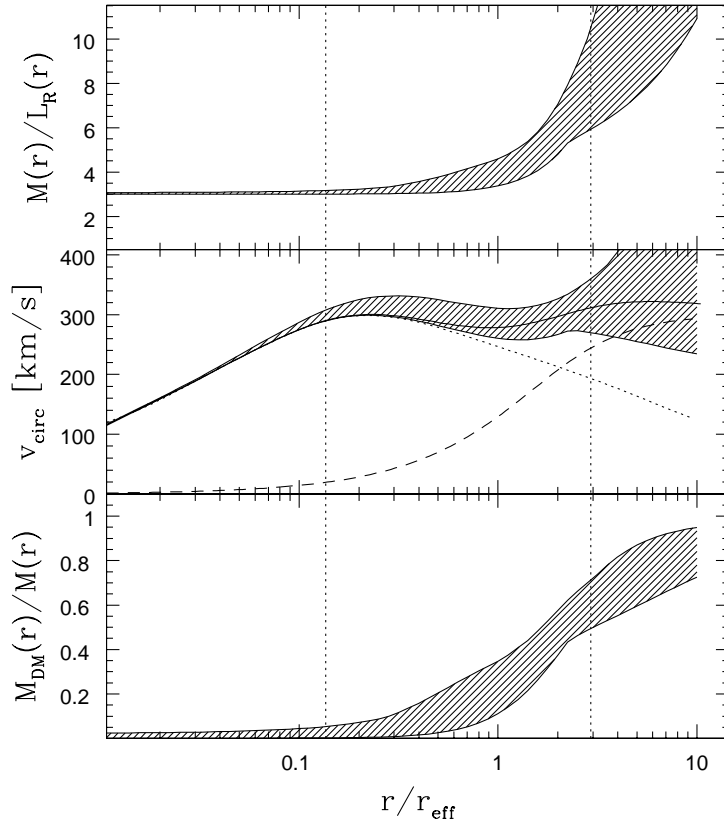


Figure 3.13: Mass-structure of NGC 4807. Shaded regions are constructed as for Fig. 3.9. In the middle panel, the circular velocity curve of the best-fitting orbit model (solid line) and its decomposition into the stellar (dotted) and dark matter part (dashed) are displayed.

In accordance with the isotropic rotator simulations the halo parameters r_c and v_c are not well constrained – demonstrated by the 68, 90 and 95 per cent confidence contours in Fig. 3.14. The tilted contour cones are narrower than expected from Fig. 3.10. Note however, that we have rescaled the χ_{GH}^2 and hence effectively reduced the error bars as compared with the simulations. Therefore, also the shaded areas in Fig. 3.13 are smaller than the corresponding in Fig. 3.9.

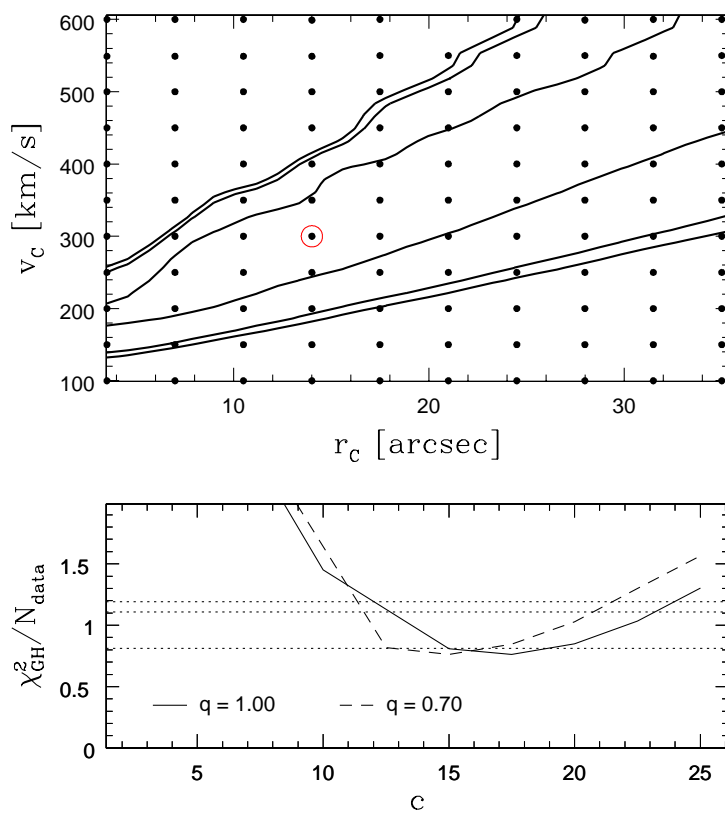


Figure 3.14: As Fig. 3.10, but for libraries fitted to the kinematics of NGC 4807. The best-fitting LOG-model is designated by the ring. In the lower panel results for spherical (solid line) as well as flattened NFW halos are illustrated (dashed line: $q = 0.7$).

In the lower panel of Fig. 3.14 the goodness of fit $\chi_{\text{GH}}^2/N_{\text{data}}$ is plotted versus concentration c for the one parameter family of NFW-profiles. As in the simulations of Sec. 3.5.3, the halo flattening is not constrained and with

a best-fit $\chi_{\text{GH}}^2/N_{\text{data}} \approx 0.77$ spherical as well as flattened NFW-halos provide almost indistinguishable good fits to the data as the best-fitting LOG-halos. In the innermost regions of those libraries that match the observations, we find $\rho/\rho_{\text{DM}} > 10$; the logarithmic density slope of the best-fitting spherical NFW model is $\gamma = -1.8$ at the outermost major-axis data point and $\gamma = -2.41$ at the outer edge of the orbit library. Hence, as already pointed out in Sec. 3.5.3, the mass distributions of the data-allowed NFW models – over the modelled spatial region – resemble halos of LOG type. Fig. 3.15 illustrates the data-allowed range of dark matter densities along the major axis. Note that the lower limit on ρ_{DM} is likely due to the limited range of profile shapes probed in our study. Dark matter distributions with negative central density slopes $\gamma < 0$ (not tested here) might also provide acceptable orbit models.

Models at $i = 50^\circ$ are ruled out by more than 68, but less than 90 per cent confidence. The best-fitting case is confronted with the kinematic observations in Fig. 3.16. Representative for all low-inclination models, it fails to reproduce the minor-axis H_4 -profile, but the mass structure of this model joins to the profiles in Fig. 3.13 and the inferred structural properties of the galaxy are robust against the assumed inclination.

3.7 Stellar motions in NGC 4807

Visual inspection of the surfaces of section reveals that none of the orbit libraries for NGC 4807 contains a significant fraction of chaotic orbits. In the best-fitting models, at all inclinations, no indication for chaos is detectable at all.

The internal orbital structure of the best-fitting edge-on halo model near the major and minor axes is shown in Fig. 3.17. Around the equatorial plane, at radii $1 r_{\text{eff}} < r < 3 r_{\text{eff}}$, the model is characterised by radial anisotropy. Enhanced radial velocity dispersion σ_r causes $\beta_\vartheta \approx \beta_\varphi \approx 0.3$, whereas $\sigma_\vartheta \approx \sigma_\varphi$. Taking the large rotation velocity into account, energy in azimuthal motion turns out to be roughly equal to the energy in radial motion, $\langle v_\varphi^2 \rangle \equiv v_{\text{rot}}^2 + \sigma_\varphi^2 \approx \sigma_r^2$. On the other hand, motion perpendicular to the equator is suppressed. Approaching the central parts the velocity structure changes to isotropy and inside $r < 0.5 r_{\text{eff}}$ stays isotropic.

Close to the minor axis, NGC 4807 appears nearly isotropic in the outer parts $1 r_{\text{eff}} < r < 3 r_{\text{eff}}$ with decreasing radial dispersion towards the centre, such that $\beta_\vartheta \approx \beta_\varphi < -0.5$ inside $r < 0.5 r_{\text{eff}}$.

68 per cent confidence intervals analogous to Fig. 3.9 for velocity anisotropies β_ϑ and β_φ as well as internal rotation velocities near the major and minor axes are shown in Fig. 3.18. Most tightly constrained is the major-axis rotation, rising from the central parts outwards until settling constant between r_{eff} ($v_{\text{rot}} = 124 \pm 6$ km/s) and $3 r_{\text{eff}}$ ($v_{\text{rot}} = 107 \pm 4$ km/s). Velocity anisotropy is determined to at least $\Delta\beta \leq 0.2$ and the trends in the anisotropy structure of the best-fitting model in Fig. 3.17 are clearly seen in all allowed orbit models.

Fig. 3.19 illustrates the internal close-to-major axis kinematics of the best-fitting orbit model at $i = 50^\circ$. In contrast to the edge-on models $\beta_\vartheta \approx 0$

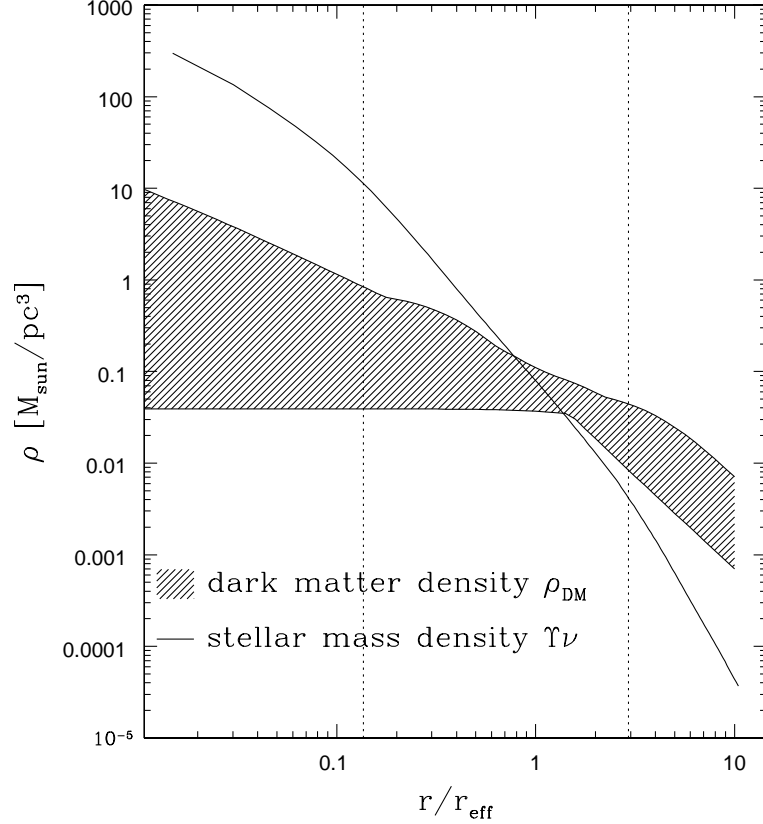


Figure 3.15: Major-axis stellar mass-density according to the edge-on deprojection (solid line, $\Upsilon = 3.0$) and data allowed dark matter densities. Both, LOG and NFW-halos are included in the plot. (The shaded area is constructed analogously to Fig. 3.9.)

over almost the whole region constrained by observations, with a slight raise towards the centre. Isotropy in the meridional plane ($\sigma_r \approx \sigma_\vartheta$) is accompanied by suppressed azimuthal dispersion σ_φ . But in contrast to the edge-on model of Fig. 3.17, the rotation of the actual model causes $\langle v_\varphi^2 \rangle / \sigma_r^2 \approx 1.7$, so that this model is dominated by azimuthal motion near the equatorial plane.

3.8 Phase-space structure of NGC 4807

In Fig. 3.20 phase-space densities w_i/V_i of individual orbits are plotted against orbital energy E for the best-fitting orbit model of NGC 4807. The top panel

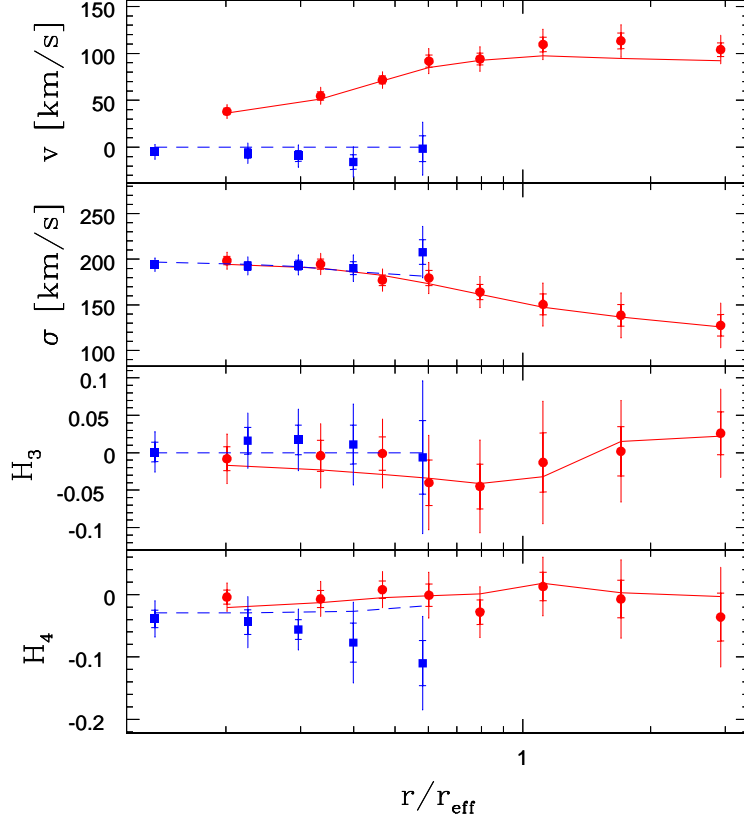


Figure 3.16: As Fig. 3.12, but for the best-fitting model at $i = 50^\circ$.

only includes orbits whose maximally reached latitude, ϑ_{\max} , is lower than $\vartheta_{\max} < 45^\circ$. These orbits are confined to a cone with opening angle $\vartheta < 45^\circ$ around the equatorial plane. The remaining orbits are plotted separately in the bottom panel. As in Figs. 3.3 and 3.4 the phase-space densities are scaled according to $\sum w_i = \sum V_i = 1$, where w_i and V_i are the orbital weights and orbital phase volumes, respectively. Whereas the orbits maintaining the bulge of the galaxy follow a DF similar to the one shown in Fig. 3.3, some of the orbits confined around the equatorial plane are strongly depopulated. Around $E \approx 3000 \text{ km}^2/\text{s}^2$ phase-space densities are up to 20 orders of magnitude below the main stream DF.

In the upper panel of Fig. 3.21 orbital phase densities are plotted against maximum orbital elongation ϑ_{\max} in the meridional plane. The three rows show orbits located in three different spatial regions separately. The top row

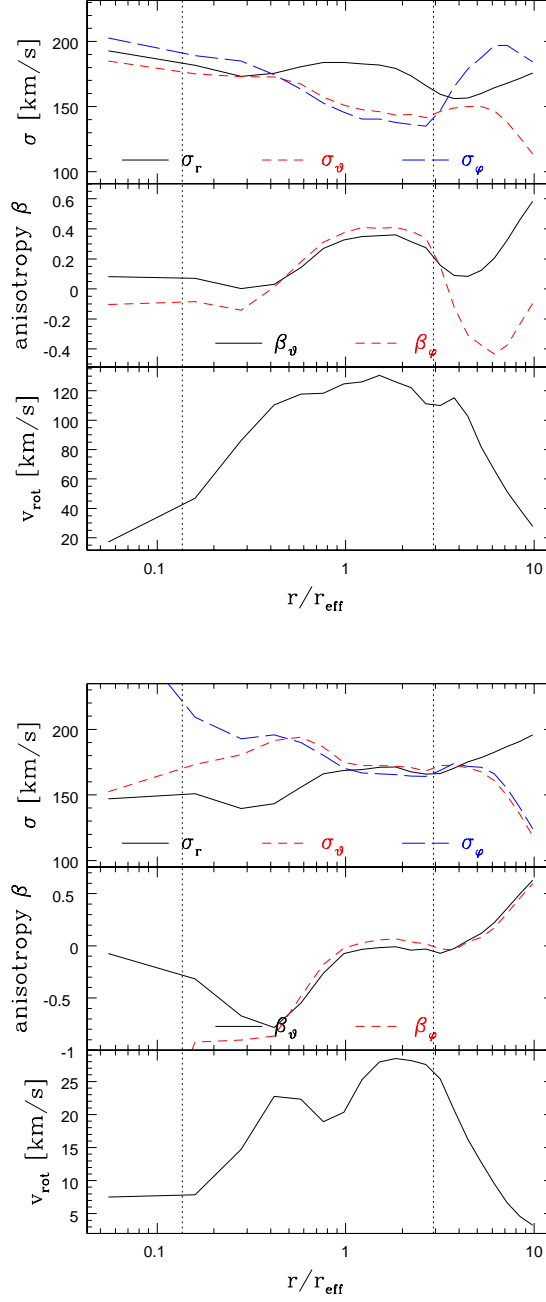


Figure 3.17: Internal kinematics of the best-fitting halo model near the major axis (top panel; position angle $\vartheta = 2.9^\circ$) and near the minor axis (bottom panel; $\vartheta = 77.1^\circ$), respectively. From top to bottom: velocity dispersions σ_r (solid), σ_ϑ (short-dashed) and σ_φ (long-dashed); velocity anisotropy β_ϑ , β_φ ; internal rotational velocity $v_{\text{rot}} = v_\varphi$. Vertical, dotted lines indicate the innermost and outermost radius of kinematic data. Note, that the minor axis data reach only out to $0.6 r_{\text{eff}}$.

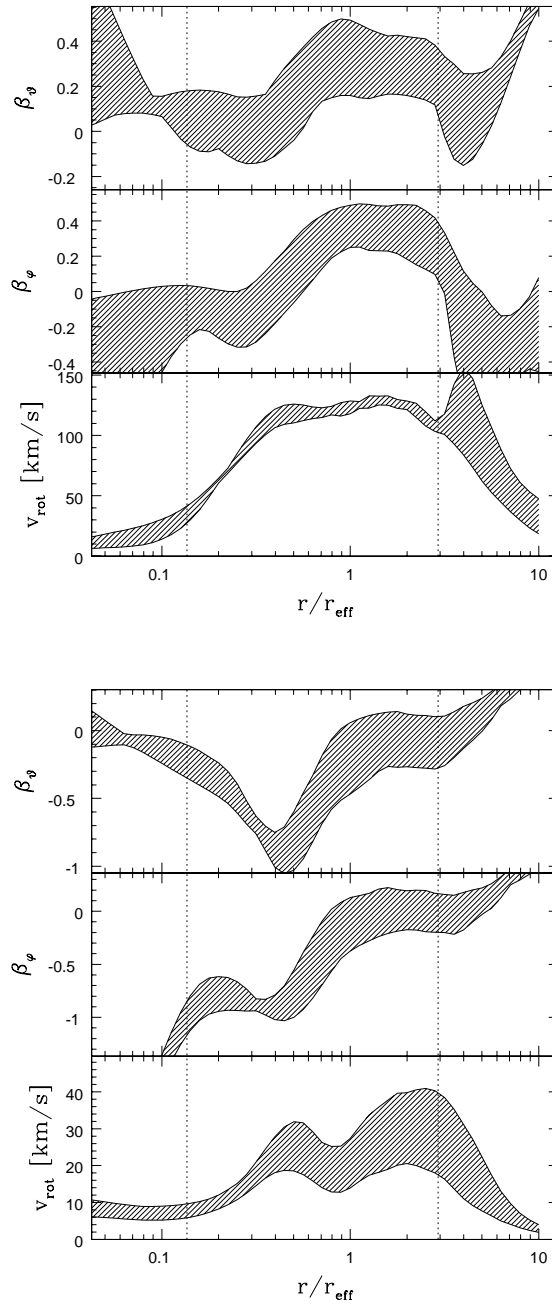


Figure 3.18: Confidence regions for meridional velocity anisotropy β_ϑ , azimuthal velocity anisotropy β_φ and internal rotational velocity v_{rot} (upper panel: near major axis, position angle $\vartheta = 2.9^\circ$; lower panel: near minor axis, position angle $\vartheta = 77.1^\circ$) of NGC 4807. Shaded areas are constructed as for Fig. 3.9.

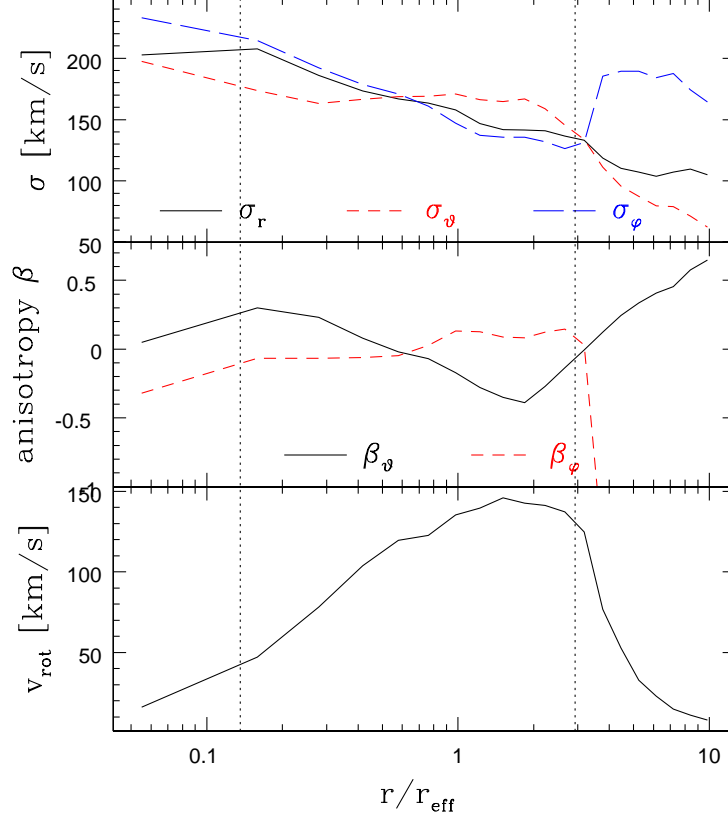


Figure 3.19: Internal close-to-major axis kinematics (position angle $\vartheta = 2.9^\circ$) of the best-fitting orbit model at $i = 50^\circ$. Line definitions as in Fig. 3.17.

includes only orbits whose invariant curves in the surface of section are confined to $0.5 r_{\text{eff}} < r_{\text{SOS}} < 1 r_{\text{eff}}$ ³. The spatial regions for the other two rows are $1 r_{\text{eff}} < r_{\text{SOS}} < 2 r_{\text{eff}}$ and $2 r_{\text{eff}} < r_{\text{SOS}} < 4 r_{\text{eff}}$, respectively. Crosses denote orbits with positive $L_z > 0$ while open circles denote orbits with negative $L_z < 0$. From the centre outwards, orbits with negative angular momentum are progressively depopulated as compared with their counterparts at positive L_z . The difference between prograde and retrograde orbits is most noticeable near the equatorial plane and disappears completely for bulge orbits reaching up to higher latitudes. In the bottom panel of Fig. 3.21 orbital phase densities are plotted against

³Here we use r_{SOS} as a short cut for the radii of orbital equatorial crossings, defining the surface of section. Fig. 1 in Thomas et al. (2004) gives an example of a typical surface of section in the actual context. The equatorial crossings locate orbits in the meridional plane fairly well.

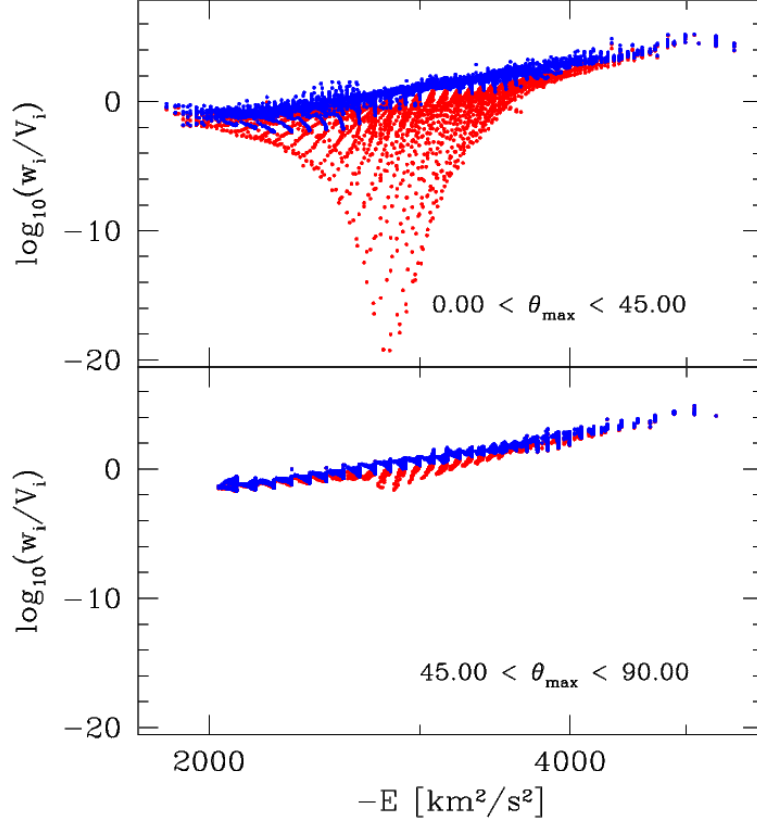


Figure 3.20: Reconstructed distribution function of the best-fitting orbit model at $\alpha = 0.02$. Each dot represents the phase-space density along a single orbit. Upper row: orbits confined to a konus with opening-angle $\vartheta_{\max} < 45^\circ$ around the equator; lower row: remaining orbits.

$L_z/L_{z,\text{circ}}$, $L_{z,\text{circ}}$ being the angular momentum of a circular orbit with the actual energy. Phase-space densities are extracted in the same spatial regions as for the upper panel of the Figure. It is now apparent that the keel in the DF of Fig. 3.20 is caused by a depopulation of (retrograde) circular orbits (at $|L_z| \approx L_{z,\text{circ}}$).

In fact, depopulation of retrograde near-circular orbits leading to the just described keel appears in all data-allowed DFs, with a slight tendency to be less pronounced in flattened halos. Even the DFs obtained assuming NGC 4807 is inclined by $i = 50^\circ$ are featured by this structure, albeit there, the keel is not exclusively made of retrograde orbits: also some of the prograde orbits

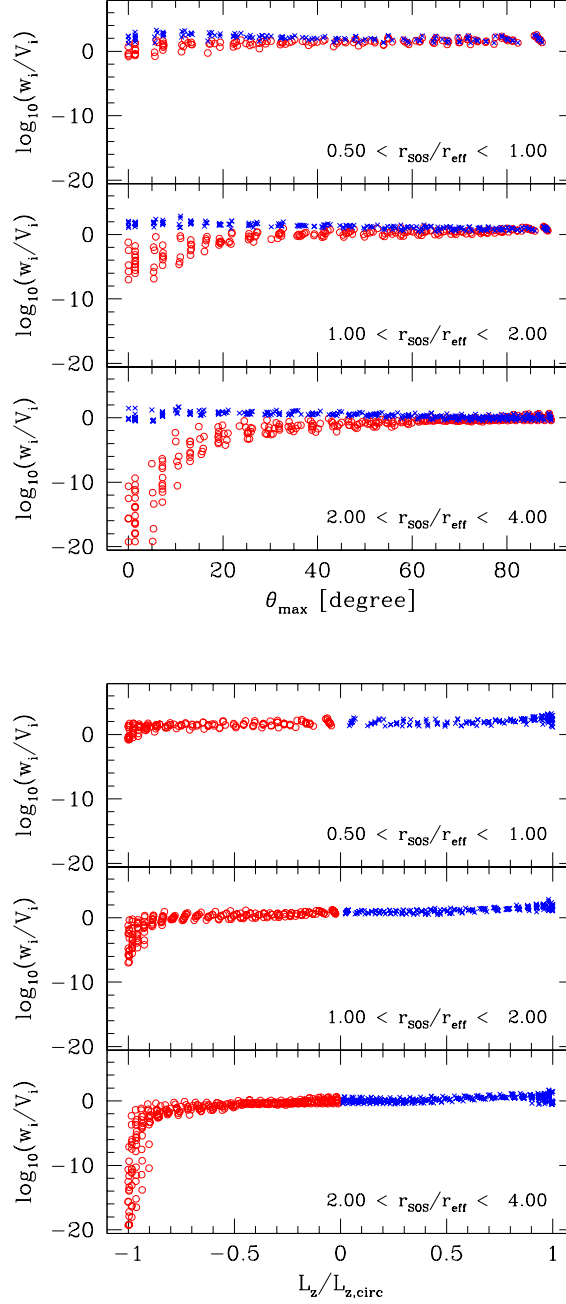


Figure 3.21: The same model as in Fig. 3.20. Top panel: phase densities versus maximum orbital elongation ϑ_{\max} in the meridional plane. Bottom panel: phase densities versus “circularity” (L_z scaled by the angular momentum $L_{z,\text{circ}}$ of a circular orbit with same energy). Crosses (open circles) denote orbits with positive (negative) L_z . Orbits are extracted from different spatial regions of the model as designated in the panels (see text for details). For each spatial region the number of prograde orbits (crosses) equals the number of retrograde orbits (open circles).

are suppressed. In the low inclination DFs a third prominent substructure in phase-space emerges in form of a significant fraction of high-energy orbits (around $E \approx -2500 \text{ km}^2/\text{s}^2$) being suppressed by about 6 orders of magnitude in density, independent from L_z . This structure partly overlays the keel and is caused by the distorted luminosity density at $i = 50^\circ$ since it shows up even in the maximum entropy models ($\alpha \approx 0$) which are only forced to reproduce the density profile, but not fitted to the kinematics.

Orbits in the keel together with their prograde counterparts (approximately all orbits i with $w_i^+/w_i^- > 99$, where $w_i^\pm \equiv w(E_i, \pm L_{z,i}, I_{3,i})$, $1 \leq i \leq N_{\text{pro}}$ and N_{pro} prograde orbits in the model) make only 4.3 per cent of the total model. Without these orbits, a slowly rotating bulge ($v \approx 70 \text{ km/s}$ at $r > r_{\text{eff}}$) with a slightly peaked velocity distribution ($H_4 > 0.04$ at $r > r_{\text{eff}}$) appears (see also Sec. 3.9.4). On the other hand, the extracted orbits rotate with about 200 km/s and produce a narrow, low-dispersion LOSVD. They develop a dumbbell-like structure extending to $2r_{\text{eff}}$ above the equatorial plane. The fraction of extracted orbits additionally obeying $\vartheta_{\text{max}} < 10^\circ$ shrinks to 0.7 per cent of the total model.

3.9 Summary and Discussion

3.9.1 Regularised orbit models

We have investigated how closely the internal mass distribution and kinematic structure of a galaxy can be recovered from a sparse kinematic data set typical for our project aimed at investigating a sample of flattened early-type galaxies in the Coma cluster. The degree to which orbit models follow internal galaxy properties depends on the amount of regularisation applied in the fits. In the maximum entropy technique of Richstone & Tremaine (1988) used here, a regularisation parameter α controls the relative importance of entropy maximisation (regularisation) on the one side, and fit to the data on the other. To find out which choice of α is optimal with respect to our goal of determining galaxy structural parameters, we simulated observationally motivated isotropic rotator models under realistic observational conditions. The models are based on a prototypical elliptical in our sample, NGC 4807. By varying α in the fits of appropriate orbit libraries to pseudo data of the reference models, the match between internal velocity moments of input model and orbital reconstruction can be evaluated as a function of regularisation.

Our simulations indicate that the mass-structure of an elliptical can be recovered to about 15 per cent accuracy in terms of mass-to-light ratio and circular velocity curve, if a regularisation parameter $\alpha = 0.02$ is applied. For the dynamical models tested here, the optimal choice of α turns out to be roughly independent from the galaxy's gravitational potential. The same accuracy as for the mass structure is achieved in the reconstruction of internal velocity moments. On the other hand, halo flattening and galaxy inclination are only weakly constrained by our data.

Regularisation biases orbit models towards some given idealised galaxy model, assumed to represent the object under study reasonably well. For early-type galaxies, regularisation has been commonly implemented to isotropize the final fit. How much of regularisation is optimal in the reconstruction of a given galaxy depends on the specific data set (spatial coverage, quality) on the one hand and the degree to which the regularisation bias approximates the given galaxy on the other. Isotropizing the DF might, for example, be a good recipe for relaxed early-type galaxies but less favourable for lenticulars with a significant, dynamically cold, component. In that case either the value of α or, preferentially, the functional form of S has to be reconsidered. In any case, and for any regularisation technique, the optimal balance between fit to data and smoothing of the DF can be examined case-by-case from simulations similar to those described here.

Cretton et al. (1999) and Verolme & de Zeeuw (2002) have determined optimal regularisation for an implementation of Schwarzschild’s method with two-integral components by reconstructing similar DFs as used here. The resulting regularisation has proven to yield plausible results in subsequent applications (e.g. Cappellari et al. 2002; Verolme et al. 2002; Copin, Cretton & Emsellem 2004; Cretton & Emsellem 2004; Krajnović et al. 2005). It is difficult to quantitatively compare the amount of regularisation applied in these works with the results of our simulations since the regularisation techniques differ. However, in each case the achieved accuracy in the recovery of test model parameters and the derived dynamical structure of real galaxies indicate that the applied amount of regularisation is comparable.

3.9.2 Luminous and dark matter in NGC 4807

We then applied our code with the simulation-derived regularisation to the elliptical NGC 4807. The dynamical models require substantial dark matter in the outer parts of the galaxy. Evidence for dark matter in the form of flat circular velocity curves from (integrated) stellar kinematics of ellipticals has also been found by Rix et al. (1997), Gerhard et al. (1998), Emsellem, Dejonghe & Bacon (1999), Cretton, Rix & de Zeeuw (2000), Kronawitter et al. (2000), Saglia et al. (2000) and Gerhard et al. (2001). Dynamical models of five galaxies with planetary nebulae kinematics complementing stellar kinematics out to $\approx 5 r_{\text{eff}}$ lead the authors to different appraisals: Romanowsky et al. (2003) argue for non-dark matter models consistent with three galaxies observed by the planetary nebulae spectrograph, while Peng, Ford & Freeman (2004) require dark matter in NGC 5128 and the models of NGC 1399 also point at a dark halo (Saglia et al. 2000).

Spherical models for the 21 round ellipticals in the sample of Kronawitter et al. (2000) reveal dark matter fractions of 10 – 40 per cent at $1 r_{\text{eff}}$ and dark mass equals luminous mass at roughly $2 - 4 r_{\text{eff}}$ (Gerhard et al. 2001), both comparable to our results for NGC 4807. The halo core density ρ_c of our best-fitting model is about 30 per cent below the predictions of their $\rho_c - L_B$ relation (taking $M_B = -20.76$), although still consistent with it. Among the allowed

LOG-halos however, the core densities vary by a factor of ten and taking into account NFW-fits, even halos 90 times denser than the best-fitting model are consistent with the data (cf. Fig. 3.15). From the concentration of our best-fitting (spherical) NFW-halo nevertheless a relatively low formation redshift $z_f \approx 2.5$ follows. Still, we need a larger number of flattened ellipticals modelled in sufficient generality to recover the detailed properties and physical origin of their mass distributions.

To crosscheck our mass decomposition for NGC 4807 we compared stellar mass-to-light ratios of the orbit superpositions with stellar mass-to-light ratios determined completely independent. In Fig. 3.22 mass-to-light ratios from stellar population models (Maraston 1998; Thomas, Maraston & Bender 2003; Maraston 2004) of NGC 4807's major-axis spectrum (Mehlert et al. 2000; Mehlert et al. 2003) are compared to the best-fitting orbit models (dashed line: stellar mass-to-light ratio in orbit model; hatched region: 68 per cent confidence region of surface mass SM over surface brightness SB in orbit models; different symbols refer to different initial-mass-functions (IMFs) underlying the populations). Systematic uncertainties stemming from the unknown IMF are roughly comparable to the statistical errors, indicated for the Kroupa-IMF by the pointed area. Only libraries with $\Upsilon = 3.0$ are taken into account in the figure.

As the figure demonstrates, the stellar mass-to-light ratios determined dynamically agree with stellar populations following a Kroupa IMF to $\Delta\Upsilon \approx 0.5$. This (1) confirms our mass decomposition and (2) justifies a posteriori the assumption of a constant stellar mass-to-light ratio. The total surface mass of the dynamical models, as indicated by the shaded region in Fig. 3.22, exceeds the stellar contribution by far and underlines the evidence for dark matter in NGC 4807. Since our best-fitting orbit models have LOG-halos (or NFW-halos imitating the mass distribution of LOG-halos over the kinematically sampled spatial region) they have maximum stellar mass (e.g. Gerhard et al. 1998). This is in accordance with most previous studies that did not require steep central dark matter profiles (Gerhard et al. 1998; Emsellem, Dejonghe & Bacon 1999; Cretton, Rix & de Zeeuw 2000; Kronawitter et al. 2000; Saglia et al. 2000 and Gerhard et al. 2001). On the other hand, Rix et al. (1997) found such profiles consistent with NGC 2434.

3.9.3 Comparing the kinematics: χ_{GH}^2 versus χ_{LOSVD}^2

The confidence intervals for the structural properties of NGC 4807 have been derived from χ_{GH}^2 as defined in equation (3.10). However, our models do not explicitly minimise χ_{GH}^2 but instead χ_{LOSVD}^2 as given by equation (3.8). In order to investigate how the properties of the best-fitting orbit model and the corresponding confidence limits of the halo parameters depend on the choice of χ^2 we have analysed the Monte-Carlo simulations as well as the models for NGC 4807 also in terms of

$$\hat{\chi}_{\text{LOSVD}}^2 \equiv \chi_{\text{LOSVD}}^2 / \hat{N}_{\text{data}}, \quad (3.11)$$

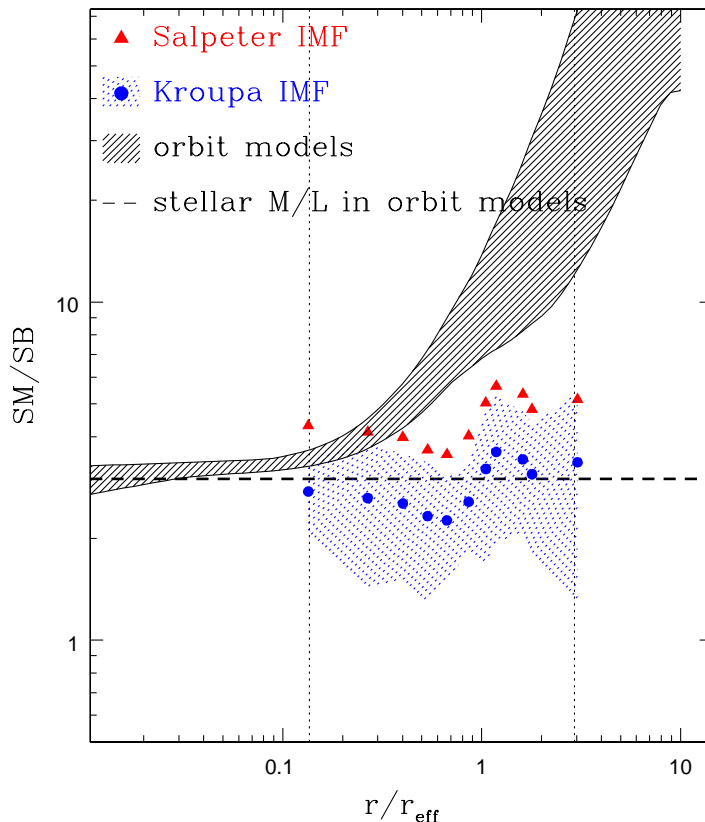


Figure 3.22: Projected mass-to-light ratio along the major axis of NGC 4807. Hatched area: 68 per cent confidence region of surface mass (SM) over surface brightness (SB) for all orbit models with $\Upsilon = 3.0$ (dashed line). For comparison the projected stellar mass-to-light ratios from population analysis (see text) are shown for two different IMFs: Salpeter-IMF (triangles), Kroupa-IMF (dots). The pointed area encompasses the statistically allowed Υ based on the Kroupa-IMF. For the sake of clarity, the similar, but shifted, error region for the Salpeter-based Υ is omitted.

where \hat{N}_{data} is the number of velocity bins for which $\mathcal{L}_{\text{dat}}^{jk} > 0$ (cf. equation 3.8).

Fig. 3.23 shows the best-fitting halo parameters and corresponding confidence intervals for the simulated isotropic rotator model of Sec. 3.5.3. The figure is as Fig. 3.10, besides that all confidence regions and model-with-data comparisons are computed in terms of $\hat{\chi}_{\text{LOSVD}}^2$. Comparing Figs. 3.10 and 3.23, it turns out that both χ^2 -definitions yield identical best-fitting models (desig-

nated by the rings in the upper panels, and given by the minima of the two curves in the lower panels). Concerning the confidence regions, however, the computations based on $\hat{\chi}_{\text{LOSVD}}^2$ lead to smaller confidence limits for both, the logarithmic and the NFW-halos.

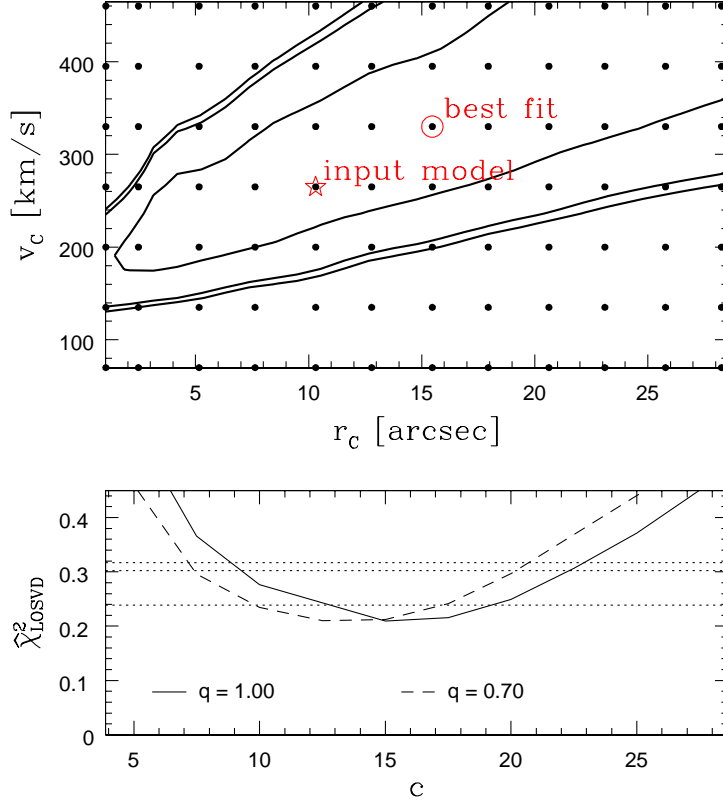


Figure 3.23: As Fig. 3.10, but the confidence regions are derived from $\hat{\chi}_{\text{LOSVD}}^2$ (see Sec. 3.3.5).

For NGC 4807, the analysis based on $\hat{\chi}_{\text{LOSVD}}^2$ leads to the results shown in Fig. 3.24. Again, besides the different χ^2 -definition applied, it is as Fig. 3.14. The best-fitting NFW-halos in Fig. 3.24 are the same as in Fig. 3.14. The shapes of the $\hat{\chi}_{\text{LOSVD}}^2$ curves for $q = 1.0$ and $q = 0.7$ in the bottom panel of Fig. 3.24 prefer halos slightly more concentrated than in the χ_{GH}^2 -case, but, as for the isotropic rotator simulations, the differences in the results obtained from χ_{GH}^2 and $\hat{\chi}_{\text{LOSVD}}^2$ are small.

Regarding the best-fitting logarithmic-halo models (marked by the rings in

the upper panels) both χ^2 -calculations give consistent, but, in contrast to the Monte-Carlo simulations, not identical results. As already indicated in the NFW-fits, the logarithmic halo that best fits in the sense of $\hat{\chi}_{\text{LOSVD}}^2$ is more concentrated: the dark matter fraction inside r_{eff} is $M_{\text{DM}}/M = 0.35$, compared with $M_{\text{DM}}/M = 0.22$ for the best-fitting model in the upper panel of Fig. 3.14. A more striking difference between the upper panels of Fig. 3.14 and 3.24 is the closure of the 68 per cent $\hat{\chi}_{\text{LOSVD}}^2$ -confidence contour to the upper right. The contour differences may be related to the ignorance of γ_0 in equation (3.10), since the mismatch between model and data intensities progressively increases from the lower left to the upper right in the upper panel of Fig. 3.14.

Nevertheless, the comparison of the results obtained from χ_{GH}^2 and $\hat{\chi}_{\text{LOSVD}}^2$ reveals that both methods – within the errors – give the same results. The confidence limits quoted in this paper, based on equation (3.10), are the more conservative choice, but may be slightly too pessimistic.

3.9.4 The outer parts of NGC 4807

Based on a recent refinement (Thomas et al. 2004) of the Schwarzschild code of Richstone & Tremaine (1988) and Gebhardt et al. (2000a), we recovered a depopulation of retrograde, near-circular orbits in the phase-space DF of NGC 4807, giving rise to a keel when plotting orbital phase-space densities against orbital energy. The prograde counterparts of the depopulated orbits form a dumbbell-like structure extending about $\approx 2 r_{\text{eff}}$ above the equatorial plane.

To investigate what might cause the depopulation of retrograde orbits in the outer parts of NGC 4807, we projected a sequence of distribution functions in which all orbits involved in the keel ($w_i^+/w_i^- > 99$, see Sec. 3.8) are repopulated according to

$$\begin{aligned} w_{i,\text{new}}^+ &\equiv \xi \times (w_i^+ + w_i^-) \\ w_{i,\text{new}}^- &\equiv (1 - \xi) \times (w_i^+ + w_i^-). \end{aligned} \quad (3.12)$$

Since $w_{i,\text{new}}^+ + w_{i,\text{new}}^- = w_i^+ + w_i^-$ this does not alter the fit to the luminosity profile but just levels the relative fraction ξ of light on the prograde and retrograde specimen of all keel-involved orbit pairs. Roughly speaking, equation (3.12) transforms the keel into a narrow cloud of points parallel to the main-stream DF with an offset increasing with $|\xi - 0.5|$. Figure 3.25 shows the resulting projected (major-axis) kinematics for $\xi = 0.7, 0.94, 1.0$. As expected, shifting light from prograde to retrograde orbits reduces the amount of rotation v and lowers H_3 in the outer parts, while at the same time leading to a larger velocity dispersion σ and enhanced H_4 . As shown by the goodness of fit in the lower panel of Fig. 3.25, the best fit to the data is achieved for $\xi = 1.0$ (all retrograde keel-orbits completely depopulated). Comparing the corresponding solid lines in Fig. 3.25 with the upper panel of Fig. 3.12 reveals that $\xi = 1.0$ provides essentially the same fit as the best-fitting orbit model. Consequently, the retrograde keel-orbits can be regarded as completely depopulated in our models of NGC 4807. Reducing the relative fraction of light on the prograde counterparts of keel-orbits to $\xi = 0.94$ is only consistent with the observations at the 68 per

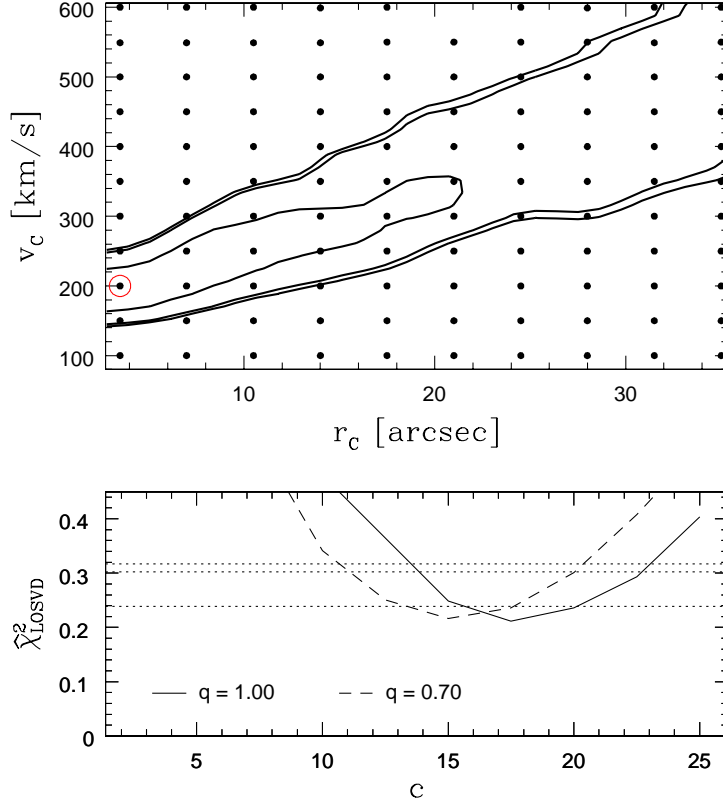


Figure 3.24: As Fig. 3.14, but the confidence regions are derived from $\hat{\chi}_{\text{LOSVD}}^2$ (see Sec. 3.3.5).

cent confidence level. A further equalisation to $\xi = 0.7$ is already incompatible with the observed velocity profiles.

The outer major-axis LOSVDs of NGC 4807 might indicate weak triaxiality, for example in form of a weak, nearly end-on bar (e.g. Bureau & Athanassoula 2005). A weak bar-like structure would also fit to the boxy appearance of the galaxy’s outer isophotes. Assuming that NGC 4807 is slightly triaxial, the keel in the DF might be an artifact of the assumption of axisymmetry. Note, however, that NGC 4807 is consistent with being axisymmetric, albeit then the depopulation of single orbit families, especially around the equatorial plane, is hard to understand in the course of dynamical processes.

Depopulation of retrograde orbits in the outer parts of the galaxy is accompanied by a change in stellar ages from $\tau \approx 5$ Gyr inside $r < r_{\text{eff}}$ to $\tau \approx 10$ Gyr

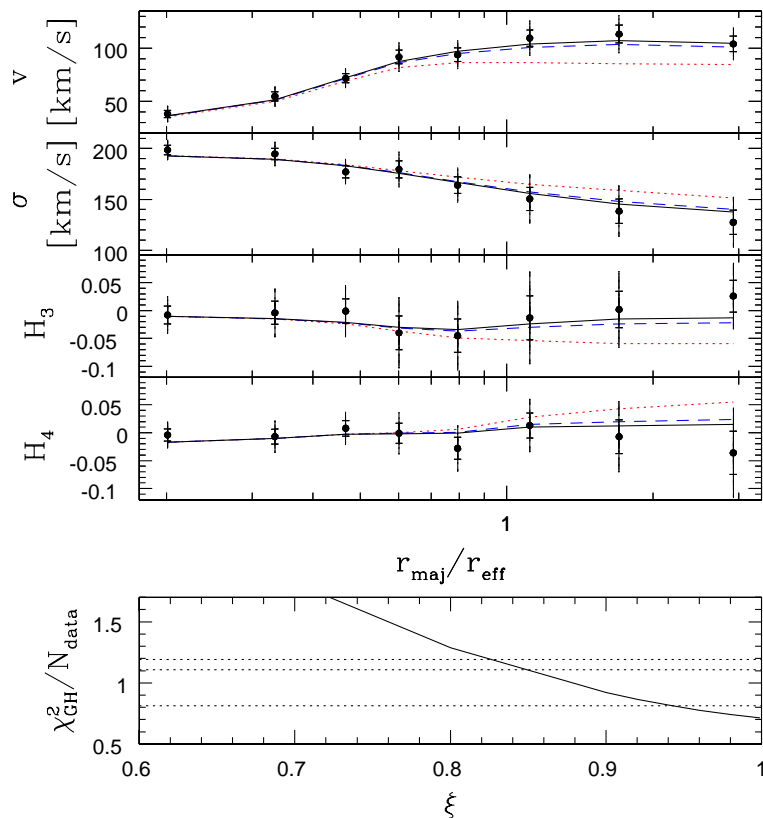


Figure 3.25: Upper panel: projected major-axis kinematics of three distribution functions calculated in the gravitational potential of the best-fitting mass model: (1) all retrograde orbits in the keel depopulated completely (solid); relative fraction of light on prograde keel-orbit counterparts (2) $\xi = 0.94$ (short-dashed) and (3) $\xi = 0.7$ (dotted). Lower panel: goodness of fit (including the minor-axis LOSVDs, which are not affected by the redistribution of keel-involved orbits) as a function of the relative fraction ξ of light on prograde keel-orbit correspondents; horizontal dotted lines indicate 68, 90 and 95 per cent confidence levels.

at larger radii (Mehlert et al. 2003). Towards $3r_{\text{eff}}$ stellar ages become uncertain and no clear trend is visible. It seems also possible, that the keel in the DF is an artifact related to a distinct stellar component and an associated (slight) change in Υ . It should be noted that because the orbit models are fitted to deprojections and stellar kinematics, the derived DFs characterise the amount of *light* per volume element in phase-space, not the *mass*-density in phase-space.

Accordingly, depressions in the DF might (at least partly) reflect enhanced Υ .

A distinct stellar component in the outer parts must not necessarily take the form of a bar, but could also be a faint axisymmetric stellar disk. Indeed, the photometry as well as the orbit models suggest that NGC 4807 is close to edge-on, but a dynamically cold, outer stellar disk made of only 0.7 per cent prograde orbits at latitudes $\vartheta < 10^\circ$ (see Sec. 3.8) is consistent with the non-disk isophotes ($\max a_4 < 1$). A disk carrying 2 per cent of the total luminosity would show up with $\max a_4 \approx 4$ when seen exactly edge-on and $\max a_4 < 1$ for such a disk would require $i < 75^\circ$ (Rix & White 1990). From our simulations it seems impossible to distinguish kinematically between $i = 70^\circ$ and $i = 90^\circ$ and, consequently, there is some freedom for an outer disk in NGC 4807.

In any case further investigations are necessary to verify the significance of the keel-structure in the DF of NGC 4807. (1) Kinematic measurements along intermediate position angles in the galaxy would likely put more constraints on the DF. (2) Detailed comparison of orbit superpositions with realistic galaxy models are required to estimate how relics of triaxiality, faint disks and multi-component (multi- Υ) structures show up in our axisymmetric models. These questions will be addressed in a forthcoming publication.

3.9.5 Internal stellar kinematics of NGC 4807

Along the major-axis, NGC 4807 is mildly radially anisotropic. Radial anisotropy has been found in a number of ellipticals (Gerhard et al. 1998; Matthias & Gerhard 1999; Cretton, Rix & de Zeeuw 2000; Gebhardt et al. 2000a; Saglia et al. 2000). The amount of anisotropy ($\beta \approx 0.3$) in the outer parts as well as the isotropy of the central region (inside $0.3 r_{\text{eff}}$) matches with the typical anisotropy structure found for round, non-rotating ellipticals by Gerhard et al. (2001). Along the minor axis, NGC 4807 is dominated by tangential motions. Gebhardt et al. (2003) report tangential anisotropy for some galaxies (mostly enhanced azimuthal, but suppressed meridional dispersions) and also Dejonghe et al. (1996), Cretton & van den Bosch (1998), Statler, Dejonghe & Smecker-Hane (1999), Cappellari et al. (2002), Verolme et al. (2002) and Copin, Cretton & Emsellem (2004) find predominantly tangential motions. For NGC 3115 Emsellem, Dejonghe & Bacon (1999) notice $\sigma_z > \sigma_r$. All these studies are based on data sets with different spatial sampling and use various dynamical modelling techniques, particularly differing in the amount and functional form of the applied regularisation. As for the mass structure and the dark matter properties, a large and homogeneous sample of galaxies is needed to address the physical processes shaping elliptical galaxies.

Chapter 4

The coma sample and its modelling: general survey

Before analysing the Coma galaxies in detail, the present chapter aims to provide a general overview about the observations and the modelling of the Coma galaxies.

4.1 Summary of observations

As already outlined in the introduction the Coma sample comprises in total nine early-type galaxies: eight ellipticals and one lenticular. The galaxies span a moderate range in luminosities between $-20.3 < M_B < -21.4$ with a single fainter elliptical at $M_B = -18.8$ (magnitudes from Hyperleda; cf. Tab. 4.1¹). Similarly, their effective radii vary only between $6''.7 < r_{\text{eff}} < 18''.4$ ($r_{\text{eff}} = 3''.3$ for the fainter elliptical; cf. Tab. 4.1). They all share the same distance and, thus, the spatial resolution in the photometric as well as the kinematical observations is comparable in all galaxies.

Photometric observations are summarised in Tab. 4.1. For all galaxies but GMP1176 a composite photometry has been constructed from ground-based (outer parts) and HST imaging (inner parts), as described in Sec. 3.2.1. For the lenticular GMP1176 no archival HST photometry is available (cf. the comments in Sec. 4.3 and the additional discussion in App. B).

The kinematical data is resumed in Tab. 4.2. Apart from GMP0144 (diagonal slit) and GMP1176 (major-axis parallel slit) all galaxies have kinematical observations along two position angles (major and minor axis).

¹ The Coma sample is subdivided into two classes (different colours in Tabs. 4.1, 4.2, 4.3 and all subsequent tables and plots dealing with the whole sample). The two classes distinguish galaxies with different dark matter halos as discussed in Sec. 5.4.1. Up to that section the subdivision is actually insignificant but is kept anyhow throughout the whole thesis for better comparison of different parts of the thesis. Within each subclass, galaxies are ordered according to their B -band luminosity.

galaxy		type	photometry		r_{eff} [arcsec]	M_B [mag]	$\text{rms}\langle\mu_{\text{grd}} - \mu_{\text{HST}}\rangle$ [mag]
GMP	NGC		HST	grd			
(1)	(2)	(3)	(4)	(5)	(6)	(7)	(8)
5279	4827	E2	L97	M00	13.6	-21.36	0.019
3792	4860	E2	L97	J94	8.5	-20.99	0.071
0282	4952	E3	L97	M00	14.1	-20.69	0.009
3510	4869	E1	L97	J94	7.6	-20.40	0.033
1176	4931	S0	-	M00	7.4	-20.32	-
3958	IC 3947	E3	L97	J94	3.3	-18.79	0.024
1750	4926	E1	L97	J94	11.0	-21.42	0.058
0144	4957	E3	L97	M00	18.4	-21.07	0.011
5975	4807	E2	L97	M00	6.7	-20.73	0.015

Table 4.1: Summary of photometric data. (1,2) galaxy id (GMP No. from Godwin, Metcalfe & Peach 1983); (3) morphological type from Mehlert et al. (2000); (4,5) photometry (L97 = HST V-band WFPC2 data, Principal Investigator: John Lucey, Proposal ID: 5997; M00 = Kron-Cousins R_C -band CCD photometry from Mehlert et al. 2000; J94 = Gunn r CCD photometry from Jørgensen & Franx 1994); (6) effective radius from Mehlert et al. (2000); (7) absolute B-band magnitude (from Hyperleda; $H_0 = 70$ km/s/Mpc); (8) $\text{rms}\langle\mu_{\text{grd}} - \mu_{\text{HST}}\rangle$ between shifted HST surface brightness μ_{HST} and corresponding ground-based μ_{grd} (see Section 3.2.1 for details).

galaxy		type	maj	min	off	dia
GMP	NGC		[r_{eff}]	[r_{eff}]	[r_{eff}]	[r_{eff}]
(1)	(2)	(3)	(4)	(5)	(6)	(7)
5279	4860	E2	1.6	0.7	-	-
3792	4869	E2	1.1	1.0	-	-
0282	4952	E3	1.7	0.5	-	-
3510	4827	E1	2.0	1.1	-	-
1176	4931	S0	4.7	0.8	3.7	-
3958	IC 3947	E3	1.7	0.9	-	-
1750	4926	E1	0.9	0.9	-	-
0144	4957	E3	1.4	0.7	-	0.2
5975	4807	E2	2.9	0.5	-	-

Table 4.2: Summary of kinematic data. (1-3) as Tab. 4.1; (4-7) radius of the outermost kinematic point along various slit positions: maj/dia/min = position angle of $0^\circ/45^\circ/90^\circ$ relative to major axis; off = parallel to major axis with an offset of $r_{\text{eff}}/2$.

4.2 Modelling setup and regularisation

Each Coma early-type galaxy has been modelled using exactly the same deprojection technique and library setup as introduced in Chap. 3. For each galaxy but GMP1176 three representative inclinations have been probed: (1) at $i = 90^\circ$ (edge-on); (2) at a minimum inclination where the deprojection looks like an E7 from edge-on; (3) at an intermediate inclination, where it looks like an E5 from edge-on. Limited by computation time it was not possible to probe a finer grid of inclinations. For the lenticular GMP1176 only the edge-on case has been considered, because the galaxy is rather flat and disk ($\epsilon \approx 0.6$ and $a_4 \gtrsim 5$ in the outer parts). Already an inclination of $i = 77^\circ$ yields an edge-on E7 deprojection. In view of the MC simulations of Sec. 3.4.2 it is barely possible to discriminate between $i = 77^\circ$ and $i = 90^\circ$ from the dataset at hand.

As it has been pointed out in Sec. 3.4, the optimal regularisation parameter α has to be derived ideally case-by-case for each galaxy. The reason is firstly that spatial resolution and coverage as well as signal-to-noise of the observations vary from galaxy to galaxy. The smoothing in the models should be adapted to the particular data set in each case, which mainly requires to adjust the relative weight of regularisation constraints to data constraints in each single case. More subtle problems arise from structural differences between galaxies. The essential reason is that the concept of smoothing must be matched to the system at hand. Specifically the maximum entropy method seems a natural choice for dynamically hot, relaxed stellar systems, but already the presence of rotation leads to deviations from maximum entropy. Moreover, galaxies may be dynamically inhomogeneous. Consider, for example, a cold disk inside a hot spheroid. To fit the rotation of the disk α should be large, but on the other hand, in the dynamically more relaxed regions of phase-space, a large α will amplify the noise in the models. The dilemma as to the choice of α could be solved by defining an appropriate function S that allows different amounts of smoothing in different regions of phase-space.

Concluding, different data sets require the specific balance of regularisation and data-match to be adjusted for each galaxy, while structural differences require additional modification of the regularisation constraints itself (the functional form of S). For the Coma sample it has been decided to use the same function S and the same regularisation parameter α for all galaxies. The reason is, that the determination of α takes as much computer time as the complete data analysis for a galaxy. From the overall homogeneity of the Coma data one would expect only slight variations of α over the sample and the effort to calculate these seems not justified. Moreover, structural differences between the galaxies, especially the fact that some rotate and other do not, are likely the more critical issue. Accordingly, it would be necessary to explore different forms of S , which is out of the scope of this work. In view of the fact that α has been determined from isotropic rotators (cf. Sec. 3.4.2) its value may be too large for the non-rotating galaxies, but is unlikely to be too small for the rotating galaxies. In any case, the dependency of the modelling results on α is discussed for each galaxy in Secs. 5.6 and 6.7, respectively.

galaxy		type	r_C	v_C	c	Υ_{dyn}	i	$(\hat{\chi}_{\text{GH}}^2)_0$
GMP	NGC		[kpc]	[km/s]		$[M_{\odot}/L_{\odot}]$		
(1)	(2)	(3)	(4)	(5)	(6)	(7)	(8)	(9)
5279	4860	E2	28.4	482	–	6.5	90	0.10
3792	4869	E2	–	–	10.0	8.0	40	0.35
0282	4952	E3	17.97	502	–	5.0	60	0.24
3510	4827	E1	11.64	287	–	5.5	90	0.39
1176	4931	S0	9.70	150	–	3.0	90	1.03
3958	IC 3947	E3	6.79	274	–	5.0	90	0.16
1750	4926	E1	2.67	300	–	6.0	90	0.46
0144	4957	E3	–	–	17.9	4.5	65	0.14
5975	4807	E2	1.70	228	–	2.5	90	0.17

Table 4.3: Summary of bestfit model parameters. (1-3) as Tab. 4.1; (4,5) core radius r_C and asymptotic velocity v_C of NIS-halo (if NIS halo fits best); (6) concentration c of NFW-halo (if NFW-halo fits best); (7) stellar Υ_{dyn} (R_C -band); (8) inclination i ; (9) bestfit $(\hat{\chi}_{\text{GH}}^2)_0 \equiv \min(\chi_{\text{GH}}^2/N_{\text{data}})$.

The bestfit model parameters are summarised in Tab. 4.3. A detailed analysis of the models follows in Chaps. 5-7. Notes on individual galaxies are the subject of Sec. 4.3.

4.3 Notes on individual galaxies

Figs. 4.1 - 4.9 survey the photometric and kinematical observations together with the model fits. In the upper panels the appearance of the models from edge-on is shown for comparison with the photometric data. The majority of bestfit models is edge-on and blue and red lines (deprojection fit and edge-on reprojection, respectively) coincide. Note, that the models are not fitted directly to the kinematical data shown in the lower panels, but to a symmetrized data set (cf. Sec. 3.2.3). The last column (9) in Tab. 4.3 is computed from the symmetrized input data as well.

GMP5279. GMP5279 is one of the two brightest galaxies in the sample. As most galaxies in the sample it has a fairly flat ellipticity profile. Apart from weak boxiness in the very outer parts significant deviations from elliptical isophotes lack. Rotation is marginal, but peaks distinctly around $0.3 r_{\text{eff}}$ accompanied by a dip in H_3 . Possibly a dynamically cold subsystem, maybe a ring or small disk, causes this peak, but there is no corresponding photometric evidence for this. The galaxy’s minor-axis dispersion is slightly larger than along the major-axis and both profiles are rather flat. Noteworthy, the strongly negative H_4 -profile along the minor-axis. The bestfit yields $i = 90^\circ$, possibly because of the rotational structure seen along the major-axis. On the other side, in all galaxies with negative minor-axis $H_4 < 0$ the bestfit model is edge-on.

GMP3792. GMP3792 appears a bit rounder than GMP5279, especially near the centre. In the outer parts the diskiness rises strongly, unfortunately only outside the kinematically sampled region. In the inner region there is barely any rotation. Instead, the large and spatially constant major-axis dispersion together with the steeply decreasing minor-axis dispersion hint for the presence of two counter-rotating flat subsystems. In that case the relatively round isophotes would imply that the system is seen significantly inclined. Indeed, the bestfit dynamical model predicts $i = 40^\circ$.

GMP0282. GMP0282 shows a wealth of structure: most noteworthy a local peak in a_4 around $0.5 - 1.0 r_{\text{eff}}$ followed by strong diskiness in the outer parts. Around the inner peak in a_4 the major-axis exhibits a little break in v and a dip in H_3 . Along the same axis the dispersion falls off steeply from the centre outwards and levels in the outer, disk-like region roughly with rotation – possibly indicating a smooth transition to an outer disk-like orbital configuration. In the outer parts the LOSVDs become triangular shaped ($H_4 > 0$). According to Tab. 4.3 the bestfit model is at $i = 60^\circ$, but the difference to the edge-on case is marginal (the latter is overplotted by the dashed lines in the lower panel of Fig. 4.3).

GMP3510. The observations of GMP3510 are difficult to interpret. While the a_4 parameter hints at a central disk, the ellipticity peaks around $r_{\text{eff}}/3$. None of these features can easily be traced into the kinematical structure, which is instead characterised by a smooth but mild increase of rotation and a corresponding decrease of dispersion with radius. Significant deviations from Gaussian LOSVDs lack at all. Interestingly, the minor-axis dispersion profile is rather flat (but noisy). Along the minor-axis H_4 becomes negative. As stated above, this may cause the models to prefer $i = 90^\circ$.

GMP1176. The lenticular GMP1176 is the flattest object in the sample. The central decrease in ellipticity is likely caused by the uncorrected seeing ($\sigma = 2'' \approx r_{\text{eff}}/3$). The a_4 parameter exhibits two distinct maxima in the outer parts (at $1 - 2 r_{\text{eff}}$ and $5 r_{\text{eff}}$, respectively). In between ($\approx 2 r_{\text{eff}}$) the major-axis rotation drops and $H_3 \approx 0$. Moreover, around the inner a_4 -peak rotation is anti-correlated with H_3 , while towards the very outer parts, where H_3 tends to rise, the dynamical structure might change. The dashed lines in the lower panel of Fig. 4.5 show that the fit can be improved with less regularisation – reasonably in view of a possibly strong disk that causes substantial deviations from maximum entropy. The main uncertainty for the models of this galaxy, however, comes from the unknown central light profile. This issue is further discussed in App. A.

GMP3958. The faintest galaxy of the sample is GMP3958. HST photometry and ground-based imaging do not match very well (revealed by the discontinuity in ϵ slightly beyond the half-light radius). From the HST image evidence for

a disk comes from $a_4 > 0$ (although the profile oscillates). A rotating disk superimposed on a dynamically hot spheroid is also consistent with the anti-correlation of v and H_3 around the apparent major-axis. Along the small axis H_4 is negative, possibly driving the fit towards $i = 90^\circ$.

GMP1750. The brightest galaxy in the sample is GMP1750. It is quite featureless in both the photometric and kinematical observations. Its luminosity and the low but distinct rotational signal around $r_{\text{eff}}/3$ let it appear similar to GMP5279. In contrast to this galaxy, however, GMP1750 lacks of the negative $H_4 < 0$ in the minor-axis kinematics. Even more, the major and minor-axis kinematics, respectively, are remarkably similar, making GMP1750 a candidate (close-to) face-on system. Quite in opposite, the bestfit model is at $i = 90^\circ$. As in the case of GMP0282 the significance of this result is marginal (less than one sigma; the bestfit model at $i = 50^\circ$ is overplotted in the lower panel of Fig. 4.7).

GMP0144. GMP0144 is a complex system. As discussed in more detail in App. B, the observations provide evidence that its central region lacks of axial symmetry. Even around r_{eff} the major-axis dispersion (and H_4) shows a plateau (and dip) which may reveal some additional dynamical substructure. GMP0144 is among the systems with negative minor-axis H_4 , but – exceptionally – the bestfit model is not edge-on. On the other hand, the model does not follow the H_4 -observations very well (even with low regularisation).

GMP5975. GMP5975 has already been discussed in Chap. 3.

Summary. Phenomenologically, the sample is best summarised as a family of objects related by qualities that some – but never all – galaxies share. These qualities itself and the affinities they imply are not mutually associated. For example, some galaxies show photometric characteristics of disks, partly in the centre but more prominently in the very outer parts. Most of these galaxies also rotate, but not all (e.g. GMP3792 does not). Among those objects that rotate, in turn, not all are disky/boxy (e.g. GMP3510 is neither). Rotation itself is partly correlated with H_3 , partly anti-correlated – both independent from diskiness. A few galaxies have negative H_4 along the minor-axis, again unrelated to rotation and/or diskiness/boxiness.

Note on H_4 . Every *model* with negative H_4 at the small axis is edge-on. This hints at a certain combination of major-axis and minor-axis kinematics on the one side with axisymmetry on the other that interrelates negative H_4 with inclination in the fits. It is not clear yet, what causes this correlation and whether the objects in question are really close to edge-on. The relevant orbital distributions are discussed in Sec. 6.3.

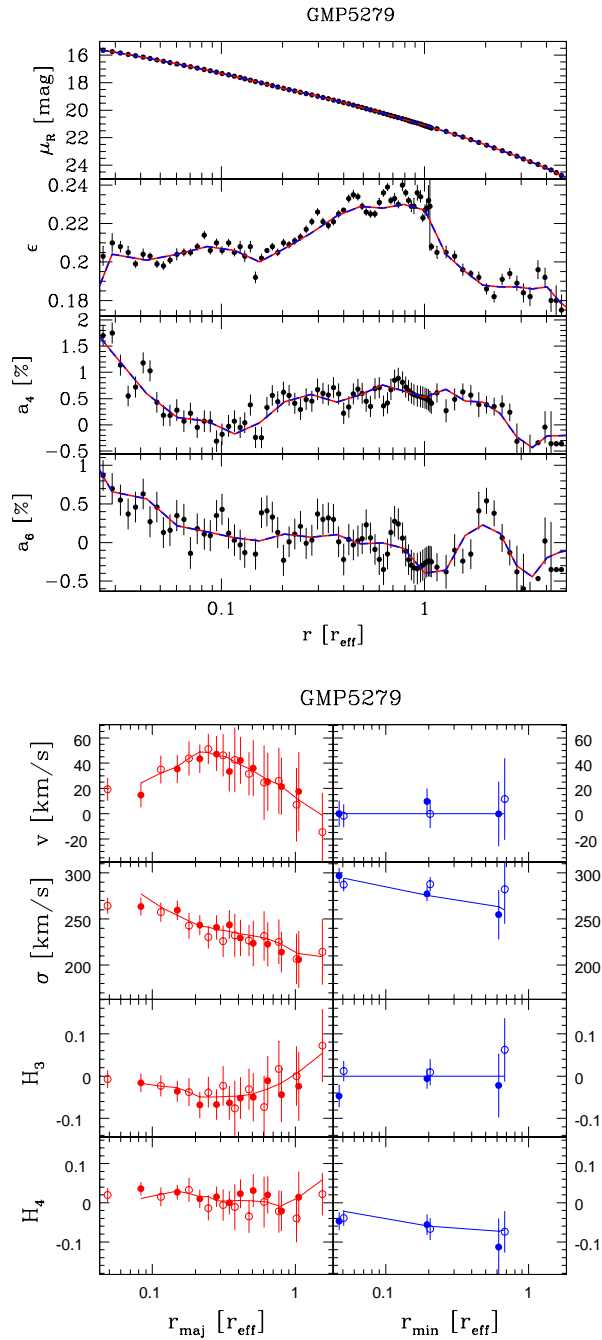


Figure 4.1: Upper panel: Joint ground-based and HST photometry of NGC 4827. Lines: bestfit deprojection (red) and its edge-on reprojection (blue). Lower panel: stellar kinematics along major (left/red) and minor axis (right/blue).

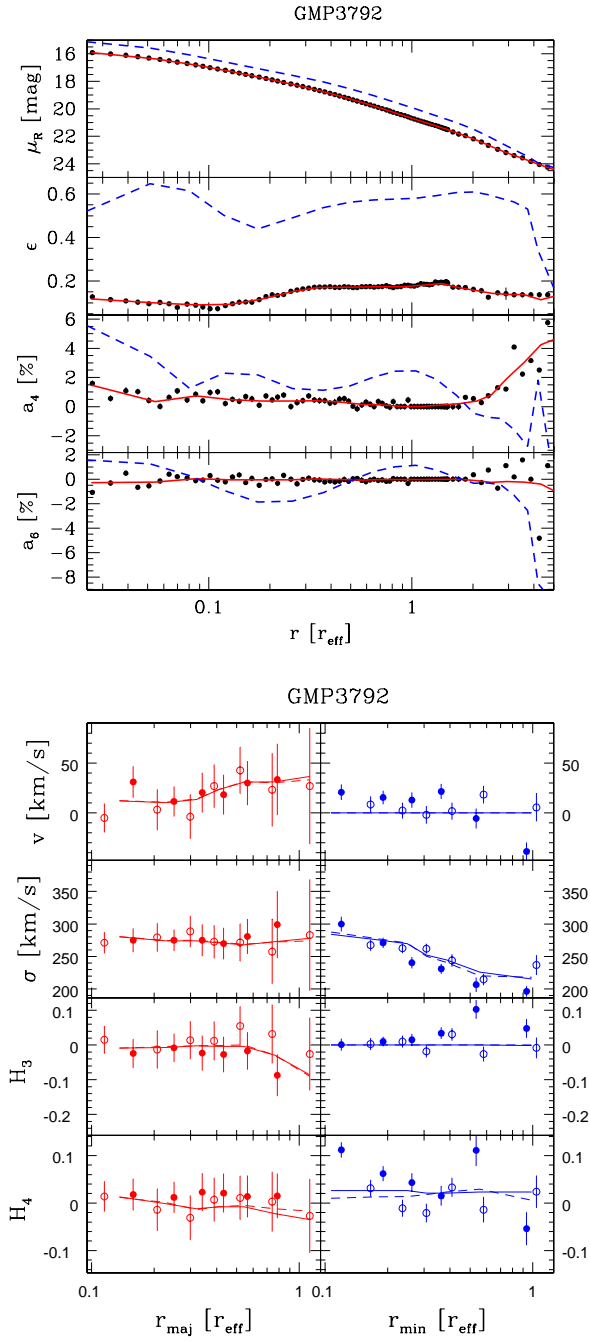


Figure 4.2: As Fig. 4.1, but for NGC 4860. Solid (dashed) lines in lower panel: bestfit model at $i = 40^\circ$ ($i = 90^\circ$).

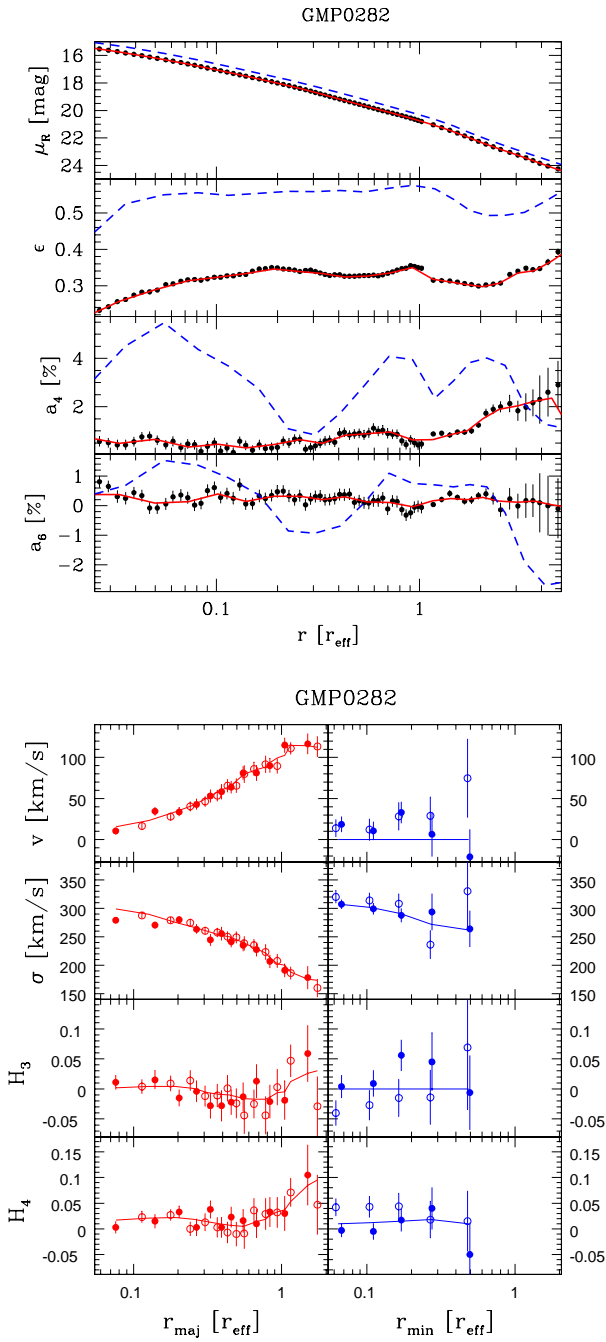


Figure 4.3: As Fig. 4.1, but for NGC 4952.

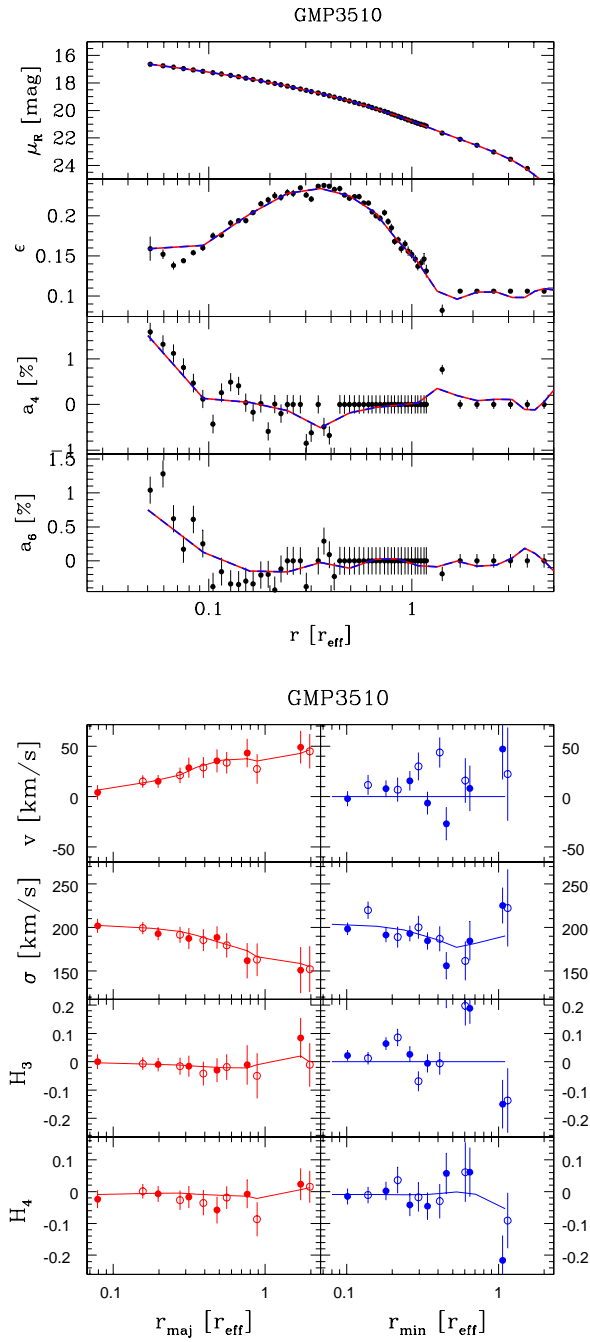


Figure 4.4: As Fig. 4.1, but for NGC 4869.

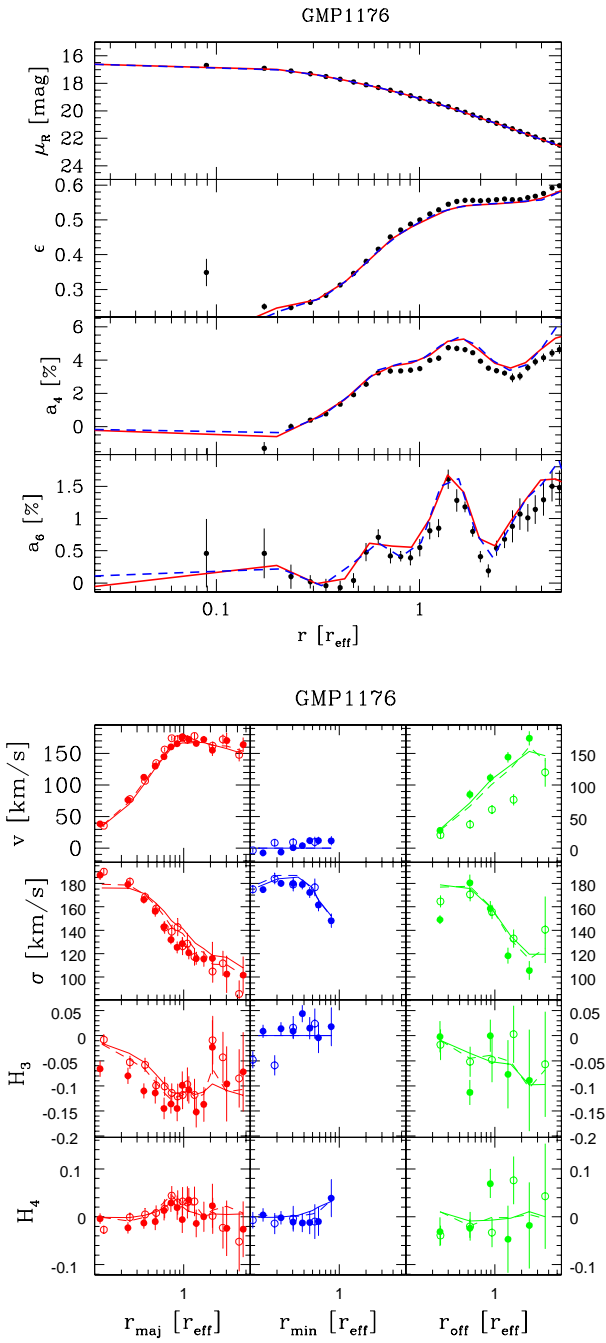


Figure 4.5: As Fig. 4.8, but for NGC 4931. Solid (dashed) lines in lower panel: bestfit models with $\alpha = 0.02$ ($\alpha = 0.9$).

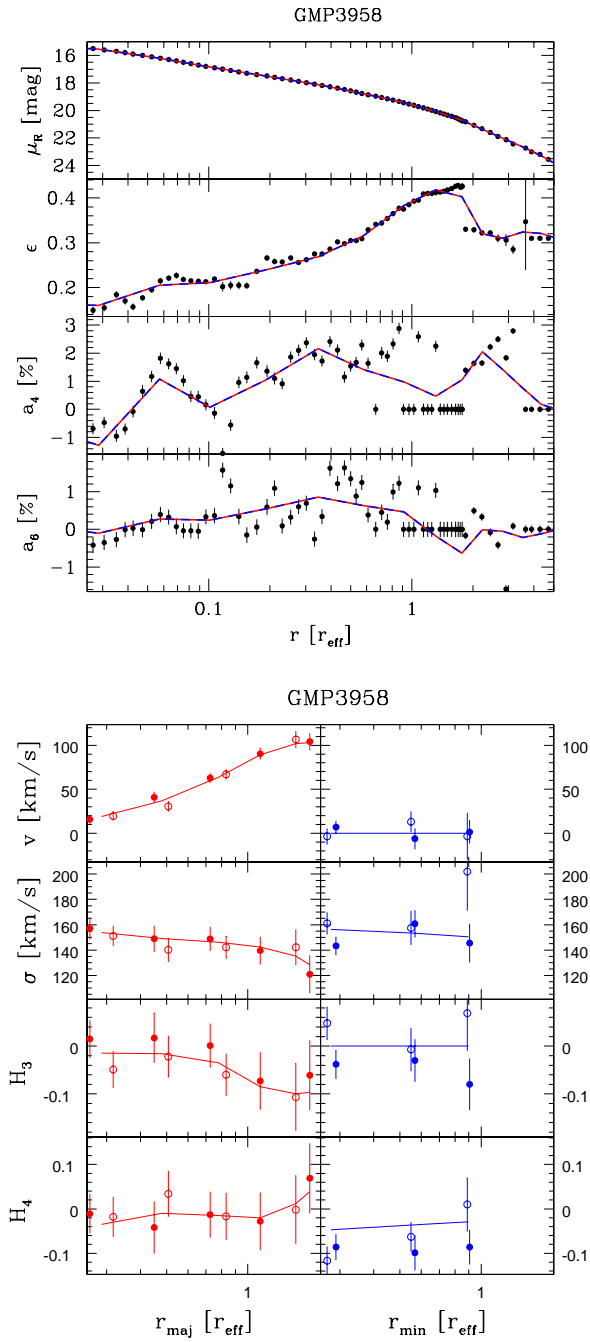


Figure 4.6: As Fig. 4.1, but for IC 3947.

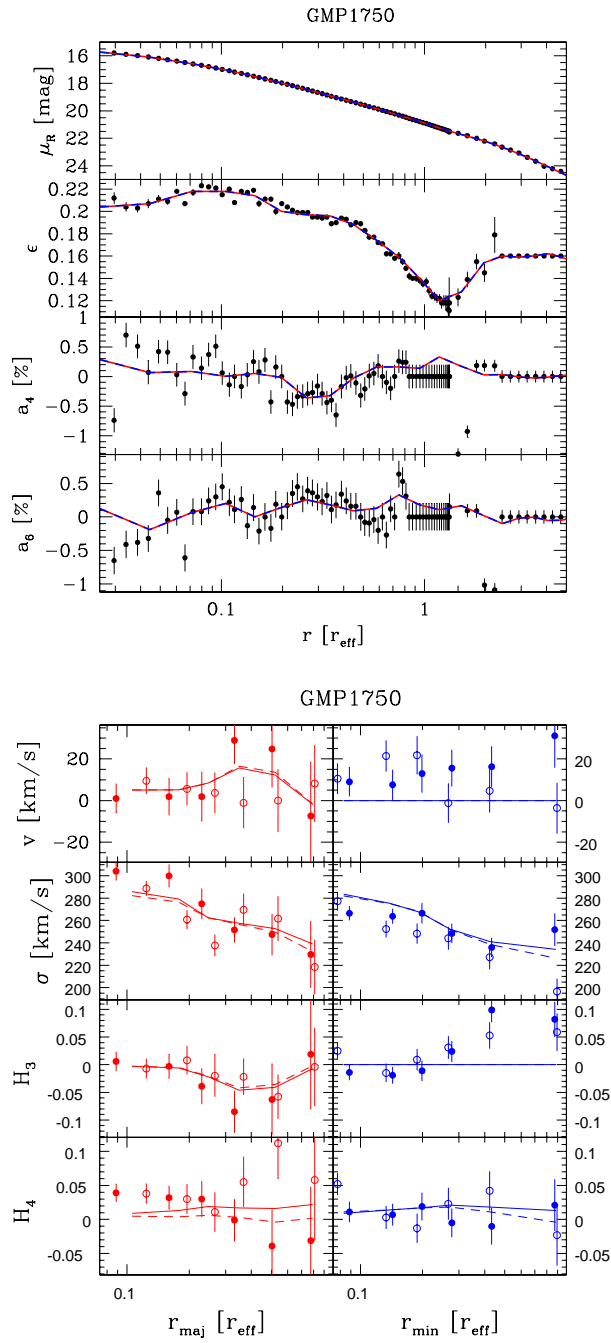


Figure 4.7: As Fig. 4.1, but for NGC 4926. Solid (dashed) lines in lower panel: bestfit models at $i = 90^\circ$ ($i = 50^\circ$).

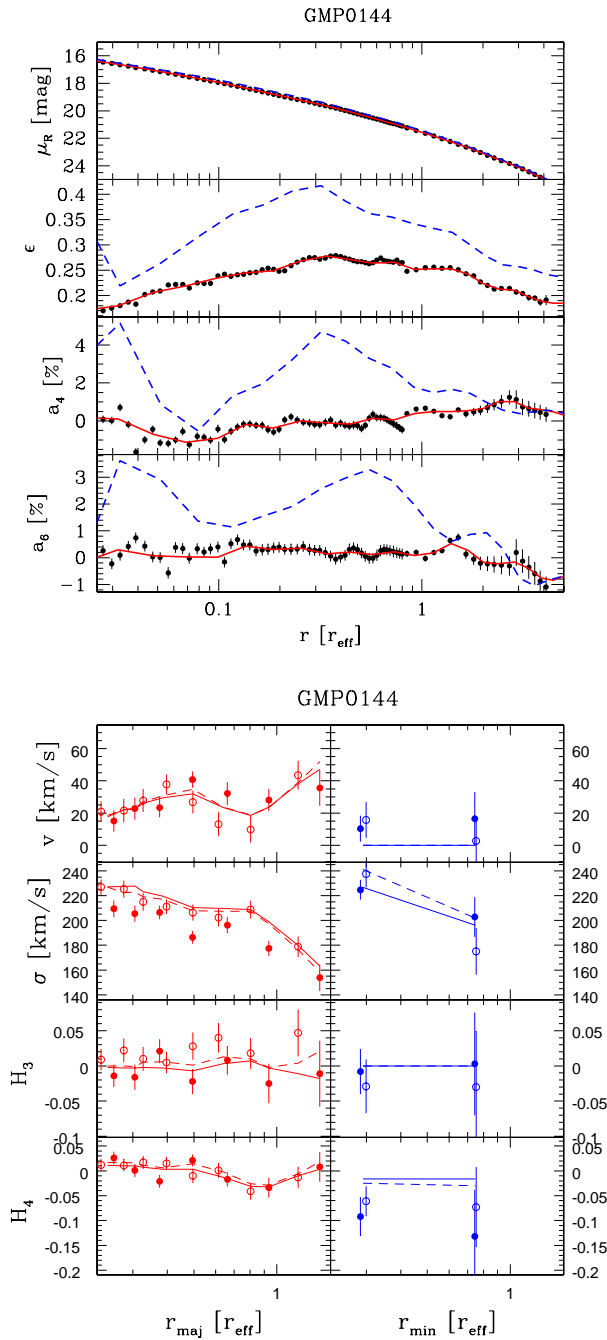


Figure 4.8: As Fig. 4.1, but for NGC 4957. Solid (dashed) lines in lower panel: bestfit models at $\alpha = 0.02$ ($\alpha = 0.9$).

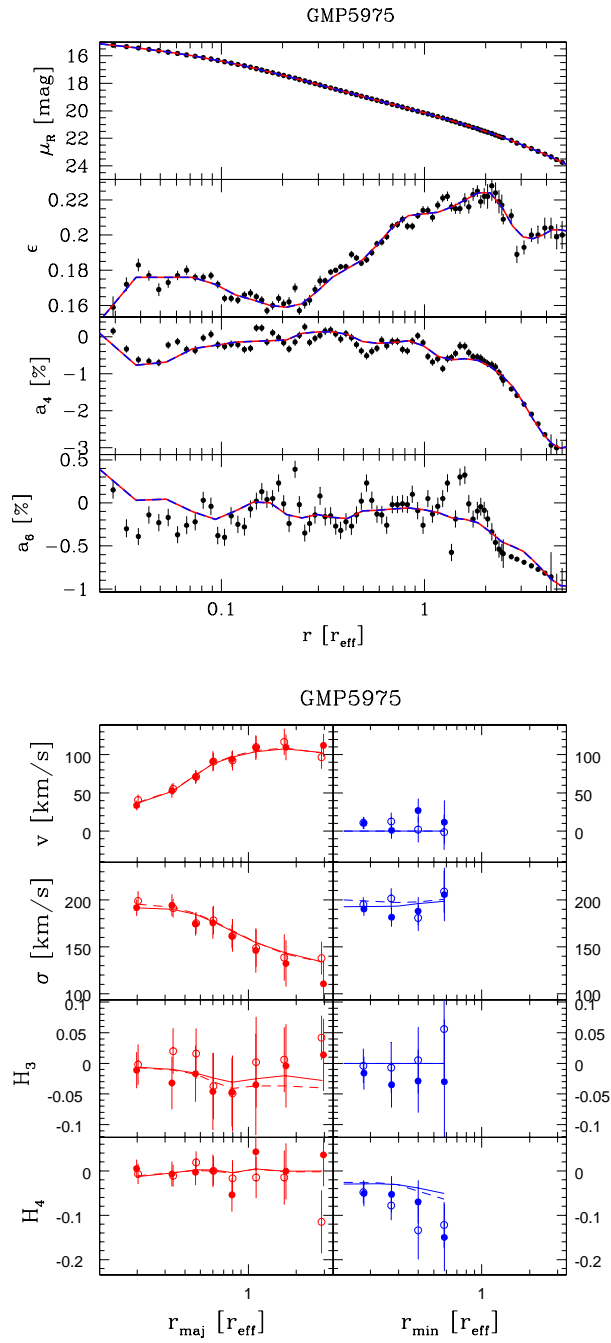


Figure 4.9: As Fig. 4.1, but for NGC 4807. Solid (dashed) lines in lower panel: bestfit models with $\alpha = 0.02$ ($\alpha = 0.9$).

4.4 Confidence levels

Using the same regularisation α for all galaxies allows in principle to adopt the χ^2 -levels from the MC simulations for GMP5975 to calculate confidence intervals. In case of GMP5975, however, $\hat{\chi}_{\text{GH}}^2 \equiv \chi_{\text{GH}}^2/N_{\text{data}}$ was rescaled to compute confidence intervals, because the minimum

$$(\hat{\chi}_{\text{GH}}^2)_0 \equiv \min(\hat{\chi}_{\text{GH}}^2) \quad (4.1)$$

in the fits turned out to be lower than the mean minimum $\langle(\hat{\chi}_{\text{GH}}^2)_0\rangle$ in the MC simulations (performed with the same error bars and the same regularisation). The χ^2 -distributions of fits and simulations were matched via

$$\left. \frac{\Delta\hat{\chi}_{\text{GH}}^2}{(\hat{\chi}_{\text{GH}}^2)_0} \right|_{5975} = \left. \frac{\Delta\hat{\chi}_{\text{GH}}^2}{(\hat{\chi}_{\text{GH}}^2)_0} \right|_{\text{MC}}. \quad (4.2)$$

Rescaling the errors of GMP5975 is justified, because the point-to-point scatter in the data is small compared to individual error bars. However, it follows from equation (4.2) that the actual χ^2 -level,

$$\Delta\hat{\chi}_{\text{GH}}^2|_{5975} = (\hat{\chi}_{\text{GH}}^2)_0|_{5975} \times \left. \frac{\Delta\hat{\chi}_{\text{GH}}^2}{(\hat{\chi}_{\text{GH}}^2)_0} \right|_{\text{MC}}, \quad (4.3)$$

from which confidence intervals are computed, scales with $(\hat{\chi}_{\text{GH}}^2)_0$. Modelling the other galaxies revealed a correlation of $(\hat{\chi}_{\text{GH}}^2)_0$ with the number of minor-axis data points, which is shown in the upper panel of Fig. 4.10. In the lower panel of the same figure is demonstrated that this correlation is mostly due to minor-axis rotation. Not correcting for this effect would imply that the uncertainties of model quantities depend on the occurrence of minor-axis rotation.

Minor-axis rotation can arise from:

- (i) Rotation of an axisymmetric, prolate object around its axis of symmetry
- (ii) A slight misalignment of the observing slit with respect to the minor axis
- (iii) Intrinsic deviations from axial symmetry

Case (i) should not affect $(\hat{\chi}_{\text{GH}}^2)_0$, because it can be fit by the models at hand. For the Coma galaxies, however, this case is not relevant since all galaxies with signs of minor-axis rotation have simultaneous major-axis rotation.

A slight misalignment of type (ii) should also not affect $(\hat{\chi}_{\text{GH}}^2)_0$, given that it is known to the models. A reconstruction of the exact slit orientation for the Coma galaxies is practically impossible, however.

Finally, if some galaxies are intrinsically non axisymmetric, the minor-axis rotation cannot be fitted in the models, but the corresponding mismatch accumulates to $(\hat{\chi}_{\text{GH}}^2)_0$. Thereby $(\hat{\chi}_{\text{GH}}^2)_0$ will be more affected in galaxies with a relatively large fraction of minor-axis data points. In practice, the same will follow if the minor-axis rotation arises according to case (ii). Both adds in principle to the systematic errors of the models. In absolute terms, the amount of

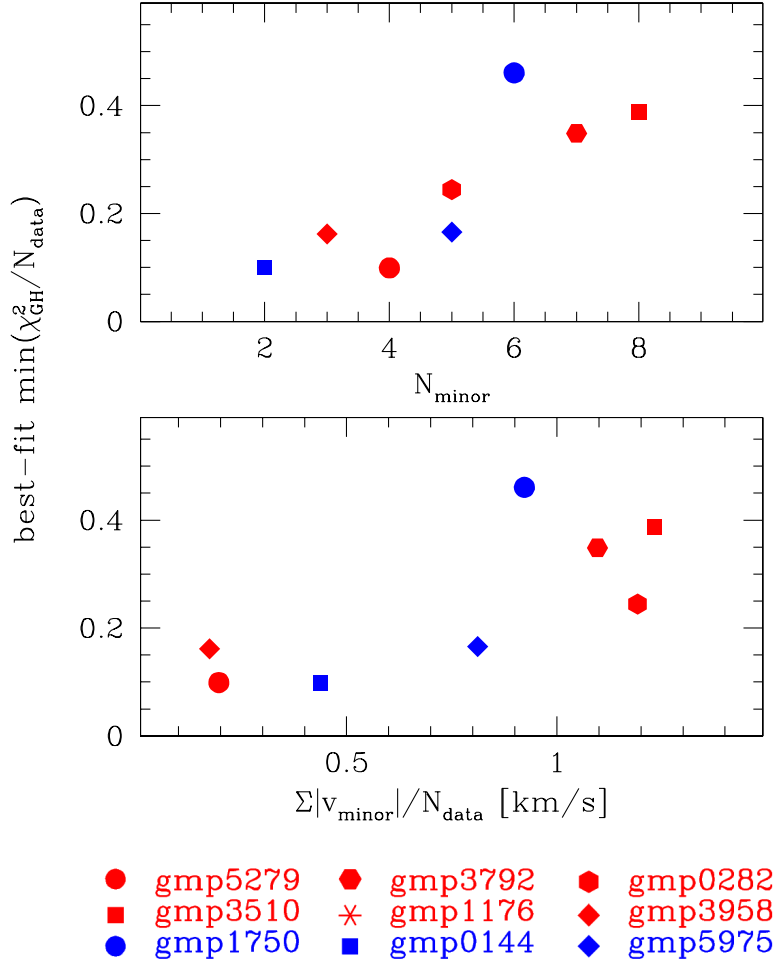


Figure 4.10: Best-fit $\min(\chi_{\text{GH}}^2)$ versus number of minor-axis data points (top) and minor-axis rotation (bottom), respectively. GMP1176 is not included in the plot since its unusually large $\min(\chi_{\text{GH}}^2) = 1.033$ is likely affected by the missing seeing correction and too strict regularisation.

rotation is so small ($v/\sigma < 0.1$) that its negligence in the models is energetically unimportant. In any case however, it should not be mixed with the statistical errors.

Classically, for systems with one degree of freedom², confidence levels are derived from “ $\Delta\chi^2 = 1$ ”, without scaling by the number of data points. Specif-

²For all error bars assigned to internal model quantities given in the following the models are marginalized about all other relevant quantities.

ically for the kinematical data at hand one would use

$$\Delta\chi_{\text{GH}}^2 \equiv \Delta\hat{\chi}_{\text{GH}}^2 \times N_{\text{data}}. \quad (4.4)$$

Inserting the numbers for GMP5975 (after rescaling the fits according to equation 4.3) yields

$$\Delta\chi_{\text{GH}}^2|_{5975} \approx 1.1, \quad (4.5)$$

a bit more conservative than the classical value. A possible reason for the offset may be the relatively low number of simulations performed (cf. Sec. 3.4.2). Independent of its exact value, using $\Delta\chi_{\text{GH}}^2$ avoids the correlation with minor-axis rotation discussed above. Therefore, all model uncertainties for the Coma galaxies are based on

$$\Delta\chi_{\text{GH}}^2 \equiv 1.1 \approx \Delta\chi_{\text{GH}}^2|_{5975}. \quad (4.6)$$

Chapter 5

Mass composition of Coma ellipticals

5.1 Outline

In the present chapter the mass composition of the Coma galaxies is analysed in detail. By the nature of gravity only the *total* mass can be derived from the data. Its decomposition into contributions from luminous and dark matter is a question of interpretation of the fitted mass profile. For the present work mass profiles with two components, one that follows light plus an additional halo component are probed (cf. Sec. 3.3.2). It is assumed that the mass-to-light ratio of the first component represents the stellar mass-to-light ratio and that evidence for dark matter comes from an increase of the total mass-to-light ratio with radius. Evidence for increasing total mass-to-light ratios in the Coma galaxies is discussed in Sec. 5.2. Because the mass decomposition is not constrained by photometric and kinematical observations, it needs other verification. Stellar population modelling provides an independent method to derive stellar mass-to-light ratios. In Sec. 5.3 the dynamically derived stellar mass-to-light ratios are crosschecked with stellar population modelling. The spatial distribution of dark and luminous matter is then presented in Sec. 5.4 and ambiguities of the mass decomposition are further discussed in Sec. 5.5. The dependency of the results on regularisation is analysed in Sec. 5.6. Another probe of the mass decomposition, its stationarity, is the subject of Sec. 5.7. Sec. 5.8 closes the chapter with a short summary

5.2 Evidence against constant mass-to-light ratios

Fig. 5.1 quantifies the different levels to which the kinematical data can be reproduced under different assumptions about the distribution of luminous and

dark matter: the mass-follows-light hypothesis (dotted) yields in all cases less accurate fits than the assumption of an additional outer halo (solid: NIS; dashed: NFW; cf. Sec. 3.3.2). On the basis of the plotted curves self consistent models are ruled out with at least 90 percent confidence.

Two galaxies are best fit with an NFW halo but in the majority of cases NIS halos match marginally better ($\Delta\chi_{\text{GH}}^2 \lesssim 1$). With the data at hand no clear decision for one of the two profiles is possible.

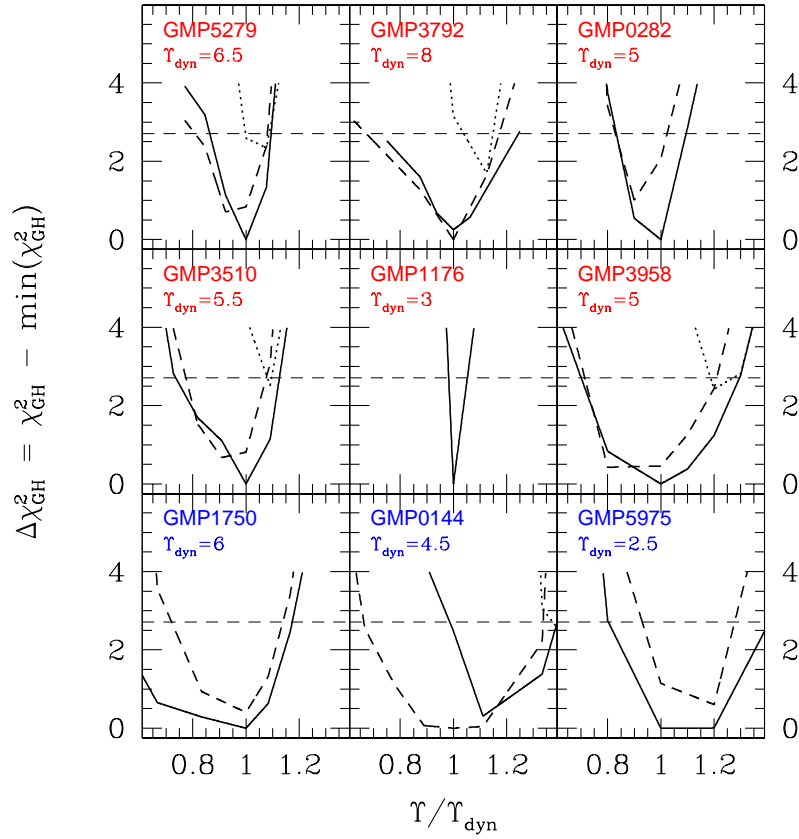


Figure 5.1: Confidence levels $\Delta\chi_{\text{GH}}^2$ versus Γ (normalised to the best-fit Γ_{dyn}). Solid: NIS; dashed: NFW; dotted: mass follows light; horizontal dashed: 90 percent confidence limit. Where a dotted line is missing the self-consistent case is ruled out with more than 95 percent confidence.

5.3 Crosscheck with stellar populations

Luminous and dark matter are identified in the models according to their radial density distributions. Even if the assumption that luminous mass follows light is adequate for real ellipticals, the derived Υ_{dyn} can differ from the actual stellar value Υ_* (see below). A reliable interpretation of Υ_{dyn} requires comparison with independent results from stellar population modelling.

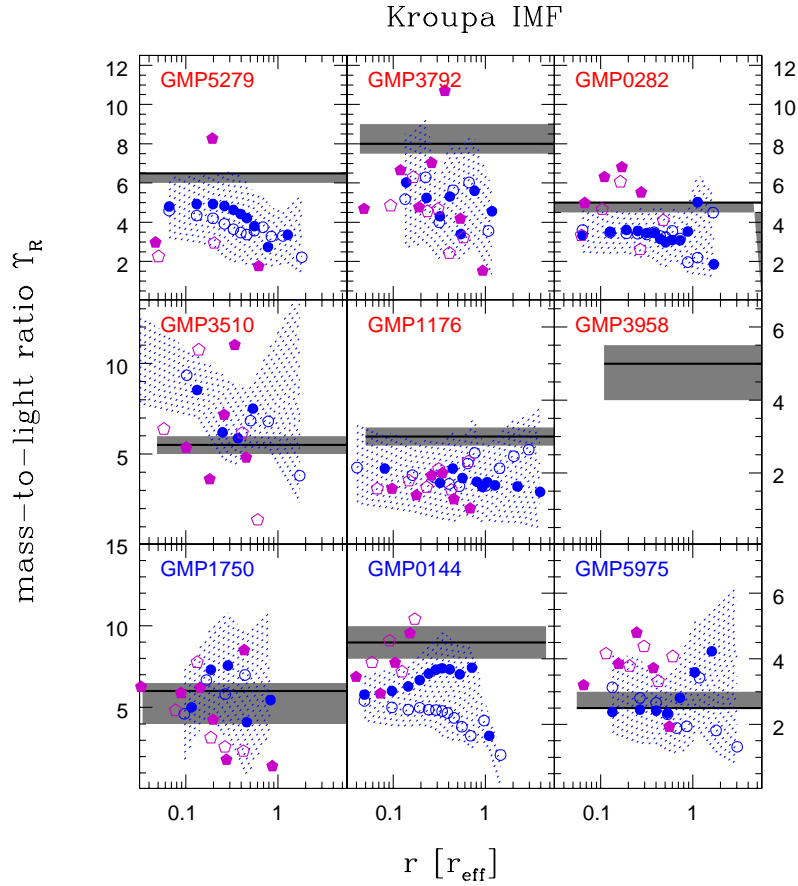


Figure 5.2: Comparison of line index based Υ_{SSP} and dynamical Υ_{dyn} for the Kroupa IMF (all mass-to-light ratios in R_C band). Solid black/shaded: Υ_{dyn} with error; blue: major-axis Υ_{SSP} (with errors); magenta: minor-axis Υ_{SSP} (errors are of the order of the point-to-point scatter). Note different scalings in the lower two rows.

5.3.1 Independent stellar mass-to-light ratios

This comparison is the content of Figs. 5.2 and 5.3, which show radial profiles of dynamical Υ_{dyn} and single stellar population (SSP) Υ_{SSP} (derived from the models of Maraston 1998; Thomas, Maraston & Bender 2003; Maraston 2004). Mass-to-light ratios of SSP models depend on the assumed initial stellar mass function (IMF), which is not well constrained by observations. Two representative cases are considered in the following: Kroupa’s IMF with a shallow run at low masses (Fig. 5.2) and Salpeter’s steeper IMF with an accordingly higher Υ_{SSP} (Fig. 5.3)¹. The IMF of real galaxies can be of any other form as well, or even spatially varying inside a galaxy. The following discussion is restricted to either the Kroupa or the Salpeter case with the aim to delimit a range of plausible cases.

The comparison with stellar population models implies two important issues. Firstly, in every galaxy $\Upsilon_{\text{dyn}} \gtrsim \Upsilon_{\text{SSP}}$ if Kroupa’s IMF is adopted (cf. Fig. 5.2). Dynamical Υ_{dyn} larger than Υ_{SSP} could imply that a fraction of the mass included in Υ_{dyn} is not of stellar nature. In any case, it is not in conflict with stellar population modelling. Inconsistency between dynamical and stellar population modelling is only indicated where $\Upsilon_{\text{dyn}} < \Upsilon_{\text{SSP}}$. This is not the case for the Kroupa-IMF and, consequently, dynamical models are in every galaxy consistent with a Kroupa-IMF. In the majority of galaxies $\Upsilon_{\text{dyn}} > \Upsilon_{\text{SSP}}$, but occasionally dynamical models directly agree with SSP-models ($\Upsilon_{\text{dyn}} \approx \Upsilon_{\text{SSP}}$ in GMP1750 and GMP5975). Noteworthy, where $\Upsilon_{\text{dyn}} > \Upsilon_{\text{SSP}}$ the offset in many cases exactly accounts for the differences between a Kroupa and a Salpeter IMF (cf. Fig. 5.3; for example GMP0282). A direct interpretation of Υ_{SSP} in terms of the intrinsic stellar population is hampered by the second important issue brought up by Figs. 5.2 and 5.3, respectively: the presence of radial as well as vertical stellar population gradients.

Before following this point further the stellar population ages implied by the SSP models devote some further examination. They are shown in Fig. 5.4 and are often unphysically large (exceeding the age of the universe, ≈ 14 Gyr). Although the statistical errors are large this point is important because a comparison of Figs. 5.2 and 5.4 reveals that age variations are the main driver behind the Υ_{SSP} variations. A possible source of error in SSP models is gas emission, which refills the stellar $H\beta$ absorption feature. If not corrected, the resulting stellar populations are biased mainly towards higher ages and, consequently, higher mass-to-light ratios. The $H\beta$ -profiles of the Coma ellipticals are plotted in Fig. 5.5 and indeed reveal occasionally low $H\beta$ detections connected to large ages. Consistent with the usually patchy distribution of emitting gas most of the scatter and most of the asymmetries with respect to the centre in some major-axis SSP models (e.g. GMP5279) can be traced back to corresponding $H\beta$ features. Hence, gas emission cannot be neglected in the discussion of the stellar populations but must be regarded as a source of systematic uncertainties.

¹For the sake of clarity, minor-axis errors on Υ_{SSP} are omitted in both figures. They are in every case of the order of the (large) point-to-point scatter.

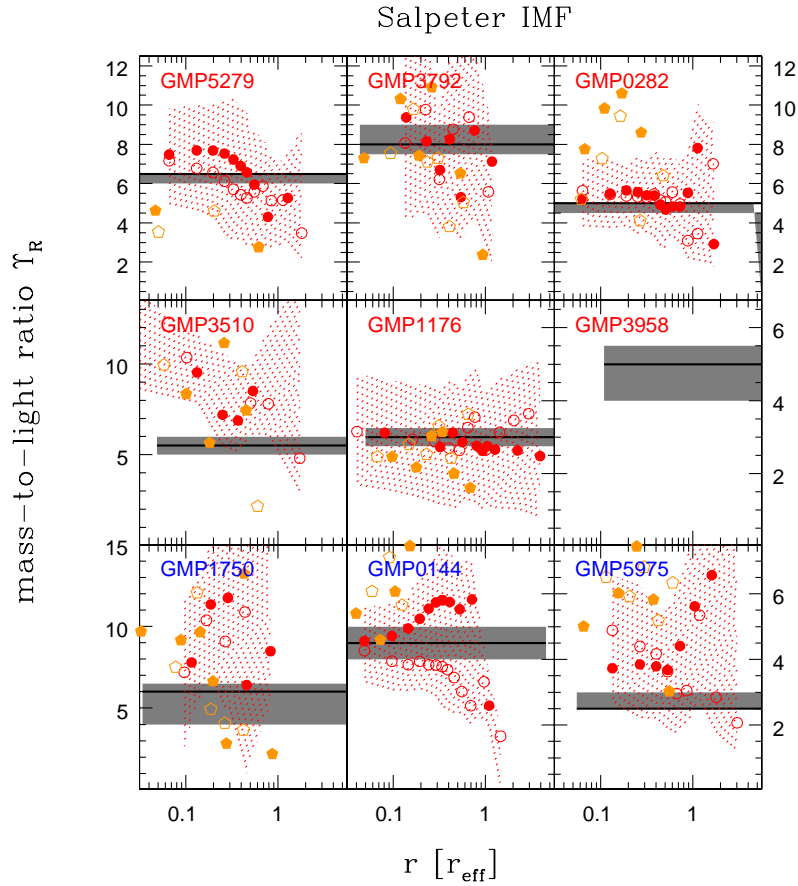


Figure 5.3: As Fig. 5.2 but for the Salpeter IMF. Red: major-axis Υ_{SSP} (with errors); orange: minor-axis Υ_{SSP} .

5.3.2 Stellar population gradients

The presence of stellar population gradients can affect the comparison between dynamical and stellar population mass-to-light ratios in several ways. It is thereby out the scope of this work to explore a possible bias in SSP models arising if line-of-sight projection and population modelling are not commutable. In that case the effective population derived from the line-of-sight averaged indices would differ from the line-of-sight average of the true intrinsic population. Leaving this point aside the four following topics have to be considered in the present context:

- (i) **Subsystems.** If the difference between stellar populations along different slits is due to a minor subsystem oriented along one observing slit (e.g. a

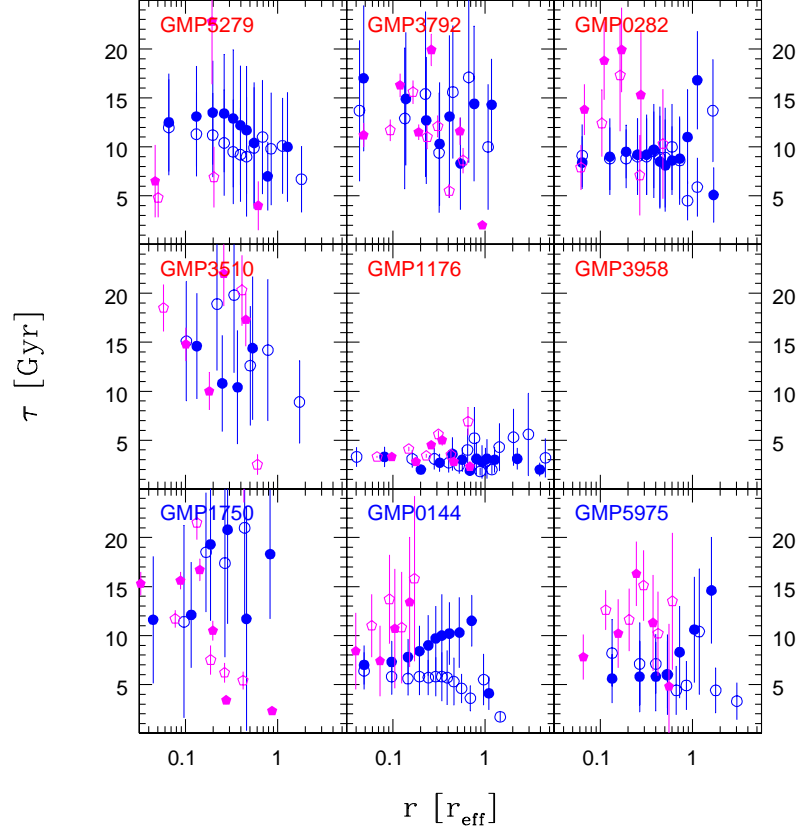


Figure 5.4: Stellar population ages according to the SSP models used for Fig. 5.7. Blue: major-axis; magenta: minor-axis; open/closed symbols: different sides of galaxy.

disk along the major-axis or a polar ring along the minor-axis) than the corresponding Υ_{SSP} of this slit may not be representative for the bulk of stars in the galaxy and the population models of that slit should not be used in the comparison to Υ_{dyn} . This concerns the comparison mostly in edge-on systems.

- (ii) **Positive Υ_{SSP} -gradients.** Radially increasing Υ_* are well covered by the “constant Υ + halo” models probed in this work. It is therefore reasonable to expect a good match of Υ_{dyn} with the central minimum of Υ_* . The corresponding “halo” component in the models, however, may be rather massive accounting for both, possible outer dark matter and the increasing stellar mass. Implications are (1) that the dark matter fraction may be

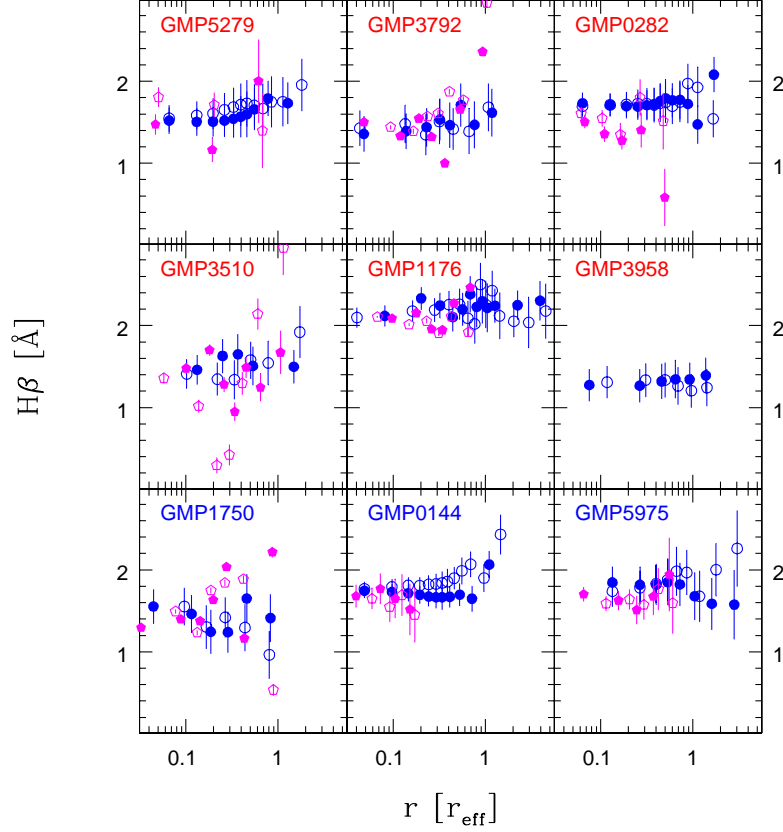


Figure 5.5: Observed $H\beta$ for all galaxies. Symbols and colours as in Fig. 5.4.

overestimated and (2) that the comparison between Υ_{dyn} and Υ_{SSP} should be restricted to the central regions.

- (iii) **Negative Υ_{SSP} -gradients.** Radially decreasing Υ_* are not explicitly included in the models here and, hence, can be reconstructed only approximately. Contrasting case (ii) it is generally unlikely that Υ_{dyn} will match the central maximum of the intrinsic Υ_* , because the constancy of Υ_{dyn} would then imply too much mass in regions further out. Instead, Υ_{dyn} will likely equal an average $\langle \Upsilon_* \rangle$ representing a region whose extension will depend on the details of $\Upsilon_*(r)$ and the distribution of matter in a possible halo. Opposite to case (iii) the comparison between Υ_{dyn} and Υ_{SSP} should not be done in the central regions.

- (iv) **Projection effects.** In both cases (ii) and (iii) projection effects may be important, depending on the galaxy's inclination and the detailed Υ_* -profiles.

Before discussing the Coma galaxies with respect to the above issues the next subsection is aimed to provide an order of magnitude estimation of pure projection effects as raised under (iv).

5.3.3 Projection effects

To give an example of how projection effects can enter the comparison between Υ_{dyn} and Υ_{SSP} , assume that Υ_{dyn} approximates the local intrinsic stellar mass-to-light ratio, $\Upsilon_{\text{dyn}} \approx \Upsilon_*(r)$. Assume further that Υ_{SSP} is a pure projection of $\Upsilon_*(r)$, i.e. $\Upsilon_{\text{SSP}} \approx \Sigma_M/\Sigma_L$, where

$$\left(\frac{\Sigma_M}{\Sigma_L}\right)(r) \equiv \frac{\int \Upsilon_*(r) \times \nu(r) dz}{\int \nu(r) dz}, \quad (5.1)$$

with Σ_M and Σ_L denoting the surface mass and surface brightness, respectively, ν being the intrinsic luminosity profile, and the integration being performed along the line of sight. If, for example, a galaxy's intrinsic Υ_* is monotonically decreasing with radius r , then the projected mass-to-light ratio $\Sigma_M/\Sigma_L(R)$ (at projected radius R) will be smaller than the intrinsic $\Upsilon_*(R)$. This, because along the line of sight $r > R$ and, thus, $\Upsilon_*(r) < \Upsilon_*(R)$ in the integral of equation (5.1).

To quantify this effect, the projection quadratures in equation (5.1) have to be solved for different $\Upsilon_*(r)$. This can be done conveniently by means of orbit libraries as calculated for each galaxy. To this end, recall that the integrated luminosity dL^j and surface brightness dSB^j in bin j of an orbit model read

$$dL^j = \sum_i w_i dL_i^j \quad (5.2)$$

and

$$dSB^j = \sum_i w_i dSB_i^j \quad (5.3)$$

(cf. equation 2.5; dSB_i^j is the total projected light of orbit i in bin j). The orbital weight w_i equals the total amount of light carried by the corresponding orbit. Given an arbitrary $\Upsilon_*(r)$, a mass weight μ_i can be assigned to orbit i via

$$\mu_i \equiv w_i \times \Upsilon_*(\langle r_{\text{orb}} \rangle_i), \quad (5.4)$$

where $\langle r_{\text{orb}} \rangle_i$ is the mean orbital radius defined in App. C. Analogously to equations (5.2, 5.3) the intrinsic and projected mass in bin j can be expressed via

$$dM^j = \sum_i dL_i^j \mu_i \quad (5.5)$$

and

$$dSM^j = \sum_i dSB_i^j \mu_i. \quad (5.6)$$

Equations (5.2, 5.3) and (5.5, 5.6), respectively, determine the projected mass-to-light ratio (in bin j)

$$\left. \frac{\Sigma_M}{\Sigma_L} \right|^j \equiv \frac{dSM^j}{dSB^j} \quad (5.7)$$

the local mass-to-light ratio

$$\left. \frac{\rho}{\nu} \right|^j \equiv \frac{dM^j}{dL^j} \quad (5.8)$$

and the cumulative mass-to-light ratio

$$\left. \frac{M}{L} \right|^j \equiv \frac{\Sigma_{k<j} dM^k}{\Sigma_{k<j} dL^k}. \quad (5.9)$$

The sums on the right hand side of equation (5.9) are intended to comprise every bin k with radius smaller than that of the actual bin j . Note, that the local mass-to-light ratio ρ/ν of the final orbit superposition will not necessarily equal the original $\Upsilon_*(r)$ of equation (5.4) exactly. Apart from noise due to finite orbit sampling and finite bin sizes the main reason is that radially extended orbits spread the Υ_* of their mean radius to larger and smaller radii. In this sense, an orbit library calculated in a (not necessarily self-consistent) gravitational potential that allows for a superposition with much emphasis on radially confined orbits will yield ρ/ν closer to $\Upsilon_*(r)$ than another potential that requires a substantial fraction of radially floating orbits. For the purpose here, however, the exact shape of ρ/ν doesn't matter but only the consistency between ρ/ν and Σ_M/Σ_L . The aim is to cover the profile shapes found in Figs. 5.2 and 5.3 with a handful of representative profiles only whose global qualities such as being monotonic or having a maximum/minimum need to be specified. In any case, application of equation (5.4) has the advantage of ensuring that the final ρ/ν is supported by an orbit distribution and, thus, is stationary.

Fig. 5.6 shows exemplary for GMP5975 projected, local and cumulative mass-to-light ratio profiles for three different $\Upsilon_*(r)$ with piecewise constant logarithmic gradient

(i) left column:

$$\frac{d \log \Upsilon}{d \log r} \equiv \pm 0.23 \quad (5.10)$$

(ii) middle column:

$$\frac{d \log \Upsilon}{d \log r} = \pm \begin{cases} 0.15 & : r \leq 0.75 r_{\text{eff}} \\ -0.7 & : r > 0.75 r_{\text{eff}} \end{cases} \quad (5.11)$$

(iii) right column:

$$\frac{d \log \Upsilon}{d \log r} = \pm \begin{cases} 0 & : r \leq 0.75 r_{\text{eff}} \\ 1 & : r > 0.75 r_{\text{eff}} \end{cases} \quad (5.12)$$

(Υ_* and r are scaled to solar units and the half-light radius r_{eff} , respectively). The projections are performed in the best-fit mass distribution of GMP5975. In the lower panel of the figure the fractional difference

$$\mathcal{D} \equiv \text{diff} \equiv \frac{\Sigma_{\text{M}}/\Sigma_{\text{L}} - \text{M}(r)/\text{L}(r)}{\text{M}(r)/\text{L}(r)} \quad (5.13)$$

between $\Sigma_{\text{M}}/\Sigma_{\text{L}}$ and $\text{M}(r)/\text{L}(r)$ is plotted. As will become clear below it provides conservative limits on the offset between Υ_* and $\Sigma_{\text{M}}/\Sigma_{\text{L}}$.

As expected, for a monotonic Υ_* the local ρ/ν is bracketed between $\Sigma_{\text{M}}/\Sigma_{\text{L}}$ (steeper than Υ_*) and $\text{M}(r)/\text{L}(r)$ (shallower than Υ_*). In case (i) \mathcal{D} is below 20 percent inside $0.2 r_{\text{eff}}$ but increases to about 35 per cent at large radii. A monotonic Υ_* with a break like in case (iii) bounds \mathcal{D} to about 10 percent inside $0.2 r_{\text{eff}}$ but results in a steeper increase with radius. Finally, in case (ii) the sign change in the slope of Υ_* is reflected in a similar sign change of \mathcal{D} . In the particular case shown in the middle column of Fig. 5.6 \mathcal{D} reaches 40 per cent in the outer parts, but remains low near the centre (positive and negative variations along the line of sight cancel out).

The fractional difference \mathcal{D} will not only depend on Υ_* but also on the specific light profile of each galaxy. Ellipticals, to first order, follow similar light profiles, allowing to apply the above results to the whole sample for an order of magnitude estimate. Projection effects also depend on inclination. In the limit $i \rightarrow 0^\circ$ vertical gradients affect the projection as radial gradients do in the edge-on case. Vertical gradients can be generally as important as radial gradients, but are unlikely to lead to qualitatively different results. Thus, the edge-on case can be regarded as being representative to cover all possible projection effects.

The profile shapes and slope magnitudes of Fig. 5.6 roughly comprise the cases in Figs. 5.2 and 5.3, respectively. Furthermore, inspection of the blue, cyan and red curves reveals that the deviations between ρ/ν and $\Sigma_{\text{M}}/\Sigma_{\text{L}}$ are commonly smaller than those between $\text{M}(r)/\text{L}(r)$ and $\Sigma_{\text{M}}/\Sigma_{\text{L}}$ (this holds at least out to r_{eff}). Thus, the above defined \mathcal{D} limits for the Coma galaxies the possible bias between Υ_{dyn} and Υ_{SSP} related to pure projection effects.

5.3.4 Discussion

Next the impact of stellar population gradients on the comparison between Υ_{dyn} and Υ_{SSP} is discussed with respect to each galaxy. The discussion is aimed to end up in a quantitative comparison of Υ_{dyn} with a suitably defined $\langle \Upsilon_{\text{SSP}} \rangle$ reflecting the four issues (i) - (iv) related to stellar population gradients raised above. This final comparison is made for the Kroupa and the Salpeter case separately in Figs. 5.7 and 5.8, respectively. The exact specification of $\langle \Upsilon_{\text{SSP}} \rangle$ in each single galaxy is detailed below. Concluding remarks on the results follow after that.

GMP5279. The galaxy exhibits a considerable discrepancy between minor and major-axis populations and, on top of that, a pronounced radial decrease of

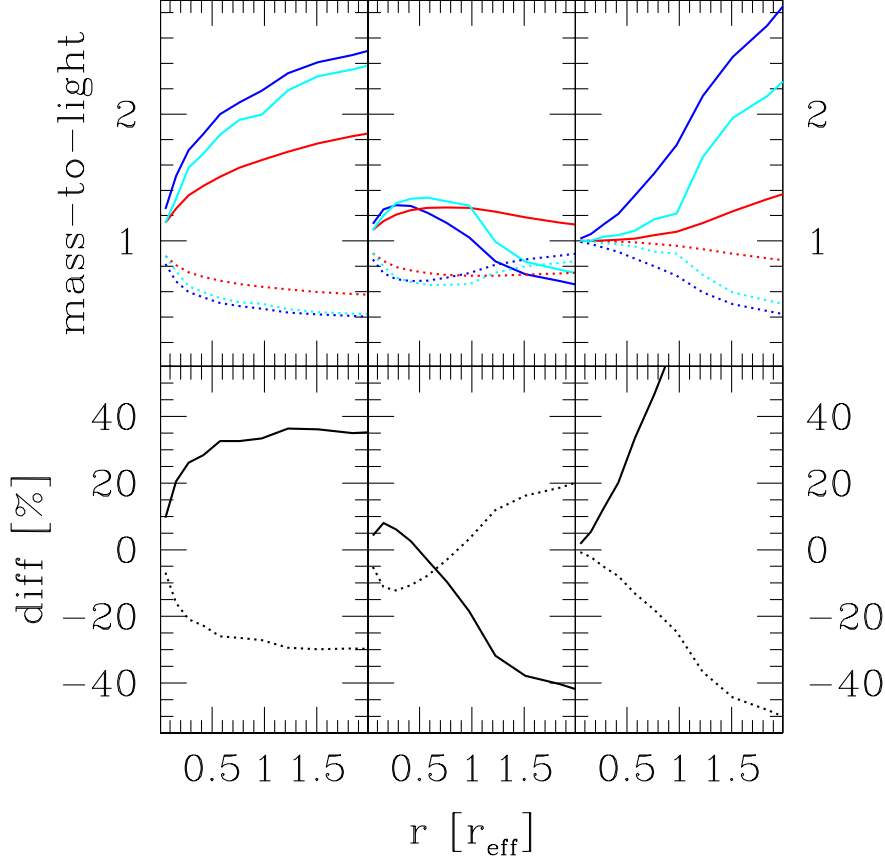


Figure 5.6: Top: projected (blue), local (cyan) and cumulative (red) mass-to-light ratios according to different internal $\Upsilon_*(r)$ (details in the text). Bottom: fractional difference between projected and cumulative mass-to-light ratios. All mass-to-light ratios are evaluated along the equatorial plane and scaled to the central value of Υ_* .

Υ_{SSP} along the major-axis. The low population ages along the short axis could indicate a distinct stellar component. A prolate configuration with a (young) disk along the minor-axis is excluded by the galaxy's major-axis rotation (cf. Fig. 4.1), unless the system would be substantially triaxial. There is no indication for triaxiality from the lack of isophotal twists (the position angle is constant to 4°) and the lack of minor-axis rotation, however. In fact, strong variations among the minor-axis $H\beta$ measurements indicate possible gas emission and restriction to the major-axis profiles seems the safest option for the comparison with Υ_{dyn} . According to the radial gradient in the major-axis Υ_{SSP}

and Fig. 5.6 the central intrinsic Υ_* may be 10-20 percent larger than the central Υ_{SSP} . This is enough to match Υ_* with Υ_{dyn} in the centre. On the other side, due to the negative Υ_{SSP} -gradient one wouldn't expect Υ_{dyn} to match the central maximum of Υ_* but rather to equal a radially averaged $\langle \Upsilon_{\text{SSP}} \rangle$. Indeed, Υ_{dyn} fits fairly well the radial average of the major-axis Salpeter Υ_{SSP} -profile (cf. Fig. 5.3). For the final comparison to Υ_{dyn} the latter is averaged within r_{eff} . No correction for projection effects is applied to the radial average since it should not depend strongly on the steepness of the Υ -slope.

GMP3792. As GMP5279 the galaxy exhibits a negative radial Υ_{SSP} gradient along the major-axis, but in contrast to GMP5279 the minor-axis mass-to-light ratios are consistent with the major-axis. This is in line with the galaxy being possibly inclined as suggested by the dynamical models. Like in GMP5279 correcting for projection effects by 10-20 percent is sufficient to match the central Υ_* with Υ_{dyn} . But (1) for the same reasons as in GMP5279 a match to the central intrinsic Υ_* is unlikely and (2) if the galaxy is really significantly inclined, projection effects are likely less important than in GMP5279. Instead, focussing on the central regions, Υ_{SSP} has been defined as the radial average of Υ_{SSP} out to r_{eff} with the only difference to GMP5279 being that for GMP3792 also the minor-axis profiles are taken into account.

GMP0282. As in the just discussed systems Υ_{dyn} is close to the major-axis Salpeter- Υ_{SSP} (cf. Figs. 5.3). Minor-axis Υ_{SSP} are significantly larger than their major-axis counterparts. Just taking the former, results in a good correspondence between Υ_{dyn} and the Kroupa- Υ_{SSP} and would be consistent with a young disk (dominating along the major-axis) embedded in an older spheroid (dominating along the minor-axis). On the other hand, the minor-axis Υ_{SSP} may be up-shifted by line emission as well (cf. Fig. 5.5). In the comparison of Figs. 5.7 and 5.8 the extreme point of view is taken that the whole difference between major and minor-axis populations is caused by line emission. $\langle \Upsilon_{\text{SSP}} \rangle$ is defined as the average of the major-axis SSP models out to r_{eff} (although in this system the averaging has no significant effect).

GMP3510. The stellar population properties of this system are hard to interpret. The large stellar ages make many of the Υ_{SSP} values questionable. For the comparison with Υ_{dyn} it has been decided to take every point predicting an age below $\tau < 14$ Gyr.

GMP1176. The lenticular exhibits rather constant Υ_{SSP} -profiles, consistent with each other along the major and the minor-axis. Their radial averages out to $0.4 r_{\text{eff}}$ are compared to Υ_{dyn} in Figs. 5.7 and 5.8 (to avoid the scatter beyond that radius). The limiting factor for this galaxy are the dynamical models, however (cf. Sec. 4.3) and for Figs. 5.7 and 5.8 Υ_{dyn} has been reduced by $\Delta \Upsilon_{\text{dyn}} = 1.0$ to correct for the unresolved central light profile.

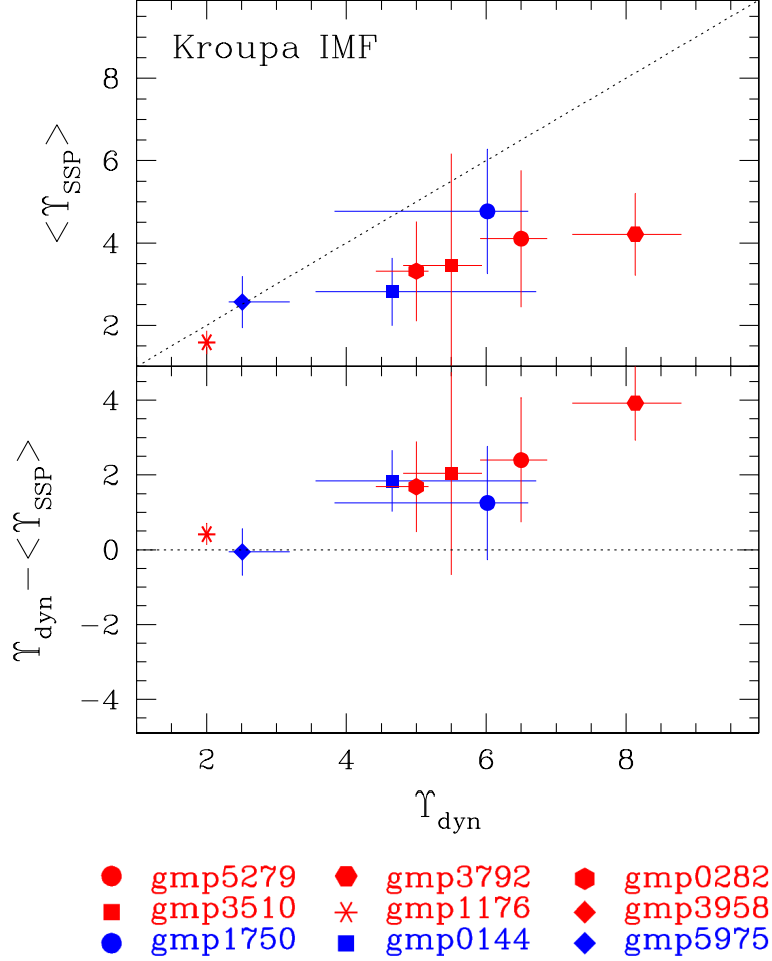


Figure 5.7: Dynamical versus stellar population modelling (upper panel). Details on the derivation of $\langle \Upsilon_{\text{SSP}} \rangle$ are given in the text for each galaxy. Dotted: $\Upsilon_{\text{dyn}} = \langle \Upsilon_{\text{SSP}} \rangle$. Lower panel: Offset between the mass-to-light ratios as function of Υ_{dyn} .

GMP3958. No stellar population models are available for this galaxy.

GMP1750. The major-axis Υ_{SSP} of this galaxy show a little bump around $0.3 r_{\text{eff}}$ but are on average constant out to r_{eff} . Along the minor-axis they drop by almost a factor of 5 over the same radial range. The dynamical Υ_{dyn} is close to the major-axis Kroupa- Υ_{SSP} , but the stellar ages along the same axes are mostly unreasonably large. If only the minor-axis Υ_{SSP} is considered Υ_{dyn}

is a factor of two larger than expected taking the radial average of Υ_{SSP} out to r_{eff} (again for the Kroupa case). On the other hand, if the bump along the major-axis is real it would be more appropriate to restrict the comparison between Υ_{dyn} and Υ_{SSP} to the central regions. This last option is supported by the dynamical M/L discussed in Sec. 5.5.2. Therefore Υ_{SSP} has been averaged about the inner $0.2r_{\text{eff}}$ for Figs. 5.7 and 5.8 (both axes are included).

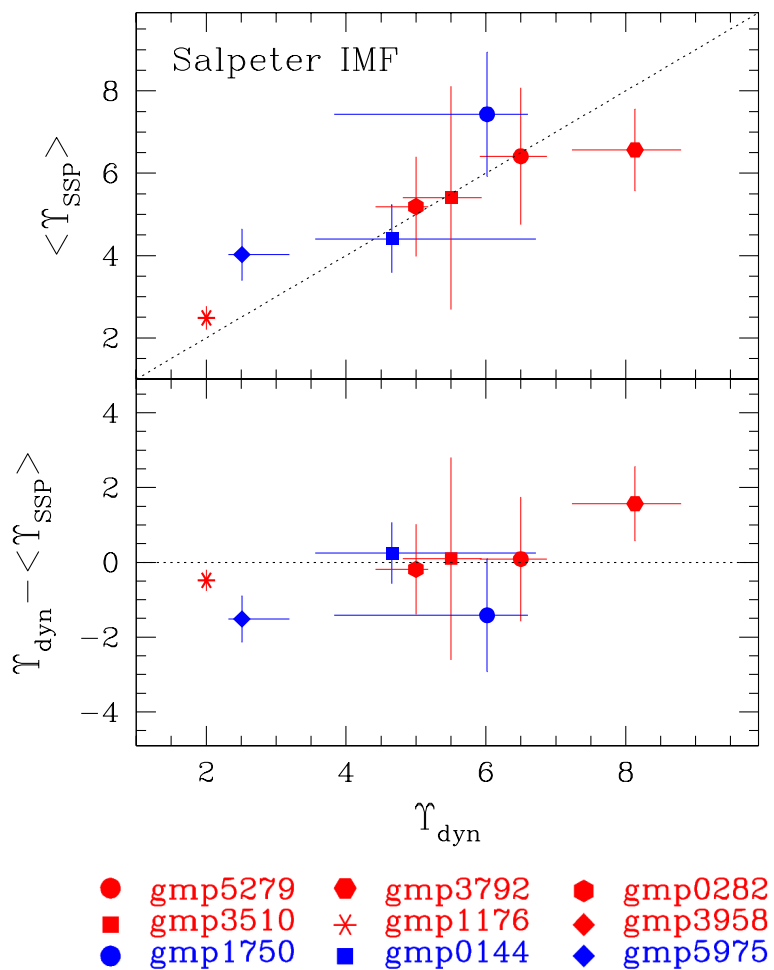


Figure 5.8: As Fig. 5.7 but for a Salpeter IMF.

GMP0144. In GMP0144 all kinds of complications arise: side-to-side asymmetries in the major-axis profiles of Υ_{SSP} , radial gradients in both major and minor-axis profiles and a difference of minor with respect to major-axis

Υ_{SSP} (at the same central distance). This allows for many different interpretations. If the lower population ages along the major-axis are interpreted as a disk embedded in an older spheroid that dominates the minor-axis Υ_{SSP} beyond $r \gtrsim 0.1 r_{\text{eff}}$, then one would expect a good match between Υ_{dyn} and the outer minor-axis Υ_{SSP} . Unfortunately, the minor-axis Υ_{SSP} rises up to the last data points such that its continuation beyond $0.2 r_{\text{eff}}$ is uncertain. On the other hand, the match of Υ_{dyn} with the mean major-axis Salpeter Υ_{SSP} is remarkably good. If the asymmetry in the SSP models is due to line emission, then the branch with the negative gradient is the more trustworthy one and Υ_{dyn} should not be expected to correspond to the central intrinsic Υ_* . The central match is instead plausible in case the lower branch is more representative. Following this point and the arguments under (ii) $\langle \Upsilon_{\text{SSP}} \rangle$ for GMP0144 is defined as the radial average of Υ_{SSP} inside the inner $0.2 r_{\text{eff}}$.

GMP5975. The last object to discuss is GMP5975. The SSP profiles are flat within r_{eff} as in GMP0282. Again as there, the minor-axis population is predicted older and more massive, driven by $H\beta$ variations with respect to the long axis. For the same reasons as in GMP0282, the comparison to Υ_{dyn} is restricted to the radially averaged major-axis Υ_{SSP} out to $0.6 r_{\text{eff}}$ (to avoid the outer jumps in Υ_{SSP}).

In GMP1750, GMP0144 and GMP5975 the flatness of Υ_{SSP} over the considered radial ranges makes projection effects insignificant. Finally to be mentioned that in every case, only those Υ_{SSP} values are considered for Figs. 5.7 and 5.8 that yield population ages $\tau < 14 \text{ Gyr}$. The case for stellar subcomponents is again addressed in Sec. 6.6 in the context of the internal dynamical structure.

5.3.5 Conclusions

The justification for $\langle \Upsilon_{\text{SSP}} \rangle$ is ambiguous in some objects and with the data at hand, a quantitative comparison between Υ_{dyn} and Υ_{SSP} remains accordingly uncertain. Nevertheless, the refined comparison confirms the impression raised by Figs. 5.2 and 5.3 that a Kroupa IMF is consistent with the dynamical models in every galaxy. However, in many systems $\Upsilon_{\text{dyn}} > \Upsilon_{\text{SSP}}$, implying that part of the mass included in Υ_{dyn} is not made of stars. The offset $\Upsilon_{\text{dyn}} - \langle \Upsilon_{\text{SSP}} \rangle$ increases systematically with Υ_{dyn} , but vanishes if turning to the Salpeter IMF (Fig. 5.8). A Salpeter IMF is excluded by stellar kinematics only for GMP1176 and GMP5975, where a steep IMF yields $\Upsilon_{\text{dyn}} < \Upsilon_{\text{SSP}}$.

From spherical models of round, non-rotating ellipticals Gerhard et al. (2001) concluded that ellipticals have roughly maximum stellar masses in their centers. If adopting a Kroupa IMF for GMP1176, GMP5975 and GMP1750 and a Salpeter IMF for the remaining galaxies, this conclusion holds for the Coma galaxies as well. The only exception is GMP3792, where the dynamical models even in the Salpeter case allow for about 20 percent of central dark matter. Accidentally, GMP0144 and GMP0282, where stellar population results are most ambiguous, are also consistent with maximum stellar mass and a Kroupa IMF if the minor-axis population models are regarded as the more representative

ones (see discussion above). At least two systems, GMP5279 and GMP3792, are incompatible with maximum stellar mass *and* a Kroupa IMF in any case.

The findings that (1) there is consistency between dynamical models and the Kroupa IMF in every case and that (2) with increasing Υ_{dyn} the mass fraction that follows light gets closer to the predictions of the Salpeter IMF are similar to results of the SAURON team for ellipticals with integral field spectroscopy (Cappellari et al. 2006). While for this thesis dark matter has been explicitly included in the models, Cappellari et al. (2006) only probe self-consistent mass distributions. The Coma results thus imply that the equivalence of Υ_{dyn} with a Salpeter IMF at large Υ_{dyn} is not due to an increasing dark matter fraction, unless dark matter follows a distinctly different radial distribution than covered by NIS and NFW profiles.

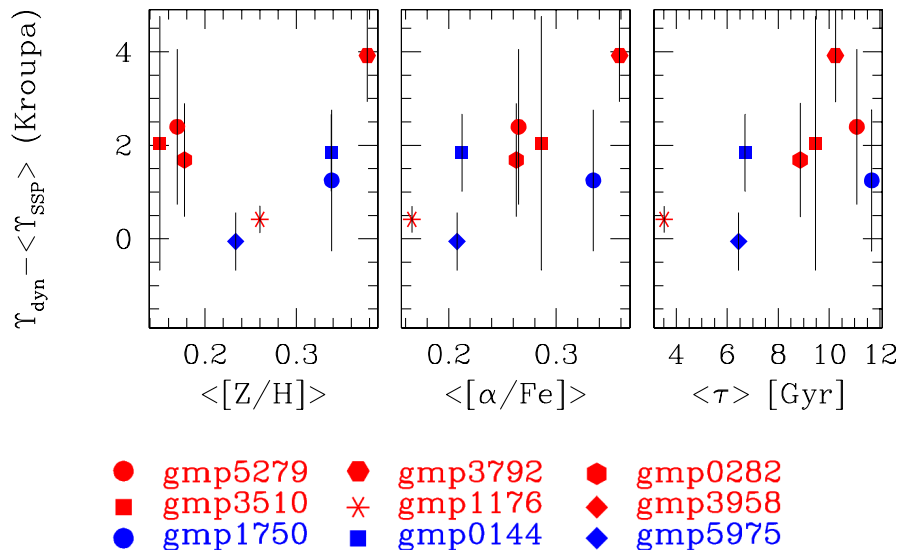


Figure 5.9: Offset between dynamical and stellar population Kroupa- Υ_{SSP} versus metallicity $\langle[Z/H]\rangle$, α -element abundance $\langle[\alpha/Fe]\rangle$ and stellar population age $\langle\tau\rangle$ (from left to right; brackets indicate averages over the same spatial regions than for $\langle\Upsilon_{\text{SSP}}\rangle$).

From the extreme point of view that dark matter always follows a distinct radial distribution than the light the difference between Υ_{dyn} and the Kroupa $\langle\Upsilon_{\text{SSP}}\rangle$ would measure the deviation of a galaxy's IMF from Kroupa's IMF. Fig. 5.9 probes whether a hypothetical IMF variation is correlated with metallicity, α -enhancement or population age, which would strengthen its significance. No strong correlation is found, but a weak trend of $\Upsilon_{\text{dyn}} - \Upsilon_{\text{SSP}}$ increasing with $[\alpha/Fe]$ and population age cannot be ruled out on the basis of the present sample.

Concluding the section, comparison of dynamical and independent stellar population modelling reveals that the mass decomposition made in Sec. 3.3.2 is approximately correct, if the IMF is allowed to vary from galaxy to galaxy within the limits set by the Kroupa and the Salpeter functions.

5.4 Spatial distribution of luminous and dark matter

The relative distribution of luminous and dark matter is now further explored based on the mass decomposition made in equation (3.6). Ambiguities of the decomposition are discussed in Sec. 5.5.

5.4.1 Circular velocity curves

Fig. 5.10 shows the best-fit circular velocity curves for the nine Coma galaxies. Based on this figure the sample is subdivided into galaxies with rising dark matter circular velocity curves all over the modelled range (red labels, referred to as galaxies with extended halos in the following) and the remaining objects (blue labels, compact halos) where the dark matter v_{circ} reaches its maximum or asymptotic value inside the library range. Albeit being almost flat (at the 15 percent level) over the kinematically sampled radial range, the circular velocity curves vary from cases with two local extrema (most luminous systems with extended halos) to a case of monotonic increase (faintest object). Galaxies with compact halos have decreasing outer v_{circ} .

To probe for variations in circular velocity curve shapes from galaxy to galaxy all profiles are scaled to their maximum value inside the observationally sampled radial region and combined in Fig. 5.11. Towards the centre, v_{circ} becomes nearly universal, at least when radii are scaled to r_{eff} (cf. right panels in Fig. 5.11). The outstanding case of GMP1176 is flagged by the dashed line. The modelling of this galaxy is unreliable in the photometrically unresolved central region. The two red and one blue lines staying roughly flat to the innermost radii represent the galaxies GMP5279, GMP0282 and GMP0144 with relatively large r_{eff} (cf. Tab. 4.1) and young outer stellar populations. The inward shifts of the peak in circular velocity may reflect differences in their outer light profiles with respect to the other systems. In any case, the offset becomes smaller when switching to absolute central distances (left panels in Fig. 5.11).

The total circular velocity curves of galaxies with extended halos and those with compact ones start to diverge beyond $2 r_{\text{eff}}$. Between $0.1 r_{\text{eff}}$ and the half-light radius circular velocities are fairly constant. In the same radial region the halo- v_{circ} of objects with extended halos and those with compact ones are already well separated. Apart from the three objects GMP5279, GMP0282 and GMP0144 mentioned above, the red and the blue curves, taken separately, have similar radial profiles. Flat circular velocity curves are ubiquitous in spiral galaxies and have been found by Gerhard et al. (2001) in spherical models of round, non-rotating ellipticals as well.

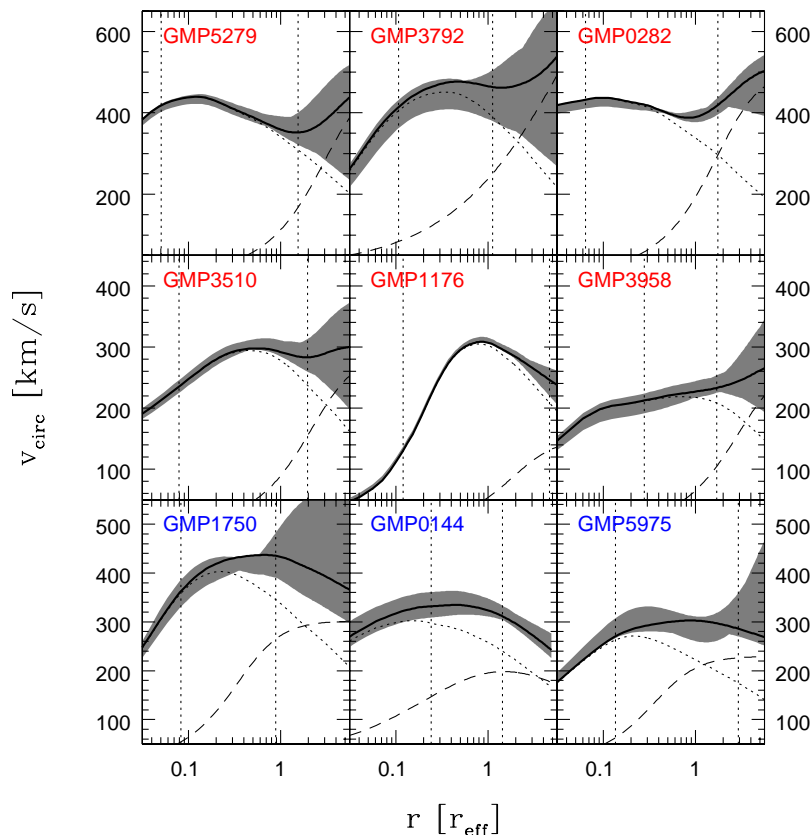


Figure 5.10: Compilation of circular velocity curves. Thick: luminous+dark (68 per cent confidence region shaded); dotted: luminous only; dashed: dark matter only; vertical dotted lines: boundaries of kinematic data.

5.4.2 Mass-density profiles

Spherically averaged mass density profiles of all Coma galaxies are surveyed in Fig. 5.12. All objects except the unresolved GMP1176 have steep central luminosity and mass distributions. The slope of the total mass profile in galaxies with compact halos smoothly changes from the inner, light dominated parts to the outer, halo regulated regions. The corresponding transition in galaxies with extended halos induces instead a noticeable break in the total mass profile – more pronounced in more massive systems. In every Coma galaxy the radius where dark matter and stellar density equal (locally) is inside the kinematically sampled region. And in every case, the central halo density is at least one order of magnitude lower than the stellar mass density – independent from the profile

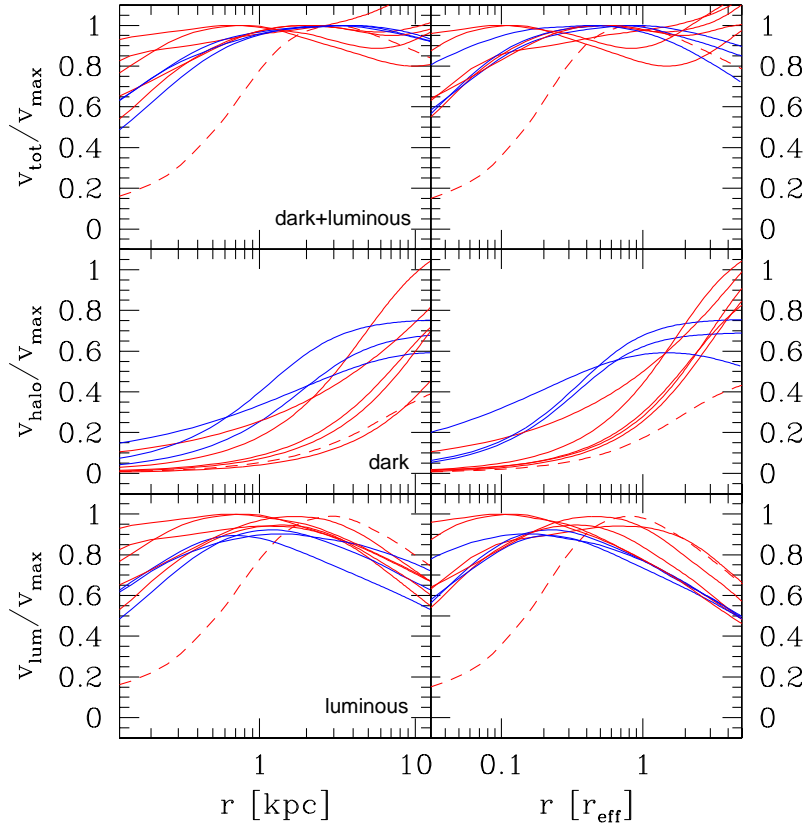


Figure 5.11: Circular velocity curves normalised by the maximum inside the observationally sampled radial range. Left: versus absolute central distance; right: in units of r_{eff} . From top to bottom: total, dark matter and luminous matter. Colors as in Fig. 5.10.

shape. In that sense even the galaxies which are best fit with a NFW halo can be regarded as having maximum central stellar masses (ambiguities related to the IMF issue left aside). Note that the lower limits for the (central) dark matter density are likely a result of ignoring halo profiles with vanishing central density.

As already implied by the approximate flatness of the circular velocity curves, the overall effect of the halo component is to keep the outer logarithmic slope of the total mass density around -2 (i.e. the case of an exactly constant v_{circ}). This can be achieved either asymptotically with NIS halos or by suitably scaled NFW halos over a limited radial range (around the scaling radius). Differences

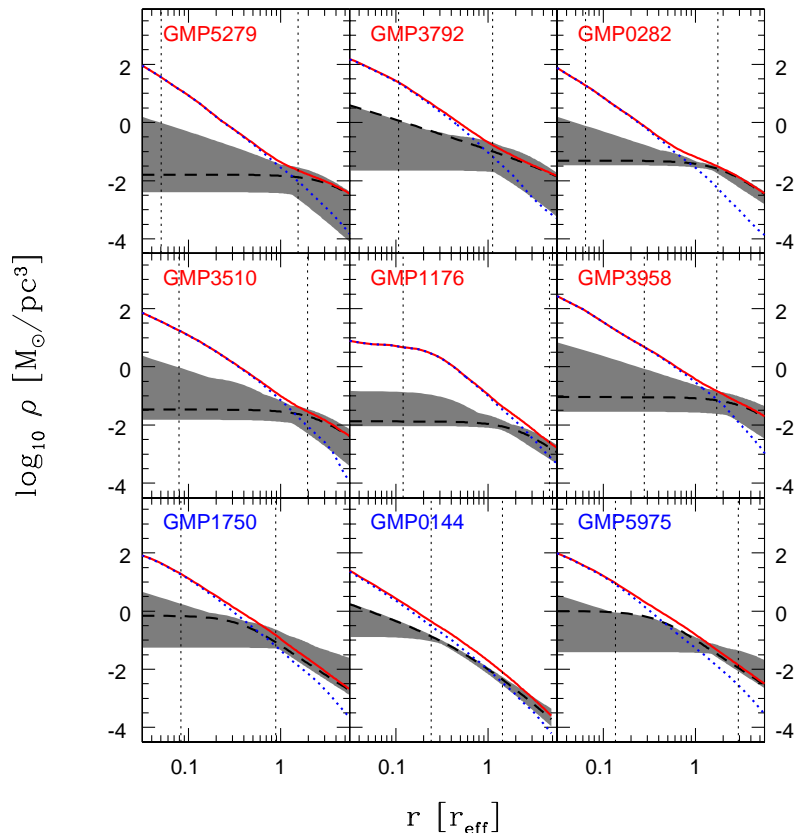


Figure 5.12: Spherically averaged mass densities. Red: total mass; blue (dotted): luminous mass; black (dashed): dark matter with errors (shaded). Vertical dotted lines as in Fig. 5.10.

in the profiles' inner slopes play a minor role because the central regions are apparently dominated by a mass distribution that follows well the luminosity profile. If elliptical galaxy circular velocity curves are roughly flat over a very extended radial range, then NFW fits will break down at some point. Vice versa, outer mass densities decreasing steeper than r^{-2} would rule out NIS halos eventually. Neither of these cases is realized within the spatial region probed by stellar kinematics ($\lesssim 3r_{\text{eff}}$).

Concluding, the nearly similar fits achieved under the quite different regimes of NIS and NFW halos strengthen the evidence that the true mass profile around r_{eff} has a logarithmic slope γ in the intersection of both cases ($-1 < \gamma < -2$).

5.4.3 Dark matter fractions

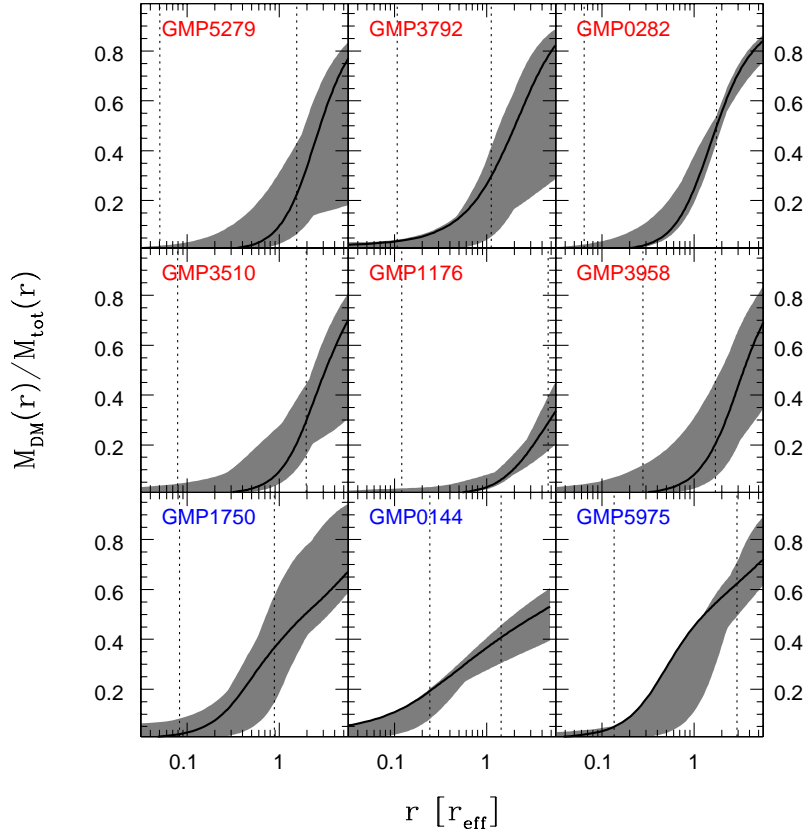


Figure 5.13: Spherically averaged dark matter fractions for the nine Coma early-types. Solid lines: best-fitting models; shaded areas: 68 per cent confidence regions; vertical dotted lines as in Fig. 5.10.

Finally, Fig. 5.13 summarises the dark matter fractions in the nine Coma objects. Galaxies with compact halos have generally larger dark matter fractions: 0.40 ± 0.04 at r_{eff} and 0.51 ± 0.06 at $2r_{\text{eff}}$, respectively. The corresponding numbers for galaxies with extended halos are 0.14 ± 0.1 at r_{eff} and 0.34 ± 0.16 at $2r_{\text{eff}}$.

5.5 Uncertainties in the mass decomposition

According to the discussion in Sec. 5.3.5 the mass decomposition is ambiguous in two directions. Firstly, a fraction of dark matter may be included in the mass assigned to the luminous component. This possibility is quantitatively treated in Sec. 5.5.1. Secondly, part of the halo mass may be made of stars in reality. This case is dealt with in Sec. 5.5.2.

5.5.1 Central dark matter

Assuming a universal Kroupa IMF, the amount of dark matter in the dynamical models consists of the generic halo component ρ_{DM} plus the fraction of extra mass

$$\rho_{\text{DM}}^+ \equiv (\Upsilon_{\text{dyn}} - \langle \Upsilon_{\text{SSP}} \rangle) \times \nu \quad (5.14)$$

that follows light on top of the stellar contribution

$$\rho_* \equiv \langle \Upsilon_{\text{SSP}} \rangle \times \nu \quad (5.15)$$

expected for a given IMF. The total dark matter density $\hat{\rho}_{\text{DM}}$ thus follows to be

$$\hat{\rho}_{\text{DM}} \equiv \rho_{\text{DM}} + (\Upsilon_{\text{dyn}} - \langle \Upsilon_{\text{SSP}} \rangle) \times \nu. \quad (5.16)$$

Fig. 5.14 shows the resulting “maximum-halo” dark matter fractions². For better comparison, shaded areas repeat the allowed range of “minimum-halo” dark matter fractions (from Fig. 5.13). The range of central dark matter fractions in Fig. 5.14 reflects the increasing $\Upsilon_{\text{dyn}} - \langle \Upsilon_{\text{SSP}} \rangle$ in the lower panel of Fig. 5.7, from the galaxy GMP5975 with no space for dark matter hidden in Υ_{dyn} up to the system GMP3792 central dark matter fractions reach up to 50 percent. In extended-halo galaxies the dark matter fraction becomes approximately constant within r_{eff} .

Corresponding maximum-halo mass densities are surveyed in Fig. 5.15. As a consequence of Fig. 5.14 in many systems the central dark and luminous mass densities become comparable. In compact-halo systems dark matter profiles keep their concave shapes, but in all other systems develop a break around r_{eff} . From Fig. 5.14 it is clear that in the extended-halo cases the dark matter distribution differs significantly from the original NIS or NFW form, respectively.

5.5.2 Radially increasing stellar mass-to-light ratios

The last point to discuss is whether in cases of an increasing stellar mass-to-light ratio the derived halo is actually tuned to (partly) follow this luminous M/L trend. This possibility is explored in Fig. 5.16, comparing major-axis stellar mass-to-light ratios from Figs. 5.2 and 5.3 with *local* dynamical ρ/ν along the same axis. Remarkably, in some cases (e.g. GMP0282, GMP1176, GMP0144

²The lack of SSP models for GMP3958 inhibits the construction of a maximum halo model. The galaxy is left out in Figs. 5.14 and 5.15.

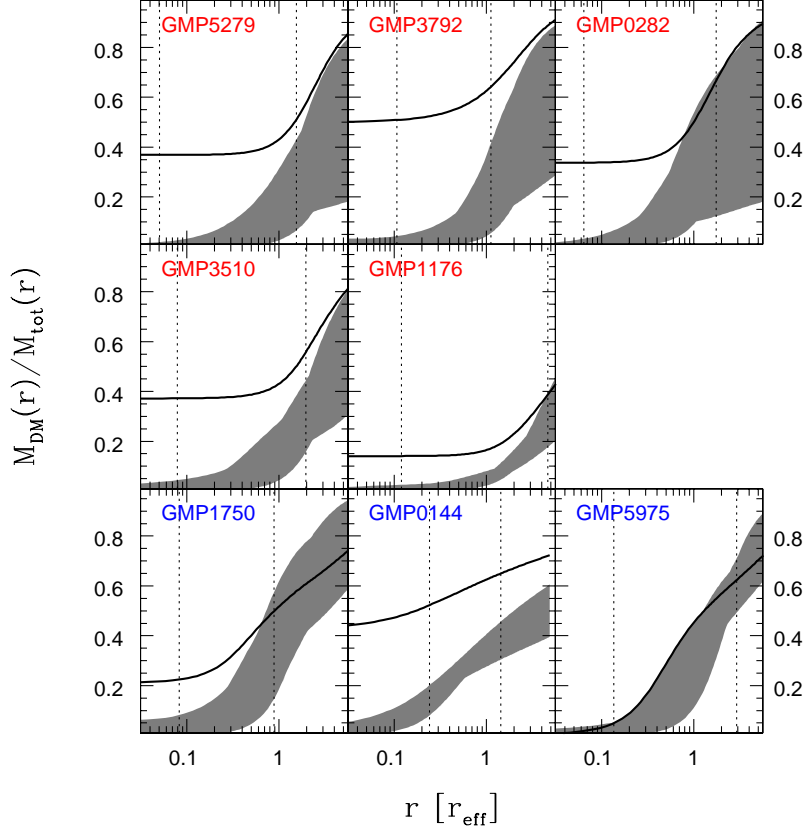


Figure 5.14: As Fig. 5.13 but for maximum halos (see text for details).

and GMP5975) the increase in ρ/ν is accompanied by a comparable increase in the stellar population Υ_{SSP} . This would support the idea that these halo components overestimate the actual dark matter content. However, if the corresponding upturn in the stellar population Υ_{SSP} is real, then by projection effects one would expect $\rho/\nu < \Upsilon_{\text{SSP}}$. The opposite is revealed by Fig. 5.16, instead. Additionally, in all cases the local enhancement of stellar population Υ_{SSP} only appears over a limited radial range and/or only along one side of the object suggesting that it could be caused by gas emission. In this case, however, the congruence between ρ/ν and the SSP features would reflect a striking coincidence.

It could be, that the increase in ρ/ν is only partly made by stars but partly by dark matter. Then, ρ/ν is no longer related to Υ_{SSP} via projection quadratures but can be larger – consistent with Fig. 5.16. Another option is that the increase

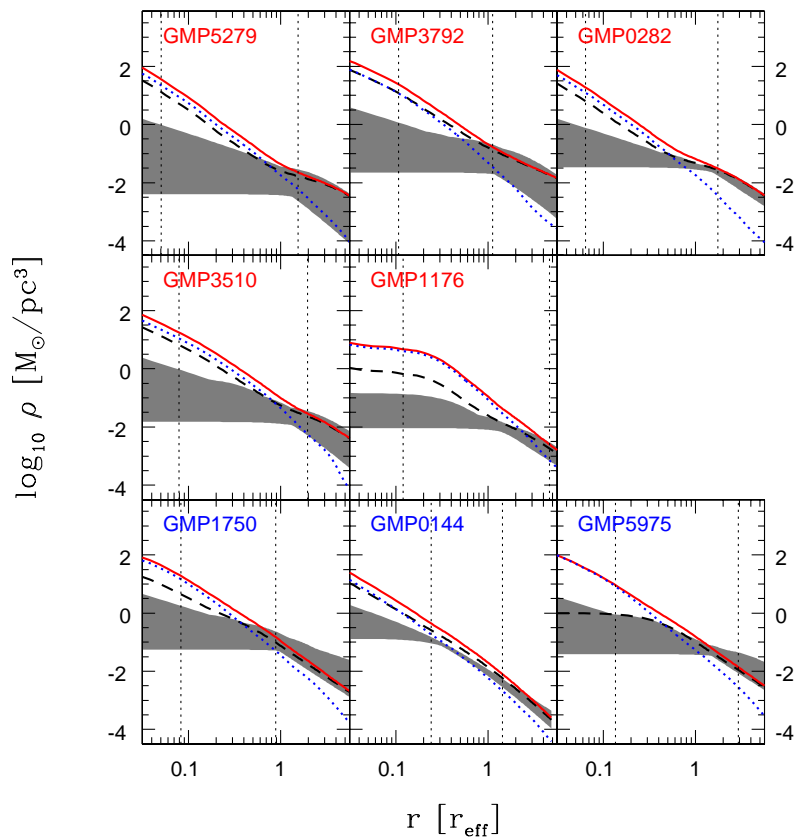


Figure 5.15: As Fig. 5.12 but for the maximum halo case (see text for details).

in ρ/ν involves baryonic matter, e.g. gas. In this case ρ/ν and Υ_{SSP} are not related via projection quadratures as well. The galaxies in question have low stellar ages in their outskirts ($\lesssim 1\text{-}5$ Gyr, deprojected ages may be even lower). A relatively recent accretion of a young, low-mass, gas-rich object cannot be directly excluded, therefore. If the increase of ρ/ν would be purely baryonic, however, gas masses of the order of the local stellar masses would be required.

Concluding, some fraction of the mass in the halos of especially GMP0144 and GMP5975 (and possibly GMP0282 and GMP1176) may be baryonic. But additional data at larger radii are required to distinguish between the different possibilities more firmly.

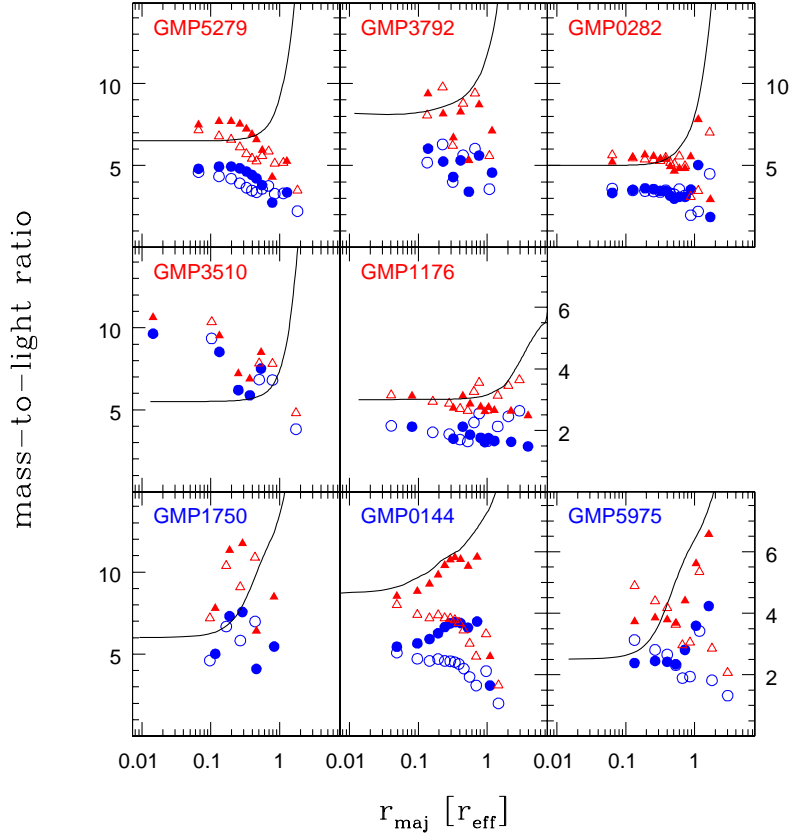


Figure 5.16: As Figs. 5.2, 5.3 but only the major-axis stellar population models are shown and compared to the local major-axis ρ/ν .

5.6 Regularisation

As has been discussed in Sec. 4.2 the same regularisation is adopted for all Coma galaxies. In the following the influence of the choice of α on the fits is investigated.

Fig. 5.17 surveys the best-fit stellar mass-to-light ratios Υ_{dyn} over the regularisation interval $\alpha \in [10^{-5}, 3]$. Two conclusions can be drawn from the figure. Firstly, no systematic trend of Υ_{dyn} with α is noticeable. In GMP5279, for example, less regularisation yields larger Υ_{dyn} , while in GMP1750 on the other hand, Υ_{dyn} drops with α . In about half of the sample galaxies, regularisation has barely any effect on Υ_{dyn} at all (e.g. GMP5975, GMP0282, GMP3510, GMP3792, GMP0144).

The best-fit dark matter fractions at three representative radii are shown in

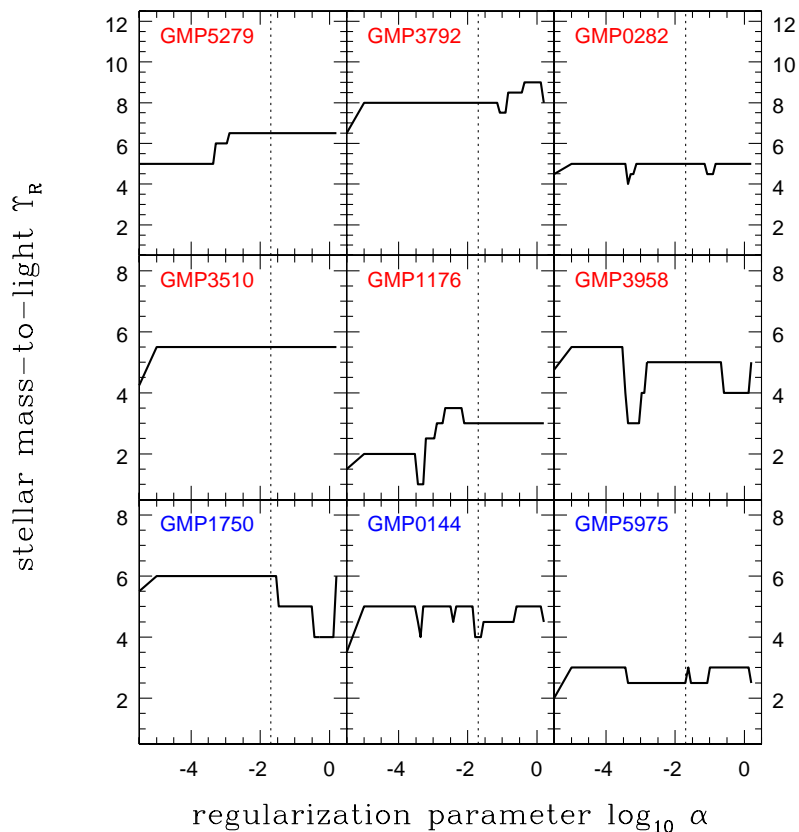


Figure 5.17: Best-fit Υ_{dyn} versus regularisation parameter α . Dotted line: $\alpha = 0.02$.

Fig. 5.19 as a function of α . As expected, occasional drops in Υ_{dyn} showing up in Fig. 5.17 are correlated with peaks in the dark matter fractions of Fig. 5.19. In general, as for the stellar mass-to-light ratio, no systematic trend of the models' dark matter fraction with α is seen and the variation of dark matter fractions with α are within the error budget of the data.

5.7 Dark matter distribution functions

As has been outlined in Sec. 5.1, the mass decomposition is not directly constrained by photometric and kinematic observations. Therefore it is valuable to collect as many independent constraints on it as possible. The most direct approach is followed in Sec. 5.3 by the comparison of dynamically and spectro-

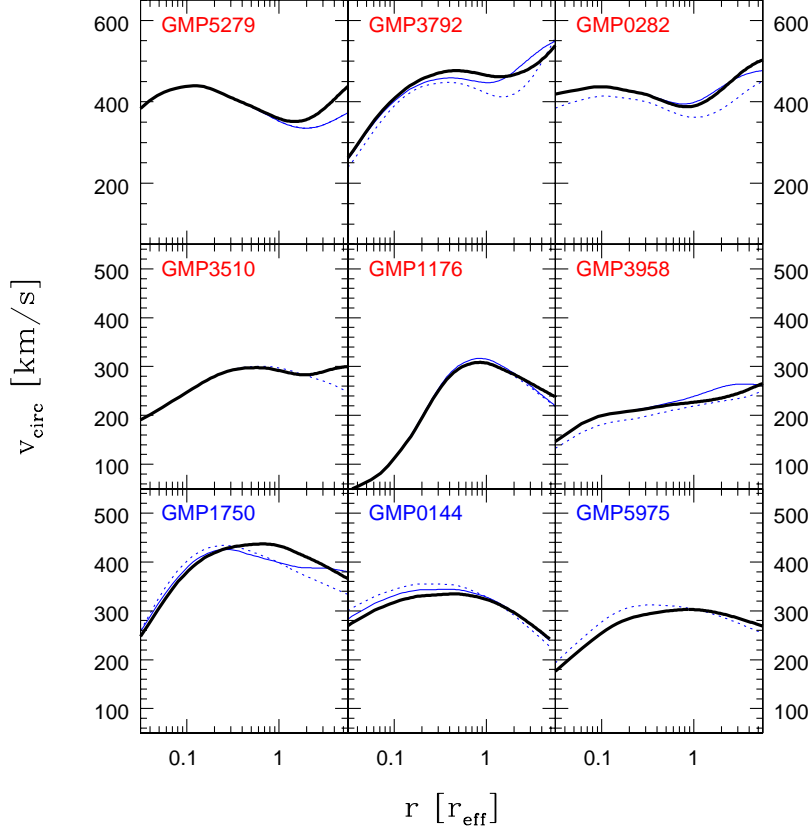


Figure 5.18: Best-fit circular velocity curves at different regularisations: $\alpha = 0.001$ (blue, solid), $\alpha = 2.7$ (blue, dotted) and the galaxy fits ($\alpha = 0.02$; black, solid).

scopically derived stellar mass-to-light ratios. Another, not yet fully followed approach is the stationarity of the mass decomposition, which is considered here.

As mentioned in Sec. 1.2, a density distribution is stationary, if it is supported by a DF that depends on the phase-space coordinates only via the integrals of motion (Jeans theorem). Furthermore, to be physically reasonable, this DF should be everywhere positive. As yet, the existence of such a DF is only ensured for the luminous mass distribution, for which it has been explicitly calculated in terms of the orbital weights w_i . It is the basic aim of this section to investigate, whether the dark matter distribution in each best-fit Coma mass-model is supported by such a DF as well. The dark matter DF can be computed with the orbit superposition technique just as the DF for the luminous matter.

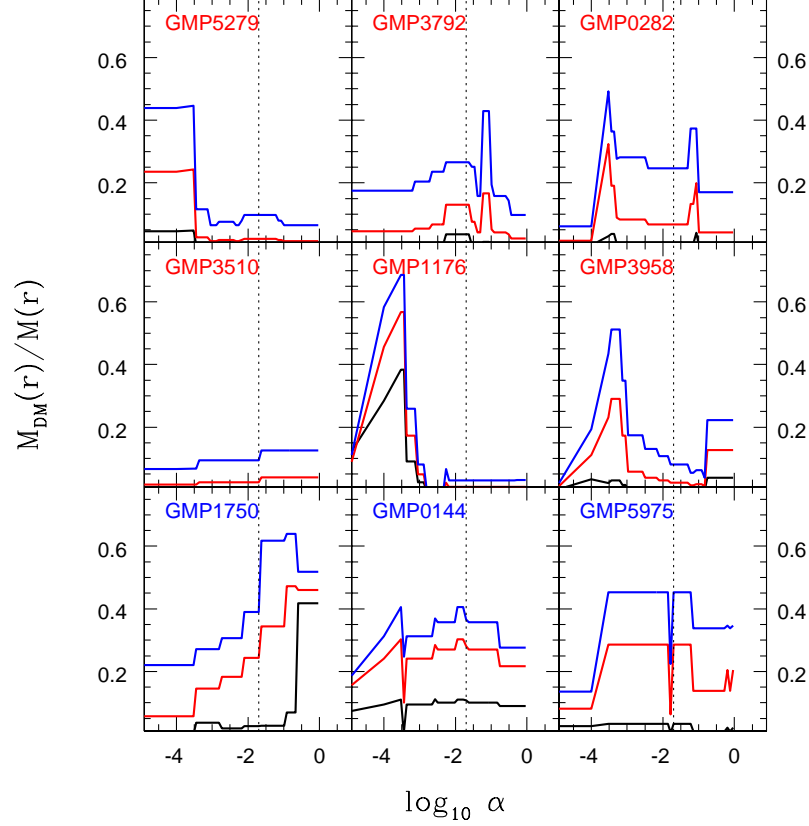


Figure 5.19: Dark matter fractions at $0.1 r_{\text{eff}}$ (black), $0.5 r_{\text{eff}}$ (red) and $1.0 r_{\text{eff}}$ (blue) versus regularisation parameter α . Vertical dotted lines: $\alpha = 0.02$.

As the only differences, the dark matter density profile has to be used as the boundary condition to solve equation (3.7) and the regularisation parameter has to be set $\alpha = 0$ (because no kinematical constraints exist).

It turns out that the dark matter distribution in the Coma models is in every case supported by a positive distribution function. Corresponding orbital phase-densities are shown in Fig. 5.20 as a function of the mean orbital radius defined in App. C. In galaxies with best-fit NFW-halos (GMP3792, GMP0144) the DF is monotonic with respect to $\langle r_{\text{orb}} \rangle$. In all other cases, the DF reaches a maximum and drops towards the centre.

Studying a two-parameter family of isotropic spherical galaxy models Baes, Dejonghe & Buyle (2003) found a similar drop of phase-densities when (1) a central black hole adds to an otherwise self-consistent gravitational potential

and (2) the central logarithmic slope γ of the density distribution is shallower than $\gamma < 3/2$. Fig. 5.20 does not reveal a drop in the galaxies with NFW-halos which have a central logarithmic slope $\gamma = 1$. However, the results of Baes, Dejonghe & Buyle (2003) cannot directly be compared to the case here, because (1) NIS halos have mass profiles different from the two-parameter family of Baes, Dejonghe & Buyle (2003) and (2) the way a black-hole modifies the central potential is different from the way a typical stellar mass distribution does. In any case, although the numerical resolution in the orbit models is not sufficient to study the innermost behaviour of the DF in detail, the drop of central phase-densities is likely not a modelling artifact.

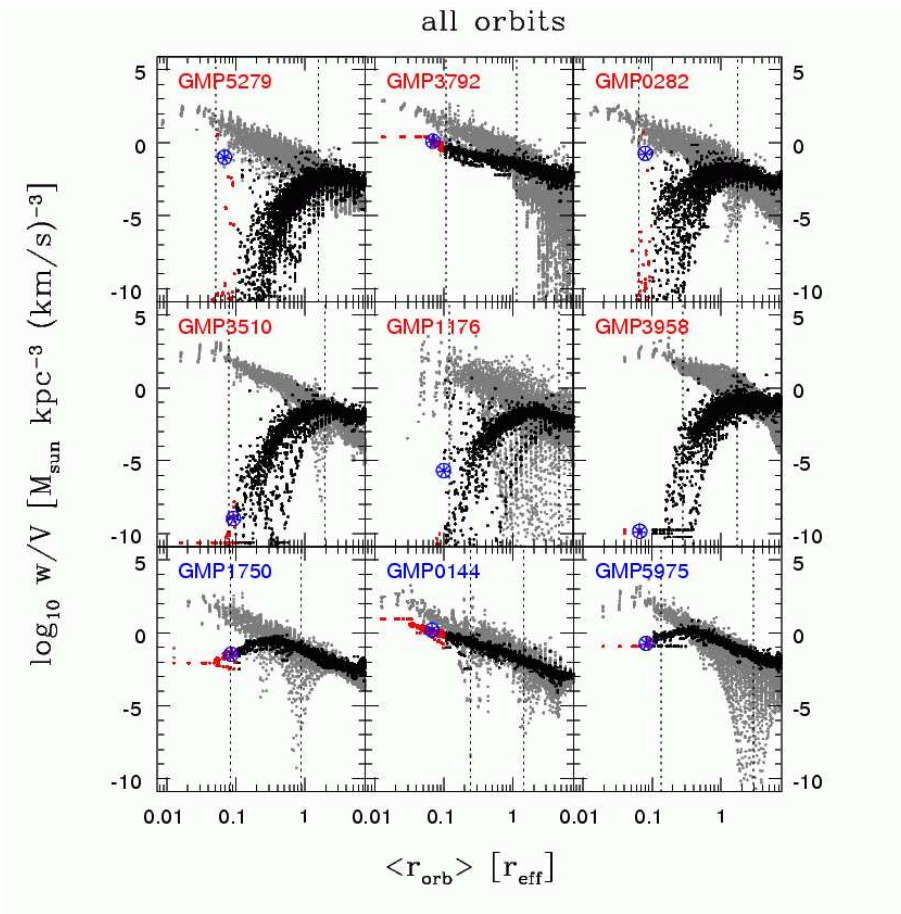


Figure 5.20: Luminous and dark matter phase-densities (all orbits). Black: dark matter; grey: luminous; red: dark matter $\langle r_{\text{orb}} \rangle < 0.1 r_{\text{eff}}$; blue average phase-density of red points; vertical dotted lines: boundaries of kinematical data.

From the orbital phase-densities shown in Fig. 5.20 a mean central phase-

density can be defined as

$$f_h \equiv \left(\frac{\sum w_i}{\sum V_i} \right)_{0.1}, \quad (5.17)$$

where the sums on the right hand side are intended to comprise all orbits with $\langle r_{\text{orb}} \rangle < 0.1 r_{\text{eff}}$. These orbits are highlighted in red in Fig. 5.20. The central halo phase-densities are used in Sec. 7.7. It should be noted that the DFs shown in Fig. 5.20 are not unique. At least, it is always possible to change the odd part of the DF with respect to L_z without affecting the density in configuration space. It may further be that DFs differing in other respects from the maximum entropy case support the dark matter distributions as well. This adds to the uncertainties of f_h .

The non-monotonic shape of the NIS-DFs implies that they could be unstable. If they are indeed unstable, then the mass decomposition discussed above is physically unreasonable. In this case a systematic survey of dark matter distribution functions could independently constrain the range of reasonable mass decompositions. A stability analysis of the halo DFs is out of the scope of this work, however.

5.8 Summary

The dynamical modelling of Coma galaxies provides evidence for dark matter in each galaxy. Dynamically derived stellar Υ_{dyn} are in good agreement with stellar population modelling, if a variation of the IMF is allowed for. In the low- Υ_{dyn} regime dynamical models are compatible with a Kroupa IMF, but with increasing Υ_{dyn} , they shift towards the predictions of a Salpeter IMF. This result is similar to the findings of Cappellari et al. (2006) from self-consistent modelling of SAURON-galaxies. A slight tendency for low- Υ_{dyn} galaxies being younger and less α -enhanced is seen in the Coma sample. For a firm conclusion the sample is too small, however.

Dark matter halos required to fit the kinematical data are in two of nine cases of the NFW-type and in all other cases of the NIS-type. Differences in the fit to the data based on one or the other halo model are marginal in every case. In combination with luminous matter, the distribution of dark matter results in roughly flat circular-velocity curves. In detail, the sample separates in two subgroups. One is characterised by an increasing outer v_{circ} , the other by an outer decreasing v_{circ} . A similar shape-variation is found in the temperature profiles of elliptical galaxy X-ray halos (Humphrey et al. 2006).

Central dark matter densities are one to two orders of magnitude lower than the corresponding mass density in stars. Between 10 and 50 percent of the mass included by the half-light radius r_{eff} is dark in the Coma galaxies. This is in agreement with results for round, non-rotating ellipticals (Gerhard et al. 2001). The distributions of dark matter and the shapes of the circular velocity curves are robust against different choices of regularisation.

For the first time, DFs for the dark matter component have been computed. In halos following the NIS-type, phase-densities drop towards the centre, while NFW-halos provide on-average monotonic DFs. Central phase densities are in each case orders of magnitudes below central stellar phase-densities.

Chapter 6

Dynamical structure of Coma ellipticals

6.1 Outline

The present chapter deals with the dynamical structure of the galaxies in the Coma sample. Velocity anisotropies as well as the orbital distribution in phase-space are addressed. The latter is fully described by the phase-space distribution function f of the isolating integrals of motion E , L_z and I_3 . Instead of exact integrals, orbital shape parameters are used in the following. To allow a fluent reading of the text, the definition of these shape parameters is separated in App. C. The DFs of the models (and of real galaxies as well) are sums of δ -functions. To illustrate the main trends in phase-space a smoothed local DF is defined that represents the average phase-density in the neighbourhood of a given orbit. The smoothing is detailed in App. D.

The chapter is composed as follows. In Sec. 6.2 the global dynamical structure is related to the flattening of the objects. In the following Secs. 6.3- 6.5 the orbital distributions around the minor-axis, intermediate position angles and around the equatorial plane are investigated separately and discussed in Sec. 6.6. The influence of regularisation is explored in Sec. 6.7 and the chapter is summarised in Sec. 6.8.

6.2 Flattening and anisotropy

The flattening of axisymmetric galaxies can be supported by different orbital configurations. Studying self-consistent synthetic 3I model galaxies, Dehnen & Gerhard (1993) identified four principal configurations. The corresponding DFs in two cases involve only two integrals of motion. In classical 2I systems with $f = f(E, L_z)$ the flattening stems from extra-light on high angular-momentum orbits. These configurations have characteristic velocity anisotropies $\beta_{\vartheta} \equiv 1 -$

$\sigma_\vartheta^2/\sigma_r^2 = 0$ and $\beta_\varphi \equiv 1 - \sigma_\varphi^2/\sigma_r^2 < 0$. This case is shortly referred to as flattening by rotation in the following. Strictly speaking, the flattening depends on the part of the DF that is even in L_z , while rotation depends on the part that is uneven in L_z . However, the exact balance of light on the prograde and retrograde specimen of each orbit does not play a role in the discussion below.

The other 2I option is flattening by a depression of orbits reaching high latitudes, or shortly, flattening by anisotropy. The corresponding velocity anisotropies are $\beta_\vartheta > 0$ and $\beta_\varphi = 0$. Other flattening mechanisms involve dependencies of the DF on all integrals and correspondingly complex anisotropy structures. The flattening of the Coma galaxies is discussed in the following.

6.2.1 Galaxy fits

Fig. 6.1 shows meridional $\langle\beta_\vartheta\rangle$ and azimuthal $\langle\beta_\varphi\rangle$ anisotropies averaged between 0.05 and $2.5 r_{\text{eff}}$, versus the average intrinsic ellipticity $\langle\epsilon_\nu\rangle$ of the models. The latter is calculated by ellipse-fits to isodensity-contours of the deprojection. The chosen radial range roughly covers the region with kinematical data. In the figure also the two 2I flattening cases mentioned above are shown for comparison. Flattening by rotation is coloured blue and the velocity anisotropies are calculated for each galaxy by solving higher-order Jeans equations with the program of Magorrian & Binney (1994). As stated above, the purpose here is only to recover the general flattening mechanism of the Coma galaxies, which depends on the even part of the DF. Therefore, rotation has been included into the azimuthal velocity anisotropy by considering

$$\beta_\varphi^* \equiv 1 - \frac{\sigma_\varphi^2 + v_\varphi^2}{\sigma_r^2}. \quad (6.1)$$

Given an arbitrary density distribution, β_φ^* is uniquely defined under the assumption that $f = f(E, L_z)$.

Concerning the second 2I flattening mechanism, flattening by anisotropy, velocity anisotropies are calculated from an approximation of the tensor virial theorem (Saglia, Bender & Dressler 1993)

$$\beta_\vartheta = 1 - (1 - \epsilon_\nu)^{0.9} \quad (6.2)$$

(red curves in Fig. 6.1). The relation (6.2) is almost linear over $\epsilon_\nu \in [0, 1]$ and can be well fit by

$$\beta_\vartheta = -0.02 + 0.99 \times \epsilon_\nu. \quad (6.3)$$

Fig. 6.1 reveals a close relationship between intrinsic flattening and meridional velocity anisotropy. A linear fit yields

$$\langle\beta_\vartheta\rangle = (-0.10 \pm 0.19) + (1.11 \pm 0.61) \times \langle\epsilon_\nu\rangle \quad (6.4)$$

and is traced by the black line in the upper panel. The actual relation in the Coma sample is slightly steeper than the red curve, but both are consistent within the errors. Most galaxies with $\langle\beta_\vartheta\rangle$ lower than expected from flattening

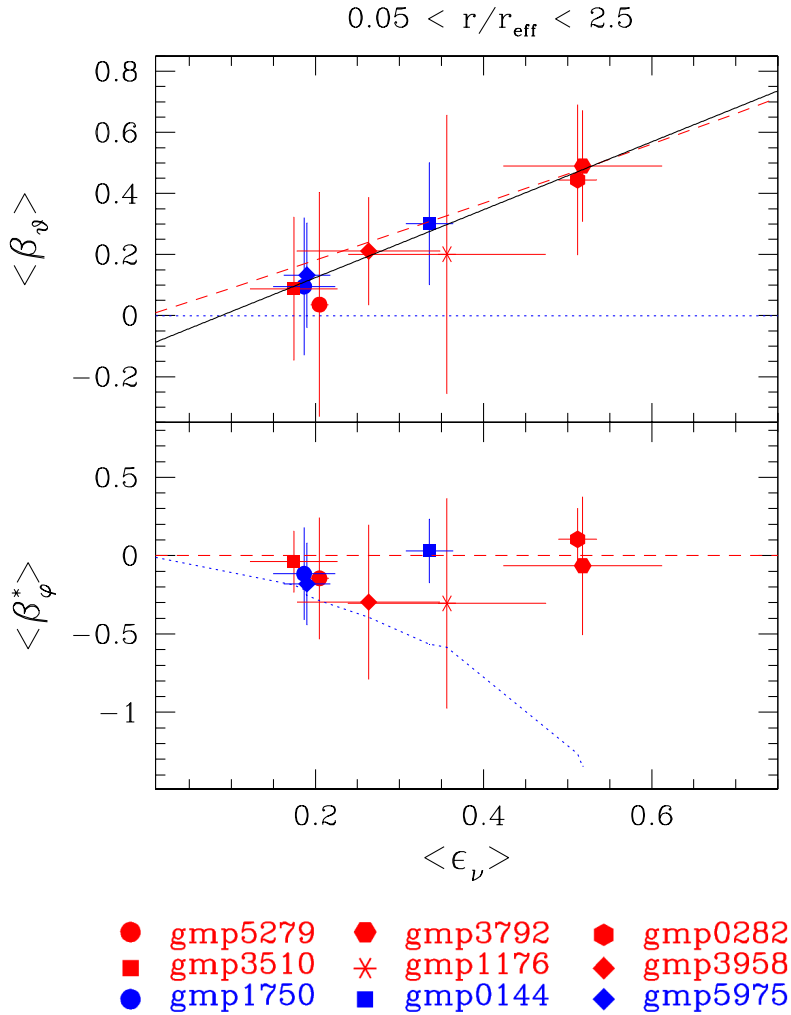


Figure 6.1: Top: meridional average velocity anisotropy $\langle \beta_\vartheta \rangle$ versus average intrinsic ellipticity $\langle \epsilon_\nu \rangle$; error bars: standard deviation about the mean; red/blue: flattening by anisotropy/rotation (cf. text); black: linear fit. Bottom: same for azimuthal anisotropy $\langle \beta_\varphi^* \rangle$ (see text for details).

by anisotropy, have azimuthal $\langle \beta_\varphi^* \rangle$ approaching the $f(E, L_z)$ case in the lower panel. An exception is GMP3958 that is close to the red line in the upper panel but close to the blue line in the lower. From the isophotal fits in Fig. 4.6 it is clear that the ellipticity of this galaxy varies strongly with radius, and from the dynamical analysis in Sec. 6.6 it will come out that the system is made of a disk superimposed on a spheroidal background. This may explain its exceptional behaviour.

A general trend in Fig. 6.1 is that from the most flattened to the roundish systems the importance of high angular-momentum orbits increases. The present sample is however too small to draw any firm conclusion about this issue.

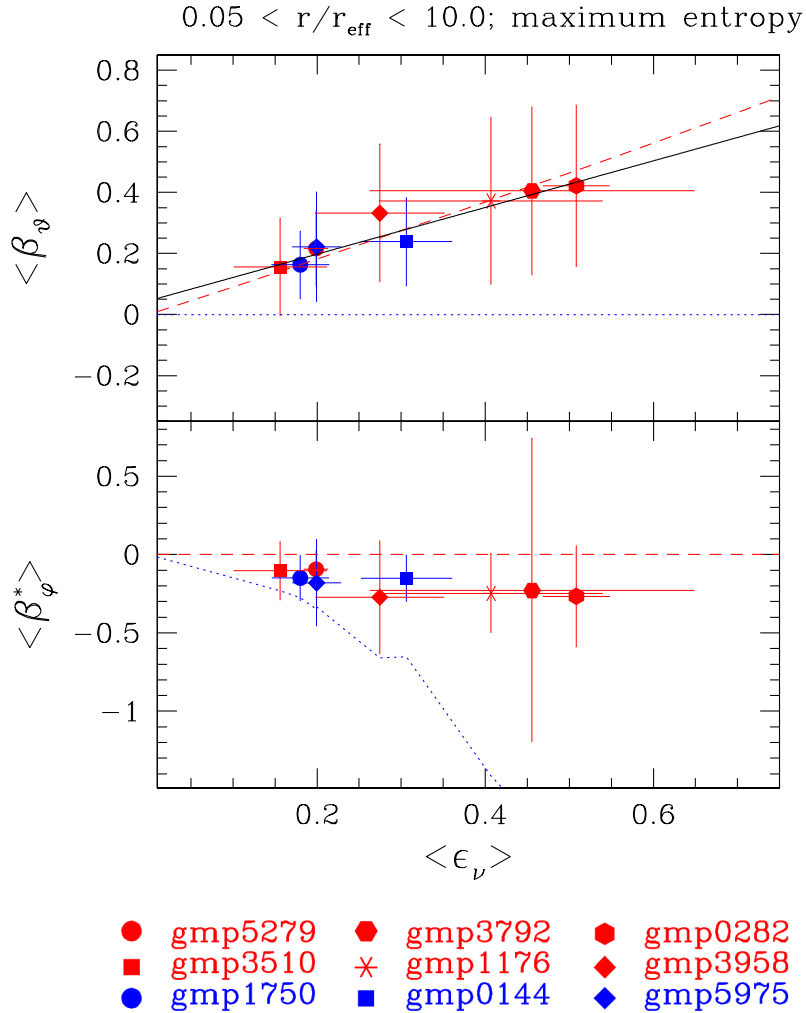


Figure 6.2: As Fig. 6.1 but for the maximum entropy models.

6.2.2 Maximum entropy models

For two reasons, it is interesting to compare the galaxy fits to maximum entropy models: (1) the fits are regularised towards maximum entropy and it is useful to understand exactly in which direction this smoothing works; (2) deviations from maximum entropy configurations may contain information about the for-

mation mechanisms and evolutionary histories of the galaxies. Fig. 6.2 shows for the maximum entropy models velocity anisotropies versus intrinsic ellipticity. Maximum entropy models are calculated in the best-fit mass distribution of each galaxy by setting the regularisation parameter $\alpha = 0$ (cf. Sec. 3.3.4). They reproduce the luminosity distribution, but do not fit to the kinematical data. Since the purpose is to understand the effects of entropy maximisation (data constraints do not matter), the comparison in Fig. 6.2 covers the whole library.

Without any boundary condition, the maximisation of S in equation (3.7) populates orbits proportional to their phase-volumes. The phase-space density thus becomes constant and any dependency of the DF on the integrals of motion is suppressed. Coupling the DF to match a flattened density distribution breaks this overall symmetry. Still, the maximisation of S under this boundary condition will minimise gradients in the DF. One may therefore expect the maximum entropy models to be close to one of the two above mentioned cases where the DF depends on only two integrals.

Indeed, in Fig. 6.2 the maximum entropy models are located closely to the relation predicted by flattening through anisotropy. A linear fit yields

$$\langle\beta_{\vartheta}\rangle = (0.05 \pm 0.16) + (0.81 \pm 0.47) \times \langle\epsilon_{\nu}\rangle. \quad (6.5)$$

It is shown as the black line in Fig. 6.2 and coincides well with the red curve over the region $\langle\epsilon_{\nu}\rangle \in [0.2, 0.6]$ covered by the Coma models. Moreover, the relation (6.5) is consistent with the galaxy fits (6.4). Interestingly, the maximum entropy models do not yield exactly $\langle\beta_{\varphi}\rangle = 0$, but tend to be slightly azimuthally anisotropic. A possible reason may be the bias of the libraries towards azimuthal anisotropy at their boundaries (cf. Sec. 2.5.3). Another issue may be that the maximum entropy models are not self-consistent, but calculated in spherical dark matter halos.

From the similarity of the dynamical structure in the maximum entropy models and the galaxy fits one may suspect that the Coma models are largely driven by the regularisation prior. However, a decrease of the fraction of energy in vertical versus horizontal motions with flattening has also been found in the SAURON survey (Cappellari et al. 2005). The models applied to the SAURON galaxies are based on a completely different regularisation scheme. Therefore, the consistency of the results of Cappellari et al. (2005) and the Coma galaxies suggests that ellipticals are mostly *flattened by anisotropy* and, accordingly, globally in a near maximum entropy state.

6.3 Local dynamical structure around the poles

6.3.1 Velocity anisotropies

Figs. 6.3 and 6.4 survey velocity anisotropy profiles along the intrinsic minor-axis of the Coma galaxy sample. By axial symmetry azimuthal and meridional velocity dispersions equal directly on the symmetry axis, implying $\beta_{\vartheta} \equiv \beta_{\varphi}$

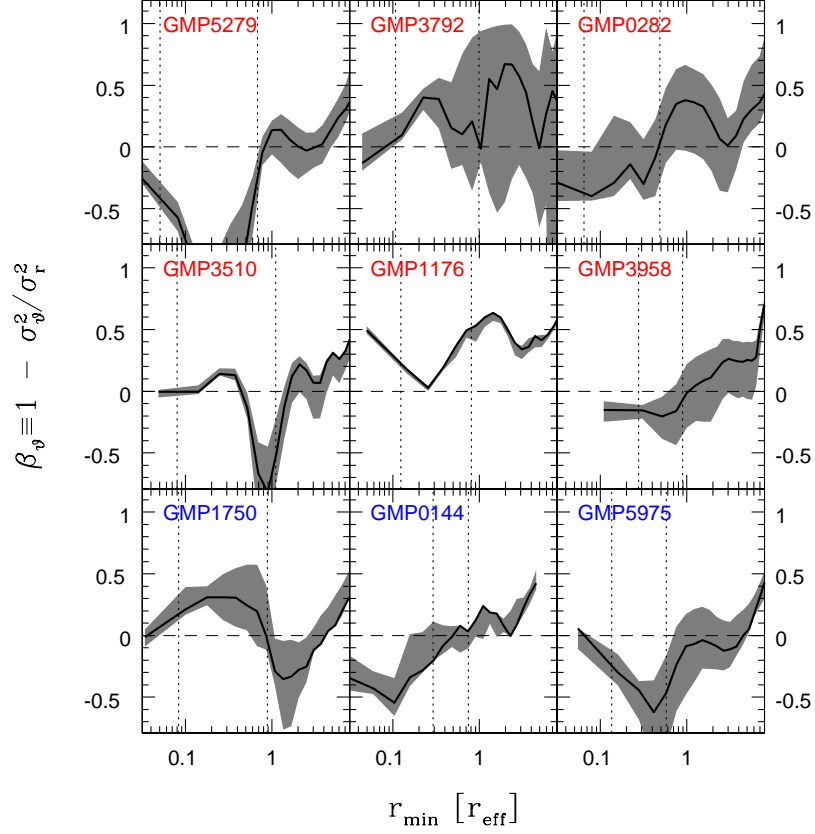


Figure 6.3: Radial profiles of meridional anisotropies β_ϑ in the minor-axis bins. Thick/shaded: best-fit model with error; dotted: range of kinematical data.

there. This explains the overall similarity between Figs. 6.3 and 6.4. They do not match exactly, because the minor-axis bins of the models form a cone with opening angle $\theta = 25^\circ$ around the z -axis. Off the symmetry axis, at latitudes $\vartheta < 90^\circ$, the equivalence of azimuthal and meridional dispersions does not hold.

In Figs. 6.3 and 6.4, the very central anisotropies should not be regarded as reliable. Firstly, because the central bins are affected from incomplete orbit sampling producing artificially large azimuthal dispersions (cf. Sec. 2.5.3). Secondly, for numerical reasons the innermost bin is not resolved in ϑ , but averaged over all $\vartheta \in [0^\circ, 90^\circ]$.

In the spatial region with kinematical data the Coma galaxies offer different degrees of minor-axis anisotropy, from strongly tangential (GMP5279) to moderately radial (GMP3792). Towards the centre $\beta_\vartheta \rightarrow 0$, while β_φ becomes

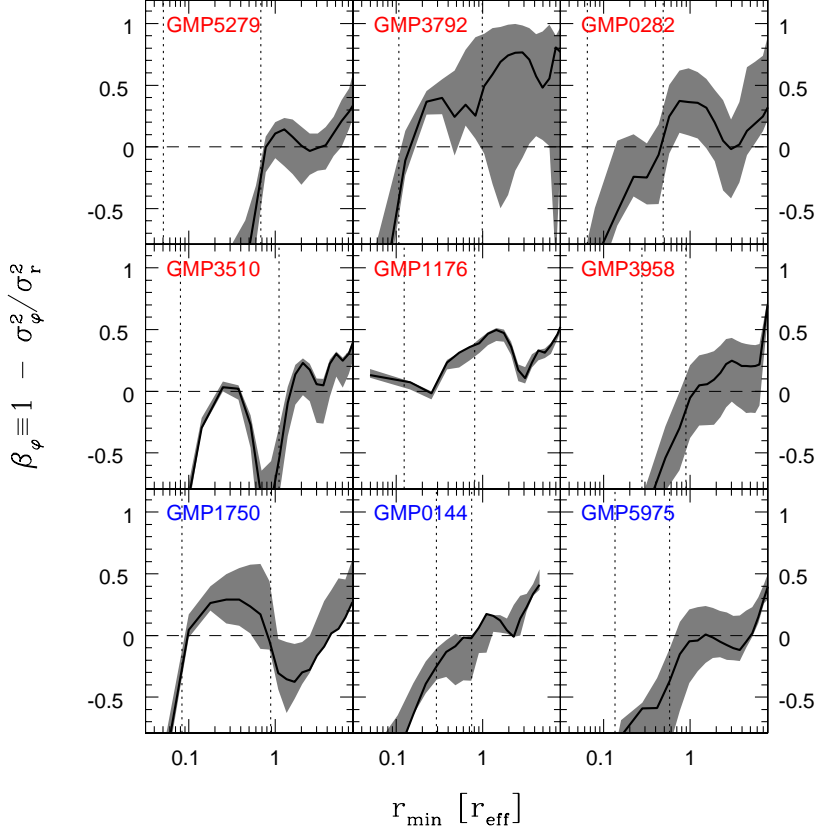


Figure 6.4: As Fig. 6.3, but for azimuthal anisotropies β_φ .

negative (most likely due to the incomplete orbit sampling). Going outward, many but not all galaxies exhibit a gradual change in dynamical structure. Often in form of a minimum or maximum in β . Around the last data points most models are isotropic or tangentially anisotropic. The only radial systems are GMP1176 and, with respect to β_φ only, GMP3792.

6.3.2 Anisotropy and H_4

The intrinsic short-axis velocity anisotropies are mostly driven by the H_4 -observations. This can be taken from Fig. 6.5, where the models' $H_4(R)$ (at projected radius R) are plotted against internal anisotropy $\beta(r = R)$ at the same radial distance. Internal radii have not been corrected for inclination since most models are edge-on. From the figure a tight correlation of β_ϑ with H_4 follows (quoted in the plot), and a weaker one of β_φ with H_4 .

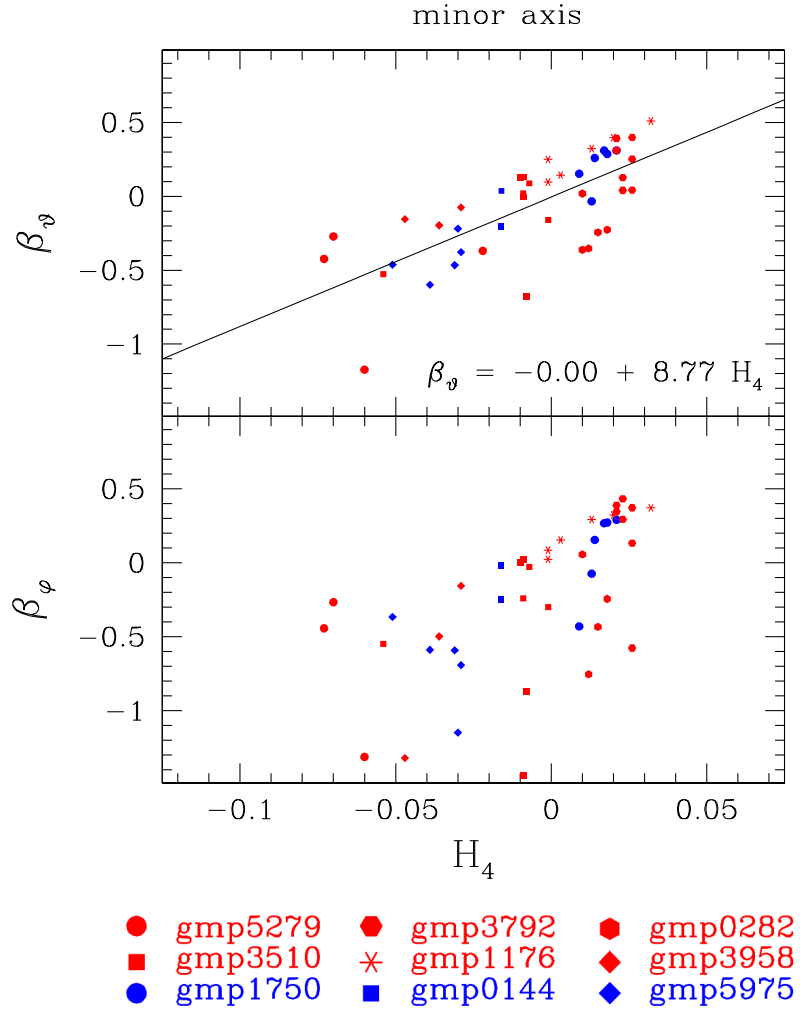


Figure 6.5: Short-axis anisotropy against minor-axis H_4 . The line in the upper panel shows a linear fit (quoted in the panel).

6.3.3 The local distribution function

The orbital structure underlying the anisotropy profiles of Figs. 6.3 and 6.4, respectively, is presented in Fig. 6.6. Curves show for each galaxy the average local DF (defined in App. D) of orbits contributing to the minor-axis bins of the models. These orbits are chosen by having maximum latitudes $\vartheta_{\max} > 70^\circ$ (cf. App. C). For convenience they are labelled minor-axis orbits or polar orbits in the following.

In axial symmetry, angular momentum conservation implies infinite azimuthal velocities $v_\varphi = L_z/r/\cos(\vartheta)$ on the symmetry axis, unless $L_z \equiv 0$. Therefore,

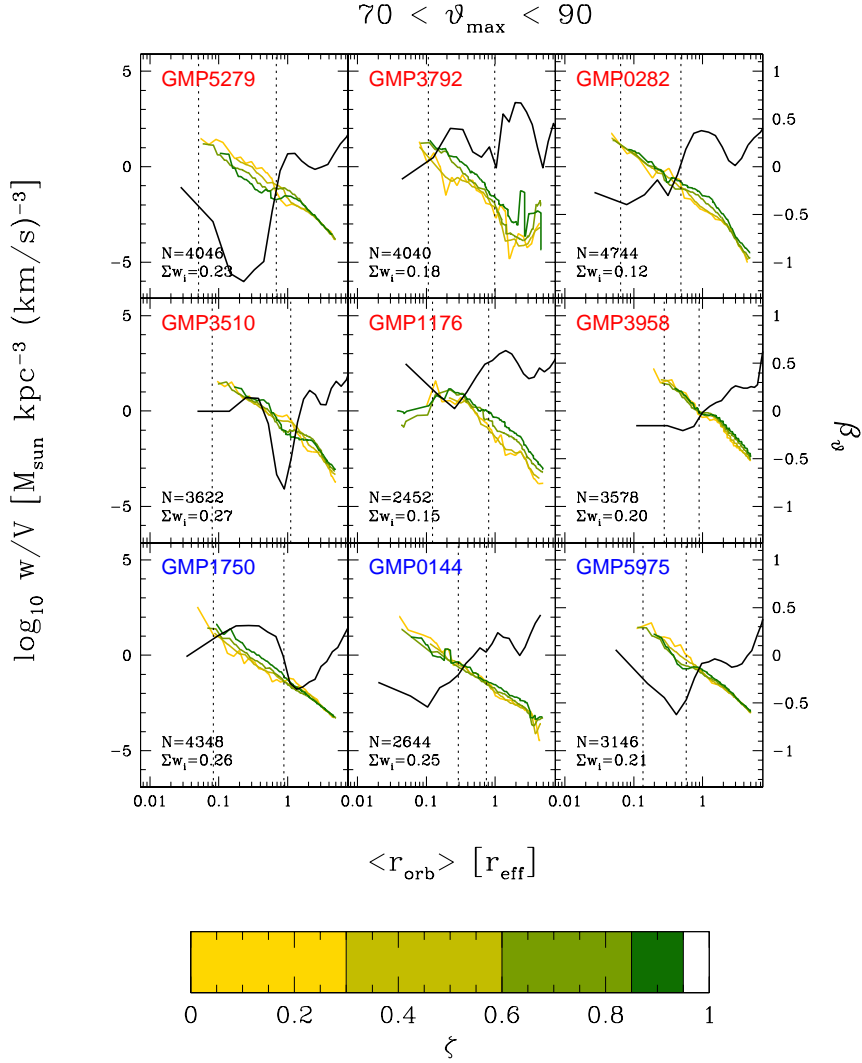


Figure 6.6: Average polar distribution function versus $\langle r_{\text{orb}} \rangle$. Orbits are arranged in radiality bins from shell orbits (low ζ , yellow) to radial orbits (large ζ , green). Over-plotted in black: meridional anisotropy β_{ϑ} along the minor-axis (scale on the right). In each panel the total number N of involved orbits and the fraction of light $\sum w_i$ they carry is quoted.

only orbits with vanishing angular momentum can reach the symmetry axis and the local DF there depends only on the two remaining integrals E and I_3 . The dependency of the DF on E is documented in Fig. 6.6 by the dependency of the smoothed DF on $\langle r_{\text{orb}} \rangle$, which is roughly equivalent to the orbital energy (cf.

App. C). The remaining part of the DF can be extracted by plotting phase-densities for orbit subsets binned in I_3 . As I_3 is not known explicitly, orbits are binned with respect to their radiality ζ (cf. App. C) in Fig. 6.6.

According to the approximate 2I-character of the local DF around the symmetry axis, the anisotropy at a given radius on the minor-axis can be expected to be directly related to the dependency of the DF on I_3 (or ζ , respectively). The latter, in turn, translates into a separation of the phase-density profiles of different orbit bins in Fig. 6.6. The velocity anisotropy β_θ is over-plotted in Fig. 6.6 for comparison (scale on the right). The ζ -bin $[0.95, 1]$, containing the most radial orbits, is omitted in Fig. 6.6, because it is contaminated by orbits with low pericentre distances r_{peri} that reach their maximum latitude ϑ_{max} close to r_{peri} but do not linger in polar bins outside the centre.

As expected, galaxies with strong tangential anisotropy (GMP5279, GMP3510 and GMP5975) are characterised by an over-density of radially confined orbits (low ζ) relative to radially floating orbits (large ζ). Likewise, radially anisotropic objects like GMP1750 or GMP0282 have enhanced phase-densities of radial polar orbits. Furthermore, gradual changes in the velocity anisotropy profiles revealed by Figs. 6.3 and 6.4 result from shell orbits (low ζ) and radial polar orbits following distinct radial distributions. For example, over the kinematically sampled radial regions in GMP5279 or GMP5975 the shell orbits exhibit a shallower radial decrease than the radial orbits. Other systems like GMP0282 and GMP3510 do not show a gradual change in velocity anisotropy. Instead they separate in regions that seem kinematically different: an isotropic inner region ($\lesssim 0.5 r_{\text{eff}}$) and anisotropic outlets. Taking GMP0282 exemplary, its radial polar orbits smoothly decrease from the inner to the outer parts while the distribution of shell orbits exhibits a break, located around the outermost data point. The situation is similar in GMP3510, albeit the roles of shell and radial orbits in the outer parts have flipped.

By the close relationship between H_4 and velocity anisotropy (cf. Fig. 6.5) most of the structure in the DF is a result of the minor-axis H_4 -profiles. To check, whether these just reflect structural differences in the luminosity profile or contain independent information about the internal kinematics, Fig. 6.7 shows the best-fit DF of Fig. 6.6 normalised to the maximum entropy DF f_S ($\alpha = 0$, cf. Sec. 6.2.2). A galaxy in a maximum entropy state should show up with $\log(f/f_S) \equiv 0$ in Fig. 6.7. For orbits that are not significantly constrained by observations, regularisation implies $f \approx f_S$, as well.

The latter is most likely responsible for all DFs converging with the maximum entropy distributions in the outer parts that are not covered by kinematical observations. However, in the data-covered inner regions, the radial and tangential anisotropies require deviations from maximum entropy. As could have been expected, the relation between H_4 and anisotropy is therefore not driven by the luminosity profiles.

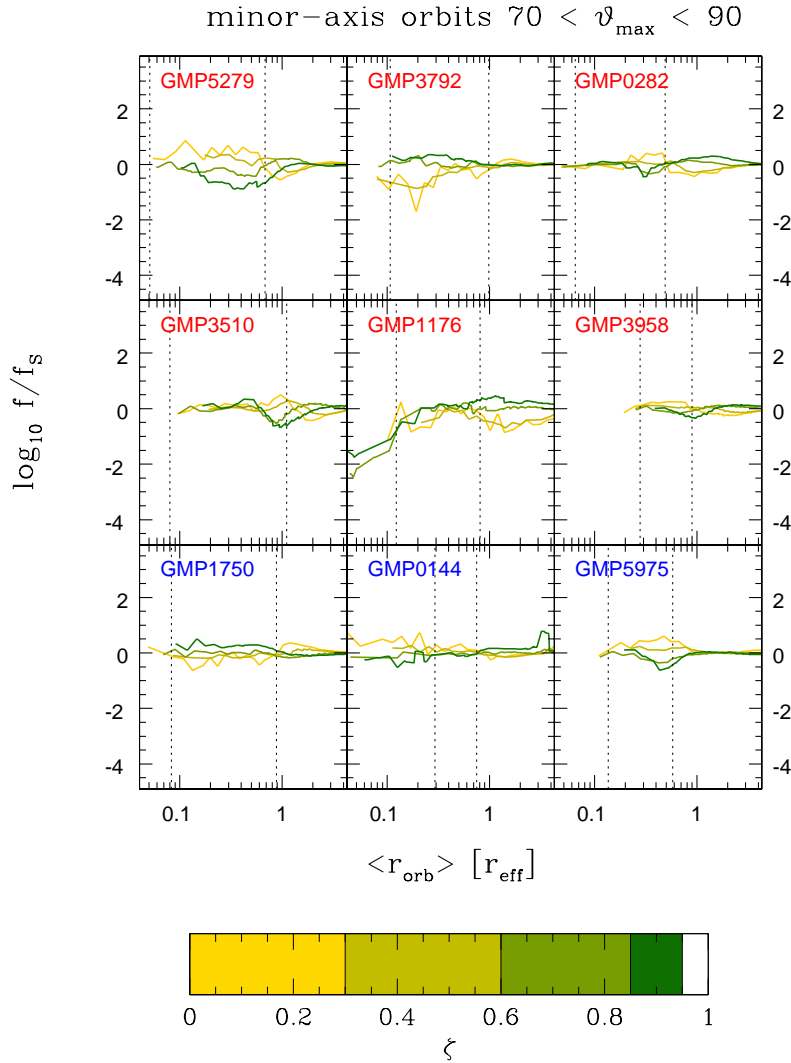


Figure 6.7: Difference between best-fit model DF $f = \log(w/V)$ and corresponding maximum entropy DF f_s .

6.4 The bulk of stars at intermediate latitudes

According to the last section, the orbital distribution around the short-axis is closely coupled to the observed H_4 . By projection, orbits with lower ϑ_{\max} contribute to the minor-axis LOSVDs as well. The present section is aimed to investigate in how far these orbits are constrained by the observations. To this end Fig. 6.8 repeats Fig. 6.6, but for orbits at intermediate latitudes $30^\circ < \vartheta_{\max} < 70^\circ$.

The distribution of orbits at intermediate latitudes in Fig. 6.8 is much smoother than in Fig. 6.6. Most systems appear slightly radial in the sense that orbits with large ζ owe the highest phase-densities. In GMP1750, this trend continues the orbital distribution around the minor-axis. But in the three galaxies with strong minor-axis anisotropy (GMP5279, GMP3510 and GMP5975) it implies a sudden change in the orbital structure between the poles and intermediate latitudes. Considering the differential DF in Fig. 6.9 (the analog to Fig. 6.7), the DFs of Fig. 6.9 differ not much from maximum entropy functions. This can be read in two ways. Either, the system of intermediate orbits has higher entropy, or alternatively, it is less constrained by the data. The second variant seems more plausible for two reasons. Firstly, all orbits involved in Fig. 6.8 spent most of their time in regions not covered by kinematical data. Second, as will be discussed in the next section, in both neighbouring regions (along the poles as well as along the equator) the orbital system deviates from maximum entropy. It would be hard to understand why, in every case, it is more entropic in between.

6.5 Local dynamical structure around the equatorial plane

6.5.1 Velocity anisotropy

Velocity anisotropy profiles in the equatorial plane are shown in Figs. 6.10 and 6.11. In contrast to Figs. 6.3 and 6.4 axial symmetry does not imply any relationship between β_φ and β_ϑ at low latitudes.

Meridional anisotropy. Contrasting the situation around the poles, no galaxy exhibits tangential anisotropy $\beta_\vartheta < 0$. The only exception is the central region of GMP1176, where negative β_ϑ and β_φ imply $\sigma_r < \sigma_\varphi, \sigma_\vartheta$. The low radial dispersion may be an artifact of the unresolved central light profile and the resulting extended flat density core (cf. Fig. 5.12). Better resolved photometry is needed to clarify this issue. Apart from GMP1176, the lack of tangential anisotropy reflects the relation between flattening and meridional anisotropy discussed in Sec. 6.2.

Azimuthal anisotropy. More diversity is offered by azimuthal velocities. In GMP3792, for example, the negative β_φ supports the hypothesis that the system may be composed of two flattened subsystems with low overall angular momentum, resulting in large φ -motions. GMP3510, GMP1176, GMP3958 and GMP0144 are relatively isotropic ($\sigma_r \approx \sigma_\varphi$) over the kinematically sampled spatial region. GMP1750, instead, offers $\beta_\vartheta \approx \beta_\varphi > 0$, implying $\sigma_r > \sigma_\varphi, \sigma_\vartheta$ over the kinematically sampled radial region in this system.

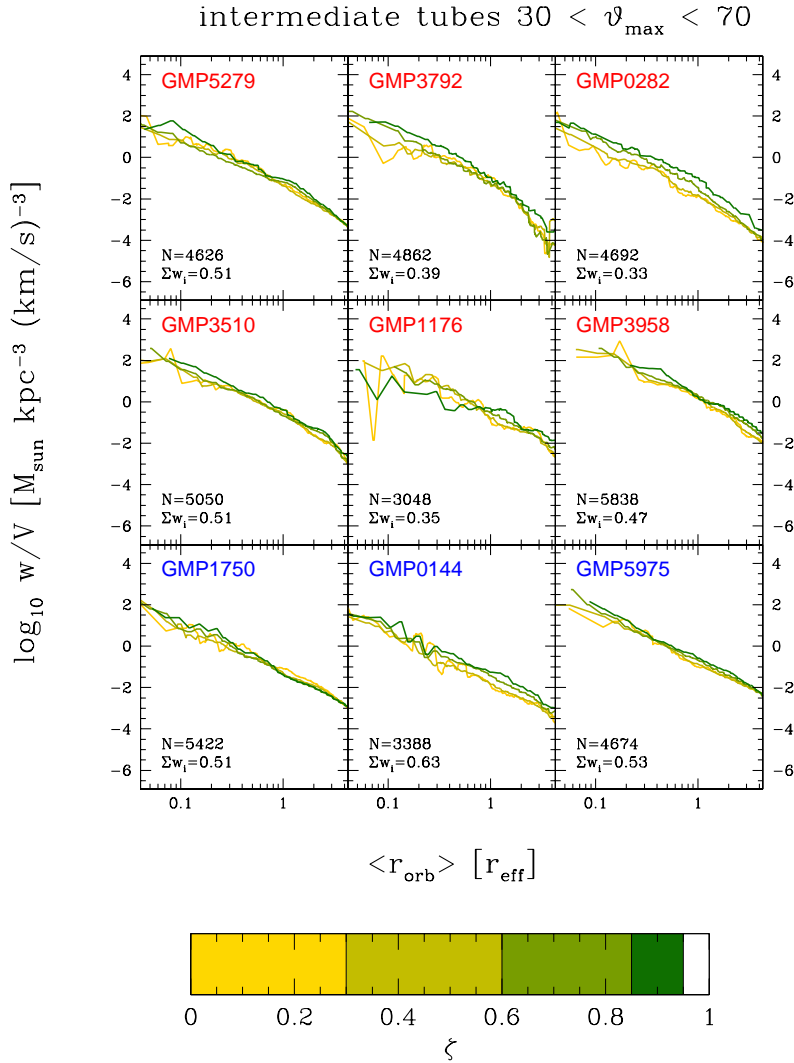


Figure 6.8: As Fig. 6.6, but for orbits at intermediate latitudes $30^\circ < \vartheta_{\max} < 70^\circ$.

6.5.2 The local distribution function

The orbital structure responsible for the anisotropy profiles along the equatorial plane is more complex than around the poles. The reason is that in the potentials considered here all orbits cross the equatorial plane and, thus, all orbits contribute to the anisotropy there. The local DF therefore depends on all three integrals. On the other side, the close relation between minor-axis H_4 and the distribution of polar orbits discussed in Sec. 6.3 implies that the minor-axis

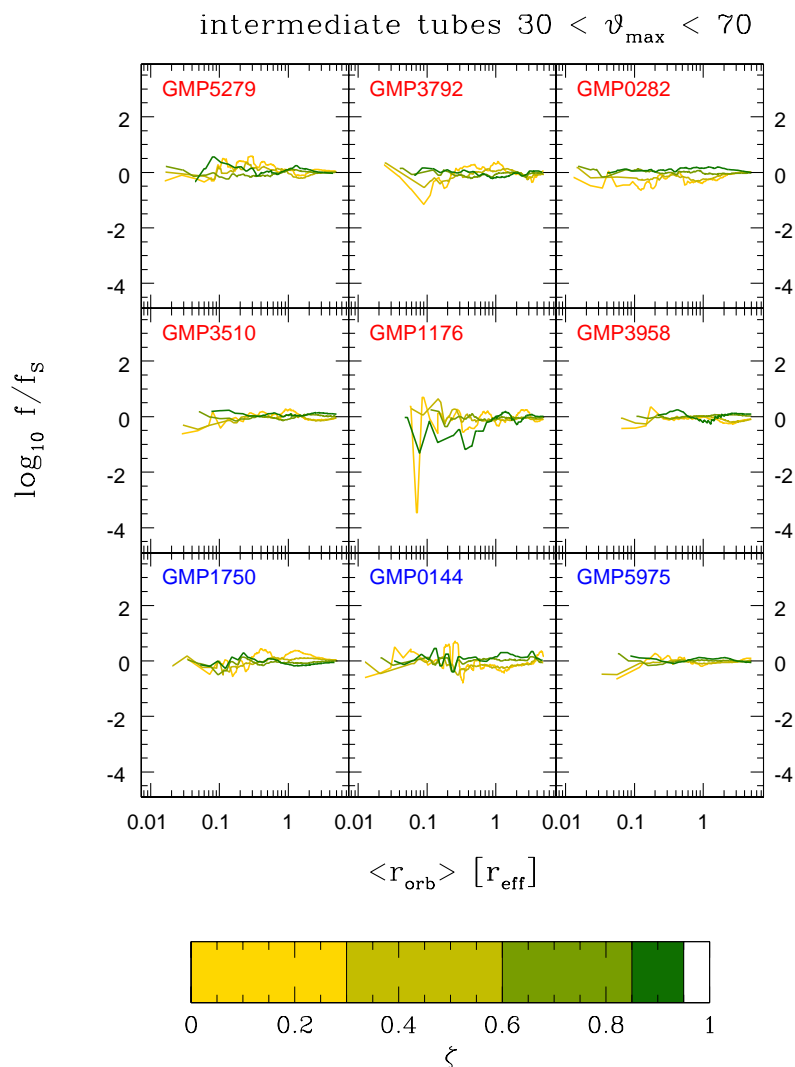


Figure 6.9: As Fig. 6.7, but for the orbits of Fig. 6.8.

orbits are little affected by the major-axis observations. The smoothness and maximum-entropy fashion of the orbital distribution at intermediate latitudes likewise implies that it is little influenced by the major-axis data (cf. Sec. 6.4). Both considerations are plausible in view of the fact that the corresponding orbits cross the equatorial plane with large orthogonal velocities, spent little time there and contribute accordingly little light to the major-axis LOSVDs. In turn then, these LOSVDs do not put tight constraints on their phase-densities.

The major-axis data therefore mostly constrains orbits that do not extend

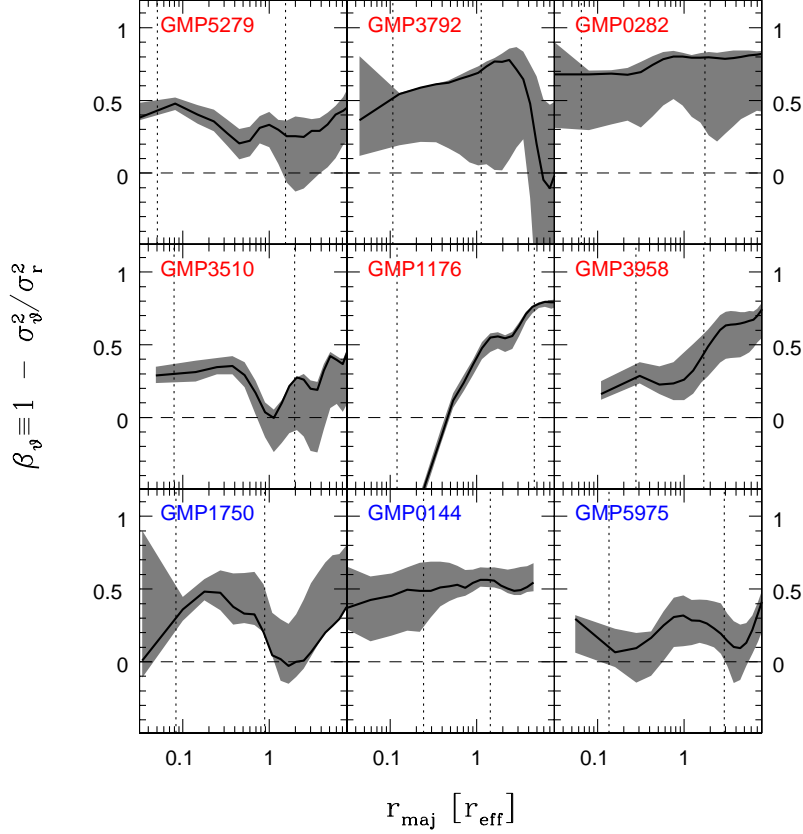


Figure 6.10: As Fig. 6.3, but for the major axis.

much above the equatorial plane (low z_{\max} ; cf. App. C for an exact definition of z_{\max}). Orbits become planar in the limit $z_{\max} \rightarrow 0$ and the local DF of these, constrained, orbits depends only on energy and angular momentum, or $\langle r_{\text{orb}} \rangle$ and ζ , respectively. This limit should be kept in mind when interpreting Fig. 6.12 that shows the local DF around the equatorial plane. It is analogous to Figs. 6.6 and 6.8, but only orbits entirely covered by the major-axis slit (in the vertical direction) are considered. Let the major-axis slit-width be w , then all orbits with $z_{\max} < w/2$ are included in Fig. 6.12. These orbits are shortly referred to as equatorial orbits or major-axis orbits below. In Fig. 6.12 orbits are binned with respect to ζ . Circular orbits have $\zeta \rightarrow 0$ and are plotted in blue (prograde) and red (retrograde). Radially floating orbits correspond to $\zeta \rightarrow 1$ and are plotted light blue (prograde) and light red (retrograde).

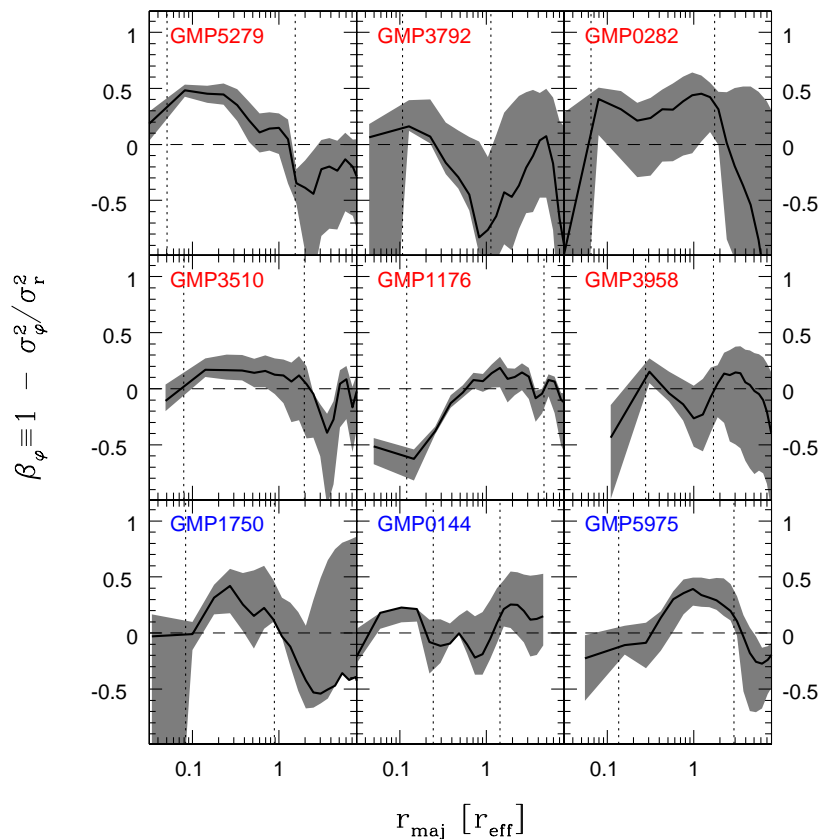


Figure 6.11: As Fig. 6.4, but for the major axis.

Rotating galaxies. Necessarily, rotating galaxies (GMP0282, GMP3510, GMP3958, GMP1176 and GMP5975) have angular momentum gradients in their DFs. In the Coma sample these tend to increase with radius. Mostly, because retrograde circular orbits are strongly suppressed towards the outer parts. GMP3958 is an exceptional case, as in this galaxy retrograde orbits follow a power-law like distribution up to the outermost data points. In GMP1176 and GMP3958 the radial phase-density profiles of prograde circular orbits form a plateau of roughly constant phase-density ($\log f \approx 1$) and the dominant orbits are circular.

The other three rotating galaxies lack of a comparable plateau and are not clearly dominated by circular orbits. These only occasionally exceed the densities in radial orbits (GMP3510 around $1.5 r_{\text{eff}}$, GMP5975 around $0.8 r_{\text{eff}}$) or are continuously populated on a lower level (outer parts of GMP0282).

Non-rotating galaxies. In the most luminous objects GMP5279 and GMP1750 circular orbits are suppressed. In GMP5279, only the prograde component reaches the level of radial orbits but only around $0.3 r_{\text{eff}}$, a region with a weak rotational signal (cf. Fig. 4.1). Similar, in GMP1750 around $r_{\text{eff}}/2$ a local circular orbit enhancement occurs with a weak rotational signal. Overall, both galaxies are dominated by radial orbits, with little difference between prograde and retrograde specimen. GMP3792 appears homogeneous with respect to ζ on the major-axis. The structure of GMP0144 is uncertain as its central parts lack of axial symmetry.

For the sake of completeness Fig. 6.13 shows the differential DF corresponding to Fig. 6.12 (analogously to Figs. 6.7 and 6.9). Since maximum entropy enforces equal densities on the prograde and retrograde specimen of each orbit any rotation causes a deviation from the regularisation prior. Thereby it is clear from Fig. 6.13 that these deviations are much larger along the equatorial plane than anywhere else in the models.

The distribution of major-axis orbits in GMP3792 is compatible with maximum entropy and the same holds for the central regions of the rotating systems GMP0282, GMP3510, GMP3958 and GMP5975. The dominance of circular orbits in GMP1176 implies low entropy, while rotation in GMP0282 and GMP5975 is different and less deviant from maximum entropy. The depression of circular orbits in GMP5279 and GMP1750 is not compatible with maximum entropy at all.

Apart from the obvious fact that certain angular momentum gradients are caused by rotation it is difficult to qualify what drives the orbital DFs around the equatorial plane. For example, no correlation between H_4 and velocity anisotropy is found as can be drawn from Fig. 6.14, the equatorial counterpart of Fig. 6.5.

The only loose connection recovered is between the steep drop of retrograde orbits in GMP0282, GMP3510, GMP1176 and GMP5975 and H_3 . To illustrate this, Fig. 6.15 shows the phase-densities of the most circular and most radial, respectively, prograde and retrograde equatorial orbits of Fig. 6.12. Over-plotted is the H_3 -profile (scale on the right). In the rotating systems positive¹ H_3 occurs whenever (1) retrograde orbits are strongly underpopulated and (2) radial prograde orbits roughly level with circular orbits. In the only rotating system that is not affected from the retrograde orbit suppression (GMP3958) H_3 is negative and rotation is mostly maintained by near circular orbits. Noteworthy, the depopulation of retrograde orbits is restricted to the outer regions (beyond r_{eff}) in each case.

6.5.3 The vertical structure

To complete the analysis of orbits around the major-axis, Fig. 6.16 shows the vertical structure of the DF. Orbits are binned with respect to their vertical

¹Note that the observed rotation is always scaled positive. Thus, positive H_3 are (positively) correlated with v , while negative are anti-correlated. Inside the effective radius H_3 and v are anti-correlated in most ellipticals (Bender, Saglia & Gerhard 1994).

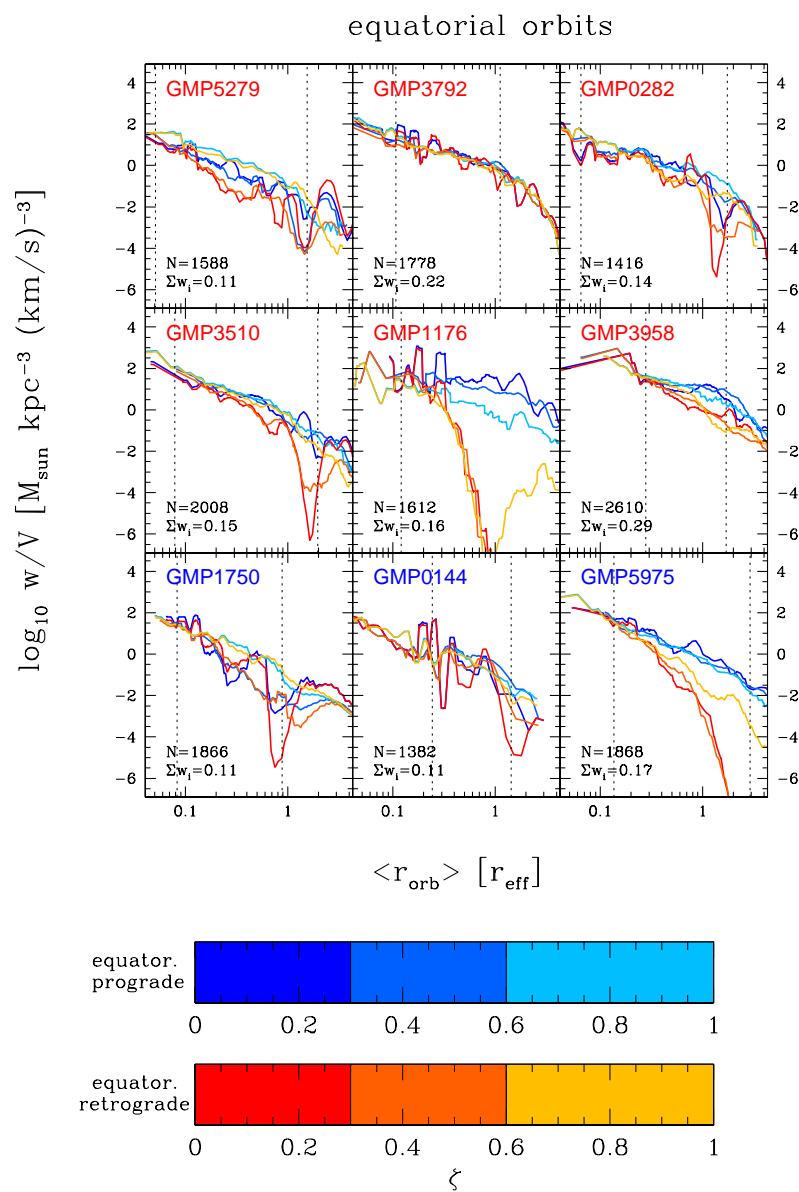


Figure 6.12: As Fig. 6.6, but for orbits entirely covered by the major-axis slit. Prograde orbits are plotted in blue colours, retrograde orbits in red colours (cf. colour bar).

extension in slices of $\Delta z_{\text{max}} = 0.2 r_{\text{eff}}$. As in previous figures, prograde and retrograde orbits are plotted in blue and red colours, respectively.

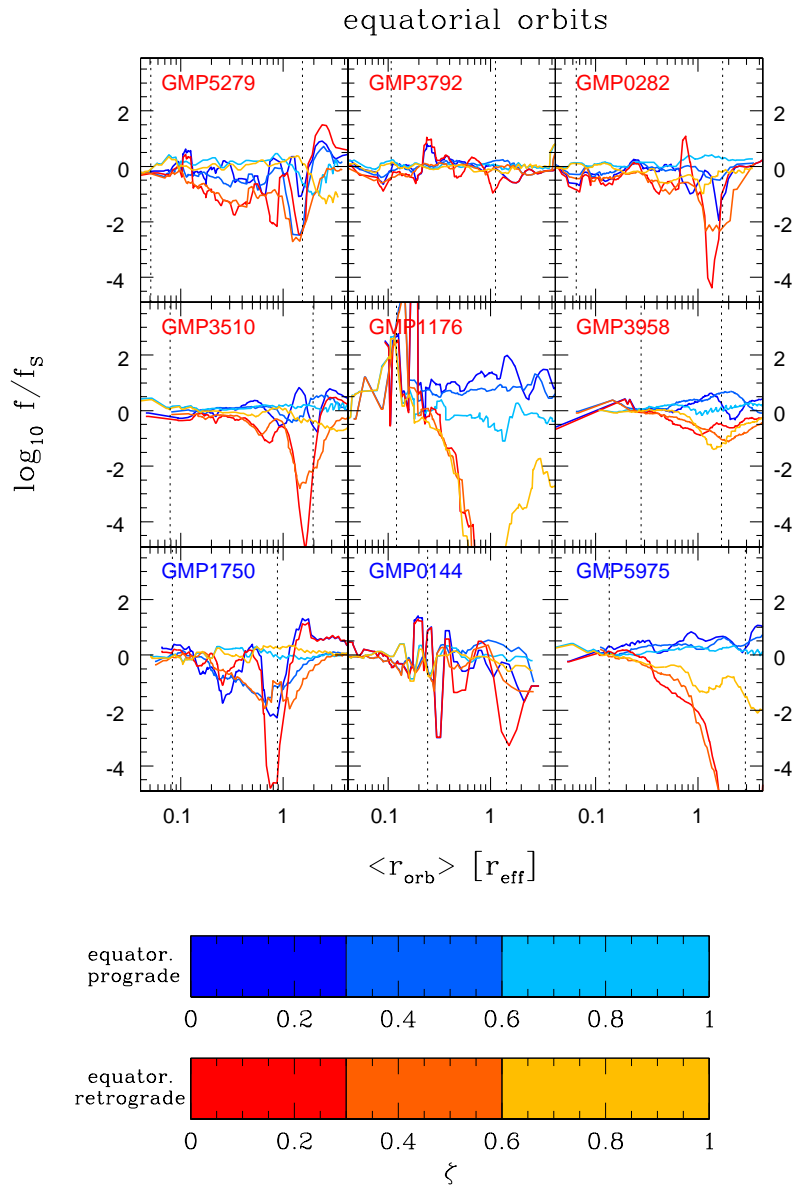


Figure 6.13: As Fig. 6.7, but for the orbits of Fig. 6.12.

From the figure it can be seen that the vertical structure of the orbital systems varies, especially among the rotating galaxies. For example, GMP3958, the galaxy that lacks the depression of retrograde orbits, is characterised by a thin rotating structure where orbits closest to the equatorial plane are populated

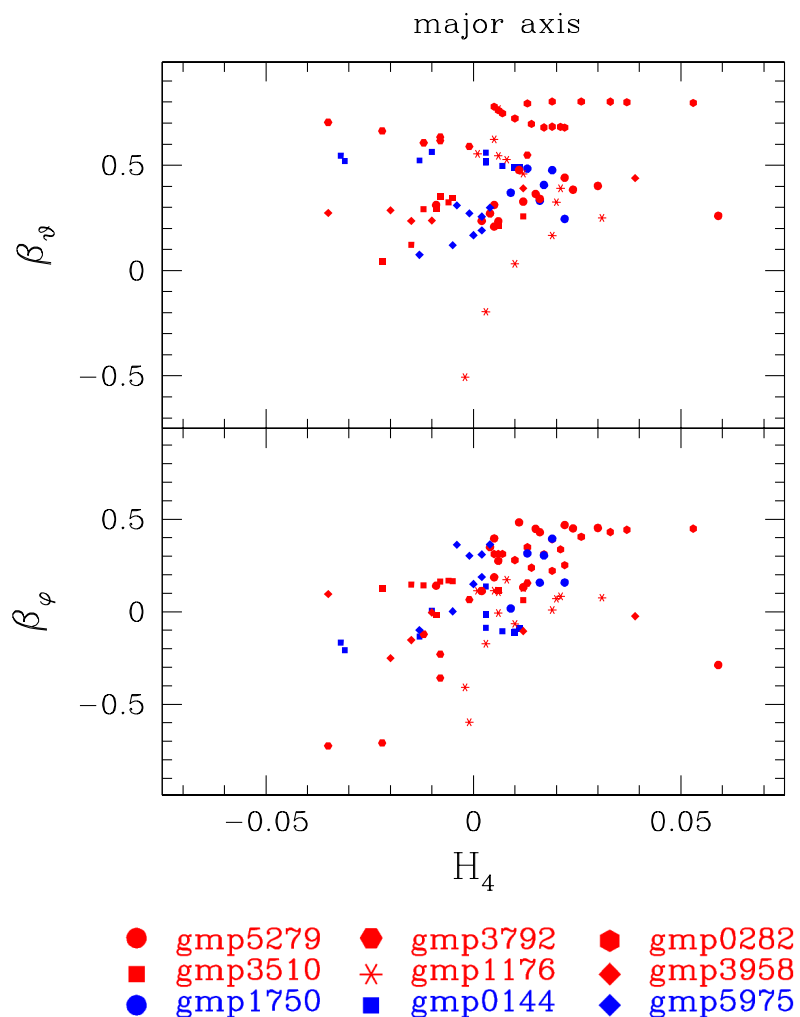


Figure 6.14: As Fig. 6.5, but for the major-axis.

strongest. This configuration extends up to the outermost data-point. Completely different is GMP5975. While up to r_{eff} the galaxy is as well characterised by a thin rotating component the over-density in the lowest z -bin disappears towards larger radii. There, instead, orbits with higher vertical extension carry most of the phase-density. The transition from the inner, thin to the outer, thick rotation structure spatially coincides with the onset of boxiness in the galaxy's outer parts (cf. Fig. 4.9).

The phase-densities of prograde orbits in GMP3958 and GMP1176 decrease with z . However, concerning retrograde orbits, GMP1176 resembles GMP5975 in that this trend is reversed and phase-densities decrease towards the equator.

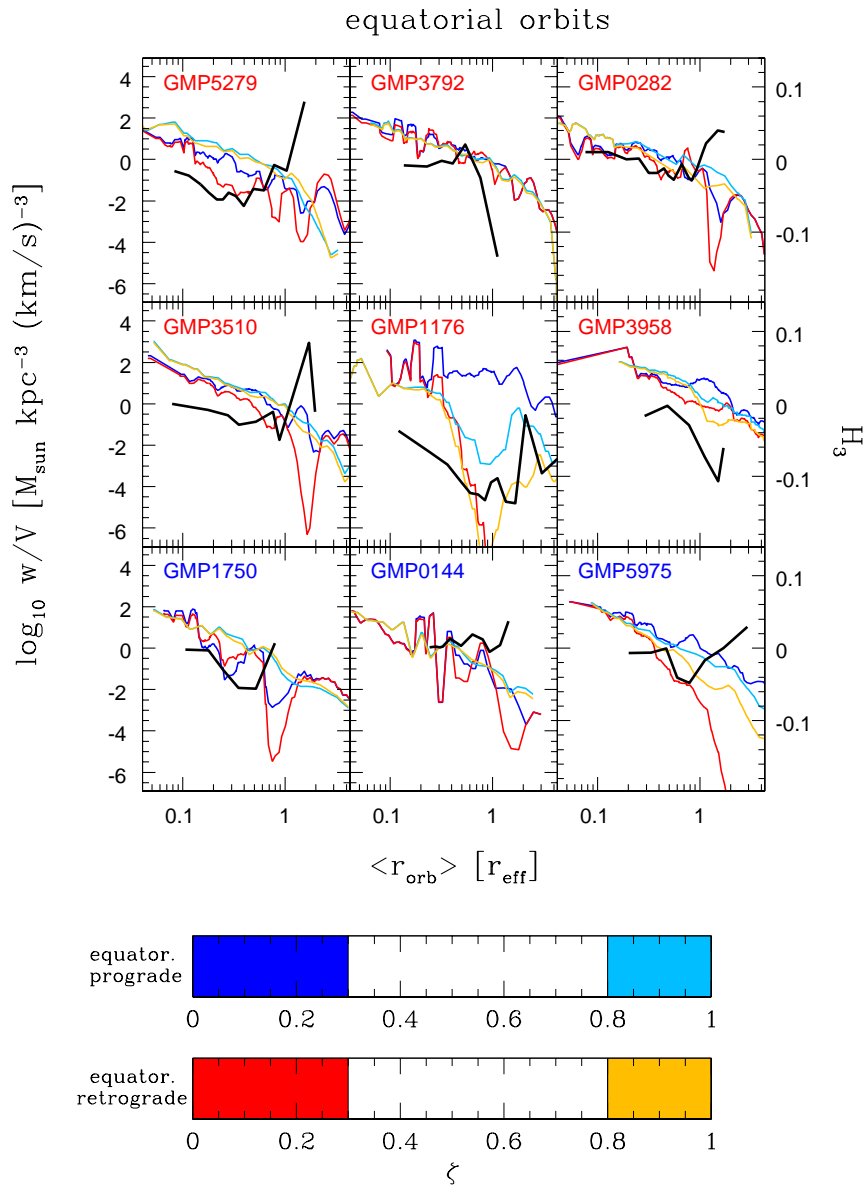


Figure 6.15: As Fig. 6.12, but only the most circular prograde and retrograde orbits are considered. Over-plotted to the orbital phase-densities is the observed major-axis H_3 (black, scale on the right).

In GMP3958 the phase-densities of retrograde orbits do not change much with z .

Non-rotating galaxies are mostly featureless with respect to z (the case of GMP0144 is uncertain due to the lack of axial symmetry in the centre). However, GMP3792 is dominated by orbits close to the equatorial plane.

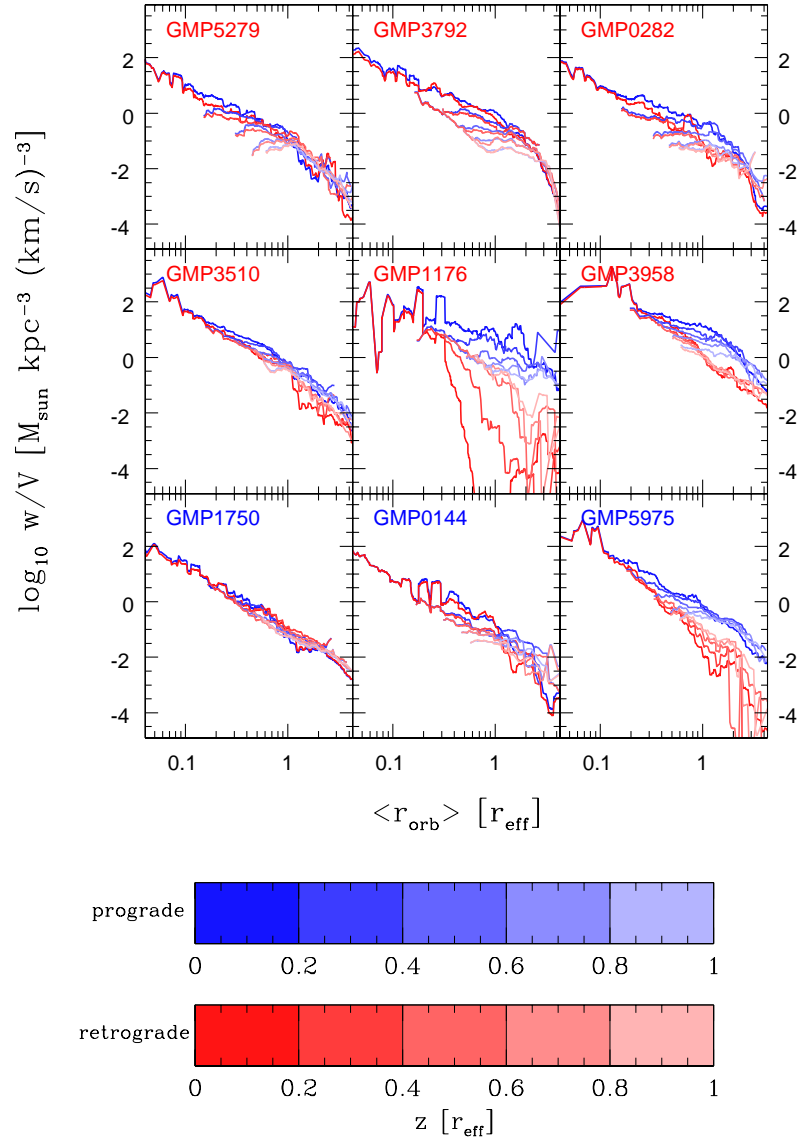


Figure 6.16: As Fig. 6.12, but orbits are binned in z_{max} from $z_{\text{max}} = 0$ to $z_{\text{max}} = r_{\text{eff}}$ in bins of $\Delta z_{\text{max}} = 0.2$. Blue/red colours distinguish prograde/retrograde orbits (averaged about the angular momentum).

6.6 Discussion of the dynamical structure

Analysis of the local DFs of orbits around the equatorial plane and around the poles, where the observations at hand constrain the orbits best, has recovered a wealth of disparate structures. The present section is aimed to interpret these in terms of the global dynamical composition of the systems. To this end, Fig. 6.17 combines the DFs of Figs. 6.6 and 6.12, respectively. For the sake of clarity only the radially most extended and radially most confined orbits of Fig. 6.6 are shown (and referred to as radial polar orbits and shell orbits in the following). The equatorial orbits (shortly disk orbits) are binned in each two prograde and two retrograde families, a more circular one ($\zeta < 0.5$, in following just circular orbits) and a more radial one ($\zeta > 0.5$, in following just radial orbits).

GMP5279. GMP5279 is one of the galaxies with strong minor-axis anisotropy. As Fig. 6.17 reveals, the responsible phase-space structure along the short-axis has a correspondent along the equator: the distribution of shell orbits in the inner parts ($r \lesssim r_{\text{eff}}/2$) resembles the distribution of radial orbits along the equator. At the same time, the distribution of radial polar orbits coincides with retrograde, circular disk orbits. Such coincidences of orbital distributions are interesting, because the involved orbits are constrained by completely independent data sets. One may speculate that spatially separated orbital families that share the same DF behaviour have a common origin. Vice versa, distinctly different phase-space profiles may indicate distinct assembly mechanisms for other orbit families.

GMP3792. An example for a system that may be composed of two components, one spheroidal and one equatorial, is GMP3792. Both, the equatorial as well as the polar orbits follow similar, but distinct radial density distributions. Thereby, the equatorial component dominates over most of the radial range. This confirms the conjecture that the system may be composed of two counter-rotating flat structures. On top of these, Fig. 6.17 reveals a faint background spheroidal component. However, the lack of any ζ -gradient in the equatorial component (or angular momentum gradient, respectively) and its rather maximum-entropy like fashion lets the equatorial component appear as a homogeneous entity. Maybe the galaxy is such inclined, that any intrinsic angular-momentum gradient is washed out by projection. It could also be, that the equatorial structure is not a two component system, but a relaxed, highly flattened dynamical entity.

GMP0282. The orbital distribution of GMP0282 is hard to interpret. Nearly all orbital subclasses exhibit small-scale structures in terms of local density-enhancements (most prominently the peak in the retrograde near circular orbits around $\approx 0.6 r_{\text{eff}}$). Interesting in this object, that the outer rotation is not

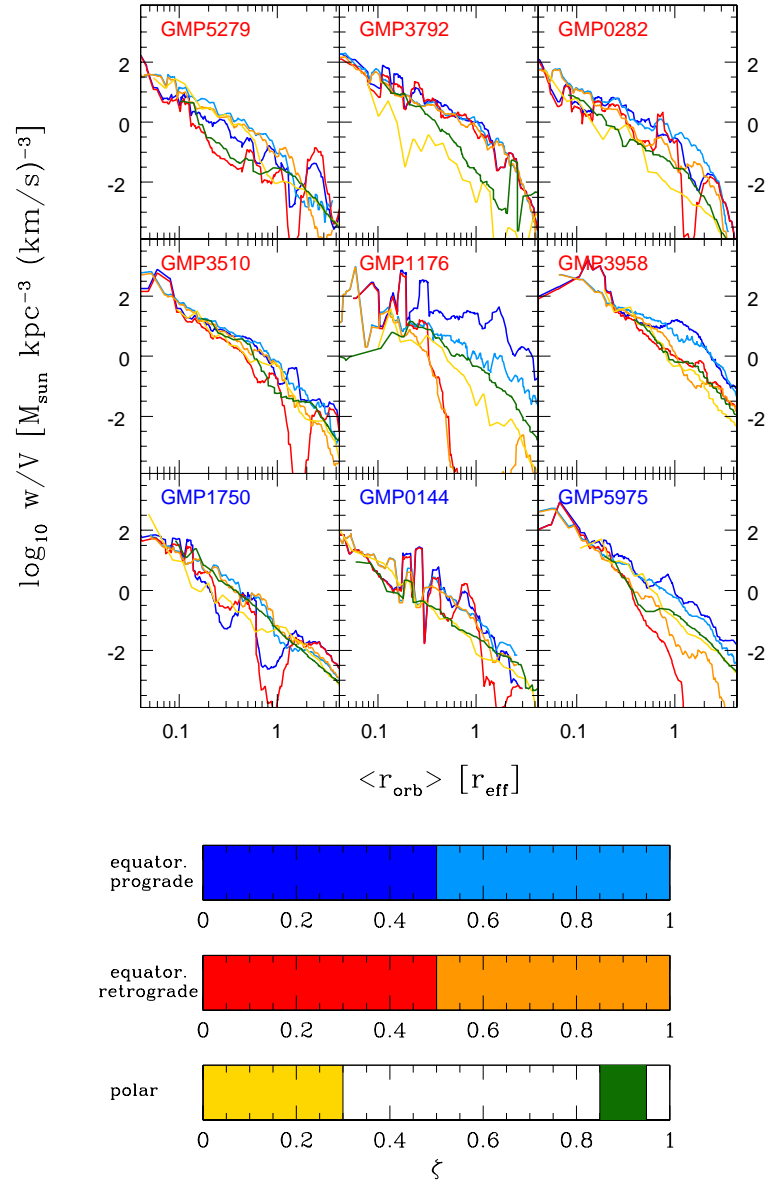


Figure 6.17: Combination of Figs. 6.6 and 6.12. Orbital binning as specified in the colour bars.

supported by the most circular orbits but by an over-density of orbits that are radially extended.

GMP3510. GMP3510 offers some similarity with GMP5279 in the sense that polar orbits and disk orbits partly follow similar radial distributions. However, in GMP3510 the structure is more complex. In the inner regions the distributions of shell orbits and retrograde circular orbits are similar. Likewise, the distributions of radial polar orbits and prograde disk orbits are similar. Around $r_{\text{eff}}/2$ the radial polar orbits drop as the prograde circular orbits do. Over the same region the shell orbits join with the equatorial orbits and follow their distribution towards larger radii. This transition in the dynamical structure causes the peaks in the anisotropy profiles (cf. Figs. 6.3, 6.4 and 6.10, 6.11). Beyond r_{eff} a radially localised region of high density in prograde circular orbits appears, similar to the feature in the retrograde orbits of GMP0282 around $0.6 r_{\text{eff}}$. This could unravel a ring, but a firm conclusion needs systematic orbit modelling of synthetic templates with known structures. In the region of the hypothetical ring, retrograde circular orbits are effectively missing.

GMP1176. The lenticular GMP1176 is dominated by prograde disk orbits. Most striking is the absence of retrograde orbits beyond $r_{\text{eff}}/2$, which is more pronounced in this galaxy than in GMP3510 and includes retrograde orbits of all shapes. It is hard to imagine how such a selective depression of retrograde orbits could result from a merger or a collapse. On the other hand, if first a bulge-like object forms in a rapid collapse the orbit distribution would be radially anisotropic (van Albada 1982) and circular orbits (both prograde and retrograde) orbits would be less populated. At this stage, the polar orbits could gain their actual phase-space distribution. Later, a relatively quiescent assembly of stars on prograde orbits could bring their phase-densities step by step to their present values without altering the retrograde orbits much. It is not clear, whether such a mechanism could account quantitatively for the structure of GMP1176. In any case one would expect older stars along the minor-axis than along the major-axis. While the stellar ages around the major-axis are indeed low, the case on the minor-axis is ambiguous (cf. Fig. 5.4).

The strong depression of retrograde orbits may also be an artifact in the models to compensate for intrinsic non-axial symmetry in the outer parts. In this case, the DFs cannot be interpreted directly, but first axisymmetric models need to be fit to synthetic triaxial template objects to investigate if and, as the case may be, which orbital configurations are mapped by orbit depressions as, for example, in GMP1176.

GMP3958. A clear-cut case for a two-component system is GMP3958. In this galaxy, polar orbits follow the same radial distribution as retrograde equatorial orbits. The latter are not vertically structured. Prograde equatorial orbits exceed the density of all other orbits. All together this can be interpreted as a system that is composed of a relatively featureless spheroidal component (polar

orbits, retrograde equatorial orbits) on top of which a prograde equatorial component is superimposed (prograde equatorial orbits). The prograde component is thereby relatively thin. According to the dynamical status one may speculate that the spheroidal background has formed before the equatorial rotating component has grown on top of it. This could imply that the system is made of two distinct stellar populations and could explain why SSP models failed for this object.

GMP1750. Little can be said to GMP1750, but that the radial equatorial and polar orbits follow roughly the same distribution. As stated above the galaxy is a candidate (close-to) face-on system, but the model prefers an edge-on configuration. To the expense that circular orbits need to be taken out to account for the overall similarity of the minor and major-axis observations, respectively (this symmetry is broken most effectively by circular and shell orbits). On the other hand, an under-population of circular orbits may result from a collapse, as discussed for GMP1176. Data along more position angles would be valuable for this system.

GMP0144. The orbital structure of GMP0144 is likely affected by the lack of axial symmetry in the centre. It is therefore not further discussed here.

GMP5975. In GMP5975, as in GMP5279 and GMP3510, the distinct distributions of radial polar orbits and shell orbits have correspondents in the prograde and retrograde disk orbits: shell orbits follow prograde equatorial orbits, radial polar orbits follow retrograde equatorial orbits. In the outer parts, retrograde circular orbits lack as in GMP1176, rising the same implications as already discussed there.

Additional remark. In Sec. 5.3 the possibility was discussed that the increase of stellar population ages along the minor-axis of GMP0282, GMP0144 and GMP5975 could imply the presence of a flat, distinct stellar population localised along the major-axis (a young disk, basically). The dynamical analysis supports the view-point taken in Sec. 5.3, that this is likely not the case. The strongest evidence against a distinct equatorial component is provided by GMP5975, where the dominating orbits along the poles (shell orbits) and along the equatorial plane (prograde orbits) follow the same radial distribution. This does not proof, but makes likely, that they share the same origin and carry more or less the same stellar populations. In GMP0282 and GMP0144 the situation is less obvious. In any case, the DFs of GMP0282 and GMP0144 certainly do not show the clear two-component structure as found in GMP3958. The arguments against distinct major and minor-axis stellar populations given for GMP5975 also apply to GMP5279 with its low minor but large major-axis stellar ages.

6.7 Regularisation

In the present section the influence of α on the dynamical structure of the galaxy fits is investigated. To this end Figs. 6.18 and 6.19 show best-fit meridional and azimuthal velocity anisotropies at three representative radii in the best-fit models as a function of α . The figures show that maximum entropy fits ($\alpha \rightarrow 0$) yield isotropy along the minor-axis. Lowering the weight on regularisation constraints increases the amount of anisotropy in the models. There is no specific trend of β with α . Some systems gain more tangential anisotropy with increasing α (e.g. GMP5279), while others become more radial (GMP1176). In most cases the dependency of β on α is monotonic, ensuring that the global quality of a galaxy being tangentially or radially anisotropic does not depend on α . However, the exact degree of anisotropy depends on α .

From Fig. 6.18 it is clear that the relation between anisotropy (α -dependent) and H_4 (α -independent) changes with the amount of regularisation in the models. This is illustrated in Fig. 6.20, which repeats the upper panel of Fig. 6.5 for two different values of α . For comparison the linear fit of Fig. 6.5 is shown by the dashed line. The figure shows that the general effect of lowering regularisation is to increase the scatter about the mean relation. The relation itself is robust against different choices of α . The general conclusion for the polar axis is therefore that no systematic change of the dynamical structure with α is noticeable.

This holds for the major-axis as well. To show this, major-axis velocity anisotropies are plotted in Figs. 6.21 and 6.22 analogously to Figs. 6.18 and 6.19, respectively. In contrast to the minor-axis, there is no object with $\beta_\vartheta = 0$ along the major-axis at $\alpha = 0$. The reason is the relation between intrinsic flattening and meridional anisotropy discussed in Sec. 6.2 together with the lack of apparently round objects in the Coma sample. The figure also reflects the tendency of maximum entropy models to yield $\beta_\varphi \lesssim 0$ (cf. Sec. 6.2). Compared to the minor-axis, the variation of intrinsic velocity anisotropies with α is slightly lower along the equator. Since the trend of β with α is again monotonic in most cases, the general properties of the galaxies (being radially or tangentially anisotropic) are insensitive to the particular choice of α .

The general conclusion of this section is that the dynamical structure of the fits depends stronger on the choice of α than the mass distribution does (cf. Sec. 5.6). Thereby, no clear trend of velocity anisotropies with α is noticeable. The monotonic trend of β with α could rise the suspicion that increasing α does not only amplify the noise in the models, but that low- α models are biased towards isotropy. However, at least the H_4 -anisotropy relation does not change significantly with α . The main effect of larger α is to increase the scatter around the relation.

As a general note of caution, Fig. 6.23 exemplifies the distribution of orbital weights in the best-fit mass-model of GMP5975 for three different α . As can be seen, the model at large α is dominated by a few orbits that carry almost the entire light. All other orbits are essentially missing in the model (only orbits with weights $\log w > -15$ are included in the plot). The model at $\alpha = 0.02$ is

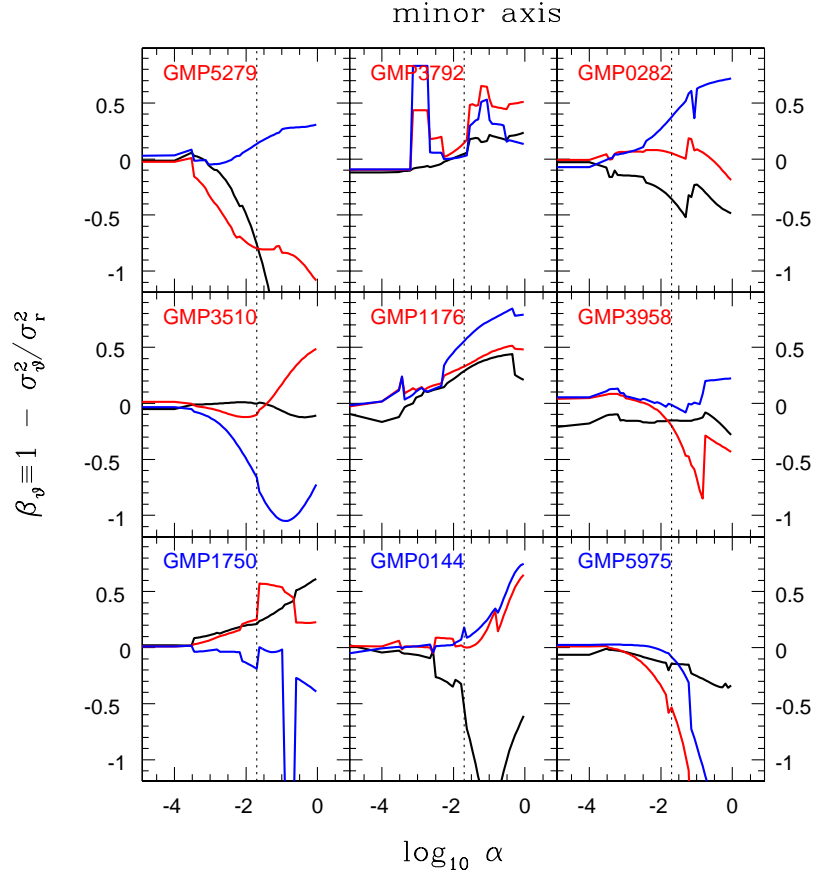


Figure 6.18: Best-fit meridional anisotropy at $0.1 r_{\text{eff}}$ (black), $0.5 r_{\text{eff}}$ (red) and $1.0 r_{\text{eff}}$ (blue) on the minor-axis versus regularisation parameter α . Horizontal dotted lines: $\alpha = 0.02$.

still relatively close to the maximum entropy distribution.

6.8 Summary

The analysis of the dynamical structure of the Coma galaxies has revealed that they are mostly flattened by anisotropy. This is consistent with the systems being globally close to maximum entropy. No system shows the typical anisotropy structure found in cold collapse simulations with an isotropic centre and increasing radial anisotropy towards the outer parts. Instead, the orbital structure around the poles and along the equator, that are best constrained by the data at hand, reveals a wealth of individual structures. Along the poles these are driven

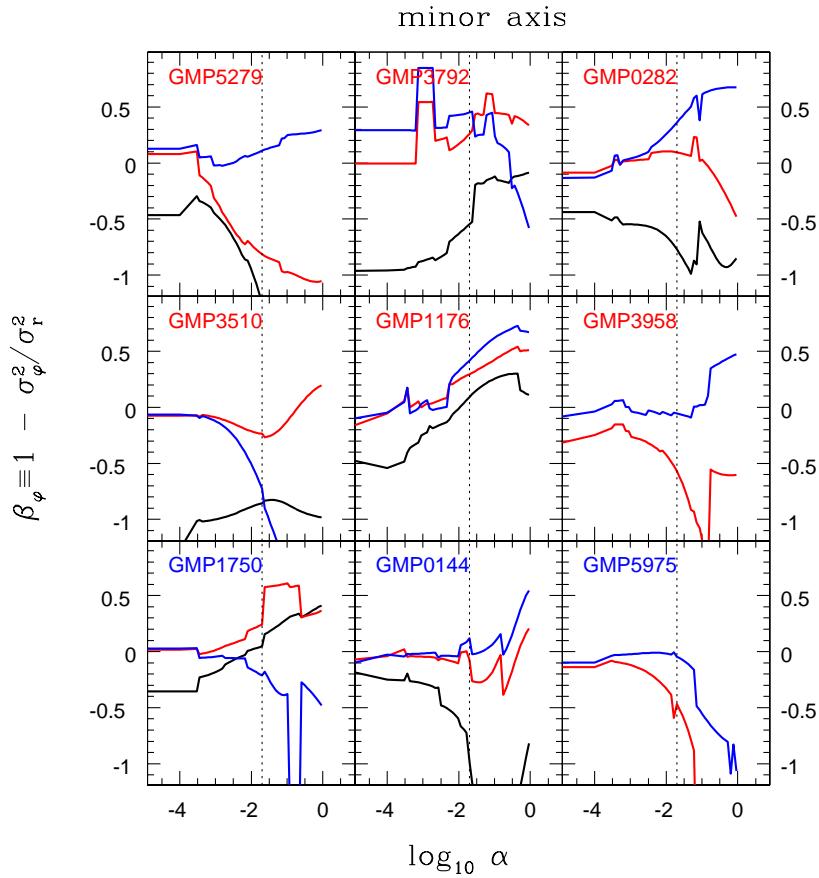


Figure 6.19: As Fig. 6.18, but for azimuthal anisotropy.

by the H_4 observations, which turn out to be closely related to the minor-axis anisotropy. Such a relation could in principle reflect the influence of regularisation. A comparison of the orbital structure along the poles and around the equator – two regions that are constrained from completely independent data sets – recovers several correspondences. These strengthen the significance for the H_4 -anisotropy relation. If it would be just an regularisation artifact, it would be hard to understand why independently constrained orbits share similar distributions. Moreover, the relation is relatively robust against different choices of α , albeit the scatter around it increases at lower regularisation.

Similarity in the phase-space properties of orbits separated in configuration space may possibly suggest a common origin. Together with occasional breaks, peaks and plateaus in the radial profiles of certain orbit families, the phase-space structures of the galaxies may contain important signals of individual

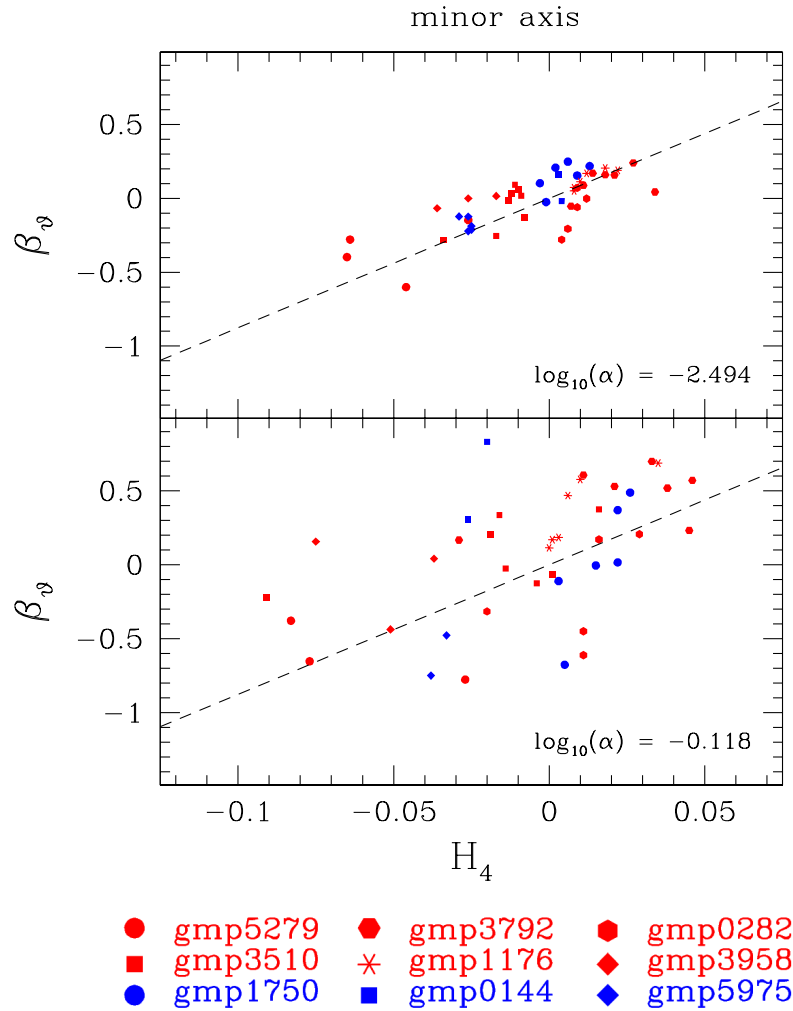


Figure 6.20: As upper panel of Fig. 6.5, but for different values of the regularisation parameter α (indicated in the panels). Dashed: linear fit for $\alpha = 0.02$ (cf. Fig. 6.5).

evolutionary events in their histories. A further interpretation of these phase-space structures requires systematic modelling of elliptical galaxy simulations with a similar modelling approach.

The orbital analysis has confirmed the conclusions on the stellar population analysis drawn in Sec. 5.3 in the sense that no strong kinematical evidence exists for distinct equatorial components. The only exception is GMP3958, where the orbital structure clearly recovers a disk superimposed on a background spheroid. Most gradients of SSP-models do not coincide with obviously distinct dynamical

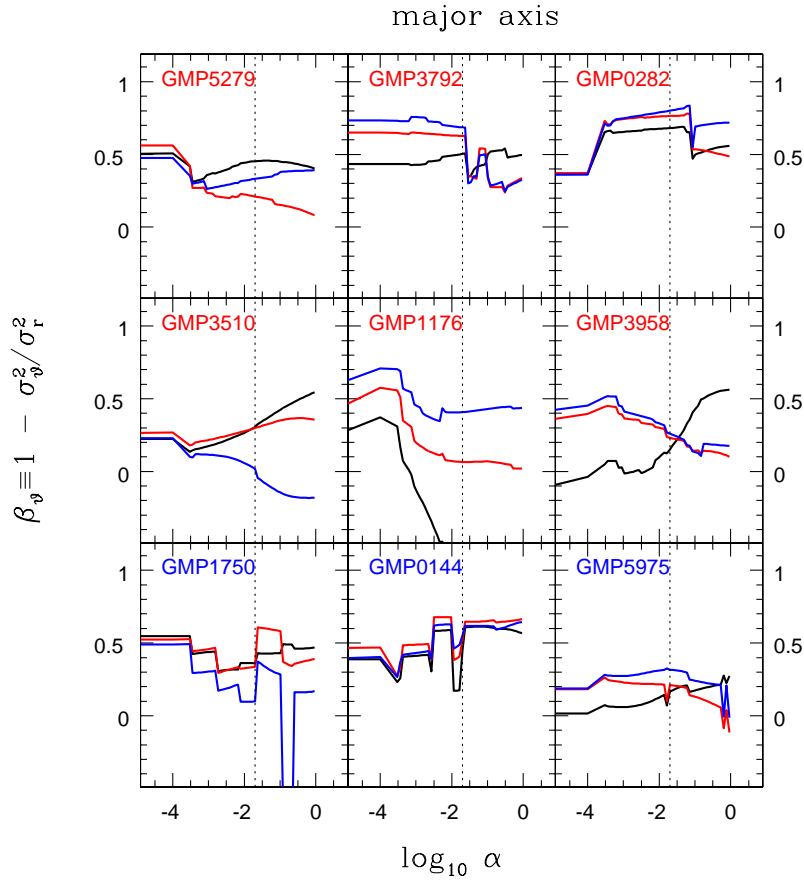


Figure 6.21: As Fig. 6.18 but for the major axis.

cal components in the Coma sample. Possible reasons for a discrepancy could be gas emission driving SSP-gradients (cf. Sec. 5.3) or inadequacies in the dynamical models. If the inclination in the dynamical models is overestimated, for example, the signal of a hypothetical equatorial component could be washed out. On the other hand, gradients in stellar populations could well represent gradual changes instead of component superpositions. Analysis of further galaxies, ideally with data covering the full two-dimensional area of the galaxy on the sky and combined modelling of stellar populations and kinematics may clarify the situation in the future.

Rotation occasionally occurring in the outer parts of some systems is mostly not disk-like and involves a depression of retrograde orbits. The two-component system GMP3958 is the only counterexample. It proves, that the depression of retrograde orbits is not a modelling artifact related to rotation, but is driven

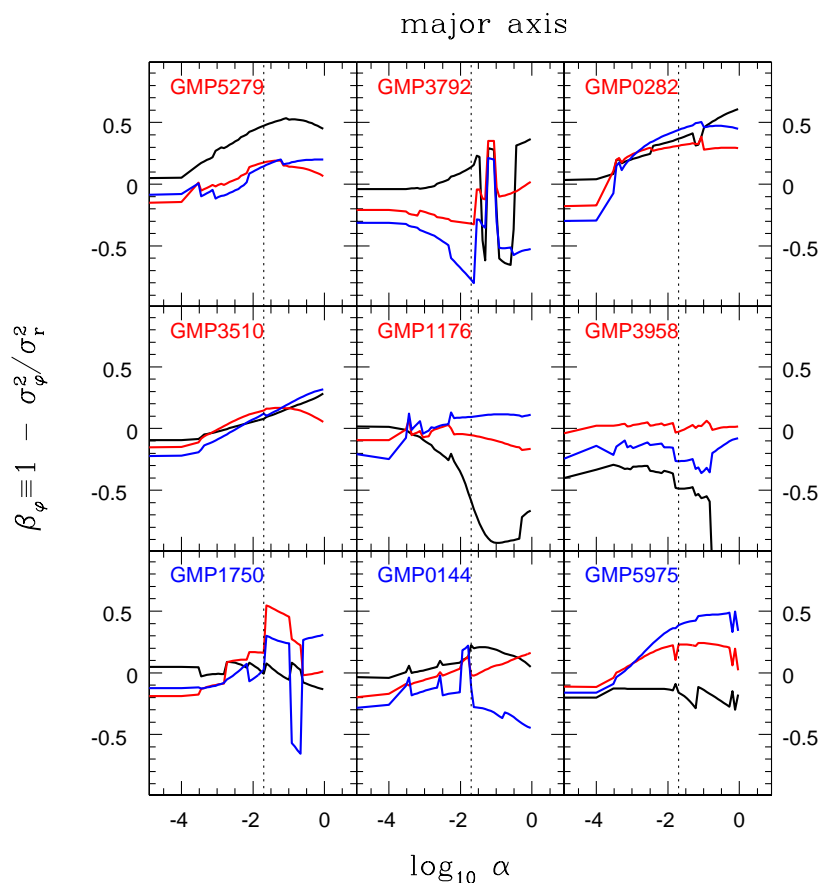


Figure 6.22: As Fig. 6.19 but for the major axis.

by the details of the LOSVDs. Generally, angular momentum gradients become larger, where stars become younger. An increasing diversity in the dynamical structure and the related lower degree of relaxation towards the outer parts could just reflect the longer dynamical time scales in low-density regions. On the other hand, the coincidence of large angular momentum gradients with young stellar ages suggests a recent, dynamically relatively quiescent stellar assembly in the outer parts of some, rotating, systems.

Concerning regularisation, its effect on the dynamical structure is more significant than on the mass distribution. In general the overall quality of a galaxy to be radially or tangentially anisotropy does not depend on the specific weight of regularisation versus data constraints. With increasing α anisotropies become larger, without a systematic preference of tangential or radial anisotropy, however. The H_4 -anisotropy relation is robust against different α , albeit the

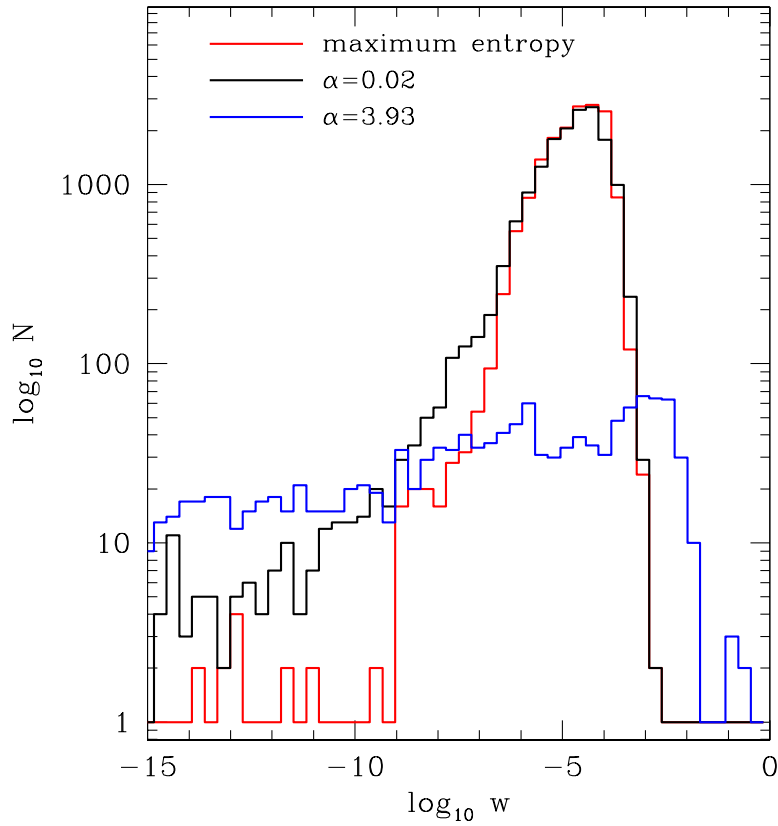


Figure 6.23: Distribution of orbital weights for three differently regularised models in the best-fitting mass distribution of NGC4807. Red: maximum entropy; black: galaxy fit with $\alpha = 0.02$; blue: $\alpha = 3.93$.

scatter around the relation increases with the regularisation parameter.

Chapter 7

Scaling relations

7.1 Outline

In the previous Secs. 5 and 6 the Coma sample galaxies were addressed individually. In the present chapter scaling relations are investigated and compared to other works.

As outlined in the introduction, a directly comparable dynamical study has not yet been undertaken. The three relevant samples to which the results of this work (shortly COMA in the following) are compared to in the remainder of this chapter, are

- **SAURON** The subsample of the SAURON-survey modelled with self-consistent, axisymmetric orbit models (Cappellari et al. 2006)
- **NUKER** The ten ellipticals of Gebhardt et al. (2003) modelled with axisymmetric orbit models
- **ROUND** The 21 round, non-rotating ellipticals with spherical models of Gerhard et al. (2001)

The chapter is organised as follows. Mass-to-light ratios are discussed in Sec. 7.2. The comparison of internal velocity moments is made in Sec. 7.3. In Secs. 7.4, 7.5 and 7.6 the FP-relation, the Tully-Fisher relation for ellipticals and the relation between outer circular velocity and central velocity dispersion are discussed, respectively. Dark matter scaling relations are analysed in Sec. 7.7 and compared to the results of Gerhard et al. (2001).

7.2 Stellar mass-to-light ratios

Stellar mass-to-light ratios of the Coma galaxies are compared to the SAURON, NUKER and ROUND-sample, respectively, in Fig. 7.1. The SAURON-results for the I -band are transformed to B -band using apparent magnitudes m_B from Hyperleđa and the distance modulus of Cappellari et al. (2006). NUKER- Υ_V

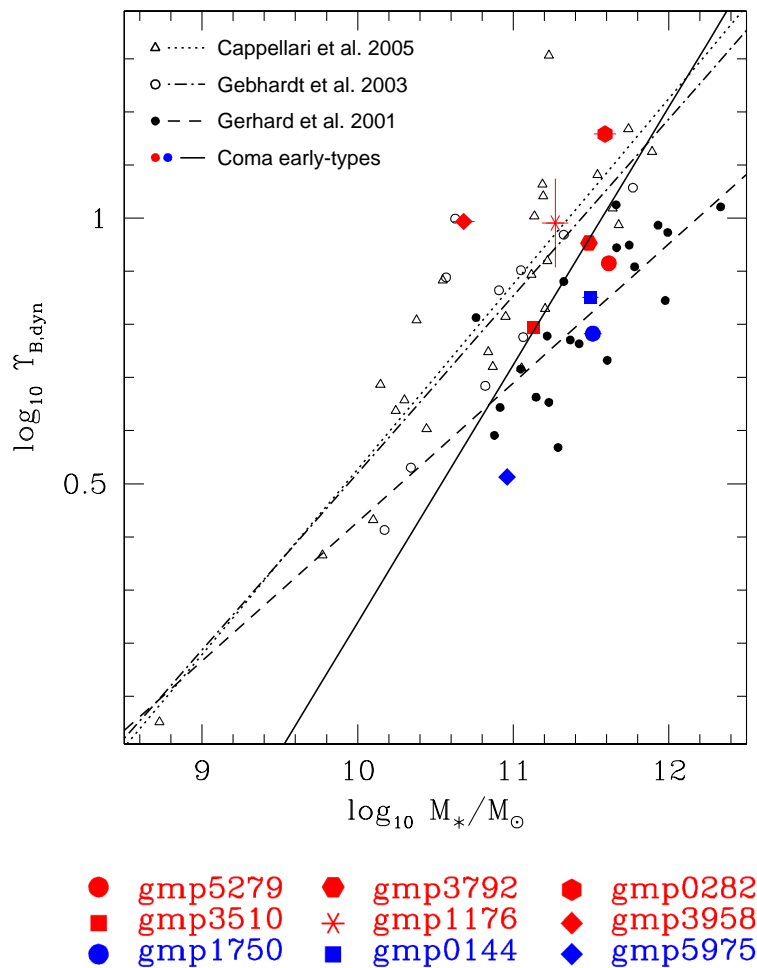


Figure 7.1: Comparison of dynamical mass-to-light ratios. Solid: COMA; dot-dashed: SAURON; short-dashed: ROUND; dotted: NUKER.

are converted to B -band using M_B of Gebhardt et al. (2003) and $B - V$ colours from Hyperleda. Stellar masses are taken from the corresponding literature where given, or are calculated from the luminosity and the stellar mass-to-light ratios.

Inspection of Fig. 7.1 reveals that models based on the assumption that mass-follows-light (SAURON, NUKER) yield larger Υ_{dyn} than those taking into account dark matter explicitly (this work, ROUND). Focussing on the first kind of models, linear fits to the SAURON and the NUKER sample yield almost identical scalings of Υ_{dyn} with M_* (cf. Tab. 7.1). Both samples have been

sample	in Fig. 7.1	m	n
(1)	(2)	(3)	(4)
COMA	solid	0.49 ± 0.06	-4.64 ± 0.67
SAURON	dotted	0.35	-2.96
NUKER	dot-dashed	0.33	-2.81
ROUND	dashed	0.26	-2.19

Table 7.1: Summary of fits in Fig. 7.1. (1,2) sample and appearance in Fig. 7.1; (3,4) linear-fit parameter $\log \Upsilon = m \times \log (M_*/M_\odot) + n$. Fits to the Coma sample have been obtained with “fitexy” of Press et al. (1992), all other fits with “olsq” of Super Mongo.

analysed with similar models, but the SAURON-survey provides integral field kinematics, while the NUKER-sample is based on long-slit data. The similarity of the Υ_{dyn} -scaling suggests that the usage of integral field kinematics does not yield qualitatively different results, which implicitly strengthens the results of this work, that are based on long-slit data.

Regarding models taking into account dark matter, the scaling of Υ_{dyn} in the COMA-sample is steeper, in the ROUND-sample is shallower than in self-consistent models (cf. Tab. 7.1). That both samples provide different scaling relations could be due to the different modelling symmetries or due to low-number statistics. The fact that the COMA and the ROUND-sample yield lower Υ_{dyn} than self-consistent models is not surprising, as Υ_{dyn} in the former only quantifies the luminous fraction of the total mass. This is further illustrated in Fig. 7.2, which is similar to Fig. 7.1 except that total mass-to-light ratios (stellar + dark) are considered, where available (COMA, ROUND). As the linear-fit parameters in Tab. 7.2 proof, the scaling relations of the different samples are now consistent within the errors.

In Fig. 7.1, the distribution of Coma- Υ_{dyn} is closer to the SAURON- Υ_{dyn} in more massive systems. Although the scatter is large and the range of M_* probed in the present sample is relatively narrow, this could indicate that more massive systems are better compatible with the assumption that mass-follows light (within r_{eff}) than lower-mass systems.

sample	in Fig. 7.2	m	n
(1)	(2)	(3)	(4)
COMA	solid	0.38 ± 0.07	-3.24 ± 0.82
SAURON	dotted	0.35	-2.96
NUKER	dot-dashed	0.33	-2.81
ROUND	dashed	0.33	-2.84

Table 7.2: As Tab. 7.1, but for Fig. 7.2.

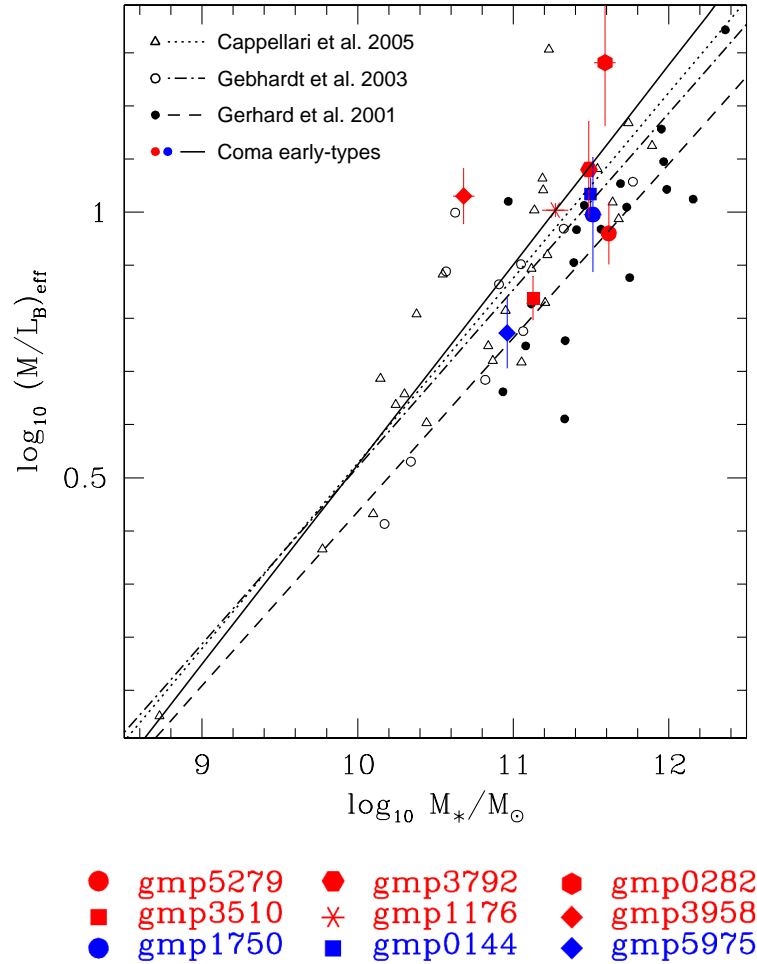


Figure 7.2: As Fig. 7.1, but total (stellar + dark) mass-to-light ratios are considered for the COMA and the ROUND-sample, respectively.

7.3 Orbital anisotropy

The comparison of orbital anisotropies with previous work is split into two parts. Luminosity weighted average orbital anisotropies of the Coma galaxies are compared to the ROUND-sample in Fig. 7.3. Radially averaged anisotropies are compared in Fig. 7.4 additionally to the NUKER-galaxies.

Concerning the comparison with spherical models the bottom panel of Fig. 7.3 reveals on average similar anisotropies in the two samples. However, spherical models have equal anisotropies along every position angle, whereas in axisym-

metric models anisotropies along the major and the minor-axis can differ. According to the upper two panels of Fig. 7.3, the COMA-galaxies are more tangentially anisotropic than the ROUND-models along the minor-axis. Along the major-axis, both samples yield comparable anisotropies. The latter is somewhat surprising in view of the relation between meridional anisotropy and intrinsic flattening revealed by Fig. 6.1. According to this relation one would expect the axisymmetric models to have larger β_ϑ . However, only two objects in the Coma sample are flattened enough to have anisotropies $\langle\beta_\vartheta\rangle \approx 0.5$. One of the two – GMP0282 – is indeed most deviant from the ROUND-galaxies in the upper panel of Fig. 7.3. The other – GMP3792 – is dominated by equatorial orbits of all kinds resulting in large azimuthal motions and, thus, in $\beta_t \approx 0$ (inside r_{eff}). There is no systematic trend of orbital anisotropy with $v_{\text{circ,max}}$. Instead, both samples are compatible with approximate dynamical homology of elliptical galaxies.

Fig. 7.4 extends the comparison to the NUKER-sample. For the latter neither luminosity weighted anisotropies nor maximum circular velocities are available. Therefore, radially averaged velocity anisotropies and absolute B -band magnitudes are used in Fig. 7.4. The comparison is made separately for the major-axis (upper two panels) and the minor-axis (lower two panels). For each axis, it is further split into a comparison of azimuthal and meridional anisotropies, respectively. For comparison, average anisotropies of the ROUND-sample are shown as well.

It is clear from Fig. 7.4 that meridional anisotropies in the NUKER and the COMA-sample are roughly consistent, although the Coma models with $i \neq 90^\circ$ (GMP3792, GMP0282 and GMP0144) yield larger β_ϑ as a result of the relation between β_ϑ and flattening. Both samples have thereby meridional anisotropies consistent with spherical models. On the other hand, the NUKER-models predict significantly larger azimuthal velocities – on both axes – than found in the COMA-sample. This discrepancy could either indicate a real difference between the galaxies in the NUKER and the COMA sample or could be related to differences in the modelling (and the data). The first case cannot be excluded, as the NUKER-ellipticals are on average fainter than the COMA and the ROUND samples.

The second case, especially differences in the modelling approach, could be checked directly by analysing the same galaxy with the different versions of the modelling software. This is beyond the scope of this work. Here, it can only be speculated about possibly relevant issues: (1) the orbit sampling in the NUKER-analysis potentially leaves out shell orbits (cf. Sec. 2.2.3). This could be responsible for the differences between meridional and azimuthal anisotropies in the NUKER-models along the minor-axis. Although it cannot be expected that $\beta_\vartheta = \beta_\varphi$ holds exactly (along the minor-axis, cf. Sec. 6.3), the differences between both anisotropies are significantly larger in NUKER-models than in this work. (2) NUKER-models are based on the assumption that mass follows light. This may lead to an underestimation of mass, preferentially around the outermost data points, which may be compensated in the models by an enhanced fraction of energy in azimuthal motions. (3) NUKER-models are not regularised.

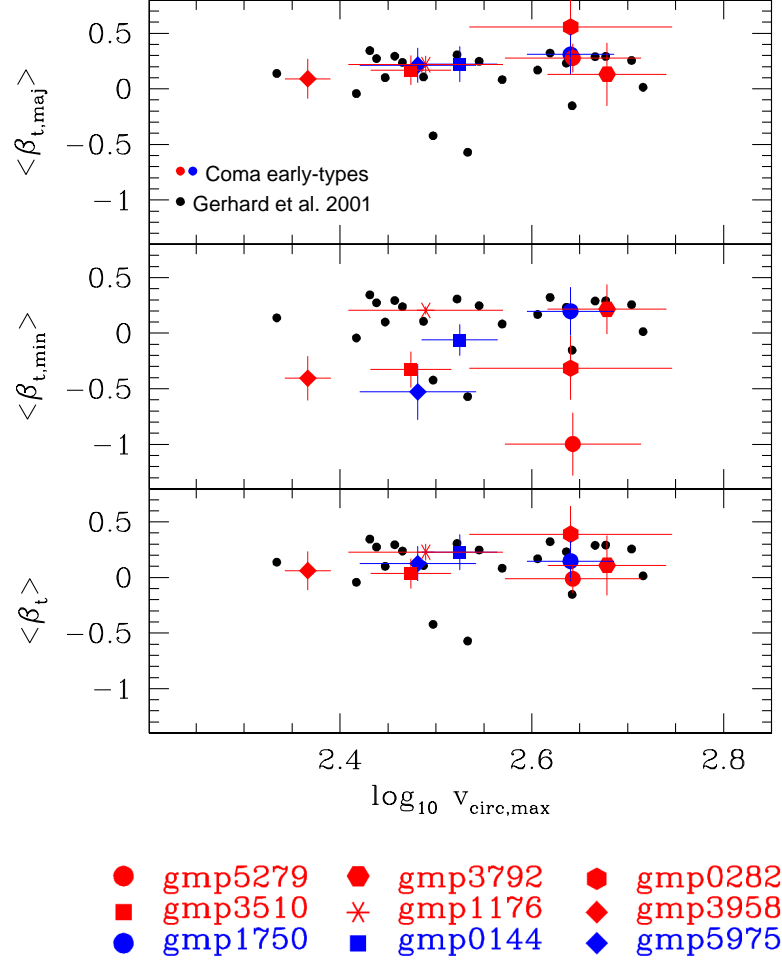


Figure 7.3: Comparison of luminosity-weighted, average tangential anisotropies $\langle \beta_t \rangle \equiv \langle (\beta_\phi + \beta_\vartheta)/2 \rangle$. Coloured: COMA; black: ROUND; top/middle: major/minor-axis (each averaged out to maximum data-radius along the corresponding axis); bottom: whole model, averaged out to the larger of r_{eff} and outermost data-radius r_{dat} . ROUND-anisotropies are similarly averaged out to $\max(r_{\text{eff}}, r_{\text{dat}})$.

As has been shown in Sec. 6.7, lower regularisation can in principle lead to larger anisotropies. However, this increase in internal anisotropies has no preferred direction, but is related to the particular data of each galaxy. Therefore, it seems unlikely that regularisation alone can account for the differences in the azimuthal anisotropies. But it could amplify small differences between the NUKER and

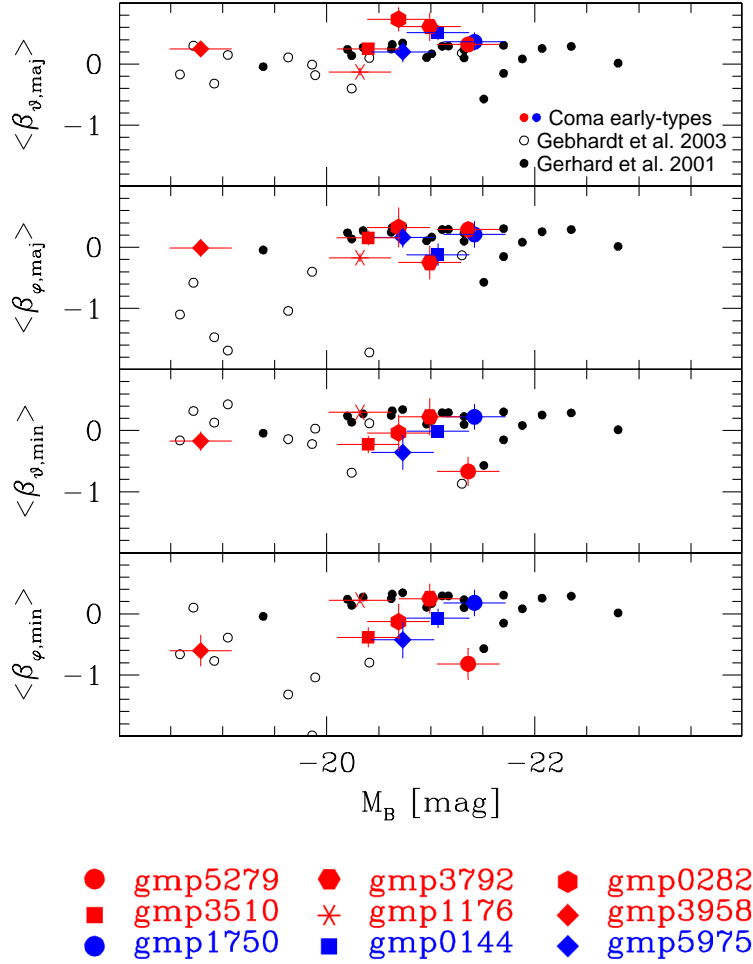


Figure 7.4: Similar to Fig. 7.3, but anisotropies are plotted versus absolute M_B and split into their meridional and azimuthal components. Coloured/open: COMA/NUKER, radially averaged within r_{eff} ; black: ROUND-anisotropies from Fig. 7.3.

the COMA galaxies.

7.4 Fundamental plane

As outlined in the introduction elliptical galaxies follow a close relation between effective radius, effective surface brightness and central velocity dispersion, the fundamental plane (FP). According to virial equilibrium, luminosity L and mass

M of a galaxy obey

$$L = c_L 2\pi r_{\text{eff}}^2 \langle I \rangle_{\text{eff}} \quad (7.1)$$

and

$$M = \frac{3c_M}{G} r_{\text{eff}} \sigma_{0.1}^2, \quad (7.2)$$

where $\langle I \rangle_{\text{eff}}$ is the average surface brightness within the effective radius and c_L and c_M , respectively, are structure constants (Faber et al. 1987). Thus, the virial theorem predicts

$$\log r_{\text{eff}} = \log \frac{\sigma_{0.1}^2}{\langle I \rangle_{\text{eff}} (M/L)} - \log \frac{G c_L 2\pi}{3c_M} \quad (7.3)$$

and, for a homologous dynamical family with constant c_L and c_M , a correlation of $\log r_{\text{eff}}$ with $\log \sigma_{0.1}^2 / \langle I \rangle_{\text{eff}} / (M/L)$ with a slope of one. If additionally M/L is constant then a slope-one relation follows between the observables $\log r_{\text{eff}}$ and $\log \sigma_{0.1}^2 / \langle I \rangle_{\text{eff}}$:

$$\log r_{\text{eff}} \sim 2 \log \sigma_{0.1} - 1 \log \langle I \rangle_{\text{eff}}. \quad (7.4)$$

The actual relation observed for ellipticals is instead (e.g. Jørgensen, Franx & Kjaergard 1996)

$$\log r_{\text{eff}} \sim 1.24 \log \sigma_{0.1} - 0.82 \log \langle I \rangle_{\text{eff}}. \quad (7.5)$$

This tilt between the observed FP (7.5) and the virial prediction (7.4) could be either caused by structural non-homology or by a systematic variation of M/L with galaxy luminosity (or by a combination of both). Stellar dynamical modelling suggests the tilt to reflect a systematic variation of the mass-to-light ratio M/L with mass/luminosity (Gerhard et al. 2001; Cappellari et al. 2006). The present work is implicitly consistent with that, insofar as the scaling of the total dynamical M/L with stellar mass in the Coma galaxies is similar to these works.

The case of the Coma sample is further illustrated in Fig. 7.5. The upper panels show virial scaling relations according to equation (7.3). As a linear fit with slope one (black line) reveals, the galaxies are fully consistent with the assumption of structural homology. The scatter around the virial relation is plotted in the lower panels against

$$\Lambda_C \equiv \text{sgn}(r_{\text{eff}} - r_C) \times \sum (w^+ - w^-). \quad (7.6)$$

Thereby sgn is the signum-function

$$\text{sgn}(x) \equiv \begin{cases} 1 & : x \geq 0 \\ -1 & : x < 0 \end{cases} \quad (7.7)$$

and $\sum (w^+ - w^-)$ is the difference between the fractional amount of light $\sum w^+$ on prograde and, $\sum w^-$, on retrograde orbits (all orbits with $\langle r_{\text{orb}} \rangle \leq 3 r_{\text{eff}}$ are considered). The quantity r_C in equation (7.6) is the halo core-radius. For NIS-halos it is defined in equation (3.2), for NFW-halos it is explicitly defined

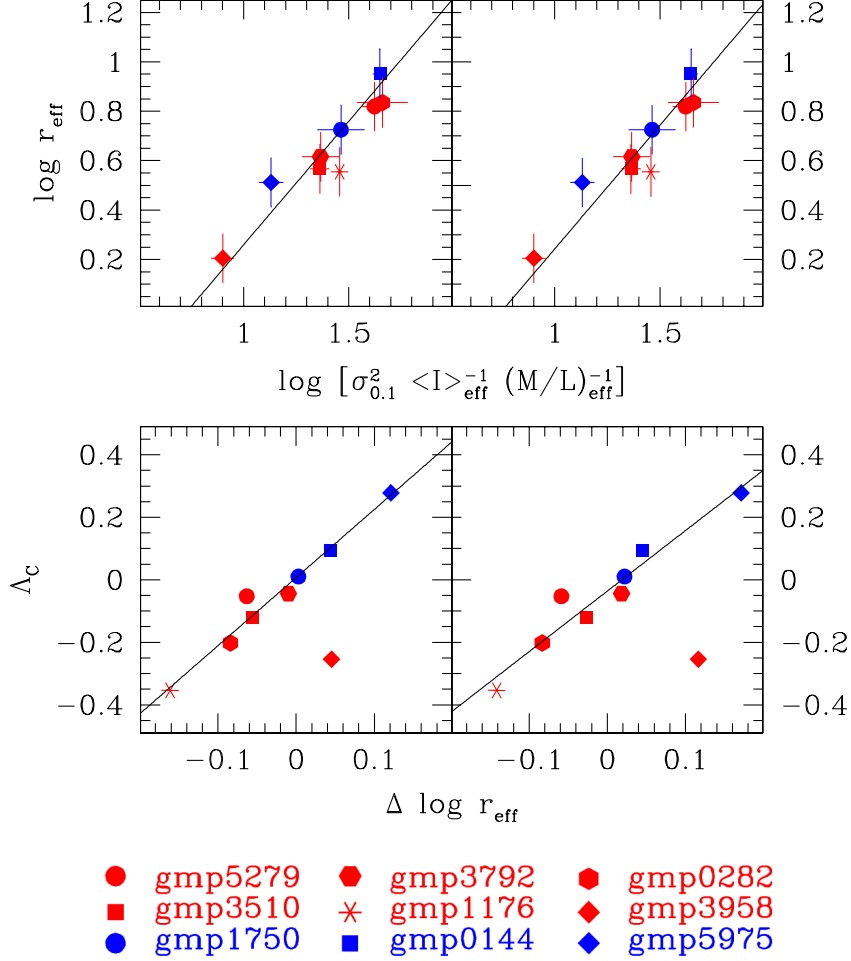


Figure 7.5: Top: Virial scaling relations for a homologous dynamical family compared with the Coma ellipticals. Solid line: best-fit relation with fixed slope of one to all galaxies (left) and to the non-rotating galaxies (right). Bottom: residuals from the fit in the upper panels versus angular momentum in the models (see text for details).

in Sec. 7.7 below. For the purpose here, the only important issue related to r_C is that Λ_C is defined to be negative in galaxies with extended halos and positive in galaxies with compact halos. The use of r_C in equation (7.6) is nothing but a convenient way to formalise the division between compact halos ($r_C \leq r_{\text{eff}}$) and extended halos ($r_C > r_{\text{eff}}$) in the Coma sample. The close relationships apparent in the lower panels of Fig. 7.5 can be read as follows. (1)

Deviations from the virial relations increase with the total angular momentum in the models, measured by $\sum(w^+ - w^-)$. (2) Rotating galaxies with compact halos have r_{eff} larger than predicted from virial relations, while rotating galaxies in extended halos have r_{eff} smaller than predicted from virial relations. The only clear outlier in the lower panels is the two-component system GMP3958, whose offset from the virial relations has a different origin compared with the other systems.

Deviations of the models with respect to virial scaling relations are not unexpected since angular momentum gradients are not included in equation (7.4), but characteristic for rotating galaxies. Moreover, the systematic variation of circular velocity curve shapes among the sample (cf. Sec. 5.4.1) implies the models to be non-homologous, again in contrast to the assumptions underlying equation (7.4). Non-homology in the total mass-distribution is thereby likely driven by non-homology of the luminous mass, because the halos are homologous in the models (all but two are NIS-distributions, the remaining two NFW-halos are similar to NIS-halos over the observationally sampled radial region). What is surprising in Fig. 7.5 is that both sources of scatter are correlated and that rotation can scatter galaxies to both sides of the virial relation. In Sec. 5.5.2 it has been pointed out that especially in rotating galaxies (except in the two-component system GMP3958) the onset of dark matter (where ρ/ν starts to increase, cf. Fig. 5.16) is correlated with outliers in the Υ_{SSP} -profiles, which may originate from gas emission. If this indicates a fraction of dark matter to be baryonic, it could explain a correlation like in the lower panels of Fig. 7.5, if rotation (and the related excess mass) is more centrally concentrated in galaxies with compact halos than in galaxies with extended halos.

In any case, regardless of its physical origin, the rms scatter in $\log r_{\text{eff}}$ is 0.086 in the upper left panel. It reduces to 0.031, if all $\log r_{\text{eff}}$ (but that of GMP3958) are corrected according to the relation in the lower left panel. The corresponding numbers for the right panels are 0.084 and 0.029, respectively.

If the tilt of the FP is driven by M/L-variations, then the question remains whether these are due to a variation of the dark matter fraction or due to a variation of stellar populations. Based on Figs. 7.1 and 7.2 the answer is that both contribute. On the one side, Fig. 7.1 implies that stellar mass-to-light ratios in the Coma galaxies do vary systematically with M_* . On the other side, the tilt between the fits in Fig. 7.1 and 7.2 leads to the conclusion that this scaling is different from the scaling of the total M/L with M_* , that corresponds to the tilt of the FP. It follows that the dark matter fraction must vary with M_* in a way correlated to the scaling of Υ_{dyn} with M_* . It has been argued in Sec. 5.3 that the variation of Υ_{dyn} over the COMA-sample is not purely an age, metallicity or α -abundance effect. If Υ_{dyn} is purely stellar, then its variation implies a change of the IMF from Kroupa-like at low Υ_{dyn} to Salpeter-like at large Υ_{dyn} . From the tilt between the COMA-fits in Figs. 7.1 and 7.2 it further follows that lower-mass ellipticals must have larger dark matter fractions (but this point is uncertain yet, cf. Sec. 7.2). All in all then, a steeper IMF would be related to a lower dark matter fraction. Another possibility is that Υ_{dyn} is not purely stellar and that the increasing offset to the Kroupa-IMF reflects

an increasing amount of dark matter approximately following the same radial distribution as the luminous matter.

With the data at hand, these cases cannot be firmly distinguished. A variation of the IMF-slope with stellar mass implies a rotation of the FP with redshift (Renzini & Ciotti 1993), which has been observed recently at $z \approx 1$ (di Serego Alighieri et al. 2005; Jørgensen et al. 2006) but not yet fully analysed with respect to an IMF-variation. Final conclusions on this issue require also more local galaxies to be analysed, ideally with data reaching further out to allow a better distinction between different dark matter profiles. A combined orbit modelling of kinematical and spectral observations would be helpful to reduce ambiguities in the comparison with stellar mass-to-light ratios and to put better constraints on the IMF.

7.5 Tully-Fisher relation of ellipticals

The rotation velocity of spiral galaxies is closely related to their luminosity by the Tully-Fisher (TF) relation (Tully & Fisher 1977). Ellipticals do not necessarily rotate, but the flatness of their outer circular velocity curves allows to define an effective rotation velocity for these systems as well. ROUND-ellipticals have been shown to follow a Tully-Fisher like relation, thereby being about $\Delta M_B = 1$ magnitude fainter than spiral galaxies at the same circular velocity (Gerhard et al. 2001). The results for the Coma galaxies are presented in Fig. 7.6.

A linear fit to the Coma sample (cf. Tab. 7.3) yields a slope fully consistent with that of spiral galaxies in the B -band (Sakai et al. 2000). The offset to spirals is $\Delta M_B \approx 1$, as in the ROUND-sample. In detail, the slope of the Coma relation is slightly steeper than in the ROUND-ellipticals. Reasons could be the relatively small sample size or the fact that the fit to the Coma ellipticals is partly driven by the single fainter object GMP3958. More galaxies have to be modelled in the axisymmetric approximation to clarify this point. In any case, the ROUND and the COMA results are consistent within the errors. Lenticulars in Fig. 7.6 homogeneously populate the region in the TF-plot between elliptical galaxies and spiral galaxies.

sample	in Fig. 7.6	m	n
(1)	(2)	(3)	(4)
Coma	solid	-7.68 ± 1.45	-0.96 ± 3.75
Gerhard et al. (2001)	dashed	-5.92	-6.02
Sakai et al. (2000)	red, dashed	-7.97	0.13

Table 7.3: As Tab. 7.1 but for Fig. 7.6 ($M_B = m \times \log v_{\text{circ,max}} + n$).

Differences in M_B at the same galaxy mass could partly reflect different stellar population properties of ellipticals and spirals. A more direct comparison between stellar masses in ellipticals and spirals is provided by the baryonic TF-

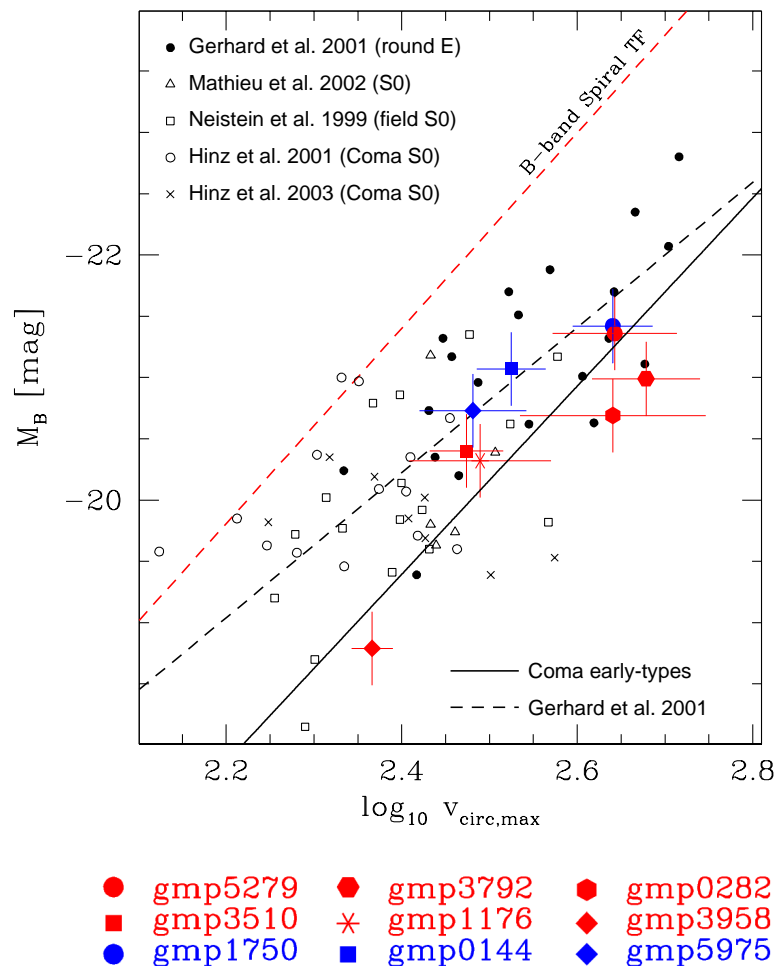


Figure 7.6: Tully-Fisher relation of early-type galaxies. Coloured: COMA; black: ROUND; solid: linear fit to Coma galaxies; dashed: best-fit of Gerhard et al. (2001); red dashed: *B*-band spiral TF relation of Sakai et al. (2000).

relation, the scaling between stellar mass and rotation velocity. This is the content of Fig. 7.7. The best-fit linear relation between M_* and $v_{\text{circ,max}}$ for the Coma sample is

$$\log M_* = (2.95 \pm 1.0) + (3.28 \pm 0.38) \times \log v_{\text{circ,max}}, \quad (7.8)$$

slightly shallower than the slope $m = 4$ proposed by McGaugh (2005) for spirals. Independently from that, elliptical galaxies have clearly lower stellar masses than spiral galaxies of the same circular velocity.

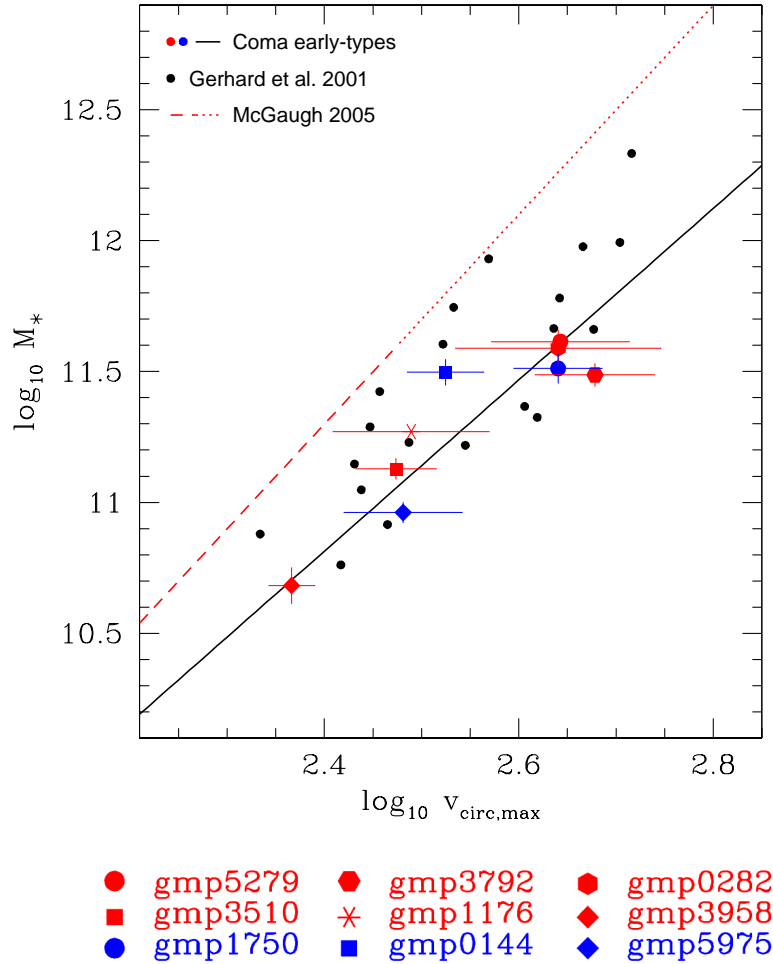


Figure 7.7: Baryonic TF relation. Black dots: Gerhard et al. (2001); black solid line: best-fit to the combined early-type galaxies with stellar dynamical models; red: baryonic TF relation of McGaugh (2005) (the dotted part is extrapolated).

7.6 Centre-halo relation

The existence of a TF-like relation between M_B and $v_{\text{circ,max}}$ together with the well-known Faber-Jackson relation (Faber & Jackson 1976) between $\sigma_{0.1}$ and M_B implies a correlation of $\sigma_{0.1}$ with $v_{\text{circ,max}}$. This can also be seen as a consequence of the uniformity of elliptical galaxy rotation curves, specifically, that their approximate flatness implies a single velocity scale (Gerhard et al. 2001). The $\sigma_{0.1} - v_{\text{circ,max}}$ relation of the Coma galaxies is displayed in Fig. 7.8. For

consistency with the ROUND-sample the same definition of $\sigma_{0.1}$ as in Gerhard et al. (2001) is adopted here. Fits to different samples of spiral and elliptical galaxies (and combinations of both) shown in the figure yield consistently the same relation (cf. Tab. 7.4).

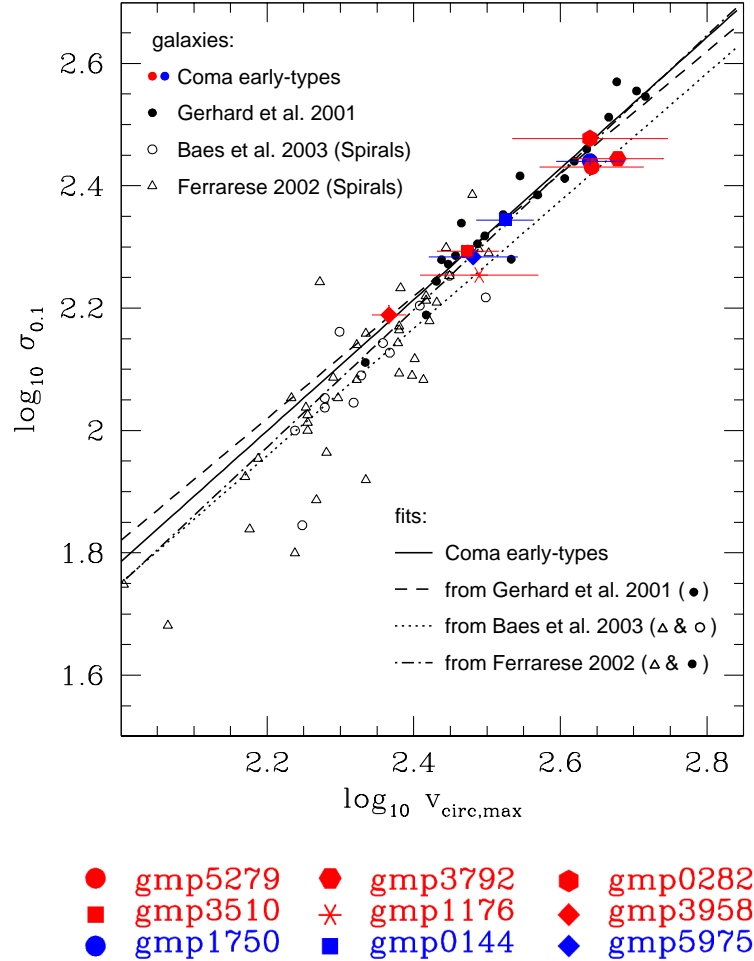


Figure 7.8: Maximum v_{circ} versus central velocity dispersion $\sigma_{0.1}$. Symbols and fits as quoted in the figure.

7.7 Dark matter scaling relations

Gerhard et al. (2001) presented for the first time dark halo scaling relations for elliptical galaxies. In the ROUND-galaxies they found ≈ 4 times smaller halo

sample	in Fig. 7.8	m	n
(1)	(2)	(3)	(4)
Coma	solid	1.07 ± 0.10	-0.36 ± 0.28
Baes et al. (2003)	dotted	1.04	-0.33
Ferrarese (2002)	dot-dashed	1.12	0.49
Gerhard et al. (2001)	dashed	1.00	-0.18

Table 7.4: As Tab. 7.1 but for Fig. 7.8 ($\log \sigma_{0.1} = m \times \log v_{\text{circ,max}} + n$).

core-radii and ≈ 25 times larger central dark matter densities than in spiral galaxies of the same circular velocity. The present section is aimed to compare these results to the COMA-sample.

7.7.1 Halo scaling relations

Fig. 7.9 plots effective radii, halo core radii r_C and halo asymptotic velocities v_C versus B -band luminosity. Strictly speaking, r_C and v_C are only defined for NIS-halos. The two galaxies with NFW-halos (GMP3792 and GMP0144) are included in the plot as follows. In a NIS-halo the circular velocity curve monotonically increases towards its asymptotic value, but in NFW-halos v_{circ} reaches a maximum and vanishes in the limit $r \rightarrow \infty$. A quantity v_C that matches with the asymptotic velocity in the NIS-case and is uniquely defined for NFW-halos is

$$v_C \equiv \sup_r \{v_{\text{circ}}(r)\}. \quad (7.9)$$

Concerning r_C , it is uniquely defined in NIS-halos by the implicit equation

$$v_{\text{circ}}(r_C) \equiv \frac{v_C}{\sqrt{2}}. \quad (7.10)$$

In NFW-halos there are two solutions of equation (7.10), one inside the radius of maximum v_{circ} and the other outside. For GMP3792 and GMP0144 the smaller of the two is used as r_C .

The separation of the red and blue symbols in the second row of Fig. 7.9 reflects the subdivision of the Coma sample in compact-halo galaxies and extended-halo galaxies, respectively (cf. Sec. 5.4.1). The two subgroups bracket the distribution of halo core-radii recovered in the ROUND-sample. Galaxies with extended halos follow closely the black line representing the case of spiral galaxies (Persic, Salucci & Stel 1996a,b).

The difference between compact and extended halos is not primarily a difference in the radius where dark matter becomes important. This can be seen by consideration of the radius r_M that encloses equal amounts of dark and luminous mass,

$$M_*(r_M) = M_{\text{DM}}(r_M), \quad (7.11)$$

or, equivalently, by the radius r_ρ of equal spherically averaged local densities,

$$\rho_*(r_\rho) = \rho_{\text{DM}}(r_\rho). \quad (7.12)$$

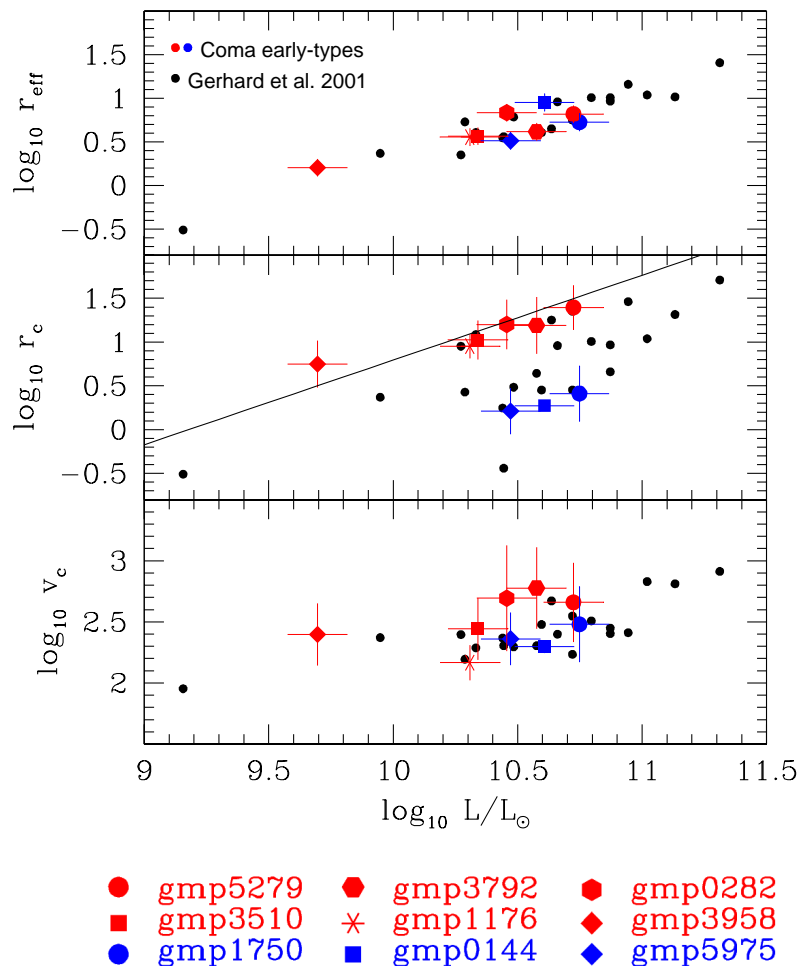


Figure 7.9: Effective radius r_{eff} , halo core radius r_C (in kpc) and halo maximum circular velocity v_C (in km/s) versus luminosity. Solid line: spiral galaxies (Persic, Salucci & Stel 1996a,b).

Fig. 7.10 illustrates the dependency of r_C , r_M and r_ρ on the effective radius r_{eff} . The separation between compact and extended halos is clearly seen in r_C (top panel) but washes out in the lower two panels dealing with r_M and r_ρ . The systematic increase of r_M with r_{eff} implies that r_C and v_C must be correlated.

That this is indeed the case can be drawn from Fig. 7.11 where r_C and v_C are plotted against each other. A linear fit to the COMA-sample yields

$$\log r_C = (-6.47 \pm 5.53) + (2.93 \pm 1.64) \times \log v_C. \quad (7.13)$$

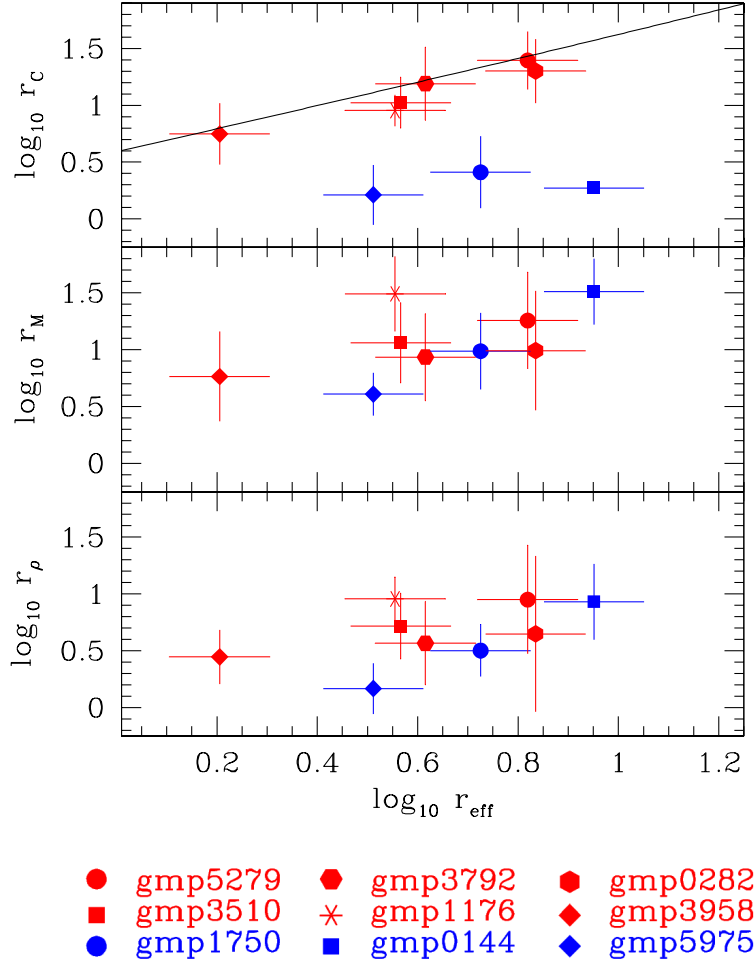


Figure 7.10: From top to bottom: dark halo core-radius r_C , equal-mass radius r_M and equal-density radius r_ρ (all in kpc) versus r_{eff} . Solid: spiral galaxies (Persic, Salucci & Stel 1996a,b).

GMP1176 has been omitted from the fit, since its v_C (and possibly also r_C) are likely affected by the unresolved central light profile. The distribution of r_C and v_C in the ROUND-sample (black dots in Fig. 7.11) is consistent with the relation (7.13).

The different scalings of galaxies with compact halos on the one side and galaxies with extended halos on the other, are therefore at least partly driven by the correlation between r_C and v_C . A relation between r_C , v_C and luminosity would not be helpful to derive approximate halo parameters from easy to de-

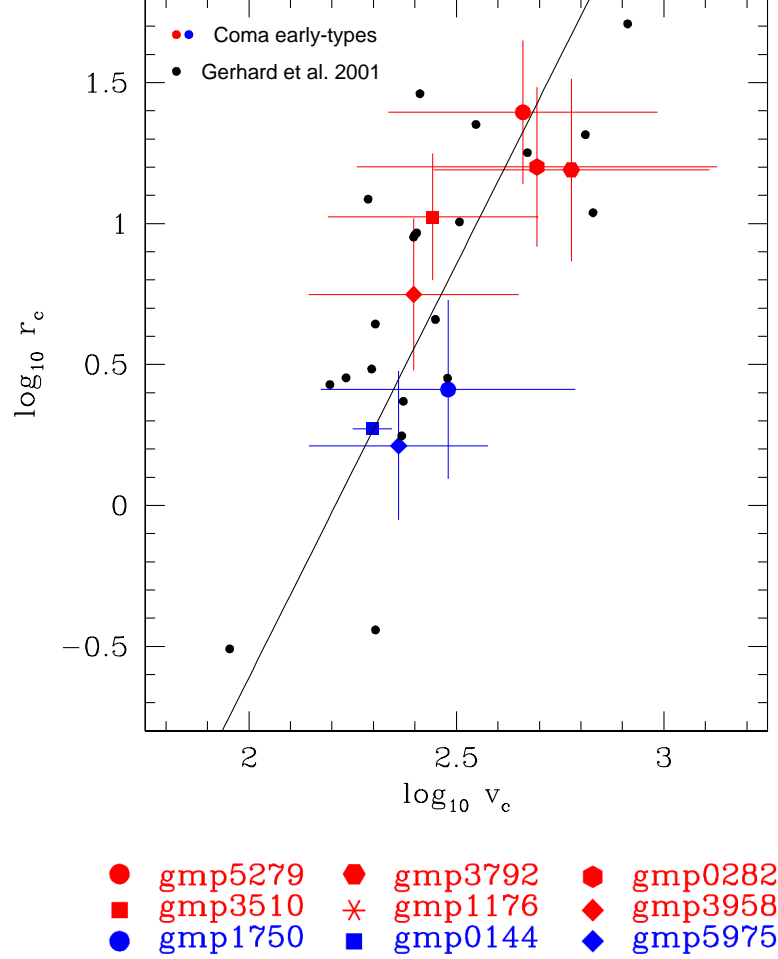


Figure 7.11: Correlation between halo core radius r_C and halo maximum circular velocity v_C . Coloured: Coma galaxies; black dots: ROUND; solid: linear fit to Coma galaxies.

termine observational quantities. However, the close relationship between outer v_{circ} and $\sigma_{0.1}$ (cf. Sec. 7.6) suggests a relation between r_C or v_C , respectively, on the one side and $\sigma_{0.1}$ and L on the other.

This is probed by Fig. 7.12, which presents the scaling of $\log v_C$ with $\log \sigma_{0.1}$ and $\log L$. The figure indeed reveals a linear relation in the COMA-sample. The best-fit (shown by the black line) is

$$\log v_C = (3.00 \pm 1.78) \times \log \sigma_{0.1} - (0.66 \pm 0.39) \times \log \frac{L}{L_\odot} + (2.28 \pm 0.09). \quad (7.14)$$

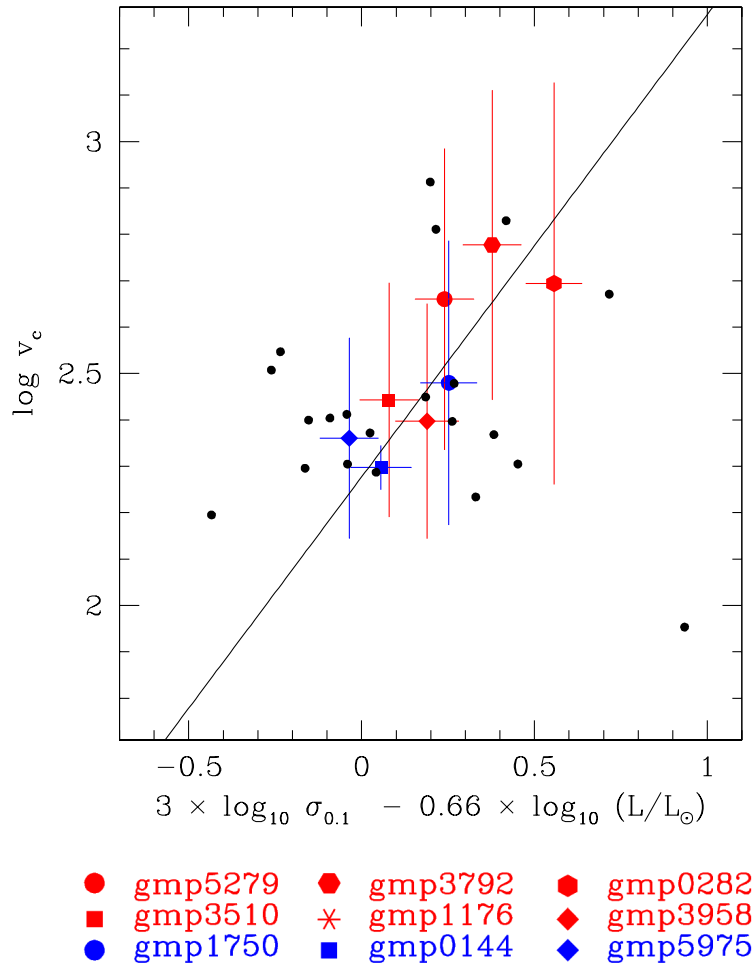


Figure 7.12: Scaling of the maximum halo velocity v_C with $\sigma_{0.1}$ and B -band luminosity L . Coloured: Coma galaxies; black dots: ROUND-sample; solid: linear fit.

As for equation (7.13), GMP1176 has been omitted from the fit. The correlation between r_C and v_C implies the existence of a similar relation between r_C , $\sigma_{0.1}$ and L . If relations (7.13) and (7.14) can be verified on the basis of a larger sample they would provide means to derive approximate halo parameters from the central velocity dispersion $\sigma_{0.1}$ and the luminosity L of ellipticals.

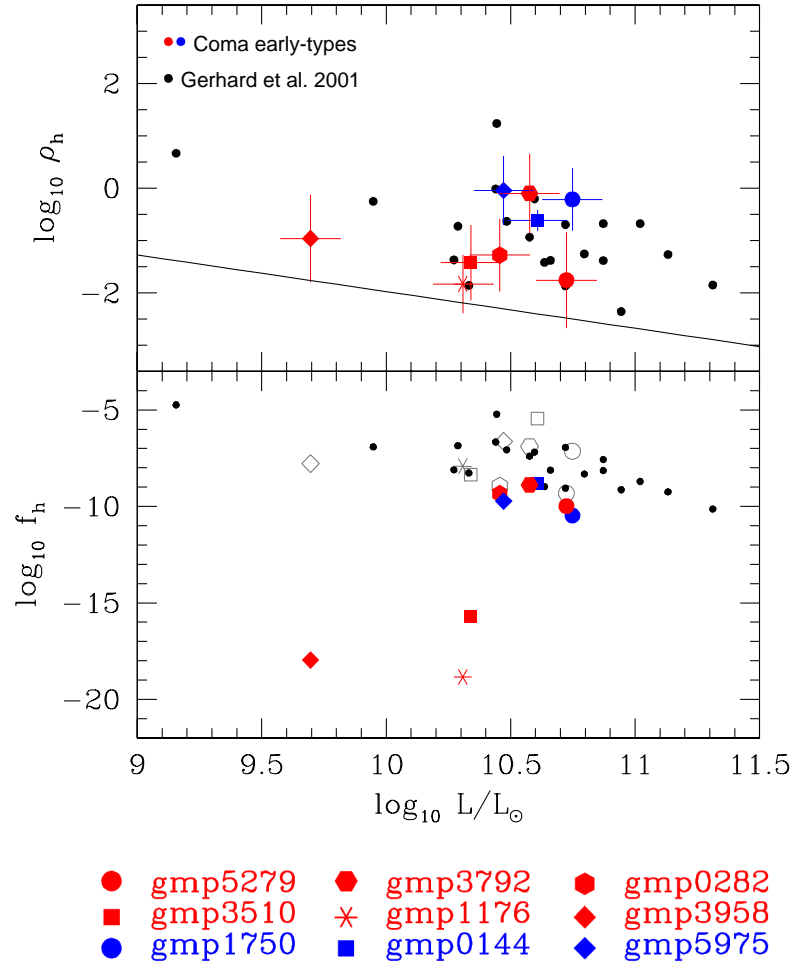


Figure 7.13: Central dark matter density ρ_h (in M_\odot/pc^3) and phase-space density f_h (in $M_\odot/\text{pc}^3/(\text{km/s})^3$) versus luminosity. Coloured: Coma phase-densities from dark matter DFs; open/grey: Coma phase-densities from equation (7.19); black: ROUND; solid: spiral galaxies (Persic, Salucci & Stel 1996a,b).

7.7.2 Central dark matter

To investigate the COMA-sample with respect to central dark matter properties, the upper panel of Fig. 7.13 plots central dark matter densities ρ_h versus luminosity. The central dark matter density ρ_h is defined as the average mass-

density of the halo inside $r < r_{\text{eff}}/4$:

$$\rho_h \equiv \frac{M_{\text{DM}}(r_{\text{eff}}/4)}{V(r_{\text{eff}}/4)}, \quad (7.15)$$

where

$$M_{\text{DM}}(r) \equiv \int_0^r \rho_{\text{DM}}(r') 4\pi r'^2 dr' \quad (7.16)$$

and

$$V(r) = \int_0^r 4\pi r'^2 dr'. \quad (7.17)$$

From the upper panel in Fig. 7.13 it can be drawn that dark matter halos of Coma ellipticals have larger central dark matter densities compared to spiral galaxies at the same luminosity. Over the luminosity range covered by the present work, the distribution of central halo densities is on average comparable to the ROUND-sample, implying in the mean ≈ 25 times higher central dark matter densities in ellipticals than in spirals of the same luminosity. Assuming proportionality between central dark matter densities and the mean cosmic density at the halo assembly epoch yields for the formation epoch z_E of an elliptical

$$\left(\frac{1+z_E}{1+z_S}\right)^3 \approx \frac{\rho_h}{\rho_S}, \quad (7.18)$$

where ρ_S is the central dark matter density in a comparably bright spiral and z_S the formation epoch of the corresponding spiral galaxy halo (e.g. Gerhard et al. 2001). With $z_S = 1$, Gerhard et al. (2001) conclude $z_E \approx 4$ unless the excess of central dark matter is due to baryonic dark mass. From the upper panel of Fig. 7.13 it can be drawn that this holds on average for the Coma sample, as well. However, the galaxies with extended halos tend to have lower central dark matter densities, only a factor ≈ 5 larger than in spirals (implying $z_E \approx 2.5$), while the compact-halo objects have central dark matter densities a factor ≈ 100 larger (yielding rather large $z_E \approx 8.5$).

The large central dark matter densities in galaxies with compact halos could indicate that a fraction of the mass in their halos is baryonic. This would be consistent with the coincidences between local dynamical mass-to-light ratios ρ/ν and Υ_{SSP} -profiles, discussed in Sec. 5.5.2 (cf. Fig. 5.16). To clarify this issue, more galaxies need to be analysed.

In the lower panel of Fig. 7.13, central densities in phase-space are compared. Coloured symbols show central phase-densities for the Coma galaxies derived from their dark matter DFs (cf. Sec. 5.7). These densities are lower than the values for the ROUND-galaxies given in Gerhard et al. (2001). The discrepancy arises from different definitions for f_h . Gerhard et al. (2001) define the central phase-density for their galaxies as

$$f_h \equiv 2^{3/2} \frac{\rho_h}{v_C^3}, \quad (7.19)$$

which corresponds to the average central phase-density of their NIS-halos in a self-consistent potential. Explicit calculation of the dark matter DFs for the Coma galaxies in Sec. 5.7 has revealed a drop of phase-densities towards the centre, if the contribution of the luminous matter to the central potential is taken into account. This explains the different results for the ROUND and the COMA-sample. For comparison, open grey symbols in the lower panel of Fig. 7.13 display Coma galaxy f_h from equation (7.19). Not surprising in view of the similar distributions of $\rho_h(L)$ and $v_C(L)$ in both samples, the grey symbols are in good agreement with the ROUND-results.

7.8 Summary

The main results from the investigation of scaling relations in this chapter are:

- The scaling of total dynamical mass (inside r_{eff}) of the Coma galaxies is similar to the scalings found in other dynamical studies.
- Orbital anisotropies show no systematic dependency on galaxy mass, revealing the overall dynamical homology of elliptical galaxies over the considered luminosity interval. This result is consistent with the findings of Gerhard et al. (2001). In contrast, the on average fainter ellipticals of the NUKER-sample are significantly more azimuthally anisotropic.
- The dynamical homology and the M/L-scalings are compatible with the tilt of the FP caused mainly by a M/L-variation with stellar mass, consistent with other recent dynamical studies (Gerhard et al. 2001; Cappellari et al. 2006). The Υ_{dyn} -scaling of the Coma models is tilted with respect to the M/L-scaling predicted by the FP-tilt. The range of stellar masses M_* probed is narrow in the present sample, but if confirmed over a broader M_* -range, this result would indicate that galaxies with lower Υ_{dyn} have larger dark matter fractions – provided Υ_{dyn} is purely stellar.
- In the Coma sample the rms-scatter around the virial relation between r_{eff} , $\sigma_{0.1}$, $\langle I \rangle_{\text{eff}}$ and M/L for a homologous dynamical family is 0.086 in $\log r_{\text{eff}}$. In all galaxies but the two-component system GMP3958 the scatter is correlated with the total angular momentum in the models. The direction of the offset from the virial relations is thereby opposite for galaxies having compact halos and those having extended halos, respectively. The correlation between offset and angular momentum can be used to decrease the scatter around the virial relation down to 0.031 in the Coma sample.
- The results of the ROUND-analysis, that (1) elliptical galaxies follow a Tully-Fisher relation similar to spiral galaxies but being about magnitude fainter at the same velocity and that (2) they have $\lesssim 3$ times lower stellar masses at the same circular velocity are confirmed by this study.

-
- Likewise, the Coma galaxies follow a similar relation between central velocity dispersion $\sigma_{0.1}$ and outer circular velocities as found for spiral galaxies and round ellipticals.
 - In the nine objects of the present sample, the halo parameters r_C and v_C are correlated. Both parameters are further correlated with the central velocity dispersion $\sigma_{0.1}$ and luminosity L . If these correlations can be verified on the basis of a larger sample, they allow to determine approximate halo parameters from easy-to-access observational properties.
 - Central halo densities in Coma galaxies are larger than in spiral galaxies of the same luminosity, confirming the results of Gerhard et al. (2001). Implicitly, their conclusion that elliptical galaxy halos assembled at higher redshifts $z_E \approx 4$ is consistent with the Coma galaxies as well. However, galaxies with extended halos in the present sample have on average ≈ 5 times larger central densities, implying $z_E \approx 2.5$, while compact-halo objects have ≈ 100 times larger central densities (yielding $z_E \approx 8.5$). This could possibly indicate that a fraction of dark matter in the latter systems is baryonic.

Chapter 8

Summary and conclusions

The main goal of the present work is a detailed analysis of nine moderately bright early-type galaxies in the Coma cluster with respect to their dynamical structure and dark matter content. In contrast to earlier studies using spherical models, axisymmetric models are applied to take into account rotation, substructure in form of disks and inclination effects in the models.

Dynamical modelling. During the first part of the work the axisymmetric orbit superposition code of Gebhardt et al. (2000a), originally developed to measure masses of supermassive black-holes in galaxy centres, was adapted to the problem of reconstructing dark matter halos. The code was advanced in three respects.

Firstly, a new implementation to calculate phase-volumes of orbits has been developed. To this end the invariant curves of orbits in surfaces of section defined by the radii and radial velocities of orbital equatorial crossings (at given E and L_z) are integrated by the use of Voronoi tessellations. Knowledge of orbital phase-volumes allows to convert the weights of orbits in superposition models into phase-space densities and vice versa. Applications include the comparison of orbit superpositions with synthetic phase-space distribution functions for accuracy tests and the determination of phase-space distribution functions from observations of real galaxies.

Secondly, a new method to sample the available phase-space with orbits for the models has been implemented. It is designed to yield a homogeneous coverage of suitably chosen surfaces of section with individual orbital invariant curves, implying a representative collection of orbits in the models. Comparisons with synthetic phase-space distribution functions via the refined orbital phase-volumes have shown that both, the implementation of phase-volumes and the new orbit sampling, yield an accurate representation of phase-space in the models (remaining deviations are significantly below the level of observational errors).

A third refinement of the modelling is the determination of the optimal amount of regularisation with respect to a typical data set in the Coma sample.

This has been achieved by Monte-Carlo simulations of observationally motivated synthetic galaxy models under realistic observational conditions. The result is that the mass distribution and the internal velocity moments can be reconstructed with about 15 per cent accuracy from the typical a data set in the sample.

The advanced orbit code has been applied to photometric and kinematic observations of nine early-type galaxies in the Coma cluster. The photometric input data is composed of HST photometry with high spatial resolution in the central parts and ground-based photometry out to $\approx 5 r_{\text{eff}}$. The kinematic data consists of measurements of the shape of the line-of-sight-velocity-distribution in terms of Gauss-Hermite parameters v , σ , H_3 and H_4 out to $\approx 3 r_{\text{eff}}$.

Mass composition. The nine galaxies have on average roughly flat circular velocity curves, similar to spiral galaxy rotation curves. In detail, the sample divides into two groups of objects. One has extended dark matter halos with rising circular velocity curves at the outer edge of the models ($\approx 10 r_{\text{eff}}$). The other group has compact halos with decreasing circular velocities at the model's outer edge. The shapes of the circular velocity curves require in each case outwardly increasing mass-to-light ratios. The contribution of the luminous matter to the overall potential is in good agreement with stellar population models, if a variation of the IMF is allowed for in the latter. Galaxies with low (dynamically derived) stellar mass-to-light ratios Υ_{dyn} are compatible with a shallow IMF at low stellar masses (Kroupa-like), while systems with larger Υ_{dyn} are closer to a steeper, Salpeter-like IMF. The offset between dynamical Υ_{dyn} and stellar population Υ_{SSP} based on the Kroupa-case is weakly correlated with population age and α -enhancement. Low dynamical Υ_{dyn} rule out a Salpeter-like IMF in a few systems. On the other hand, adopting a Kroupa-IMF in galaxies with large dynamical Υ_{dyn} implies significant amounts of dark matter (up to 50 percent) hidden in Υ_{dyn} and, thus, following approximately the same radial distribution as the luminous matter. In any case, there is at least a two-sigma evidence for an additional fraction of 10 to 50 percent of (dark) mass inside the half-light radius r_{eff} that follows a roughly isothermal radial distribution. These results are robust against different weights on regularisation in the models and confirm earlier studies of round, non-rotating galaxies (Gerhard et al. 2001).

For the first time, the phase-space distribution function of dark matter in the combined gravitational potential of luminous and dark matter has been calculated. The phase-densities of non-singular isothermal halos drop towards the very central parts, where luminous matter dominates the potential. Halos following a NFW-profile do not show a comparable phase-density drop, although with the present models the shape of the DF cannot be followed into the very central parts ($r < 0.01 r_{\text{eff}}$). The non-monotonic behaviour of dark matter DFs with respect to energy implies that the actual mass decomposition could be unstable.

Orbital structure. The dynamical models of the nine Coma galaxies follow closely the predictions of the virial theorem for galaxies that are flattened by anisotropy, meaning here that they have approximately $\sigma_\varphi \approx \sigma_r$, but $\sigma_\theta < \sigma_r$. This relation can be achieved by maximising the entropy of the DF in a given mass distribution (subject to a given luminosity distribution as boundary condition). Together with similar results found in the SAURON sample (Cappellari et al. 2006) this implies that moderately bright ellipticals are mostly flattened by anisotropy and are globally close to a dynamically relaxed maximum-entropy state.

The dynamical structure of the galaxies around their poles is largely driven by a close relationship between velocity anisotropy and the observational H_4 -parameter, $\langle \beta_\theta \rangle = 8.77 H_4$. This relation is robust against regularisation, but the scatter around it increases with lowering the weight on regularisation in the fits.

In one system a clear two-component structure in form of a rotating disk superimposed on a spheroidal background is recovered analysing the DF. Other systems show a wealth of small-scale structures. Occasionally, orbits reaching the poles and circular orbits around the equator follow similar radial phase-density distributions, which may be interpreted as that the stars on these orbits share a common origin. In all but one of the rotating galaxies, a strong depression of retrograde circular orbits towards large radii is seen in the models. The exception is the two-component system mentioned above. Density-differences between prograde and retrograde orbits are largest, where stellar ages are lowest. This could indicate that the retrograde orbit depopulation reflects recently structured and not yet dynamically relaxed regions of the galaxies.

Generally, the orbital composition of the Coma galaxies does not follow the typical anisotropy structure found in collapse simulations, where the centre comes out isotropic and the outer parts strongly radially anisotropic. Instead, the rich diversity of internal structures indicates differences in the evolutionary histories of the objects, which are a natural consequence of different initial conditions in various merging configurations.

Galaxy scaling relations. The scaling of the total mass-to-light ratio M/L with stellar mass M_* in the Coma galaxies is consistent with other recent dynamical studies with less general models or less extended data. The conclusions of these works, that the tilt of the fundamental plane is mostly due to a variation of dynamical mass with M_* (Gerhard et al. 2001; Cappellari et al. 2006), is confirmed by this work. In the Coma sample, the stellar mass-to-light ratio follows a steeper scaling relation with M_* than the total dynamical mass-to-light ratio. The sample size is too small for a firm conclusion, but if this trend is verified in a larger sample it would imply that lower mass galaxies have larger dark matter fractions inside the half-light radius, unless with increasing M_* an increasing fraction of dark matter follows the same spatial distribution as the stars and is represented by Υ_{dyn} in the models.

The rms scatter of the Coma ellipticals with respect to the virial scaling

relations of a homologous dynamical family is 0.086 in $\log r_{\text{eff}}$. The scatter is found to be strongly correlated to the angular momentum in the models. Moreover, the direction of the scatter is different for galaxies with compact halos on the one side and systems with extended halos on the other. Correcting individual systems for this correlation allows to reduce the scatter to 0.031. If this relation is not an artifact of low-number statistics in the present sample, it would provide means to measure elliptical galaxy distances with improved accuracy.

The present study confirms the results from round, non-rotating galaxies that ellipticals follow a Tully-Fisher like relation with roughly the same slope as spirals but being $\Delta M_B = 1$ magnitudes fainter in the B -band than spirals of the same circular velocity (Gerhard et al. 2001). The Coma ellipticals have thereby about 3 times lower stellar masses at the same circular velocity than spirals. As found for round ellipticals (Gerhard et al. 2001), elliptical galaxy outer circular velocity curves scale linearly with the central velocity dispersion, $v_{\text{circ,max}} \propto \sigma_{0.1}$.

In the present sample, the galaxies with extended dark matter halos follow the same scaling relation between halo-core radius and luminosity than spiral galaxies. In contrast, galaxies with compact halos have core-radii at least a factor of 10 smaller. Halo-core radii and velocities are correlated in the sense that more extended halos have larger asymptotic velocities. In the nine Coma ellipticals of the present sample halo velocities are correlated with L (luminosity) and $\sigma_{0.1}$ (central velocity dispersion). If this relation is found to hold for ellipticals in general, it allows to compute approximate halo velocities from $\sigma_{0.1}$ and L . The correlation between r_C and v_C further implies, that halo core-radii could be derived from L and $\sigma_{0.1}$ as well.

Galaxies with extended halos have on average ≈ 5 times larger central densities than spiral galaxies of the same brightness, implying a formation epoch around $z_E \approx 2.5$ (if spiral galaxy halos form around $z_S \approx 1$ and dark matter is purely collisionless). Compact-halo systems have a factor of ≈ 100 higher central dark matter densities than corresponding spirals, implying $z_E \approx 8.5$. High central dark matter densities and low halo-core radii in compact-halo galaxies could indicate that their halos are at least partly made of baryonic dark matter. This would also fit with the coincidence between the rise of the local mass-to-light ratio ρ/ν with up-shifts in stellar population Υ_{SSP} that may be related to gas emission (cf. Fig. 5.16).

Outlook. Further progress in the investigation of elliptical galaxy formation, evolution and present structure can be made by extending the analysis to a larger sample, covering a wider range of luminosities. The strength of the mass decomposition into luminous and dark matter could be improved by including not only kinematical constraints in the models, but to populate orbits with different stellar populations and try to match line-strength profiles as well. Specifically, this includes the consideration of arbitrary stellar mass-to-light ratio profiles. Independent constraints for the mass decomposition could come

from a stability analysis of dark matter distribution functions in the combined potential of luminous and dark matter.

Speculations raised in this work about relics of characteristic evolutionary events in the phase-space distribution function can be further explored by applying the same models as used here to a survey of synthetic model galaxies (N -body simulations) that systematically includes various evolutionary scenarios. Similarities between characteristic features of galaxy models and orbit models of N -body simulations could be used to link real galaxies to the corresponding evolutionary scenario.

Appendix A

The sensitivity of Υ_{dyn} on the central photometric resolution

For the lenticular GMP1176 no archival HST imaging exists. Its light profile is thus unresolved in the central parts (a seeing FWHM of $2''$ corresponds to $\approx 0.3 r_{\text{eff}}$ or ≈ 1 kpc, respectively). In principle, seeing convolution can be included in the deprojection, but it would only add another free parameter (the central steepness of the light profile) to the modelling. Since by computation time limits the range of implied deprojections can anyway not be explored fully, it has been decided to ignore seeing corrections entirely. This causes a mismatch in the central stellar mass-profile and, thus, the central gravitational potential. To investigate the sensitivity of Υ_{dyn} on this mismatch self-consistent models have been constructed with and without additional HST data exemplary for GMP5975. The resulting fits are shown in Fig. A.1 and imply the following. (1) The significance of the dark matter detection is reduced: self-consistent models based on the ground-based photometry only fit generally better (they fall below the 3σ limit). (2) The best-fit self-consistent mass-to-light ratio without additional HST data is significantly larger than in models that resolve the central light profile. A possible explanation for these results is the following: The need for dark matter in the outer parts of ellipticals implies that their total mass profiles are shallower than their luminosity profiles. Now, the overall effect of seeing is to flatten the luminosity profile and thus to reshape it towards the shallower total mass profile. Additional upscaling by a higher Υ_{dyn} then yields the better match to the mass density than in case of a fully resolved central light profile. If this is really the case then Υ_{dyn} would be always overestimated without proper resolution of the central light profile. In this sense, the results for GMP5975 likely apply also to GMP1176. The exact offset in Υ_{dyn} should be expected to depend on the actual central light profile, though, and cannot be easily quantified.

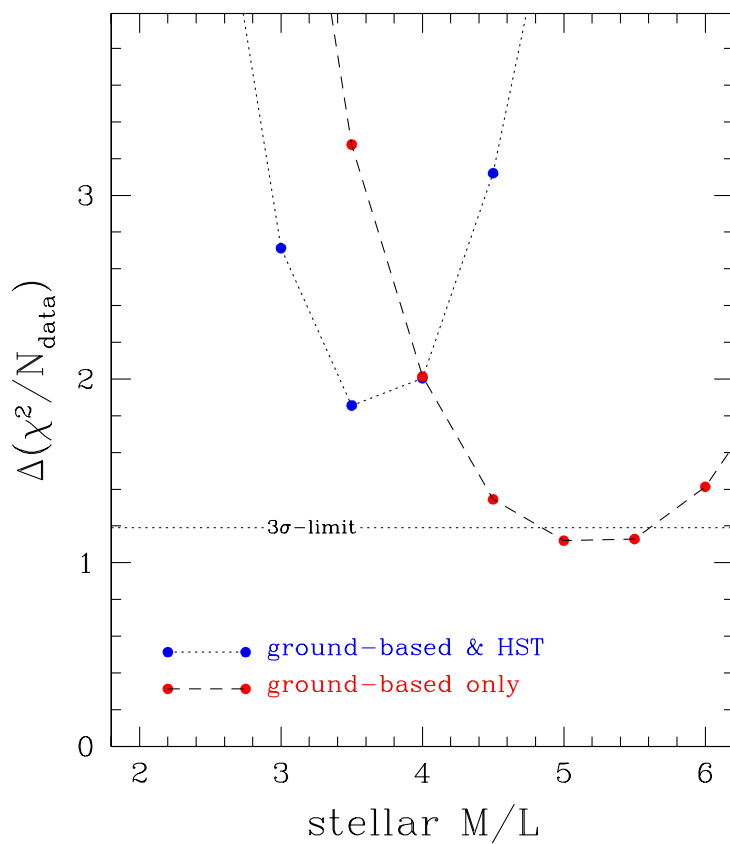


Figure A.1: Confidence levels $\Delta(\chi^2/N_{\text{data}})$ for self-consistent models of GMP5975. Blue, dotted: with joint HST + ground-based imaging; red, dashed: without ground-based photometry only.

Appendix B

The centre of GMP0144/NGC4957

The model fits to GMP0144 are unexpectedly poor, even with low regularisation (cf. Sec. 4.3). A likely explanation for the mismatch is that GMP0144 deviates significantly from axisymmetry. Observational support for this comes from: (1) significant differences in the central velocity dispersions from several long-slit observations (reviewed in Fig. B.1¹); (2) relatively large side-to-side asymmetries in all kinematical data sets (Fig. B.1); (3) isophotal twist in the central parts of the HST image (Fig. B.2). Fig. B.3 overviews the various slit positions from which the profiles of Fig. B.1 are obtained. Unfortunately, it is not possible to reconstruct the exact mapping of positive/negative radii onto the sky for every slit. So, positive/negative radii in Fig. B.1 do not necessarily refer to consistent parts of the galaxy. Albeit the definite structure in the centre of GMP0144 thus remains uncertain, the data at hand can be consistently interpreted in terms of a dynamically hot, decoupled structure in the lower-left quarter of Fig. B.3.

What ever the real structure of the centre finally is, the observations at hand are not consistent with exact axisymmetry. To avoid a direct influence of the central region on the dynamical models only the kinematical data outside $r > 0.2 r_{\text{eff}}$ have been considered for the fits. This excludes the whole diagonal axis and implies a lack of kinematical constraints inside $r < 1.8 \text{ kpc}$. Consequently, the statistical uncertainties of the galaxy models are rather large. Systematic errors due to a possible mismatch of the central potential cannot be quantified easily. These depend – among other things – on whether the centre is intrinsically really non-axisymmetric, or whether only the projection appears non-axisymmetric (due to dust, for example).

¹ The data of the three HET observing runs (provided by E. M. Corsini and R. P. Saglia, respectively) are not yet published.

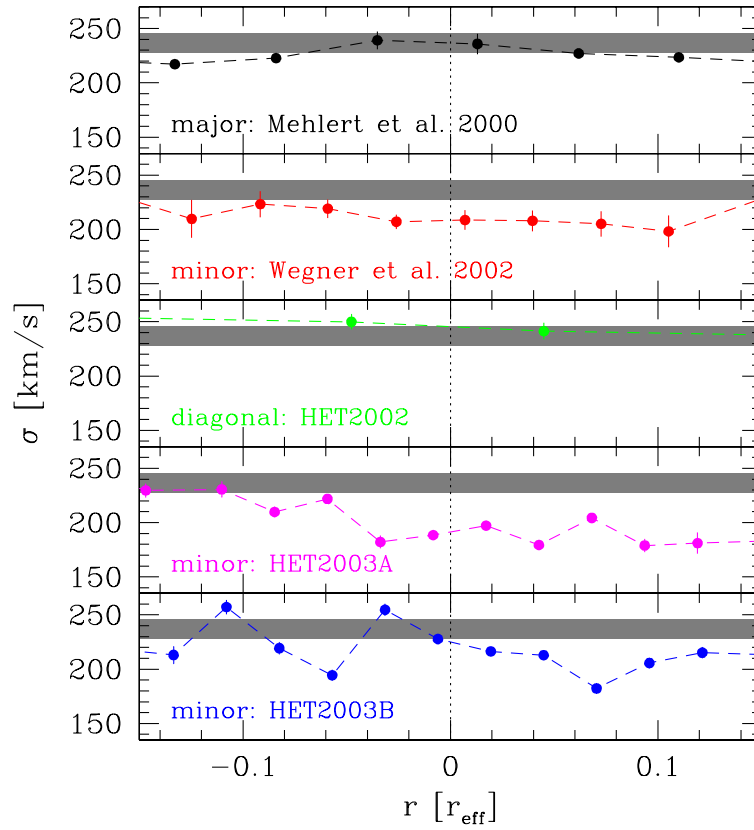


Figure B.1: Central velocity dispersion profiles from several observations (quoted in the panels; note also the exact slit positions shown in Fig. B.3). For comparison, the shaded area repeats the central major-axis dispersion (top panel) in each case.

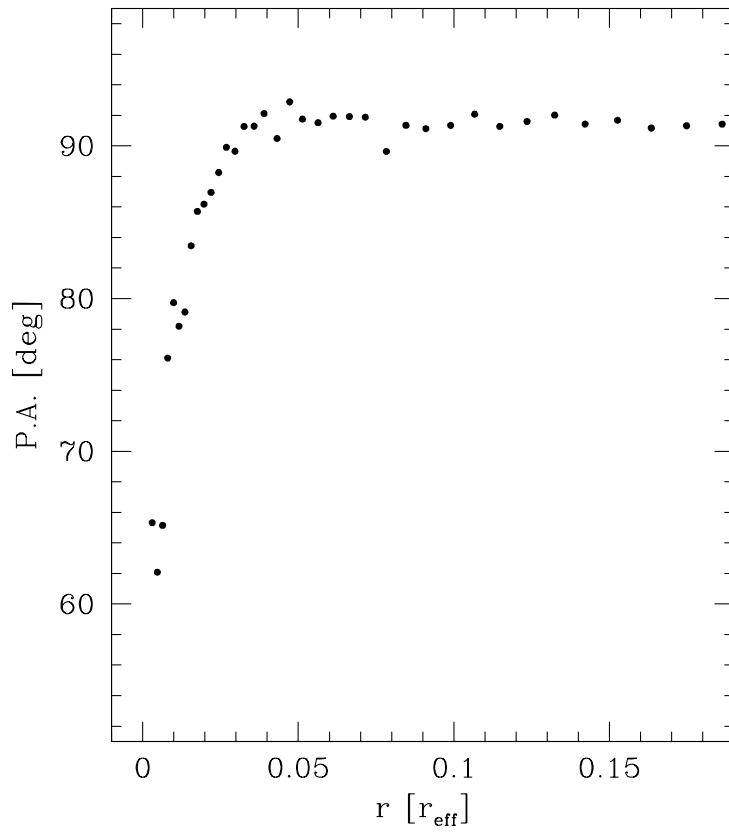


Figure B.2: Isophotal twist in the centre of GMP0144: position angles from isophotal fits to the central HST imaging.

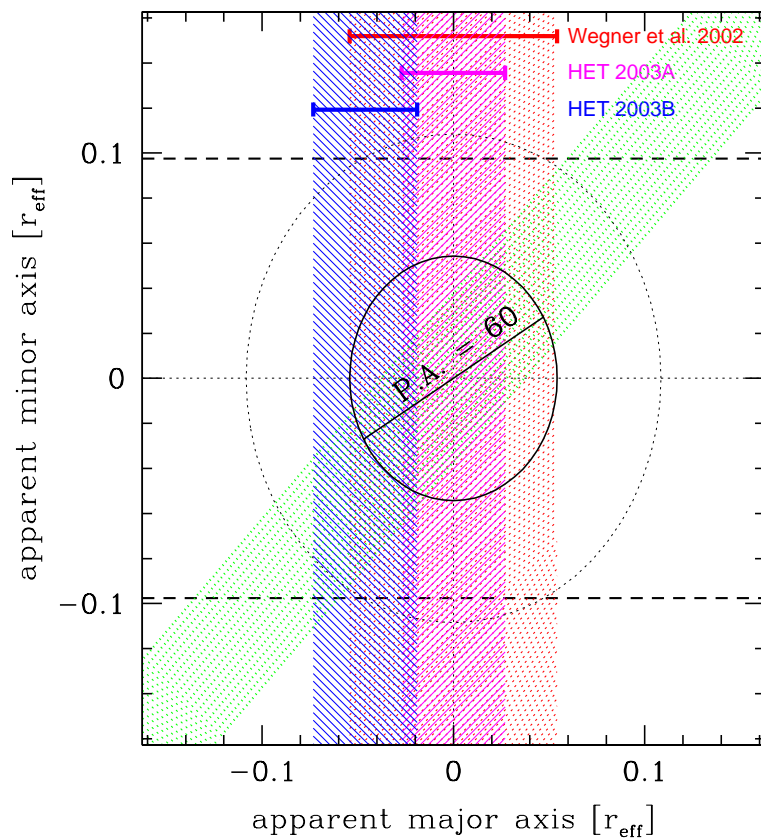


Figure B.3: Orientation of observing slits for GMP0144; colours correspond to Fig. B.1 (minor-axis observations are further labelled for the sake of clarity; the major-axis slit is bounded by the dashed lines); dotted line: PSF ($\sigma = 2'' \approx 0.1 r_{\text{eff}}$); black solid lines: distinct central structure ($r \lesssim 0.05 r_{\text{eff}}$ from Fig. B.2) and orientation of the most twisted isophote (P.A. = 60°).

Appendix C

Orbital shape parameters

Most axisymmetric potentials provide three integrals of motion: E , L_z and I_3 . While E and L_z confine orbits to the region inside the ZVC (cf Sec. 2.2.3), the third integral is related to the orbital contact points with the ZVC (e.g. Ollongren 1962). In practice, however, (1) the contact points are difficult to determine numerically and (2) the quantities E , L_z and the angle of the contact point cannot be directly interpreted in terms of the orbital shape. To label orbits with respect to their shapes Dehnen & Gerhard (1993) introduced “shape invariants” as approximate integrals of motion. Shape invariants simultaneously identify orbits (nearly) unambiguously and carry easy-to-interpret information about their shapes. In the same spirit, but with less attention on their approximate integral-of-motion character, here some computationally easy accessible orbital properties are defined that allow to identify orbits populating different regions in configuration space:

- **Mean radius.** A mean orbital radius $\langle r_{\text{orb}} \rangle$ is defined via

$$\langle r_{\text{orb}} \rangle_i \equiv \sum_k \frac{\Delta t_i^k}{T_i} r_i^k, \quad (\text{C.1})$$

where T_i is the total integration time of orbit i and r_i^k is its radius at time-step k (lasting Δt_i^k). As Fig. C.1 shows, $\langle r_{\text{orb}} \rangle$ is a measure of the orbital binding energy.

- **Radiality.** At a given energy – or mean radius – the angular momentum L_z is closely related to the pericentre r_{peri} and, thus, to the radial extension of an orbit. For the purpose of this work the radial extension near the equatorial plane (where most observational constraints come from) is of special interest. The (equatorial) “radiality” can be quantified by

$$\zeta \equiv \frac{r_{\text{sos,max}} - r_{\text{sos,min}}}{r_{\text{sos,max}}}, \quad (\text{C.2})$$

where $r_{\text{SOS,max}}$ and $r_{\text{SOS,min}}$ are the innermost and outermost crossings of an orbit with the SOS defined in Sec. 2.2.3. Radially floating orbits have $\zeta \rightarrow 1$, whereas radially localised orbits are described by $\zeta \rightarrow 0$. For orbits whose invariant curves consist of islands (near resonances) the radially ζ may differ from the true radial extension. For example, the 1:1 resonance in the meridional plane (so-called banana orbit) has $\zeta = 0$, albeit being radially spread (e.g. Richstone 1982). In any case, ζ gives the radially on the equator.

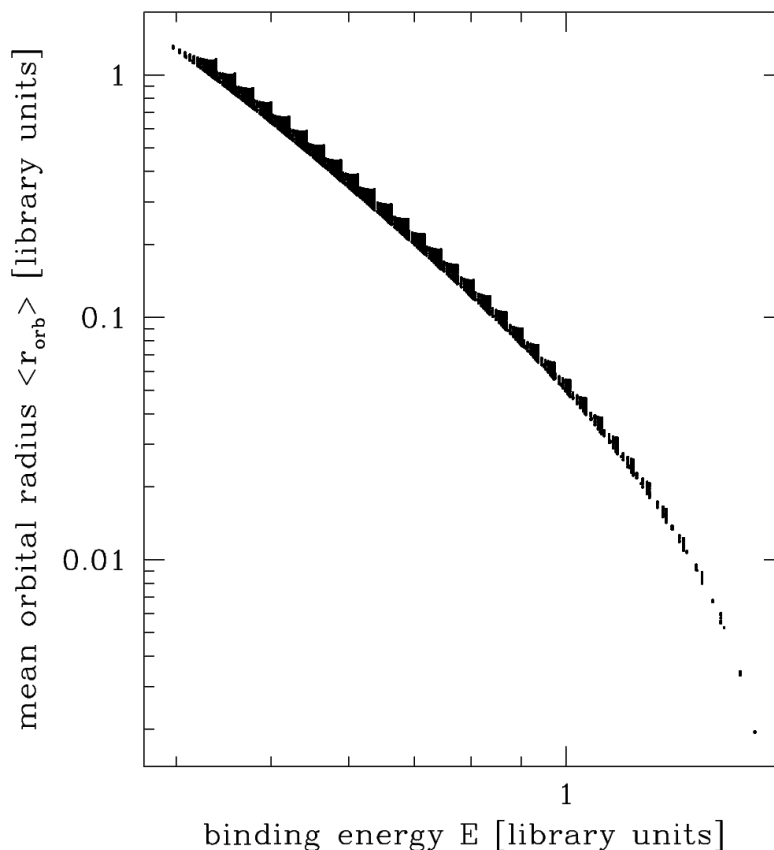


Figure C.1: Mean orbital radius $\langle r_{\text{orb}} \rangle$ versus orbital binding energy E in the bestfit potential of GMP5975.

- **Maximum latitude.** Fig. C.2 surveys orbits in a typical potential, the bestfit mass distribution of GMP5975. From the left column, for example, it can be drawn that given $\langle r_{\text{orb}} \rangle$ and ζ (roughly speaking energy and angular momentum) orbits differ basically in their vertical extension. An

appropriate measure of the latter is the maximum latitude

$$(\vartheta_{\max})_i \equiv \max_k \{\vartheta(t_i^k)\}, \quad (\text{C.3})$$

where $\vartheta(t_i^k)$ denotes the angle between the position along orbit i and the equator at time-step k .

- **Maximum vertical extension.** Similar to ϑ_{\max} the maximum vertical extension z_{\max} can be defined as

$$(z_{\max})_i \equiv \max_k \{z(t_i^k)\}, \quad (\text{C.4})$$

where z is the vertical distance to the equatorial plane.

Radiality ζ and maximum latitude ϑ_{\max} approximately correspond to the shape invariants D_R and θ_∞ of Dehnen & Gerhard (1993) and are used in the discussion of the orbital composition in Sec. 6. There, also z_{\max} is used to (1) specify orbits that are entirely covered by the major-axis slits and (2) to study the vertical structure of the DF.

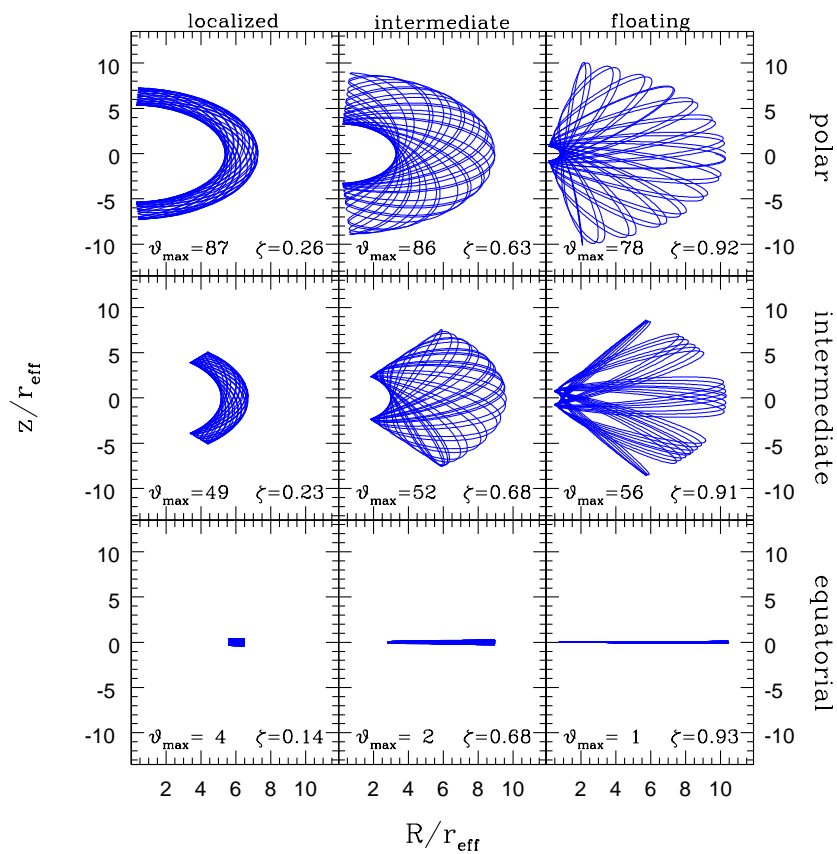


Figure C.2: Survey of orbits in the bestfit mass distribution of GMP5975. Orbits are arranged according to the scheme used in Chap. 6: polar orbits (top), intermediate tubes (middle) and disk orbits (bottom). Radiality ζ and maximum latitude ψ_{\max} are quoted for each orbit.

Appendix D

The average local distribution function

To visualise the distribution of light on different types of orbits an average local distribution function is used in Sec. 6. Given a set of orbits \mathcal{I} it is defined at every $\langle r_{\text{orb}} \rangle_i$, $i \in \mathcal{I}$, as follows:

$$f(\langle r_{\text{orb}} \rangle_i) \equiv \left\langle \frac{w}{V} \right\rangle_{\mathcal{I}(i)}, \quad (\text{D.1})$$

where

$$\mathcal{I}(i) \equiv \{j \in \mathcal{I} : |\langle r_{\text{orb}} \rangle_i - \langle r_{\text{orb}} \rangle_j| < 0.1 \times \langle r_{\text{orb}} \rangle_i\}. \quad (\text{D.2})$$

In words, the average phase-density of all orbits within 10 percent of the actual radius.

An example is given by Fig. D.1 for the most circular orbits of Fig. 6.12. Besides the red and the blue line showing the above defined average local DF f for the corresponding prograde and retrograde orbit subsets also the individual orbital phase-densities are plotted for comparison. If the scatter in the latter is large, then the average local DF traces the orbits with the largest densities (uppermost points). The low-density orbits do not contribute significantly to the average of equation (D.1). This is advantageous for the analysis of orbit models, since the modelling software cannot remove orbits completely but commonly produces a large spread among individual orbits in the low phase-density regions. Mainly, because if an orbit has a density, say, 5 orders of magnitude below the surrounding mean, its contribution to the model disappears in the numerical noise, it is effectively absent and its exact phase-density becomes insignificant.

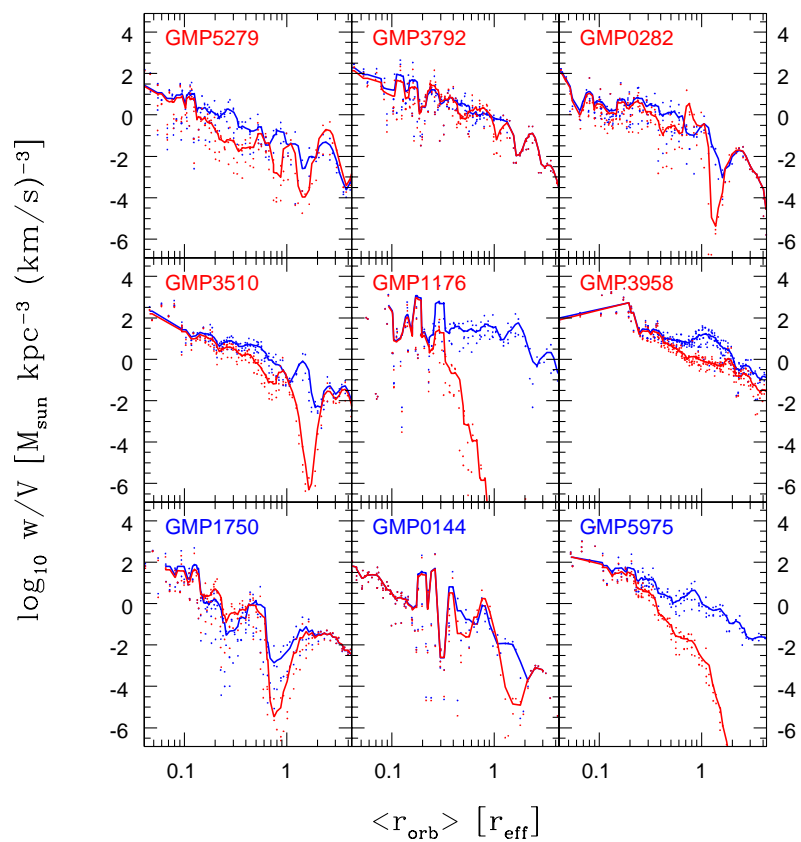


Figure D.1: Average local DF f and individual orbital phase-densities w/V of the most circular orbits from Fig. 6.12. Same colours as there. Note that blue and red curves partly overlap in the outer parts.

Appendix E

The triple nucleus of M31

In the following the paper Bender et al. (2005) on the nuclear structure of M31 is reproduced. It contains an application of the orbit superposition code advanced during the course of this work to the determination of black hole masses in the centres of galaxies.

HST STIS SPECTROSCOPY OF THE TRIPLE NUCLEUS OF M31:
TWO NESTED DISKS IN KEPLERIAN ROTATION AROUND
A SUPERMASSIVE BLACK HOLE

RALF BENDER,^{1,2,3} JOHN KORMENDY,⁴ GARY BOWER,⁵ RICHARD GREEN,⁶ JENS THOMAS,^{1,2} ANTHONY C. DANKS,⁷
THEODORE GULL,⁸ J. B. HUTCHINGS,⁹ C. L. JOSEPH,¹⁰ M. E. KAISER,¹¹ TOD R. LAUER,⁶ CHARLES H. NELSON,¹²
DOUGLAS RICHSTONE,¹³ DONNA WEISTROP,¹² AND BRUCE WOODGATE⁸

Received 2004 December 20; accepted 2005 May 9

ABSTRACT

We present *Hubble Space Telescope* (*HST*) spectroscopy of the nucleus of M31 obtained with the Space Telescope Imaging Spectrograph (STIS). Spectra that include the Ca II infrared triplet ($\lambda \simeq 8500 \text{ \AA}$) see only the red giant stars in the double brightness peaks P1 and P2. In contrast, spectra taken at $\lambda \simeq 3600\text{--}5100 \text{ \AA}$ are sensitive to the tiny blue nucleus embedded in P2, the lower surface brightness nucleus of the galaxy. P2 has a K-type spectrum, but we find that the blue nucleus has an A-type spectrum: it shows strong Balmer absorption lines. Hence, the blue nucleus is blue not because of AGN light but rather because it is dominated by hot stars. We show that the spectrum is well described by A0 giant stars, A0 dwarf stars, or a 200 Myr old, single-burst stellar population. White dwarfs, in contrast, cannot fit the blue nucleus spectrum. Given the small likelihood for stellar collisions, recent star formation appears to be the most plausible origin of the blue nucleus. In stellar population, size, and velocity dispersion, the blue nucleus is so different from P1 and P2 that we call it P3 and refer to the nucleus of M31 as triple.

Because P2 and P3 have very different spectra, we can make a clean decomposition of the red and blue stars and hence measure the light distribution and kinematics of each uncontaminated by the other. The line-of-sight velocity distributions of the red stars near P2 strengthen the support for Tremaine's eccentric disk model. Their wings indicate the presence of stars with velocities of up to 1000 km s^{-1} on the anti-P1 side of P2.

The kinematics of P3 are consistent with a circular stellar disk in Keplerian rotation around a supermassive black hole. If the P3 disk is perfectly thin, then the inclination angle $i \simeq 55^\circ$ is identical within the errors to the inclination of the eccentric disk models for P1+P2 by Peiris & Tremaine and by Salow & Statler. Both disks rotate in the same sense and are almost coplanar. The observed velocity dispersion of P3 is largely caused by blurred rotation and has a maximum value of $\sigma = 1183 \pm 201 \text{ km s}^{-1}$. This is much larger than the dispersion $\sigma \simeq 250 \text{ km s}^{-1}$ of the red stars along the same line of sight and is the largest integrated velocity dispersion observed in any galaxy. The rotation curve of P3 is symmetric around its center. It reaches an observed velocity of $V = 618 \pm 81 \text{ km s}^{-1}$ at radius $0''.05 = 0.19 \text{ pc}$, where the observed velocity dispersion is $\sigma = 674 \pm 95 \text{ km s}^{-1}$. The corresponding circular rotation velocity at this radius is $\sim 1700 \text{ km s}^{-1}$. We therefore confirm earlier suggestions that the central dark object interpreted as a supermassive black hole is located in P3.

Thin-disk and Schwarzschild models with intrinsic axial ratios $b/a \lesssim 0.26$ corresponding to inclinations between 55° and 58° match the P3 observations very well. Among these models, the best fit and the lowest black hole mass are obtained for a thin-disk model with $M_\bullet = 1.4 \times 10^8 M_\odot$. Allowing P3 to have some intrinsic thickness and considering possible systematic errors, the 1σ confidence range becomes $(1.1\text{--}2.3) \times 10^8 M_\odot$. The black hole mass determined from P3 is independent of but consistent with Peiris & Tremaine's mass estimate based on the eccentric disk model for P1+P2. It is ~ 2 times larger than the prediction by the correlation between M_\bullet and bulge velocity dispersion σ_{bulge} . Taken together with other reliable black hole mass determinations in nearby galaxies, notably the Milky Way and M32, this strengthens the evidence that the $M_\bullet\text{--}\sigma_{\text{bulge}}$ relation has significant intrinsic scatter, at least at low black hole masses.

We show that any dark star cluster alternative to a black hole must have a half-mass radius $\lesssim 0''.03 = 0.11 \text{ pc}$ in order to match the observations. Based on this, M31 becomes the third galaxy (after NGC 4258 and our Galaxy) in which clusters of brown dwarf stars or dead stars can be excluded on astrophysical grounds.

Subject headings: black hole physics — galaxies: individual (M31) — galaxies: nuclei

¹ Universitäts-Sternwarte, Scheinerstrasse 1, Munich D-81679, Germany; bender@usm.uni-muenchen.de, jthomas@usm.uni-muenchen.de.

² Max-Planck-Institut für Extraterrestrische Physik, Giessenbachstrasse, 85748 Garching-bei-München, Germany; bender@mpe.mpg.de.

³ Beatrice M. Tinsley Centennial Visiting Professor, University of Texas at Austin.

⁴ Department of Astronomy, University of Texas, RLM 15.308, C-1400, Austin, TX 78712; kormendy@astro.as.utexas.edu.

⁵ Computer Sciences Corporation, Space Telescope Science Institute, 3700 San Martin Drive, Baltimore, MD 21218; bower@stsci.edu.

⁶ National Optical Astronomy Observatory, P.O. Box 26732, Tucson, AZ 85726; green@noao.edu, lauer@noao.edu.

⁷ Emergent-IT, 1315 Peachtree Court, Bowie, MD 20721; danks@yahoo.com.

⁸ NASA Goddard Space Flight Center, Code 681, Greenbelt, MD 20771; gull@sea.gsfc.nasa.gov, woodgate@stars.gsfc.nasa.gov.

⁹ Herzberg Institute of Astrophysics, National Research Council of Canada, 5071 West Saanich Road, Victoria, BC V9E 2E7, Canada; john.hutchings@hia.nrc.ca.

¹⁰ Department of Physics and Astronomy, Rutgers University, P.O. Box 849, Piscataway, NJ 08855; cjoseph@physics.rutgers.edu.

¹¹ Department of Physics and Astronomy, Johns Hopkins University, Homewood Campus, Baltimore, MD 21218; kaiser@pha.jhu.edu.

¹² Department of Physics, University of Nevada, 4505 South Maryland Parkway, Las Vegas, NV 89154; cnelson@physics.unlv.edu, weistrop@physics.unlv.edu.

¹³ Department of Astronomy, University of Michigan, Dennison Building, Ann Arbor, MI 48109; dor@umich.edu.

1. INTRODUCTION

M31 was the second¹⁴ galaxy in which stellar dynamics revealed the presence of a supermassive black hole (BH; Kormendy 1987, 1988; Dressler & Richstone 1988). The spatial resolution of the discovery spectra was FWHM $\sim 1''$. Axisymmetric dynamical models implied BH masses of $M_{\bullet} = (1-10) \times 10^7 M_{\odot}$. The smallest masses were given by disk models, and the largest were given by spherical models.

In 1988, it was already known that axisymmetry is only an approximation to a more complicated structure. With Stratoscope II, Light et al. (1974) had observed that the nucleus is asymmetric. The brightest point is offset both from the center of the bulge (Nieto et al. 1986) and from the velocity dispersion peak (Dressler 1984; Dressler & Richstone 1988; Kormendy 1988). Then, using *Hubble Space Telescope* (HST), Lauer et al. (1993) discovered that the nucleus is double. The brighter nucleus, P1, is offset from the bulge center by $\sim 0''.5$. The fainter nucleus, P2, is approximately at the bulge center. Early concerns that an apparently double structure might only be due to dust were laid to rest when infrared images proved consistent with optical and ultraviolet images (Mould et al. 1989; Rich et al. 1996; Davidge et al. 1997; Corbin et al. 2001). These results were confirmed at higher resolution and signal-to-noise ratio (S/N) using WFPC2 (Lauer et al. 1998). With the discovery of the double nucleus, work on the central parts of M31 went into high gear.

Bacon et al. (1994, 2001) used integral-field spectroscopy to map the two-dimensional velocity field near the center of M31. They found that the kinematical major axis of the nucleus is not the same as the line that joins P1 and P2. The rotation curve is approximately symmetric about P2, i.e., about the center of the bulge. However, this is not the point of maximum dispersion. Instead, the brightest and hottest points are displaced from the rotation center by similar amounts in opposite directions.

The above results created two acute needs. First, the rich phenomenology of the double nucleus cried out for explanation. Second, the P1-P2 asymmetry raised doubts about BH mass measurements. This paper is mainly about the BH. HST allows us to take an important step inward by studying a blue cluster of stars embedded in P2. We introduce this cluster in § 1.1. Second, our spectroscopy of P1+P2 (§§ 2 and 3) provides further support for the preferred model of the double nucleus (Appendix). Since that model affects much of our discussion, we summarize it in § 1.2. For comprehensive reviews, see Peiris & Tremaine (2003) and Salow & Statler (2004).

1.1. P3: The Blue Star Cluster Embedded in P2

Nieto et al. (1986), using a photon-counting detector on the Canada-France-Hawaii Telescope (CFHT), were the first to illustrate that P2 is brighter than P1 at 3750 Å (contrast their Fig. 3 with Fig. 4 in Light et al. 1974; cf. Fig. 3 below). However, they did not realize this. Instead, they focused on the strong color gradient (bluer inward) and worried because this was inconsistent with published data. But these data were taken in the red or else had poor spatial resolution; they could not have seen the ultraviolet center. Nieto and collaborators found no problem with their data but concluded that “further observations are required to settle this question.”

King et al. (1992) confirmed the ultraviolet excess in the nucleus using the HST Faint Object Camera (FOC) at 1750 Å.

¹⁴ The first was M32 (Tonry 1984, 1987). In retrospect, the resolution was barely good enough for a successful BH detection (Kormendy 2004); i.e., the BH was discovered essentially as early as possible.

Using the same image, Crane et al. (1993a) illustrated that P2 is brighter than P1 but did not comment on this. Bertola et al. (1995) illustrated the same effect using FOC+F150W+F130LP images but again did not comment that it is P2, not P1, that is brighter in the ultraviolet.

Therefore, it was King et al. (1995) who discovered that P2 is much brighter than P1 in the ultraviolet. This result was again based on the 1750 Å FOC images. The blue light comes from a compact source that is embedded in P2 and that is similar in color and brightness to post-asymptotic giant branch (PAGB) stars seen elsewhere in the bulge (King et al. 1992; Bertola et al. 1995). King et al. (1995) proposed that the source might be nonthermal light from the weak active galactic nucleus (AGN) that is detected in the radio (Crane et al. 1992, 1993b), although they recognized that it could be a single PAGB star. Subsequently, Lauer et al. (1998) and Brown et al. (1998) resolved the source; its half-power radius is $\simeq 0''.06 = 0.2$ pc. Both papers argued that it is a cluster of stars. Lauer et al. (1998) combined the King et al. (1995) UV fluxes with optical fluxes to conclude that the source is consistent with an A star spectrum.

In this paper we present STIS spectra and show directly that the source is composed of A stars (§ 4). We also demonstrate that it is most consistent with a disk structure rather than with a dynamically hot cluster (§§ 5 and 6). Because the blue cluster is so distinct from P1+P2 in terms of stellar content and kinematics, we call it P3 and refer to the nucleus of M31 as triple.

The disk structure of P3 allows us to make a new and more reliable measurement of the central dark mass (§ 7). From the kinematics of P3 we also show that the dark object must be confined inside a radius $r \lesssim 0''.03 = 0.11$ pc. This implies that alternatives to a BH, such as a cluster of brown dwarf stars or stellar remnants, are inconsistent with the observations (§ 8).

1.2. The Eccentric Disk Model of P1+P2

Tremaine (1995) proposed what is now the standard model of P1 and P2. His motivation was the realization (see also Emsellem & Combes 1997) that the simplest alternative, an almost completed merger, is implausible. Two clusters in orbit around each other at a projected separation of $0''.49 = 1.8$ pc would merge in $\lesssim 10^8$ yr by dynamical friction. Instead, Tremaine proposed that both nuclei are parts of the same eccentric disk of stars. The brighter nucleus, P1, is farther from the BH and results from the lingering of stars near apocenter. The fainter nucleus, P2, is explained by increasing the disk density toward the center. A BH is required in P2 to make the potential almost Keplerian; only then might the alignment of orbits be maintained by the modest self-gravity of the disk.

Statler et al. (1999), Kormendy & Bender (1999, hereafter KB99), and Bacon et al. (2001) showed that the nucleus has the signature of the eccentric disk model. The most direct evidence is the asymmetry in $V(r)$ and $\sigma(r)$. Eccentric disk stars should linger at apocenter in P1; V and σ are observed to be relatively small there. The same stars should pass pericenter in P2, slightly on the anti-P1 side of the BH; the velocity amplitude is observed to be high on the anti-P1 side of the blue cluster. Because the PSF and the slit blur light from stars seen at different radii and viewing geometries, the apparent velocity dispersion should also have a sharp peak slightly on the anti-P1 side of the BH. All of the above papers demonstrated that the dispersion has a sharp peak in P2. KB99 showed further that the σ peak is slightly on the anti-P1 side of the blue cluster. Therefore, they suggested that the BH is in the blue cluster. Finally, KB99 demonstrated that the spectra and metal line strengths of P1 and P2 are similar to each other

TABLE 1
STIS INSTRUMENT CONFIGURATIONS

Parameter	Red Spectrum	Blue Spectrum
Detector gain ($e^- \text{ ADU}^{-1}$)	1.0	1.0
Grating	G750M	G430L
Wavelength range (\AA)	8272–8845	2900–5700
Reciprocal dispersion (\AA pixel^{-1})	0.56	2.73
Slit width (arcsec)	0.1	0.2
Comparison line FWHM (pixels)	3.1	3.5
$R = \lambda/\Delta\lambda$	4930	450
Instrumental dispersion σ_{instr} (km s^{-1})	56	284
Scale along slit (arcsec pixel^{-1})	0.051	0.051
Slit length (arcmin)	0.8	0.8
Integration time (s)	20790	2040

but different from those of the bulge. Therefore, P1 cannot be an accreted globular cluster or dwarf galaxy.

Peiris & Tremaine (2003) refined the eccentric disk model to optimize the fit to the higher resolution and more detailed ground-based spectroscopy now available. Even the Gauss-Hermite coefficients h_3 and h_4 , which were not used in constructing the model, were adequately well fitted. These models were then used to predict the kinematics that should be observed in our Ca triplet *HST* spectra of the red stars. This is a stringent test because the new models were used to predict observations taken at much higher resolution than those used to construct the models. Excellent fits were obtained. This is a resounding success of the eccentric disk model. The structural and velocity asymmetries of the nucleus can be explained almost perfectly if the eccentric disk is inclined with respect to the plane of the outer disk of M31. Here we publish the kinematic data used by Peiris & Tremaine (2003) in the above comparison (§ 3), and we revisit particularly interesting features of the STIS kinematics of P1+P2 in the Appendix.

The main shortcoming of the Peiris & Tremaine (2003) models is that they do not include the self-gravity of the stars in the eccentric disk. If the disk has a mass of 10% of the BH, then self-gravity is needed to keep the model aligned (Statler 1999). The most detailed such models are by Salow & Statler (2001, 2004). They model all available observations but do not fit the data as

well as the models by Peiris & Tremaine (2003). Other self-consistent models are based on N -body simulations (Bacon et al. 2001; Jacobs & Sellwood 2001); again, they reproduce only some of the observations. Sambhus & Sridhar (2002) use the Schwarzschild (1979) method to model the double nucleus. The above models differ in many details. For example, the Salow & Statler (2001, 2004) models precess rapidly, with pattern speeds of $36 \pm 4 \text{ km s}^{-1} \text{ pc}^{-1}$; the models of Sambhus & Sridhar (2002) precess at $16 \text{ km s}^{-1} \text{ pc}^{-1}$, and the simulations of Bacon et al. (2001) precess at only $3 \text{ km s}^{-1} \text{ pc}^{-1}$. Not surprisingly, the construction of dynamical models that include self-gravity is a challenge. The conclusion that such models are long lived is less secure than the result that they can instantaneously fit the photometry and kinematics of P1+P2. Tremaine (2001) gives a general discussion of slowly precessing eccentric disks.

Because of these complications, the BH mass in M31 has remained uncertain. Estimates of M_\bullet by Dressler & Richstone (1988), Kormendy (1988), Richstone et al. (1990), Bacon et al. (1994), Magorrian et al. (1998), KB99, Bacon et al. (2001), Peiris & Tremaine (2003), and Salow & Statler (2004) have ranged over a factor of about 3, $M_\bullet \simeq (3-10) \times 10^7 M_\odot$. These results are reviewed and error bars are tabulated on a uniform distance scale ($D = 0.76 \text{ Mpc}$) in Kormendy (2004). In this paper we show that an analysis of the UV-bright nucleus P3 allows us to estimate the BH mass independent of P1+P2.

2. STIS SPECTROSCOPY

The STIS CCD observations of M31 were obtained on 1999 July 23–24. The slit was aligned at P.A. = 39° . Other details of the STIS configuration are given in Table 1. We obtained a spectrum that includes the calcium triplet, $\lambda\lambda 8498, 8542,$ and 8662 , and one at $2700-5200 \text{ \AA}$ that includes several Balmer lines and Ca II H and K ($\lambda\lambda 3933$ and 3968). Both wavelength regions were observed because we wanted to analyze separately the double nucleus P1+P2 and the central blue cluster P3. Figure 1 shows that the double nucleus P1+P2 contributes almost all of the light at red wavelengths, while P3 dominates at 3000 \AA . The color difference between P1+P2 and P3 is illustrated further in the brightness cuts in Figure 3 below. The red spectrum was obtained using the $52'' \times 0''.1$ slit, while the blue spectrum was

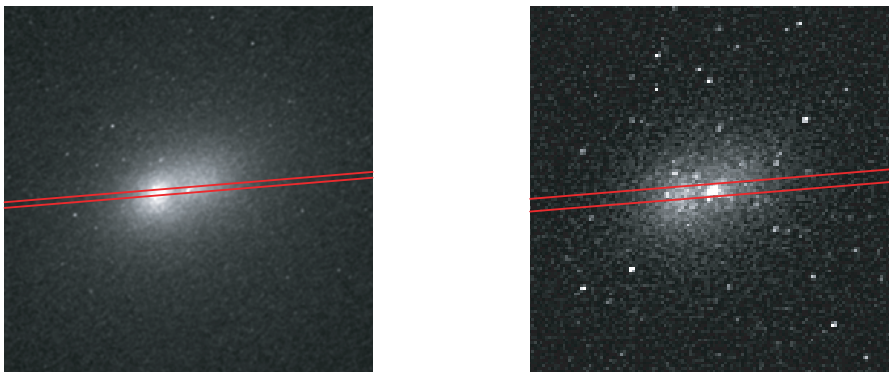


FIG. 1.—STIS slit positions superimposed on the WFPC2 images from Lauer et al. (1998). The left panel shows the $0''.1$ slit position for the Ca II spectrum on the F555W image, and the right panel shows the $0''.2$ slit position for the blue spectrum on the F300W image. The images cover the central $6''.4 \times 6''.4$. North is $55''.7$ counterclockwise from up.

taken with the $52'' \times 0''.2$ slit. A wider slit was chosen for the blue spectrum to ensure that P3 would fall inside the slit. Figure 1 shows the placement of the slit relative to the WFPC2 F555W and F300W images from Lauer et al. (1998). These slit positions were determined by comparing the light profiles along the slit in our STIS spectra with brightness cuts through the WFPC2 images. We measured the slit positions to an accuracy of $0''.005$ for the red spectrum and $0''.01$ for the blue spectrum. The total integration time for the red spectrum was split into two exposures of approximately 1200 s each per *HST* orbit. M31's nucleus was shifted by 4.1 pixels along the slit between orbits.

The total integration time for the blue spectrum was split into three equal exposures within one *HST* orbit. The nucleus was shifted by 4.3 pixels between successive exposures. Wavelength calibrations (wavecals) were interspersed among the galaxy exposures to allow wavelength calibration, including correction for thermal drifts. For the red spectrum, we obtained contemporaneous flat-field exposures through the same slit while M31 was occulted by the Earth. These provide proper calibration of internal fringing, which is significant at $\lambda \geq 7500 \text{ \AA}$ (see Goudfrooij et al. 1997).

The spectra were reduced as described in Bower et al. (2001). Unlike red spectra taken at $\lambda \geq 7500 \text{ \AA}$ with the G750M grating, blue spectra taken with the G430L grating are not affected by fringing. Consequently, we flat-fielded the G430L data using the library flat image from the STIS archive. The final reduced spectra have maximum S/N values of $S/N = 25$ (G750M) and 50 \AA^{-1} (G430L).

A stellar template spectrum is needed to measure the stellar kinematics implied by the galaxy spectra. For the red spectrum of M31, our template is the STIS spectrum of HR 7615 from Bower et al. (2001). They document the observational setup and data reduction for this spectrum. For the blue spectrum we used template A stars from Le Borgne et al. (2003), white dwarf stars observed in the Sloan Digital Sky Survey (SDSS; Kleinman et al. 2004) or modeled by Finley et al. (1997) and Koester et al. (2001), and spectral syntheses of various stellar population models by Bruzual & Charlot (2003). These sources were supplemented for checking purposes by using standard stars from Pickles (1998). Spectral resolution is not an issue for standard stars because the intrinsic width of the absorption lines in A-type stars is much larger than the instrumental width of STIS with the G430L grating and because the spectrum of P3 proves to have exceedingly broad lines.

3. KINEMATICS OF THE DOUBLE NUCLEUS P1+P2

The calcium triplet spectroscopy sees only the red giant stars that make up the double nucleus, P1+P2. It is blind to P3, which contributes essentially no light at $\lambda \simeq 8500 \text{ \AA}$. The kinematic properties of the red stars are illustrated in Figure 2.

In Figure 2, the spectrum of the bulge has been subtracted following procedures discussed in KB99. Bulge subtraction is analogous to sky subtraction in the sense that it removes the effects of a contaminating spectrum that is not of present interest. As shown in KB99, the bulge of M31 dominates the light distribution only at radii $r \geq 2''$. At $r < 1''$, it contributes about 20% of the light. So over the radii of interest in Figure 2, bulge stars are a minor foreground and background contaminant; they do not significantly participate in the dynamics of the double nucleus. It is routine to estimate the small contribution of bulge stars to the STIS red spectrum and to subtract it. Figure 2 is therefore a pure measure of the kinematics of the stars that make up the double nucleus.

Figure 2 also shows the bulge-subtracted nuclear kinematics measured with CFHT (KB99). Taking into account both the PSF

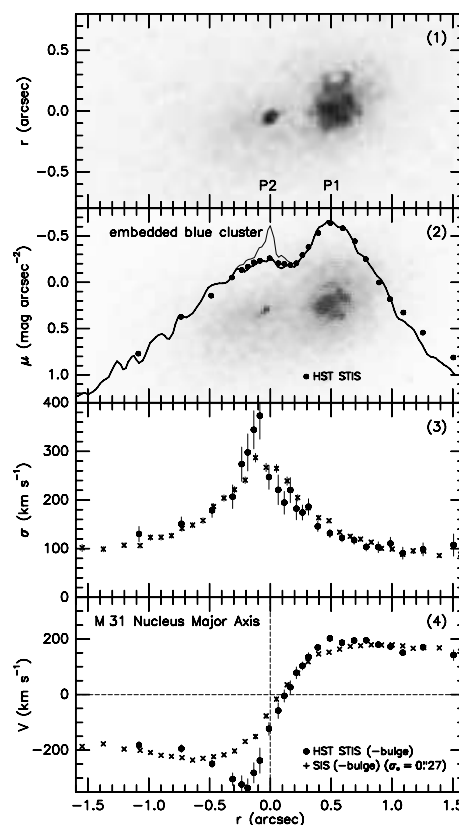


FIG. 2.—Panel 1 shows the double nucleus of M31 rotated $\sim 185^\circ$ clockwise with respect to Fig. 1. It is a $I+V+3000 \text{ \AA}$ composite from KB99. P1 is brighter than P2 in red light. Embedded in P2 is P3, i.e., a tiny cluster of blue stars that is invisible in I but brighter than P1 in the ultraviolet. The background image in panel 2 is a similar $V+3000 \text{ \AA}$ composite that better shows the small radius of P3. Panel 2 includes an I -band brightness cut along the P1-P2 axis (lower line) and a V -band cut through the blue cluster P3 (upper line). The filled circles are the brightness profile in the STIS spectrum; they are used to register the kinematics with the photometry in radius. Along the P1-P2 axis, radius $r = 0$ is chosen to be the center of P3 (note that in KB99 we centered the radius scale at $0''.068$, not P3). Panels 3 and 4 show velocity dispersions and rotation velocities along the P1-P2 axis after subtraction of the bulge. The ground-based points (crosses) are from the Subarcsecond Imaging Spectrograph (“SIS”) and the CFHT (KB99). The STIS data (filled circles) are Fourier quotient reductions. Bacon et al. (2001) made an independent reduction of our red STIS spectrum; it is consistent with ours.

and the slit, the effective Gaussian dispersion radius of the effective PSF was $\sigma_* = 0''.297$ (Kormendy 2004). The corresponding resolution of the STIS red spectroscopy is $\sigma_* = 0''.052$.

Confirming results of KB99, the dispersion profile of the red stars reaches a sharp peak slightly on the anti-P1 side of P3. The peak dispersion is higher at STIS resolution ($\sigma = 373 \pm 50 \text{ km s}^{-1}$) than at CFHT resolution ($\sigma = 287 \pm 9 \text{ km s}^{-1}$). The rotation curve is also asymmetric; the maximum rotation velocity is larger on the anti-P1 side than it is in P1. Again, the

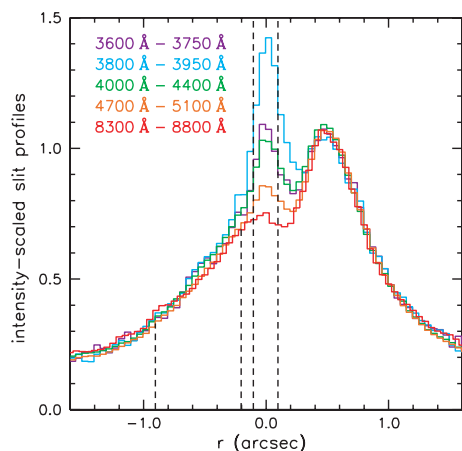


FIG. 3.—Linear intensity cuts through the blue and red spectra of P1+P2+P3. Each cut is an average over the wavelength range given in the key. The contrast between the blue cluster P3 and the underlying red nucleus P2 is largest at 4000 Å. It is smaller at redder wavelengths because the stars in P3 are blue. It is smaller at bluer wavelengths because the spectrum of P3 has a strong Balmer break (Fig. 4). The two leftmost vertical dashed lines indicate the region in which the background spectrum was derived. The two rightmost vertical dashed lines indicate the radius range over which we averaged the background-subtracted P3 spectrum shown in Figs. 4, 5, and 6.

asymmetry is larger and the radius of maximum rotation is smaller at STIS resolution than at CFHT resolution. These observations are consistent with and provide further evidence for Tremaine’s (1995) model for the double nucleus as an eccentric disk of stars orbiting the central BH. The Appendix provides more detailed discussion.

4. THE INTEGRATED SPECTRUM OF P3

4.1. P3 Is Made of A-Type Stars

P3, the compact blue cluster, is illustrated in the two panels of images in Figure 2. It is embedded in P2 but is not concentric with it; the photocenter of P2 is $\sim 0''.03$ on the anti-P1 side of the blue cluster. The center of the bulge is slightly off in the opposite direction, i.e., toward P1 (see KB99 and discussion below). Note that we choose $r = 0$ to be the center of P3, whereas KB99 chose $r = 0$ to be the center of the bulge.

We obtained our STIS spectrum at $\lambda \simeq 3500\text{--}5000$ Å in part to study this issue. Over the above wavelength range, P3 provides a strong signal, much stronger than that indicated by the V -band brightness cut in Figure 2. Figure 3 shows brightness cuts through the red and blue STIS spectra in various wavelength ranges. The blue cluster is essentially invisible at 8300–8800 Å in the red spectrum. We assume that this spectrum provides the surface brightness profile of the underlying double nucleus. With respect to this profile, P3 is, in general, more prominent at bluer wavelengths.¹⁵ The contrast over P1+P2 is

¹⁵ P3 looks fainter at 4700–5100 Å in Fig. 3 than at 5500 Å (V -band) in Fig. 2. The reason is that Fig. 2 shows a brightness cut through the deconvolved V -band image from Lauer et al. (1998); this has higher spatial resolution than an un-deconvolved STIS spectrum. Also, the V -band cut is $0''.046$ wide, while the spectrum was obtained through a $0''.2$ wide slit.

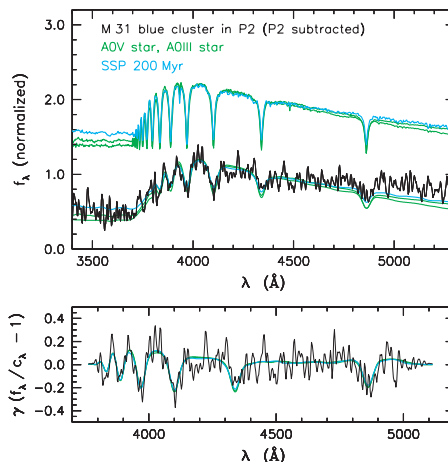


FIG. 4.—Spectrum (black line) of the central $0''.2$ of the blue cluster P3. The superposed spectrum of the stars in the bulge and nucleus has been subtracted. Flux is in arbitrary linear units. In the bottom panel, the spectrum has been divided by a polynomial c_λ fitted to the continuum; it has been normalized to zero intensity and multiplied by the mean ratio γ of the line strength in the standard stars to that in P3. The colored lines show the spectra of an A0 dwarf star, an A0 giant star, and a Bruzual & Charlot (2003) starburst of age 200 Myr before (top) and after (overplotted on the data) broadening to the LOSVD that best fits the cluster spectrum. The fit was carried out with the Fourier correlation quotient program (Bender 1990).

highest at 3800–3950 Å. Then P3 gets less prominent at 3600–3750 Å; the reason turns out to be that the spectrum has a strong Balmer break (Fig. 4). The important conclusion from Figure 3 is that the spectrum of P3 is almost as bright as the underlying spectrum of P1+P2 at just the wavelengths where hydrogen Balmer lines are strongest.

It is therefore possible to extract a clean spectrum of P3 despite the short integration time and modest S/N. We averaged the spectrum of P3 over the $0''.2$ (i.e., four spectral rows) in which it is brightest (Fig. 3, right pair of dashed lines). We approximated the spectrum of the underlying P2 stars by averaging 14 rows of the spectrum on the anti-P1 side of P3 (Fig. 3, left pair of dashed lines). The 8300–8800 Å brightness cut was used to scale this average P2 spectrum to the P2 brightness underlying P3. The result was subtracted from the four-row average spectrum of P2+P3. The resulting spectrum of P3 is shown in black in Figures 4, 5, and 6.

The stellar population of P3 is dramatically different from that of P1 and P2. The spectrum in Figure 4 is dominated by Balmer absorption lines. At least five Balmer lines are visible, starting with $H\beta$ at $\lambda_{\text{obs}} \simeq 4856$ Å. Also prominent is a strong Balmer break. In fact, the spectrum is very well matched by velocity-broadened spectra of A giant and dwarf stars. This confirms that the nucleus is made mostly of A-type stars as Lauer et al. (1998) and Brown et al. (1998) suggested.

4.2. The Remarkably High Velocity Dispersion of P3: The Supermassive Black Hole Is in the Blue Cluster

The blue cluster has a remarkably high velocity dispersion. Using an A0 dwarf star from Le Borgne et al. (2003) as a template,

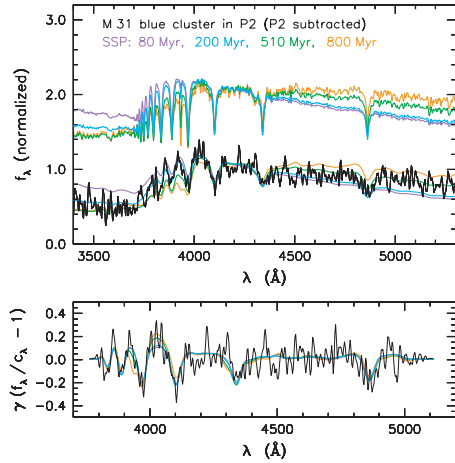


FIG. 5.—This figure is analogous to Fig. 4, except that the spectrum of the blue cluster P3 is compared with Bruzual & Charlot (2003) starbursts of various ages given in the key. The fit to the red continuum is best for an age of ~ 510 Myr, but then the strengths of the Balmer lines H_n for $n \geq 5$ are wrong relative to the strengths of the redder lines. This problem gets worse for older starburst ages. Starbursts younger than 200 Myr are too blue; their Balmer breaks are too small to fit the observed spectrum.

the Fourier correlation quotient program (Bender 1990) gives a velocity dispersion of $\sigma = 962 \pm 105 \text{ km s}^{-1}$. An A0 giant star gives $\sigma = 984 \pm 107 \text{ km s}^{-1}$. A-type stars have intrinsically broad lines, but σ is so large that the difference between using giants and dwarfs is insignificant. The above fits are illustrated in Figure 4. The match to the lines and to the Balmer break is excellent. The results are robust; plausible changes in the intensity scaling of the P2 spectrum that was subtracted produce no significant change in σ .

The best-fitting 200 Myr old stellar population model (Fig. 5, § 4.3) gives a dispersion of $\sigma = 984 \pm 106 \text{ km s}^{-1}$. We adopt the average of the dispersion values given by the A dwarf star, the A giant star, and the 200 Myr old stellar population model; this gives $\sigma = 977 \pm 106 \text{ km s}^{-1}$ as our measure of the velocity dispersion of P3 integrated over the central $0''.02$.

Despite its tiny size (half-power radius $\approx 0''.06 \approx 0.2 \text{ pc}$; Lauer et al. 1998), P3 has the highest integrated velocity dispersion measured to date in any galaxy. The velocity dispersion of P3 is even larger than the line-of-sight velocity dispersion of the Sgr A* cluster in our Galaxy ($\sigma = 498 \pm 52$ to $840 \pm 104 \text{ km s}^{-1}$, depending on the sample of stars chosen; Schönkel et al. 2003).¹⁶ The high velocity dispersion of P3 is especially remarkable in view of the observation (Fig. 2) that the velocity dispersion of the red stars *along the same line of sight* is only $\sim 250 \text{ km s}^{-1}$. The maximum velocity dispersion of P2, $373 \pm 48 \text{ km s}^{-1}$ at $\Delta r \approx 0''.06$ on the anti-P1 side of the blue cluster, is much smaller than that of P3. Even the remarkably high velocity dispersion $\sigma = 440 \pm 70 \text{ km s}^{-1}$ measured in P2 by Statler et al. (1999) is much

¹⁶ Of course, the pericenter velocities of the innermost individual stars in our Galaxy are in some cases much larger. The current record is held by S0-16, which was moving at $12,000 \pm 2000 \text{ km s}^{-1}$ when it passed within $45 \text{ AU} = 0.0002 \text{ pc} = 600$ Schwarzschild radii of the Galaxy's BH (Ghez et al. 2005).

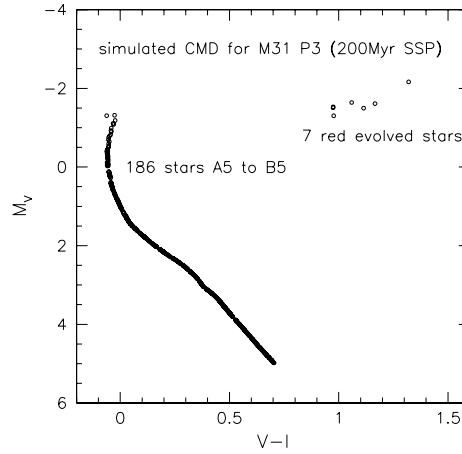


FIG. 6.—Sample CMD of a 200 Myr old single-burst population with solar metallicity and a total luminosity of $M_V = -5.7$. The spectrum is dominated by stars of $\sim 10,000 \text{ K}$ temperature. The diagram has been generated using the synthetic CMD algorithm of the Instituto de Astrofísica de Canarias (Aparicio & Gallart 2004).

smaller than the velocity dispersion of P3. This confirms the conclusion of KB99 that the M31 supermassive BH is in the blue cluster.

4.3. Fit of a Starburst Spectrum to P3

The overall continuum slope of P3 is best fitted not by a single A-type star but rather by the spectrum (Bruzual & Charlot 2003) of a single starburst population (SSP in Figs. 4 and 5) of age $\sim 200 \pm 50$ Myr and solar metallicity. The blue continuum fit is essentially perfect; the red continuum fit is improved slightly over the single-star fits. Starburst spectra with a range of ages are shown in Figure 5. Using older starbursts allows us to fix the fit to the 5000 Å continuum, but only at an unacceptable price: the bluest Balmer lines are no longer well fitted. Complicating the model further would be overinterpretation; the error in the red continuum fit could be due to imperfect P2 subtraction or to small amounts of dust. But it is clear that we cannot exclude some admixture of older stars. Reasonable changes in metallicity also do not affect the fit: metallicity changes are largely degenerate with age changes.

How many stars make up P3? For an absolute visual magnitude of $M_V \approx -5.7$ (Lauer et al. 1998), we estimate the answer in Figure 6, using IAC-STAR, the synthetic color-magnitude diagram (CMD) algorithm of the Instituto de Astrofísica de Canarias (Aparicio & Gallart 2004). A 200 Myr old, single-burst population of solar abundance implies that about 200 stars between spectral types A5 and B5 dominate the spectrum. The large number of stars at the same temperature of $\sim 10,000 \text{ K}$ explains why the spectrum of P3 is so similar to that of a single A0 star. Figure 6 also shows why P3 has a fairly smooth appearance, although surface brightness fluctuations are visible in Figure 8 below. Only a few red evolved stars are present, and they do not contribute significantly to the light of P3. Future observations with resolutions of about $0''.01$ should resolve the brightest stars close to the BH.

For a Salpeter (1955) initial mass function with a lower mass cutoff at $0.1 M_{\odot}$, the total number of stars on the main sequence at present is $\sim 15,000$; their total mass is about $4200 M_{\odot}$. If the burst originally produced stars up to $100 M_{\odot}$, then the initial total mass of P3 was $\sim 5200 M_{\odot}$. Given the inefficiency of star formation, the total gas mass required to form P3 probably was of the order $10^6 M_{\odot}$.

Forming stars so close to a BH is not trivial. It may be possible if $\sim 3 \times 10^6 M_{\odot}$ of gas could be concentrated into a thin disk of radius 0.3 pc and velocity dispersion 10 km s^{-1} . Then Toomre's (1964) stability parameter $Q \approx 1$. It is not easy to see how such an extreme configuration could be set up, especially without forming stars already at larger radii. Well before the BH makes star formation difficult, the surface density of the dissipating and shrinking gas disk would get high enough so that the Schmidt (1959) law observed in nuclear starbursting disks (Kormendy & Kennicutt 2004, Fig. 21) would imply a very high star formation rate. This star formation would have to be quenched until the gas disk got small enough to form P3. And then the star formation would have to be very inefficient to put only $\sim 5200 M_{\odot}$ of the $\sim 3 \times 10^6 M_{\odot}$ of gas into stars. Similar considerations make it difficult to understand young stars near the Galactic center BH (e.g., Morris 1993; Genzel et al. 2003; Ghez et al. 2003, 2005). Nevertheless, young stars (or at least high-luminosity, hot stars) are present. Complicated processes of star formation (e.g., Sanders 1998) may not realistically be evaluated by a simple argument based on the Toomre Q instability parameter. So, if a dense enough and cold enough gas disk can be formed, star formation may be possible, even close to a supermassive BH.

4.4. Could the Hot Stars in P3 Result From Stellar Collisions?

The alternative to a starburst could be that the hot stars of P3 are formed via collisions between lower mass stars in P3 or even in P1+P2. Yu (2003) argues that the collision timescales are too long to be of interest. It would be interesting to revisit this issue given the conclusion of § 6.1 that P3 is a cold stellar disk. In any case, it is worth noting that the conversion of, say, a high-mass, $0.5 M_{\odot}$ main-sequence star in P2 into an A star requires merging roughly six stars without mass loss. It is not easy to see how the A stars in P3 could originate by collisions.

Thus, the situation in P3 is similar to that in our Galaxy. No explanation of the hot stars looks especially plausible.

4.5. P3 Is Not Made of White Dwarf Stars

Finally, we need a sanity check to make sure that we are not completely misinterpreting the observations. Dynamically, we detect a $10^8 M_{\odot}$ central dark object. This is associated with a tiny and faint nucleus comprised of hot stars that have extraordinarily broad absorption lines. White dwarf stars have extraordinarily broad absorption lines. If they are not too old, they can easily have an A-type spectrum, and if they are not too young, they can easily contribute mass without contributing much light. It is natural to wonder, could P3 be a cluster of white dwarfs? Could they simultaneously explain the broad-lined, A-type spectrum and the central dark mass? This possibility is not excluded by stellar collision or cluster evaporation timescales (Maoz 1995, 1998).

Figures 7 and 8 show that P3 cannot be made of white dwarfs. Figure 7 compares the spectrum of P3 with that of a typical DA white dwarf observed in the SDSS. The star was chosen to have Balmer line strengths comparable to those in P3. It is approximately the best match to P3 that can be achieved with white dwarf spectra. Its lines are narrower than those of P3, so we can fit the observed line widths (Fig. 7, bottom panel) with

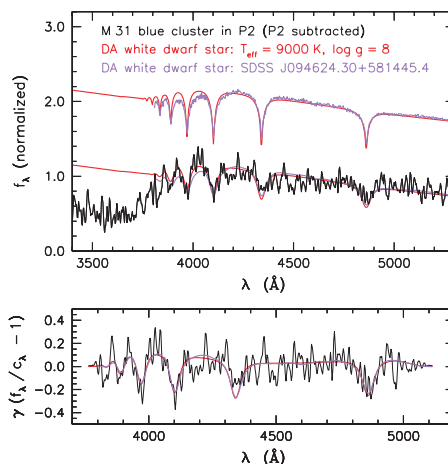


Fig. 7.—Spectrum of P3 fitted with approximately matched observed and model white dwarf spectra. The observed spectrum is from the SDSS (Kleinman et al. 2004; see <http://www.sdss.org>). The model spectra used in Figs. 7 and 8 are from Finley et al. (1997) and Koester et al. (2001). The fits of white dwarf spectra to P3 are significantly worse than the ones in Figs. 4 and 5. The absorption lines of the white dwarfs are intrinsically too strong, and the white dwarfs fail completely to fit the large Balmer continuum break in the P3 spectrum. However, the implied velocity dispersion, $\sigma = 885 \pm 126 \text{ km s}^{-1}$, is consistent with our adopted value, $\sigma = 977 \pm 106 \text{ km s}^{-1}$.

$\sigma = 885 \pm 126 \text{ km s}^{-1}$. That is, this relatively narrow-lined white dwarf gives a dispersion similar to those implied by main-sequence and giant A stars. The fit to the line widths is less good than the fit provided by A0 V stars, but it is not inconsistent with our low-S/N spectrum of P3. If we had only the spectrum of this white dwarf as observed over the relatively narrow wavelength region redward of the Balmer break, we could not exclude white dwarf stars.

However, the continua of white dwarf stars do not fit the large Balmer break in P3. SDSS J094624.30+581445.4 (Fig. 7) does not show this: it and most other white dwarfs have not been observed at blue enough wavelengths to reach the Balmer break. Therefore, we resort to model spectra kindly provided by Detlev Koester (Finley et al. 1997; Koester et al. 2001). Figure 7 shows a model spectrum that has line profiles similar to those in the observed white dwarf. The price of having narrow enough lines to fit the absorption lines in P3 is that there is essentially no Balmer break. Such a star cannot fit the continuum of P3. This result is very robust; it is not affected by uncertainties in the subtraction of the spectra of P1+P2.

Choosing different white dwarf parameters does not solve this problem. No combination of temperature and gravity allows a simultaneous match to the Balmer line strengths and the Balmer break. Figure 8 shows fits of model white dwarf spectra with temperatures $T = 7000, 8000, 10,000,$ and $12,000 \text{ K}$. For each temperature, we try surface gravities of $10^7, 10^8,$ and 10^9 cm s^{-2} .

Temperature $T \approx 7000 \text{ K}$ is too cold. The stellar lines are too weak. Not surprisingly, these stars have no Balmer break at all. Despite the bad continuum fit, the narrow lines in the white dwarf templates give dispersions $\sigma = 945 \pm 103, 987 \pm 107,$ and $1063 \pm 115 \text{ km s}^{-1}$ that are consistent with our adopted result.

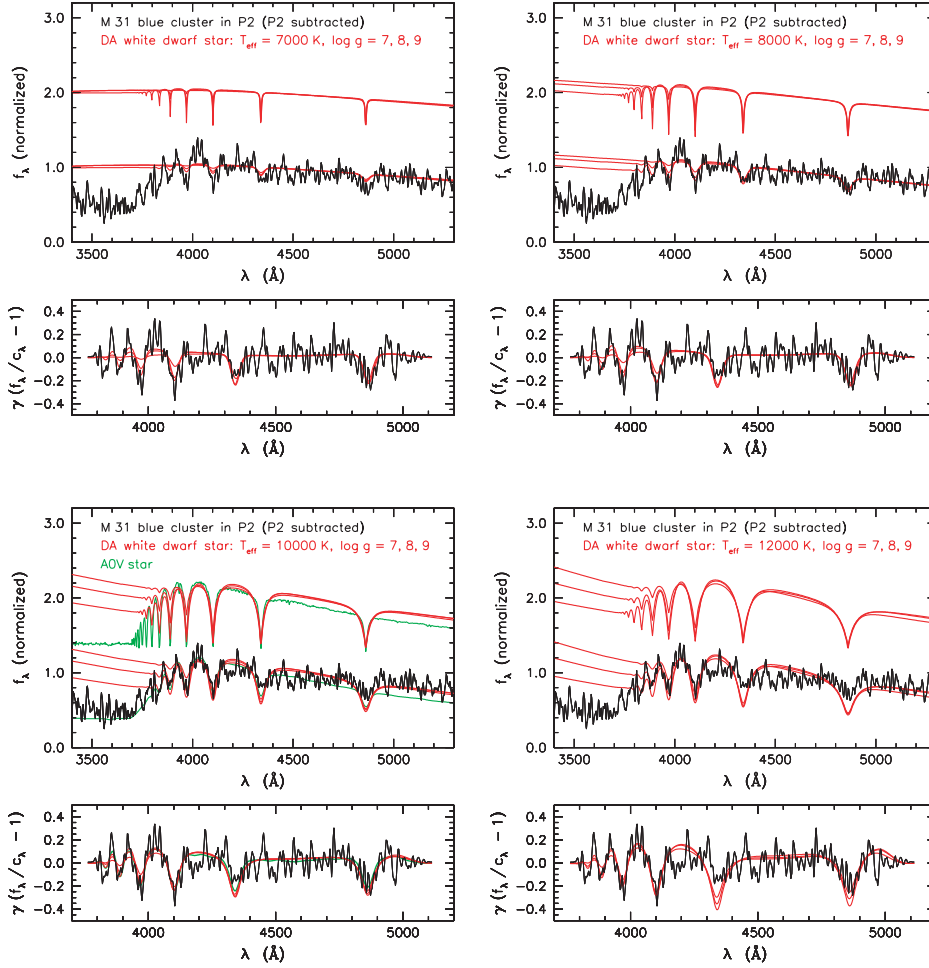


FIG. 8.—Fits to the spectrum of P3 (black line) of model white dwarf spectra (red line) with temperature $T_{\text{eff}} = 7000, 8000, 10,000,$ and $12,000$ K (see the key). At each temperature, surface gravities of $g = 10^7, 10^8,$ and 10^9 cm s^{-2} are used. The green line shows the fit of an A0 dwarf star. Compare Fig. 6.

At $T = 8000$ K, the fit to the lines is better, although not as good as for A0 dwarf or giant stars. The dispersion remains high ($\sigma = 930 \pm 101, 929 \pm 101,$ and 952 ± 103 km s^{-1}). Again, the Balmer break in the white dwarfs is too weak.

At $T = 10,000$ K, the stellar lines are much broader. The fit to P3 is acceptable after scaling the line strengths. For $\log g = 7, 8,$ and $9,$ $\sigma = 784 \pm 120, 769 \pm 134,$ and 821 ± 150 km s^{-1} , respectively. Note that without line-strength scaling, the broadened white dwarf spectrum does not fit the galaxy. And, even though the lines are now strong enough when $\log g$ is large to produce a Balmer break, it is still too small to fit the spectrum of P3. The green line emphasizes how much

an A0 V star fits the spectrum of P3 better than does any white dwarf.

Increasing the temperature further is counterproductive. At $T = 12,000$ K, the lines are too strong and too broad to fit P3, although we still obtain high dispersions ($\sigma = 705 \pm 144, 676 \pm 166,$ and 680 ± 190 km s^{-1}). Even high temperatures do not produce strong enough Balmer breaks.

We conclude that no spectral synthesis of white dwarf stars of different temperatures or gravities would fit P3. The ones that fail least badly, those that fit the lines but not the Balmer break, imply velocity dispersions that are consistent with values derived from A0 dwarf or giant stars.

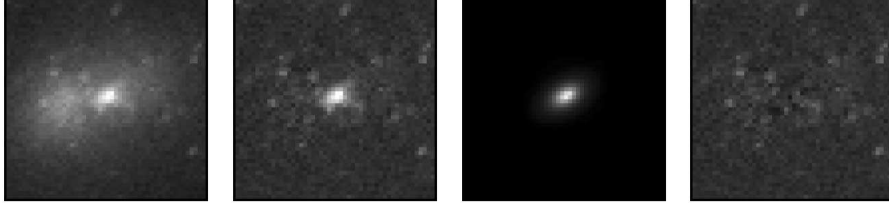


FIG. 9.—Left to right: F300W image of the blue nucleus, P3, superposed on nuclei P1 and P2; F300W image of P3 after subtraction of the F555W image intensity scaled to the F300W image in the first panel; PSF-convolved inclined disk model for P3; and difference between images in the second and third panels showing the quality of the model and the residual surface brightness fluctuations. All images are $2'5 \times 2'5$. North is $55'7$ counterclockwise from up, as in Fig. 1.

For a compact cluster of white dwarfs to be a viable alternative to a supermassive BH, it must be dark. That is, it must be old. We explore this option further in § 8.

5. LIGHT DISTRIBUTION OF P3

For a dynamical analysis of P3 (§ 6), we need its light distribution with P1+P2 subtracted. To derive this, we scaled the *HST*

F555W image to the *HST* F300W image such that P1 disappeared after subtraction. The resulting image of P3 is shown in Figure 9. We then fitted P3 with Sérsic (1968) models,

$$I(r) = I_0 \exp\left[-(r/r_0)^{1/n}\right],$$

convolved with the *HST* point-spread function (PSF) as in Lauer et al. (1998). The PSF was constructed from two exposures of the standard star GRW +70D5824 (u2tx010at, u2tx020at). The free parameters in the fit were central surface brightness SB_0 , scale length $r_0 = (a_0 b_0)^{1/2}$ (where a and b are semimajor and semiminor axis, respectively), Sérsic n , position angle P.A., ellipticity $1 - b/a$, and center coordinates. Individual faint pointlike sources in the outskirts of P3 were masked before fitting. The best fit over the radius range $r < 0''.3$ was obtained for Sérsic index $n = 1$, major-axis scale length $a_0 = 0''.1 \pm 0''.01$, PSF-convolved ellipticity $1 - b/a = 0.33 \pm 0.03$, and position angle P.A. = $63^\circ \pm 2^\circ$ (this is 119° counterclockwise from vertical in Fig. 9).

The PSF-convolved model and the difference between P3 and the model are illustrated in Figure 9. We also compare the model and P3 with respect to their isophotal parameters. Figure 10 shows the surface brightness, ellipticity, and position angle profiles of the observed P3, the model, and the PSF-convolved model. Also shown are deconvolved P3 profiles, which were obtained from 15 iterations with the Richardson-Lucy deconvolution algorithm implemented in the ESO MIDAS package. The deconvolved surface brightness profile obtained here agrees well in shape with the one by Lauer et al. (1998). Figure 10 shows that the model represents P3 reasonably well, especially over the radius range for which we can analyze the kinematics (§ 6). Surface brightness fluctuations become large at radii beyond $0''.25$. Still, the model is adequate out to $\sim 0''.4$.

If P3 is an inclined, thin disk, then the observed ellipticity implies an inclination $i = 55^\circ \pm 2^\circ$. This is compatible with the

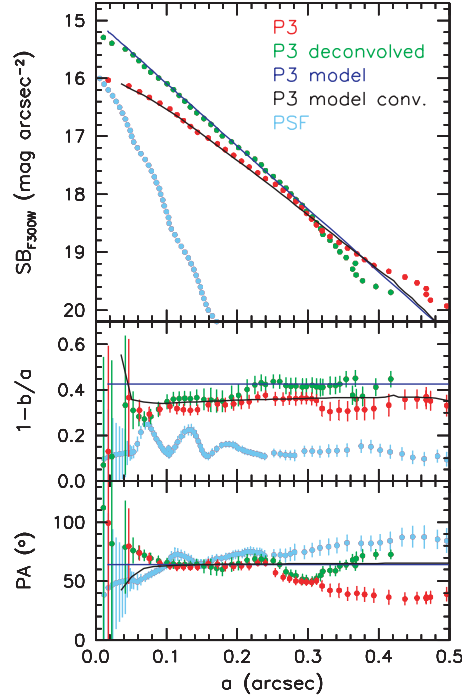


FIG. 10.—Observed radial profiles (red line) of P3 surface brightness SB, ellipticity $1 - b/a$, and position angle P.A. vs. semimajor axis a . Lucy-deconvolved profiles are shown in green. The *HST* PSF is shown in light blue (with arbitrary zero point). The inclined disk model before and after convolution with the *HST* PSF is represented by blue and black lines, respectively. The observed profiles are oversampled; neighboring points are not independent.

TABLE 2
PARAMETERS OF THE THIN-DISK MODEL OF P3

Parameter	Value
m_{F300W}	18.6 ± 0.1
M_{F300W}	-5.8 ± 0.1
Sérsic n	1
Scale length a_0 (arcsec).....	0.1 ± 0.01
$SB_{0,F300W}$ (face-on) (mag arcsec $^{-2}$).....	15.6 ± 0.1
Inclination (deg).....	55 ± 2
Position angle (deg).....	63 ± 2

inclination of the eccentric disk P1+P2: Peiris & Tremaine (2003) derive $i = 54^\circ$, and Bacon et al. (2001) get $i = 55^\circ$. The model parameters of P3 are summarized in Table 2. Whether P3 really is a thin disk can only be checked with kinematical data. We discuss these in the next section.

6. DYNAMICS OF P3

Figure 11 shows the rotation velocity and velocity dispersion profiles of P3. Table 3 lists the data. We used FCQ for the analysis but did not fit the h_3 and h_4 Gauss-Hermite parameters because the S/N of the data is only $\sim 3 \text{ \AA}^{-1}$. Outside of the central pixel, P3 rotates rapidly, with an observed amplitude of $573 \pm 61 \text{ km s}^{-1}$ (weighted mean of all points with $|r| > 0''.01$). P3 rotates in the same sense as P1+P2. The apparent velocity dispersion drops from $\sim 1200 \text{ km s}^{-1}$ in the central pixel to $< 500 \text{ km s}^{-1}$ at $r = 0''.15 = 0.55 \text{ pc}$. These values are consistent with the velocities seen in the extreme wings of the line-of-sight velocity distribution (LOSVD) of the red stars at $r \sim -0''.1$ (see the Appendix). The kinematic data securely locate the BH at the center of P3 with an uncertainty of about $\frac{1}{3}$ of a pixel, i.e., $0''.02 = 0.07 \text{ pc}$.

We wish to combine the surface brightness data (Table 2) and the kinematic data (Table 3) to make dynamical models. Because the pixel size, slit width, and PSF are all similar to the size of P3, unresolved rotation must contribute to the apparent velocity dispersion. Actually, almost all of the light of P3 falls into the slit. Despite this and despite the modest apparent flattening, P3's apparent rotation velocity and velocity dispersion are similar. Therefore, it is reasonable to expect that P3 is an intrinsically flat object with $V \gg \sigma$.

For these reasons, we first model P3 as a flat disk with an exponential profile and an inclination $i \sim 55^\circ$ (§ 6.1). Then (§ 6.2), we explore more nearly edge-on models in which P3 has some intrinsic thickness.

6.1. P3 as a Flat Exponential Disk

We construct a dynamical model in which we assume that P3 is a flat disk with the parameters in Table 2 and a negligible intrinsic velocity dispersion. The BH affects the structure of the galaxy interior to $r_{\text{cusp}} \simeq GM_\bullet/\sigma^2 = 5''.6[M_\bullet/(10^8 M_\odot)]$, where G is the gravitational constant and $\sigma = 145 \text{ km s}^{-1}$ (Kormendy 1988) is the velocity dispersion of the bulge just outside the region affected by the BH. Since P3 is tiny compared to r_{cusp} , the BH dominates the gravitational potential. The distribution of the stars is completely constrained by the photometry, so the only free parameter is the BH mass. To compare the model with the observed rotation and velocity dispersion profiles, we convolve the Keplerian velocity field with the PSF and integrate it over the $0''.2$ slit width and $0''.05$ CCD pixels (see Fig. 11, *top middle panel*). This is done with small subpixels to obtain smooth profiles of rotation velocity and velocity dispersion.

Figure 11 shows the results. The observed rotation and dispersion profiles (*open and filled symbols*) are well matched by the model (*dotted lines*). Estimating the mass of the BH is straightforward because M_\bullet is the only free parameter. The best fit gives $M_\bullet = (1.4 \pm 0.2) \times 10^8 M_\odot$. The reduced χ_n^2 is ~ 1 (Fig. 12).

The BH mass derived with the thin-disk model does not depend significantly on inclination over the range allowed by the photometry ($\pm 2^\circ$). Changing the inclination away from the best value increases V and decreases σ or vice versa. Then χ^2 increases slightly, but the shape of the χ^2 distribution as a function of BH mass does not change significantly. We also varied the

scale length of the P3 disk, its total luminosity, and its position angle on the sky within the errors. There was no significant effect on M_\bullet . The total luminosity and mass of P3 are irrelevant provided that the BH dominates the potential. The position angle would have to be changed well beyond its estimated errors to achieve a visible effect on the velocities. Changing the radial scale length redistributes light and makes the rotation and dispersion profiles flatter or steeper. Within the errors, M_\bullet is not affected.

The circular velocities for the thin-disk model are shown in the top panel of Figure 11. Future observations that resolve individual stars should see velocities of $1000\text{--}2000 \text{ km s}^{-1}$. Such measurements can also test how much the observed velocities and dispersions are affected by shot noise due to the small number of stars in P3. Checking how close to circular the disk really is will also be important.

If P3 is a thin stellar disk, can it be stable? The answer is yes, as long as its stellar mass is not very much larger than $5200 M_\odot$. Even relatively small dispersions will not lead to significant two-body relaxation. Using equation (8-71) in Binney & Tremaine (1987), we obtain relaxation times of the order of a Hubble time. Moreover, the critical velocity dispersion for local stability (Toomre 1964) is small, $\sigma_{\text{crit}} \ll 1 \text{ km s}^{-1}$. This is a consequence of the fact that the potential is dominated by the BH. That is, the P3 disk is dynamically analogous to Saturn's rings rather than to a self-gravitating disk. Therefore, if earlier starbursts contributed mass without affecting its present spectrum, the P3 stellar disk is likely to be locally stable and immune from two-body relaxation. And if P3 consists only of young stars, then it has not had time for significant dynamical evolution.

6.2. P3 Schwarzschild Models

To investigate the effect on M_\bullet of allowing P3 to have some thickness in the axial direction z and therefore to be more nearly edge-on than $i = 55^\circ$, we fitted Schwarzschild (1979) models to the photometric and kinematic data. We used the regularized maximum entropy method as implemented by Gebhardt et al. (2000a, 2003) and Thomas et al. (2004). The program was constrained to reproduce the observed surface brightness distribution of P3. We considered three inclinations $i = 58^\circ, 66^\circ$, and 90° , corresponding to intrinsic axial ratios of P3 of 0.26, 0.44, and 0.57, respectively. BH masses were varied until the kinematic data were reproduced as well as possible, as indicated by the χ^2 values in Figure 12.

In the Schwarzschild code, phase space is quantized on a polar grid that is not optimized for closed orbits. It is therefore helpful if the orbits are not quite closed. For this reason, we did not use a point mass for the central dark object but rather used a Plummer sphere with a half-mass radius $r_h = 0''.01$. Given the spatial resolution of the data, this is essentially equivalent to a BH (see Fig. 14 below).

Models that put significant weight on entropy maximization did not fit the kinematics. They rotated too slowly because they contained retrograde orbits. This is expected because entropy maximization is not appropriate for highly flattened systems with strong rotational support.

Switching off the entropy maximization (this corresponds to a high regularization parameter in Thomas et al. 2004) results in better fits. Figure 12 shows χ^2 values as a function of inclination and dark mass M_\bullet . We conclude that the lowest inclination, $i = 58^\circ$, is preferred by $\Delta\chi^2 \approx 2$ relative to the $i = 66^\circ$ model and with higher significance relative to the more inclined models.

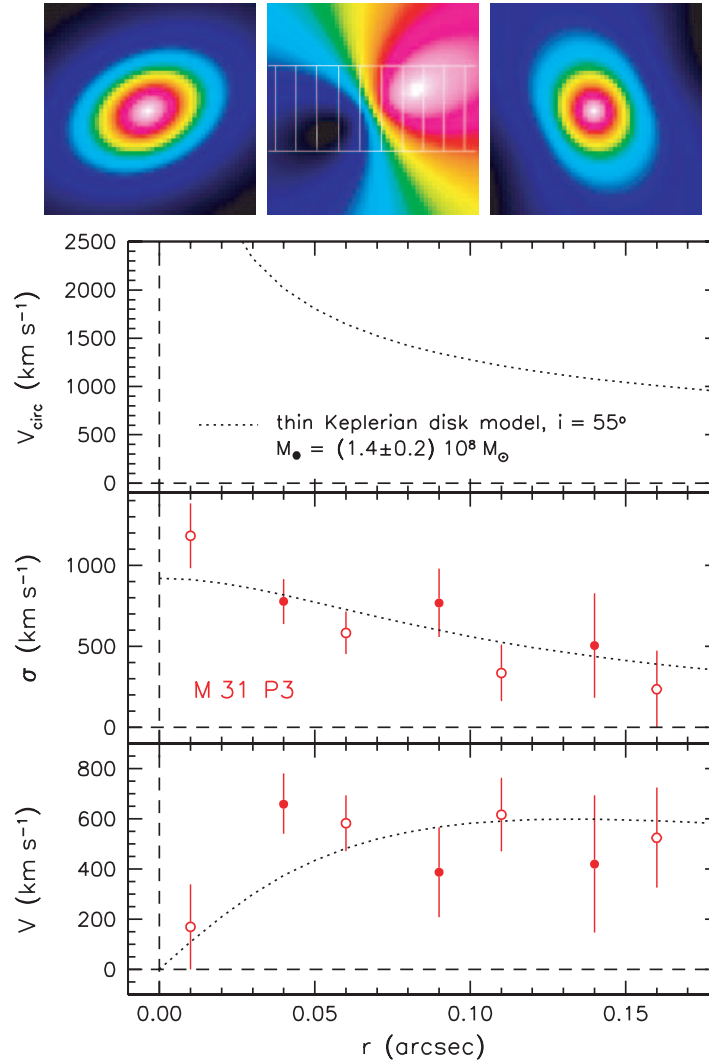


FIG. 11.—The three color images at the top show the PSF-broadened thin-disk model of P3. The images cover $0''.5 \times 0''.5$. Shown from left to right are (1) P3 surface brightness (intensities range from 0 [black] to 1 [white]); (2) P3 rotation velocity field with the slit and radial bins superposed (the velocity amplitudes range from -700 [black] to $+700$ km s^{-1} [white]); and (3) P3 velocity dispersion, ranging from 150 [black] to 1000 km s^{-1} [white]. The panels of plotted data points show the P3 radial profiles (red) of rotation velocity (bottom) and velocity dispersion (middle), folded around P3's center. Open and filled symbols are from opposite sides of the center. The sense of rotation is the same as for the eccentric disk P1+P2. The top panel shows the best-fitting Keplerian circular velocity curve as a dashed line. It implies a BH mass of $\sim 1.4 \times 10^8 M_{\odot}$. Convolution of the circular velocity field with the PSF and integrating it over the pixel size and slit width yields the model rotation and dispersion profiles shown as dotted lines in the bottom and middle panels.

TABLE 3
KINEMATICS OF P3

Radius (arcsec)	V (km s ⁻¹)	ΔV (km s ⁻¹)	σ (km s ⁻¹)	$\Delta\sigma$ (km s ⁻¹)
-0.16	525	197	237	233
-0.11	616	144	337	170
-0.06	582	111	583	131
-0.01	170	169	1183	200
+0.04	-659	117	777	139
+0.09	-387	179	769	211
+0.14	-420	273	505	322

Rotation velocity and velocity dispersion profiles for the lowest χ^2 model at each inclination are shown in Figure 13. Reassuringly, the $i = 58^\circ$ Schwarzschild model most nearly resembles the $i = 55^\circ$ thin-disk model. The fits then become progressively more different (and less good) as the models are made more edge-on.

Higher inclinations require higher BH masses. The reason is that, at higher inclinations, line-of-sight integration through the nearly edge-on, thick disk includes stars at relatively large radii that move mostly across, not along, the line of sight. They reduce the velocity moments and consequently require higher M_\bullet to match the observed rotation velocities. The preferred BH mass for the $i = 58^\circ$ and 66° Schwarzschild models is $\sim 2 \times 10^8 M_\odot$. The highest BH mass that is consistent with the data to within $\sim 1\sigma$ is given by the $i = 58^\circ$ Schwarzschild model and is $\sim 2.3 \times 10^8 M_\odot$ (Fig. 12). The lowest BH mass implied by the dynamics of P3 is given by the thin-disk, $i = 55^\circ$ model and is $\sim 1.2 \times 10^8 M_\odot$ (§ 6.1).

It is instructive to examine the $i = 58^\circ$ Schwarzschild model in more detail. Figure 14 shows its velocity moments. Rotation dominates the dynamics; V_ϕ is $\lesssim 20\%$ smaller than the circular velocity. At radii $r \gtrsim 0.1$, the model is approximately isotropic.

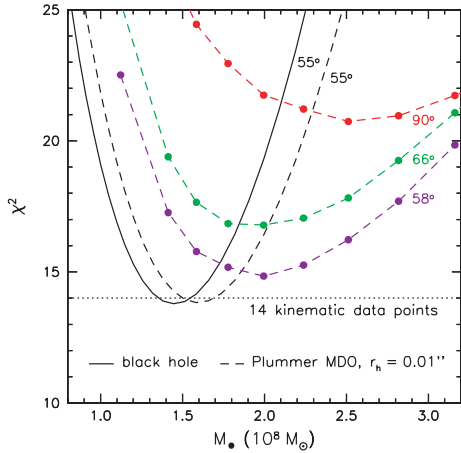


FIG. 12.—The χ^2 profiles for models of P3. The black lines refer to the thin-disk model with inclination 55° , while the colored lines show three Schwarzschild models with inclinations 58° , 66° , and 90° . The dashed lines assume that the MDO is a Plummer sphere with radius $0.01''$; the solid black line assumes a BH.

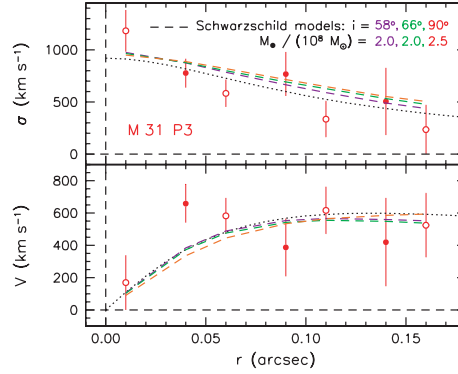


FIG. 13.—Rotation velocities and velocity dispersions of P3 as in Fig. 11 (red open and filled symbols). Overplotted as colored dashed lines are three Schwarzschild models with different inclinations and BH masses. The thin-disk model of Fig. 11 is shown as a dotted black line.

To provide the thickness that is necessitated by the inclination $i > 55^\circ$, σ_z then increases substantially inward, although it remains smaller than the rotation velocity. The difference between the adopted Plummer model and a central point mass is small except for the innermost data point.

Figure 15 shows the corresponding orbit structure. As expected for a Schwarzschild model that is not too different from the thin-disk model, retrograde orbits are strongly suppressed. However, as indicated by Figure 14, noncircular orbits get significant weight in order to produce an axial ratio $b/a \simeq 0.26$. As expected, this happens more near the center than at larger radii. However, nearly circular orbits dominate; otherwise, V_ϕ would not be almost equal to V_c in Figure 14.

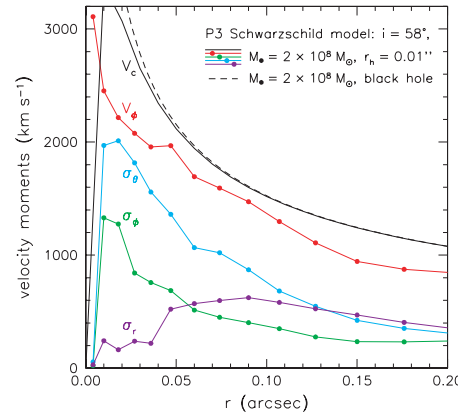


FIG. 14.—Major-axis velocity moments of the best $i = 58^\circ$ Schwarzschild model for P3, corresponding to $M_\bullet = 2 \times 10^8 M_\odot$. The MDO is a Plummer sphere with half-mass radius $r_h = 0.01''$; its circular velocity is shown as a solid black line. A BH of the same mass would produce the Keplerian circular velocities indicated by the dashed curve.

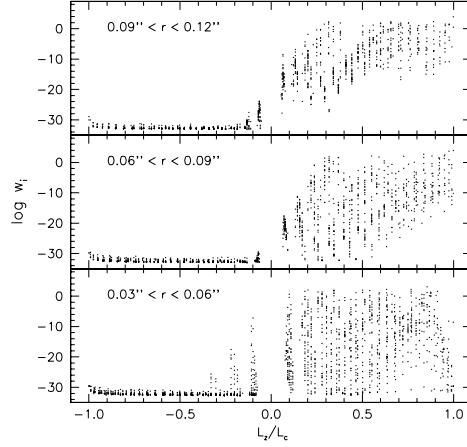


FIG. 15.—Orbit structure of the Schwarzschild model with $i = 58^\circ$, Plummer model dark mass $M_\bullet = 2 \times 10^8 M_\odot$, and half-mass radius $r_h = 0''.01$. For each orbit, the orbit weight w_i per phase space volume is shown as a function of the z -component of its angular momentum L_z normalized by the angular momentum L_c of the circular orbit that has the same energy. In this figure only, r is the average of the pericenter and apocenter radii of the orbit. Note that at all radii, only prograde orbits are significantly populated.

6.3. Summary: Comparison of P3 and P1+P2

We conclude that the triple nucleus of M31 is made of two nested, disklike systems. The P1+P2 disk is elliptical, has a radius of about 8 pc, and consists of old, metal-rich stars. If it is thin, it has an inclination of $\sim 54^\circ$ and a major-axis position angle of $\sim 43^\circ$ (Peiris & Tremaine 2003). The P3 disk is approximately circular and has a radius of about 0.8 pc. If it is thin, P3 has an inclination $i \sim 55^\circ$ that is the same as that of P1+P2. P3's major-axis position angle at $r \leq 0''.25$ is $\sim 63^\circ \pm 2^\circ$. That is, the inner P3 disk is slightly tilted with respect to the P1+P2 disk but is relatively close to the kinematical major axis, P.A. $\sim 56^\circ$, found by Bacon et al. (2001). At $r > 0''.25$, the major axis of P3 twists to $\sim 40^\circ$, essentially the position angle of P1+P2. The nested disks rotate in the same sense and have almost parallel angular momentum vectors.

7. THE MASS OF THE CENTRAL DARK OBJECT

We have demonstrated that disklike models for P3 fit both the photometry and the kinematics of P3 exceedingly well. This allowed an estimate of M_\bullet that is independent of all previous determinations. Besides BH mass, only inclination is a free parameter in the fit to the rotation curve and the dispersion profile (Figs. 11 and 13).

Could systematic effects cause additional errors that are not included in the statistical errors, especially toward low BH masses? We mentioned in the previous section that some clumpiness in the distribution of stars could be hidden by PSF blurring and may affect the measured velocities and dispersions. We carried out a simple check for this effect by fitting subsamples of data points. For example, a fit to just the innermost three points in Figure 11 typically yields BH masses about 15% higher, while omitting these three points results in 25% lower masses. All values obtained in this way fell in the range allowed by the χ^2 profiles in Figure 12, so this effect does not seem to be very important.

Some noncircularity of the P3 disk could be hidden as well. P3 could contain stars on elongated orbits that have their pericenters within the range of the kinematic data ($0''.15$) but apocenters spread out over radii well beyond this radius. Figure 9 shows faint blue stars that could be such objects. This would imply that P3's velocity amplitudes are increased by rotation velocities that are faster than circular. It is difficult to estimate the size of this effect, but pericenter velocities of very radial stars can be at most a factor of 2 larger than pericenter velocities of stars on nearly circular orbits. Averaging over a set of orbits will reduce this number considerably. And if we wanted to fully exploit this effect, many more stars of P3 would have to be found outside of $\sim 0''.18$ than inside, which is in contradiction with the observations. The Schwarzschild models also show that this trick does not work well. More radially biased models (obtained with higher entropy weighting and not shown here) require larger BH masses. Finally, if P3 originated in a star-forming gas disk, it could not contain nearly radial orbits, and we noted above that subsequent internal evolution of the P3 disk should be slow.

So, very special circumstances would be required to decrease M_\bullet below $1 \times 10^8 M_\odot$. On the high-mass end, the BH mass grows with increasing inclination of the model. However, the χ^2 values become unacceptably large for inclinations above $\sim 60^\circ$; therefore, it is unlikely that the BH mass is significantly larger than $\sim 3 \times 10^8 M_\odot$. Viable models for P3 are found in the inclination range $55^\circ < i < 58^\circ$ and in the BH mass range $1.1 \times 10^8 M_\odot < M_\bullet < 2.3 \times 10^8 M_\odot$. The upper limit takes into account that the Schwarzschild models were calculated assuming a massive dark object (MDO) with $r_h = 0''.01$ and not a BH; the upper limit for a BH is $\approx 0.2 \times 10^8 M_\odot$ lower than for an MDO with $r_h = 0''.01$. The best-fit and at the same time lowest BH mass of $M_\bullet = 1.4 \times 10^8 M_\odot$ is obtained for the thin-disk model. This model is also preferred on astrophysical grounds, if P3 formed out of a thin gaseous disk. Therefore, our best estimate for the mass of the supermassive BH in M31 is $M_\bullet = 1.4^{+0.9}_{-0.3} \times 10^8 M_\odot$.

How does this compare with previous results? The BH mass has now been estimated by five largely independent techniques: (1) standard dynamical modeling that ignores asymmetries, (2) the KB99 center-of-mass argument that depends on the asymmetry of P1+P2, (3) the Peiris & Tremaine (2003) nuclear disk model that explains the asymmetry of P1+P2, (4) full dynamical modeling that takes into account the self-gravity of the P1+P2 disk (Salow & Statler 2004), and (5) dynamical modeling of the blue nucleus P3, which is independent of P1+P2. The good news is that all methods require a dark mass with high significance. The bad news is that some of the results differ by more than two standard errors. In particular, the disagreement between the KB99 center-of-mass argument and the P3 models presented here is a concern. We therefore revisit the KB99 derivation in the subsection below. The models that best fit both the photometry and the kinematics, the Peiris & Tremaine (2003) eccentric disk model of P1+P2 and our thin-disk model of P3, agree within the errors and favor a high BH mass of $M_\bullet \sim 1 \times 10^8 M_\odot$. We also note that a higher BH mass can be accommodated more easily in almost all models than a lower BH mass.

The mass of the M31 BH derived here is a factor of ~ 2.5 above the ridgeline of the correlation between M_\bullet and bulge velocity dispersion σ_{bulge} (Ferrarese & Merritt 2000; Gebhardt et al. 2000b). Using the Tremaine et al. (2002) derivation,

$$\log\left(\frac{M_\bullet}{M_\odot}\right) = 8.13 + 4.02 \log\left(\frac{\sigma_{\text{bulge}}}{200 \text{ km s}^{-1}}\right),$$

$\sigma_{\text{bulge}} \simeq 160 \text{ km s}^{-1}$ implies that $M_{\bullet} \simeq 5.5 \times 10^7 M_{\odot}$. We derive $M_{\bullet} = 1.4_{-0.3}^{+0.9} \times 10^8 M_{\odot}$. Tremaine et al. (2002) already found significant scatter in the M_{\bullet} - σ_{bulge} relation at low masses. With the increased BH mass for M31, scatter has become even more prominent. Considering, in addition to M31, only the two closest other supermassive BHs, i.e., M32 and the Galaxy, we get the following: M32 has $\sigma_{\text{bulge}} \sim 75 \text{ km s}^{-1}$, a predicted $M_{\bullet} = 2.6 \times 10^6 M_{\odot}$, and an observed $M_{\bullet} = (2.9 \pm 0.6) \times 10^6 M_{\odot}$ (Verolme et al. 2002; corrected to distance 0.81 Mpc from Tonry et al. 2001). Our Galaxy has $\sigma_{\text{bulge}} \sim 103 \text{ km s}^{-1}$, a predicted $M_{\bullet} = 9.4 \times 10^6 M_{\odot}$, and an observed $M_{\bullet} = (3.7 \pm 0.2) \times 10^6 M_{\odot}$ (Ghez et al. 2005). So M31, M32, and our Galaxy have BH masses that are 2.5 times larger than, consistent with, and 3 times smaller than the ridgeline of the M_{\bullet} - σ_{bulge} relation, respectively. This is strong indication for significant intrinsic scatter in the M_{\bullet} - σ_{bulge} relation, at least at the low-mass end.

7.1. Black Hole Mass from the Center-of-Mass Argument: KB99 Revisited

KB99 estimated that the center of P3 (Fig. 16, blue filled circle) is offset from the bulge center (horizontal dashed line) by about $0''.06$. They then assumed that the central dark object is in P3 and estimated its mass based on the assumption that the combined system, BH+P1+P2+P3, is in dynamical equilibrium. That is, they assumed that the center of mass of BH+P1+P2+P3 is at the center of the bulge. Then M_{\bullet} is inversely proportional to its distance from the bulge center and, if the mass of P3 is negligible, is proportional to the mass of P1+P2. The latter was given by the light distribution and the measured mass-to-light ratio $M/L_V = 5.7$. The resulting BH mass was $M_{\bullet} \simeq (3.3 \pm 1.5) \times 10^7 M_{\odot}$. This is at the low end of the range of published values and a factor of ~ 4 smaller than the value derived here. As the stellar M/L_V can hardly be a factor of 4 larger, two explanations are possible for the discrepant BH masses: (1) P3 and the BH are a factor of 4 closer to the bulge center than KB99 derived, or (2) the BH+P1+P2+P3 system is not in equilibrium with respect to the bulge center.

We believe that the observations can be consistent with equilibrium and that the distance of P3 to the bulge center was overestimated by KB99 for the following reasons.

Figure 16 revisits the center-of-mass argument. It is reproduced from KB99 and shows their estimate of the position of the center of the bulge as the dashed line at $X = 0$. The isophote center coordinate X is measured along the line joining P1 and P2. KB99 calculated the average at $2''.9 < a < 25''.0$. A larger radius range was not possible because of the small size of the high-resolution images used. If $M_{\bullet} \sim 3 \times 10^7 M_{\odot}$, then the above radius range is no problem: it is beyond the radii affected by the BH. However, if M_{\bullet} is as big as $1.4 \times 10^8 M_{\odot}$, then $r_{\text{cusp}} \simeq 7''.2$ and it is necessary to calculate the mean bulge X at larger radii.¹⁷

If we calculate the bulge center outside of $r_{\text{cusp}} \simeq 7''.2$, we obtain a mean X -position of $-0''.033$ in Figure 16, i.e., halfway between the KB99 bulge center and P3. Note that, unlike KB99, we do not limit the averaging to points with $a < 25''.0$ but now also include two further points that we extracted from the

¹⁷ What we should expect at $r < r_{\text{cusp}}$ is not clear. Because the potential is dominated by the BH, asymmetries like those of the P1-P2 eccentric disk are possible and isophotes do not need to be concentric to represent an equilibrium configuration.

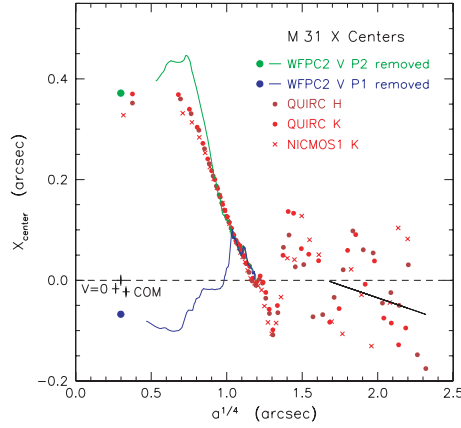


FIG. 16.—From KB99, isophote center coordinates X along the line joining P1 and P2 as a function of isophote major-axis radius a . A V -band *HST* WFPC2 image was measured twice, once masking out P2 (green) to measure the convergence of the P1 isophotes on the center of P1 (green filled circle) and once masking out P1 (blue) to measure the convergence of the P2+P3 isophotes on the center of P3 (blue filled circle). The brown and red symbols are measurements of individual isophotes in H - and K' -band images. The positions of the velocity center and of the center of mass of the BH and nucleus (if $M_{\bullet} = 3 \times 10^7 M_{\odot}$), each with error bars, are shown by the symbols labeled “ $V=0$ ” and “COM,” respectively. The dashed line at $X = 0$ marks the center position of the bulge that was adopted by KB99. It was estimated by averaging all isophote center coordinates at $2''.9 < a < 25''.0$ ($1.3 < a^{1/4} < 2.24$). However, if $M_{\bullet} = 1.4 \times 10^8 M_{\odot}$, then the BH’s radius of influence is $r_{\text{cusp}} \simeq 7''.2$. Therefore, KB99 estimated the bulge center position partly from isophotes that are at $a < r_{\text{cusp}}$. Within this radius, the BH dominates the potential and isophotes do not need to be concentric to be in equilibrium (witness the eccentric disk). Since we now believe that the BH mass is large, we should derive the bulge center from correspondingly larger radii. The solid line is a least-squares fit to the bulge X_{center} values at $a > r_{\text{cusp}}$. It shows that the isophote centers at the largest radii in the figure are approximately at the X -coordinate of P3. Therefore, the BH is close to the luminosity-weighted center of the bulge.

QUIRC H -band image beyond this radius. In addition, we omit all center coordinates with errors larger than $0''.2$.

A least-squares fit to the points with $a > 7''.2$ gives the short black line in Figure 16. It shows that the bulge isophote centers drift with increasing radius toward the X -position of P3. Thus, the luminosity-weighted center of the bulge is close to P3.

This discussion suggests that the determination of the bulge center is less reliable than KB99 assumed. There are three reasons: (1) the BH sphere of influence is much larger than KB99 assumed, (2) the bulge isophote centers drift toward P3 with increasing radius beyond $a = 2''.9$, and (3) the isophote centers oscillate (or at least fluctuate) with radius because of dust or surface brightness fluctuations or perhaps a physical effect that we have not identified. If the BH is much more massive than P1+P2, then it is so close to the center of mass that M_{\bullet} cannot be determined accurately from the center-of-mass argument.

The important conclusion, however, is that the observations of M31 are consistent with dynamical equilibrium and with a large BH mass of $M_{\bullet} = 1.4 \times 10^8 M_{\odot}$.

8. ASTROPHYSICAL CONSTRAINTS ON A MASSIVE DARK OBJECT MADE OF DARK STARS

Central dark masses are detected dynamically in 38 galaxies (for reviews see Kormendy & Gebhardt 2001; Kormendy 2004).

They are commonly assumed to be supermassive BHs, although clusters of dark stars are consistent with the dynamics in most galaxies. Justifying this assumption, many authors cite the implausibility of producing so many stellar remnants (often 100 times the mass in visible stars) in the small volume defined by the PSF in which the dark mass must lie. Another argument is the consistency of the dark masses with energy requirements for BHs to power AGNs. More rigorous arguments against dark clusters are available for two galaxies, NGC 4258 and our own Galaxy (Maoz 1995, 1998; Genzel et al. 1998; Schödel et al. 2002, 2003; Ghez et al. 2005). Clusters of failed stars are not viable because brown dwarfs collide on short timescales and either evaporate or merge and become visible stars. Clusters of dead stars are not viable because their two-body relaxation times are so short that they evaporate. In NGC 4258, the timescales associated with these processes are at least as short as $10^{8.5}$ yr. In our own Galaxy, they are remarkably short indeed, $\sim 10^4$ yr. Even balls of neutrinos with cosmologically allowable neutrino masses are excluded in our Galaxy. The BH cases in NGC 4258 and in our Galaxy are now very strong and are taken as indications that dynamically detected central dark masses in other galaxies are BHs, too.

However, a great deal is at stake. It would be very important if astrophysical arguments ruled out BH alternatives in more than two galaxies. M32 has been the next best case (van der Marel et al. 1997, 1998), but Maoz (1998, Fig. 1) shows that a white dwarf cluster could survive for $\sim 10^{11}$ yr.

Applying our results on the dynamics of P3, M31 becomes the third galaxy in which dark star cluster alternatives to a BH can be excluded. For the most conservative estimate that $M_\bullet \simeq 3 \times 10^7 M_\odot$, the arguments are discussed in Kormendy et al. (2002) and Kormendy (2004). Here we update these arguments to the best kinematic fits and resulting BH masses implied by §§ 6 and 7. More detail is given in J. Kormendy et al. (2005, in preparation).

8.1. Limits on the Size of a Dark Cluster Alternative to a BH

Figure 17 derives our adopted limit on the size of any dark cluster alternative to a BH. It shows χ^2 contours for fits to the rotation and dispersion profiles of P3 using the thin-disk model of Figure 11 that gave the lowest BH mass. As in Maoz (1995, 1998), we assume that the dark object is a Plummer sphere, i.e., a reasonably realistic dynamical model with a very steep outer profile. We wish to use a relatively truncated mass distribution, one that is not excessively core-halo, because we need to fit the rapid rise in $V(r)$ and the corresponding drop in $\sigma(r)$ (Fig. 13) with a distributed object. Dark mass that is at several times the half-mass radius r_h hurts rather than helps us to do this.

We need to know how large r_h can be and still allow an adequate fit to the kinematics. As r_h is increased, the inner rotation curve drops, and it gets more difficult to fit the high central σ and especially the rapid central rise in $V(r)$. To compensate, an adequate fit requires that we increase M_\bullet . Therefore, r_h and M_\bullet are coupled (Fig. 17). How extended can the dark object be? We adopt the parameters at the upper right extreme of the 68% χ^2 contour: $r_h = 0.031 = 0.113$ pc and $M_\bullet = 2.15 \times 10^8 M_\odot$. Note that choosing values corresponding to, e.g., the 90% χ^2 contour (or a larger one) does not significantly weaken the arguments against a dark cluster presented below because with increasing r_h the required dark cluster mass increases as well.

8.2. Arguments Against a Dark Cluster

The half-mass radius $r_h = 0.113$ pc is the same as the radius of the Ring Nebula (Cox 2000), a typical planetary nebula. We are

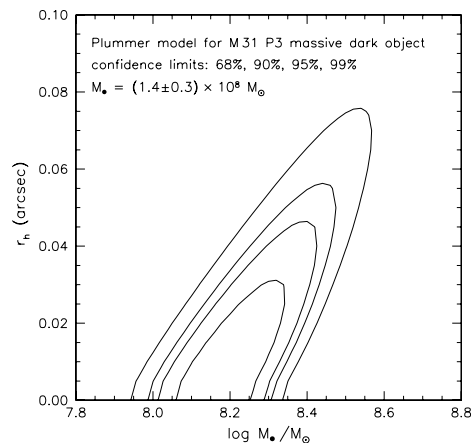


Fig. 17.—Contours of χ^2 for fits to the P3 kinematics of Plummer spheres with half-mass radii r_h and total masses M_\bullet . The P3 model is a flat disk, as in Fig. 11. Our adopted constraint on the fluffiness of the dark mass is the upper right extreme of the 68% χ^2 contour, i.e., $r_h = 0.031 = 0.113$ pc and $M_\bullet = 2.15 \times 10^8 M_\odot$.

considering a situation in which this volume contains $10^8 M_\odot$ of brown dwarf stars or stellar remnants. The mean density inside r_h is $\rho_h = 1.8 \times 10^{10} M_\odot \text{pc}^{-3}$, and the density at r_h is $\rho(r_h) = 6.5 \times 10^9 M_\odot \text{pc}^{-3}$. This is ~ 10 times larger than the largest stellar mass density observed in any galaxy, $7 \times 10^8 M_\odot \text{pc}^{-3}$ at $r = 0.1 = 0.004$ pc in the stellar cusp around Sgr A* in our Galaxy (Genzel et al. 2003). However, only about $300 M_\odot$ of stars are inside the above radius (Genzel et al. 2003). Not surprisingly, a dark cluster as extreme as the one that we require to explain the kinematics of P3 gets into trouble.

8.2.1. Brown Dwarfs Collide and Destroy Themselves

It is easiest to eliminate brown dwarfs. They collide with each other so violently that they get converted back into gas. Figure 18 shows the timescale on which every typical brown dwarf collides with another brown dwarf. As in Maoz (1995, 1998), the zero-temperature brown dwarf radius is taken from Zappolysky & Salpeter (1969) and Stevenson (1991), and the calculation is an average interior to r_h . Typical collision velocities at r_h are ~ 2500 km s^{-1} ; this is fast enough compared to the surface escape velocity (~ 600 km s^{-1} for a $0.08 M_\odot$ star and smaller for lower mass brown dwarfs) that the brown dwarfs would get destroyed, i.e., converted back into gas. Brown dwarfs are strongly excluded.

8.2.2. Intermediate-Mass White Dwarfs Collide and Make Type Ia Supernovae

Relatively short collision times provide an argument against intermediate-mass white dwarfs. For $0.8 M_\odot \lesssim m_* \lesssim 1.2 M_\odot$, collision times at the quarter-mass radius $r_{1/4}$ are $(4-7) \times 10^9$ yr. Given the implied numbers of white dwarfs interior to this radius and the fact that the collision time would be shorter at smaller radii, collisions should happen more often than every 50–150 yr. Each collision would bring the remnant well above the Chandrasekhar limit. Presumably Type Ia supernovae would result. Near maximum brightness, they would be visible to the naked eye. The fact that no such supernovae have been observed in M31 might barely

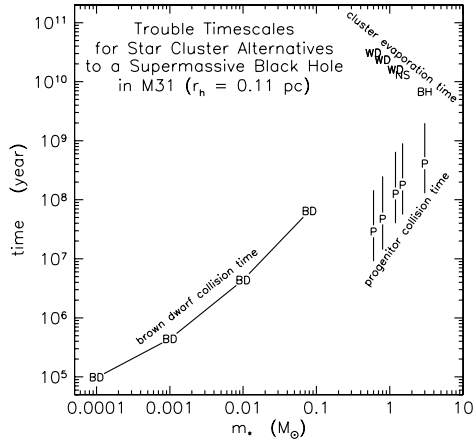


FIG. 18.—Timescales on which dark cluster alternatives to a BH get into trouble in M31. The dark star mass is m_* . For a cluster made of brown dwarfs (“BD”), the left line shows the timescales on which every typical star suffers a physical collision with another star. Points WD, NS, and BH show the times in which dark clusters made of white dwarfs, neutron stars, or stellar-mass BHs would evaporate. Points P with “error bars” are the timescales on which every typical progenitor star collides with another progenitor at the radius in the Plummer model dark cluster that contains one-quarter of the total mass. The letter P is for the time when the dark cluster is three-quarters assembled; the “error bars” end at the collision times when the cluster is half assembled (top) and fully assembled (bottom).

be consistent with the above rates, but if intermediate-mass white dwarfs in similar dark clusters are the explanation for other galaxies’ central dark objects, the resulting supernovae would easily have been seen. Intermediate-mass white dwarfs are implausible.

In addition, the supernova ejecta would be lost to the cluster. The above collision times imply that most of the mass inside $r_{1/4}$ and a significant fraction of the mass inside r_h would be lost in a few billion years. For the dark cluster to have its present mass, it would have had to be more massive in the past. All problems involving collision rates would get more severe.

White dwarfs with masses less than half of the Chandrasekhar limit will turn out to be excluded because their progenitors would be destroyed and converted into gas or, if they succeed to merge, become progenitors of intermediate-mass white dwarfs or still heavier remnants (§ 8.2.4).

White dwarfs with masses near the Chandrasekhar limit are small. Their collision times are long. For these objects, we need stronger arguments. These arguments will militate against intermediate-mass white dwarfs, also.

8.2.3. Dark Cluster Formation Scenario: Let’s Imagine Six Impossible Things before Breakfast

Heavy remnants are too small to collide. Instead, relaxation gives positive energies to a steady trickle of stars that are lost to the system. In $\lesssim 300$ half-mass relaxation times, the cluster evaporates. Figure 18 shows the evaporation times for dark clusters made of $0.6 M_\odot$ white dwarfs, $0.8 M_\odot$ white dwarfs, $1.2 M_\odot$ white dwarfs, $1.5 M_\odot$ neutron stars, and $3 M_\odot$ BHs (left to right; symbols WD, WD, WD, NS, and BH). Unlike the case in NGC 4258 and our Galaxy (Maoz 1995, 1998), these evaporation times are not

implausibly short except for $m_* \gtrsim 10 M_\odot$ BHs. So, for most remnants, we need stronger arguments.

Fortunately, we can add new arguments. They depend only on canonical, well-understood stellar evolution and simple stellar dynamics. A dark cluster made of stellar remnants is viable only if its progenitor stars can safely live their lives and deliver their remnants at suitable radii. The properties of the dark cluster constrain how it can form. We describe the most benign formation scenario in this subsection. It requires fine-tuning of the star formation in ways that we do not know are possible. However, we do not base our arguments against the resulting dark clusters on these problems, because we do not understand star formation well enough. But main-sequence stars are well understood, and we know progenitor star masses well enough for the present purposes. It turns out that progenitor stars get into trouble because they must be so close together that they collide. The consequences are untenable, as discussed in the following subsections.

Finding a plausible formation scenario is comparable to imagining six impossible things before breakfast. The argument is summarized as follows. The progenitor cluster must be as small as the dark cluster because dynamical friction is too slow to deliver remnants from much larger radii. From Lauer et al. (1998), the density of P2 at $r \sim 0.1\text{--}0.2$ pc is $\sim 10^6 M_\odot \text{pc}^{-3}$. Then the characteristic time for dynamical friction (Binney & Tremaine 1987, eq. [7–18]) to change velocities $v \sim 10^3 \text{ km s}^{-1}$ is $v/(dv/dt) \sim 10^{12}$ yr for $10 M_\odot$ stars. This drives us to imagine the following impossible things:

1. Let us form progenitor stars with a density distribution proportional to that of the dark cluster, i.e., a Plummer sphere with half-light radius $r_h = 0.113$ pc.

2. We get into less trouble with collisions if fewer progenitors are resident at one time. Therefore, the safest strategy is to form stars at a constant rate during the formation time of, say, 10^{10} yr. This is not the obvious strategy in a hierarchically clustering universe; it is more natural to postulate episodic formation by more vigorous events that are connected with major mergers. But shortening the formation time increases the number of progenitors that must be resident at the same time, and this greatly increases difficulties with stellar collisions.

3. We assume that all progenitor stars have the same mass. In particular, we cannot allow a Salpeter (1955) mass function because we cannot tolerate any significant numbers of dwarf stars with lifetimes long enough so that the stars or their white dwarf remnants remain visible today.

4. We assume that sufficient gas for star formation is always present. Some gas could come from mass lost by evolving stars, but some gas must be added continuously to make the cluster grow. We assume that stars can form despite any energy feedback from massive or evolved stars.

5. We do not worry about the fact that the young cluster is easy to unbind gravitationally by the mass loss from evolved stars. This is a difficult problem. Progenitors outmass their remnants by factors of at least a few (for low-mass stars) or ~ 10 (for high-mass stars). During the first stellar generations, the progenitors outmass the remnants. Since they lose most of their mass during the course of stellar evolution, it is easy to reduce the total mass of the cluster substantially when stars die. Impulsive loss of more than half of the mass (say, if the star formation happened in a coeval starburst) unbinds the cluster. Slower mass loss fights the formation process by expanding the cluster. We ignore all of these difficulties and assume that the cluster can safely evolve beyond the fragile initial stage when the mass of progenitors present at one time is significant.

6. We assume that the only evolution in r_h is that resulting from a gradual increase of the cluster mass. Then $r_h \propto M_*^{-1}$.

Using the above assumptions, we calculate the evolution of the cluster for various combinations of progenitors and their remnants. Progenitor masses are from Iben et al. (1996) for white dwarfs and from Brown & Bethe (1994) for BHs. The progenitor clusters get into the following trouble.

8.2.4. If M31 Is Typical, Then Progenitor Clusters Are Too Bright

The above progenitor clusters have absolute magnitudes ranging from $M_V \simeq -16.3$ to -17.5 for the duration of their formation. These absolute magnitudes are almost independent of progenitor star mass; higher mass progenitors are much more luminous, but they live much less long, so far fewer are present at one time. Nuclei as bright as the above could not be hidden in nearby (or even moderately distant) galaxies. They are rare (e.g., Lauer et al. 1995, 2005). It is unreasonable to assume that dark cluster formation lasted for $\sim 10^{10}$ yr in every bulge and then stopped recently in all galaxies.

If the formation of the dark cluster took $\ll 10^{10}$ yr, then the progenitor clusters are brighter but it is easier to hide them at large redshifts. But then all problems that involve stellar collisions get much worse (see below).

This problem applies to all types of stellar remnants.

8.2.5. Dynamical Friction Deposits Remnants at Small Radii

As noted above, progenitor stars are much more massive than the remnants of previous generations that already make up the dark cluster. The dynamical friction of the progenitors against the remnants makes the progenitors sink quickly to small enough radii so that the progenitor cluster becomes self-gravitating. Two problems result. Progenitor collision times get shorter; these are discussed further below. Second, remnants are deposited at small radii, inconsistent with the density distribution that we are trying to construct. As heavy stars sink, remnants are lifted to higher radii; the effect is not large for one generation of progenitors, but it adds up by the time the cluster is finished. The result is a dark cluster that is much more core-halo in structure than a Plummer model. That is, it is inherently impossible to make a dark cluster that is as centrally concentrated as a Plummer model via progenitor stars that greatly outmass their remnants. This is one of the stiffest problems of our formation scenario.

If the dark cluster is less compact than a Plummer sphere, then its half-mass radius must be smaller than 0.113 pc in order to fit the kinematics. All problems with stellar collisions get much worse.

This problem also applies to all types of remnants.

8.2.6. White Dwarfs that Cannot Merge to Form Type Ia Supernovae Cannot Be Relevant

Interior to r_h , essentially all progenitors of $0.6 M_\odot$ white dwarfs collide and either get destroyed (their surface escape velocities are $\sim 600 \text{ km s}^{-1}$) or, in the earlier phases of the dark cluster formation, merge. If they merge, they get converted to progenitors of white dwarfs that have masses $\gtrsim 0.8 M_\odot$. Progenitors of white dwarfs with masses $\leq 0.55 M_\odot$ live too long to have died and, provided that they were not destroyed, would still be visible. Therefore, white dwarfs that are low enough in mass so that a collision of two of them results in a remnant that is less massive than the Chandrasekhar limit are not relevant.

8.2.7. Progenitors Collide and Evaporate or Merge into High-Mass Stars

Figure 18 shows progenitor star collision times for the second half of the dark cluster formation process. At $r \lesssim r_{1/4}$,

progenitors of low-mass remnants get destroyed and converted into gas or, in earlier phases, merge to become progenitors of high-mass remnants. We note that the stellar evolution clock is reset to essentially zero in every nondestructive collision because the merging stars get thoroughly mixed. Dynamical friction is neglected in constructing Figure 18; if it is included, then most of the progenitors participate in the collisions. Also neglected is the fact that successive mergers increase the mass range and hence decrease both the dynamical friction sinking time and the relaxation time of the cluster.

Three consequences spell trouble for the formation scenario:

1. If progenitors are not destroyed, they merge up to form stars of high enough masses so that they die as Type II supernovae. Their luminosity is not a problem for the hypothetical, present M31 dark cluster because its formation process is finished or at least in hiatus. But again, if M31 is typical, then the formation of many such objects at intermediate and high redshifts should produce one Type II supernova per galaxy per ~ 100 yr at the center of the galaxy. They would have been seen.

2. The supernova ejecta again would not be bound to the dark cluster unless a large amount of gas is also present.

3. Relatively few, high-mass remnants would be formed. Dynamical friction would guarantee that they got deposited at small radii. The mass range that resulted from heterogeneous stellar merger histories would create a large mass range even if none was present initially. The result would be that relaxation times would be much shorter, plausibly an order of magnitude shorter, than the single-mass relaxation times that gave rise to the cluster evaporation times in Figure 18. For all of these reasons, evaporation times are likely to be much shorter than the several billion years indicated for $3 M_\odot$ BHs in Figure 18. This is implausibly short.

8.2.8. Summary on BH Alternatives

Therefore, astrophysically reasonable alternatives to a supermassive BH are likely to fail. The arguments against brown dwarfs seem bomb proof. The arguments against stellar remnants are more complicated, but they are based on secure aspects of stellar and star-cluster evolution. Also, there are many arguments, even a few of which are sufficient. So we are not very vulnerable to uncertainties involving any one argument ("Are we sure that we have not missed those supernovae or confused them with AGN activity?"). The problem (§ 8.2.5) that remnants are deposited at excessively small radii is particularly important. In this paper we have derived the largest published estimate of M_* using data at the smallest radii. This leaves little room for distributed dark matter, i.e., for a dark cluster with core-halo structure. In addition, § 8.2.3 on the formation scenario, while not formally part of our argument against dark clusters, presents formidable challenges. Our arguments are discussed in more detail in J. Kormendy et al. (2005, in preparation). However, our conclusion that dark cluster alternatives to a BH are excluded seems robust.

9. CONCLUSIONS

M31 is now the third galaxy in which astrophysical arguments strongly favor the conclusion that a dynamically detected central dark object is a BH. M31 is the only galaxy for which such arguments are based on *HST* observations. Similar conclusions for NGC 4258 and our Galaxy result from ground-based observations. The present result is therefore an important contribution of *HST* to the BH paradigm of AGNs. It increases our confidence that all dynamically detected central dark objects in galaxies are BHs.

We are most grateful to Don Winget for very helpful discussions about white dwarf properties and to Don Winget and Anjum Mukadam for providing digital observed spectra of white dwarf stars. We thank Detlev Koester for making his models of white dwarf atmospheres available and for insightful remarks about their systematics. We also thank the Nuker team (D. Richstone, PI) and especially Scott Tremaine for many helpful and enlightening discussions. R. B. is most grateful to the Department of Astronomy of the University of Texas at Austin for its warm hospitality and the support provided by a Beatrice M. Tinsley Centennial Visiting Professorship. We thank the anonymous referee for a careful reading of the

paper and for very helpful suggestions that led to significant improvements in §§ 1 and 8 and that prompted us to add § 6.2.

This paper is based on observations made with the NASA/ESA *Hubble Space Telescope*, obtained at the Space Telescope Science Institute, which is operated by the Association of Universities for Research in Astronomy, Inc., under NASA contract NAS5-26555. These observations are associated with program 8018 (visits 1 and 2) and were a portion of time allocated to the Space Telescope Imaging Spectrograph Instrument Definition Team key project for supermassive BHs.
Facilities: HST(STIS)

APPENDIX

Peiris & Tremaine (2003) show that their eccentric disk model fitted to ground-based kinematic data also agrees remarkably well with our STIS kinematic measurements of P1 and P2. The comparison includes not only V and σ but also the parameters h_3 and h_4 , which measure the lowest order departures from Gaussian line profiles. The data that they use are presented here in Tables 4 and 5 and Figures 19 and 20. We do not repeat their discussion. Instead, we focus on the generic properties of the LOSVDs. In particular, we confirm an unusual property of the LOSVDs that directly implies aligned, eccentric orbits. This effect was seen and interpreted in KB99, but it is much larger at *HST* spatial resolution. Since the effect was inherent in but not explicitly predicted by Tremaine (1995), it is compelling evidence in favor of his model.

Figure 19 compares the FQ and FCQ reductions of the Ca infrared triplet spectra. The velocities are almost identical. The dispersions agree where the higher order Gauss-Hermite coefficients are small and differ in the expected way when they are not. Where FCQ measures an extended wing of the LOSVD in the prograde direction ($h_3 < 0$ at $r \simeq -0.1$), it finds a smaller dispersion than FQ because FQ fits a Gaussian to the whole LOSVD, including wings. Similarly, where $h_4 > 0$ at $r \simeq +0.1$, FCQ fits a broader Gaussian than FQ and then clobbers the intermediate-velocity shoulders of the Gaussian with h_4 to make the fitted LOSVD triangular.

Kinematic asymmetries inherent in an eccentric disk provided the basic test of that model in Tremaine (1995), KB99, and Peiris & Tremaine (2003). We now know that the BH is in the blue nucleus P3 at $r = 0$ in Figure 19. Stars in the eccentric disk linger at apocenter to form P1; as a result, both the rotation amplitude $|V|$ and the velocity dispersion σ are relatively small at $r \simeq +0.5$. Other stars in the eccentric disk are passing pericenter slightly on the anti-P1 side of the BH; as a result, the rotation amplitude is large at $r \simeq -0.2$ in P2. The apparent velocity dispersion is highest at approximately the same radii because the slit and PSF average over stars moving in a variety of directions as they swing around the BH. Figures 11 and 12 in Peiris & Tremaine (2003) show that their nonaligned model accurately accounts for the asymmetric rotation and dispersion profiles.

TABLE 4
KINEMATICS OF M31 DERIVED FROM THE RED CAT SPECTRA WITH THE FOURIER QUOTIENT METHOD

Radius (arcsec)	V (km s ⁻¹)	ΔV (km s ⁻¹)	σ (km s ⁻¹)	$\Delta\sigma$ (km s ⁻¹)
-1.075	-177	14	130	15
-0.726	-189	13	151	14
-0.474	-244	13	179	14
-0.304	-299	23	207	24
-0.230	-319	32	274	35
-0.180	-332	34	298	38
-0.130	-276	36	345	39
-0.080	-232	45	373	48
-0.005	-118	23	247	25
0.070	-52	28	221	31
0.120	0	22	195	23
0.170	32	23	220	26
0.220	84	21	182	23
0.270	108	14	174	15
0.320	140	15	186	17
0.396	175	10	146	11
0.495	207	8	131	8
0.595	192	7	122	8
0.694	200	7	117	8
0.794	200	7	104	8
0.894	185	9	103	11
0.994	178	11	111	13
1.094	156	10	91	12
1.262	175	11	99	13
1.513	147	19	108	23

TABLE 5
KINEMATICS OF M31 DERIVED FROM THE RED CAT SPECTRA WITH THE FOURIER CORRELATION QUOTIENT METHOD

Radius (arcsec)	V (km s ⁻¹)	ΔV (km s ⁻¹)	σ (km s ⁻¹)	$\Delta\sigma$ (km s ⁻¹)	h_3	Δh_3	h_4	Δh_4
-1.390	-130.8	11.7	135.4	10.6	0.040	0.079	-0.092	0.079
-1.023	-189.6	11.0	140.0	11.6	0.056	0.072	-0.043	0.072
-0.776	-192.2	8.3	144.2	10.2	0.110	0.053	0.013	0.053
-0.578	-217.0	11.2	188.7	11.8	0.037	0.054	-0.046	0.054
-0.401	-267.2	7.2	168.3	7.1	0.168	0.039	-0.070	0.039
-0.254	-316.4	12.7	240.2	12.2	0.082	0.048	-0.074	0.048
-0.180	-313.6	14.4	279.6	15.5	-0.089	0.047	-0.035	0.047
-0.130	-247.9	16.3	296.5	22.1	-0.188	0.050	0.060	0.050
-0.080	-181.4	16.1	300.7	23.1	-0.264	0.049	0.084	0.049
-0.030	-137.6	14.5	273.7	18.2	-0.147	0.048	0.026	0.048
0.020	-99.0	13.0	263.9	17.3	-0.156	0.045	0.051	0.045
0.070	-59.6	15.6	286.1	27.5	-0.061	0.050	0.194	0.050
0.120	-4.8	12.6	226.0	21.5	-0.072	0.051	0.176	0.051
0.170	36.0	13.0	231.1	18.4	-0.001	0.051	0.079	0.051
0.246	96.2	8.4	184.9	11.5	0.009	0.041	0.062	0.041
0.346	152.2	7.0	170.3	8.2	-0.042	0.038	-0.007	0.038
0.446	198.2	4.8	143.3	5.7	-0.075	0.031	-0.002	0.031
0.592	203.6	3.5	126.1	3.9	-0.072	0.025	-0.021	0.025
0.788	199.2	3.5	109.2	3.8	-0.016	0.029	-0.029	0.029
0.989	185.5	5.7	117.0	6.1	-0.185	0.045	-0.037	0.045
1.213	173.6	5.9	103.1	8.2	0.014	0.052	0.075	0.052
1.569	140.3	7.0	108.7	12.5	-0.379	0.059	0.221	0.059

An important additional property of the LOSVDs (and the unusual one mentioned above) is the observation that h_3 has the same sign as V over a radius range of $\Delta r \simeq 0''.4$ centered $\sim 0''.1$ on the anti-P1 side of P3. This effect was seen at ground-based spatial resolution in KB99. It is much larger here. It is opposite to the normal behavior of rotating stellar systems, in which velocity projection along the line of sight makes h_3 antisymmetric with V (van der Marel et al. 1994; Bender et al. 1994). Also, the maximum amplitude, $h_3 \simeq -0.3$, is unusually large compared to values in other galaxies. All this is easily seen in the LOSVDs (Fig. 20; radii $-0''.15$ and $-0''.10$) as the broad wings on the $-V$ side of the line centers. These wings tell us that, on the anti-P1 side of the P3, where the average galactic rotation is toward us (V is negative in Fig. 20), many stars are rotating more rapidly and few stars are rotating more slowly than the mean rotation velocity averaged within the PSF.

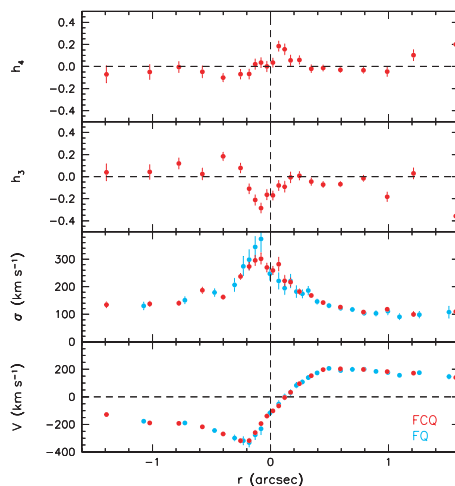


FIG. 19.—Red filled circles: Rotation velocity V , velocity dispersion σ , and Gauss-Hermite parameters h_3 and h_4 as a function of radius as derived with FCO from the red spectrum of the nucleus of M31. Blue filled circles: FQ results from Fig. 2.

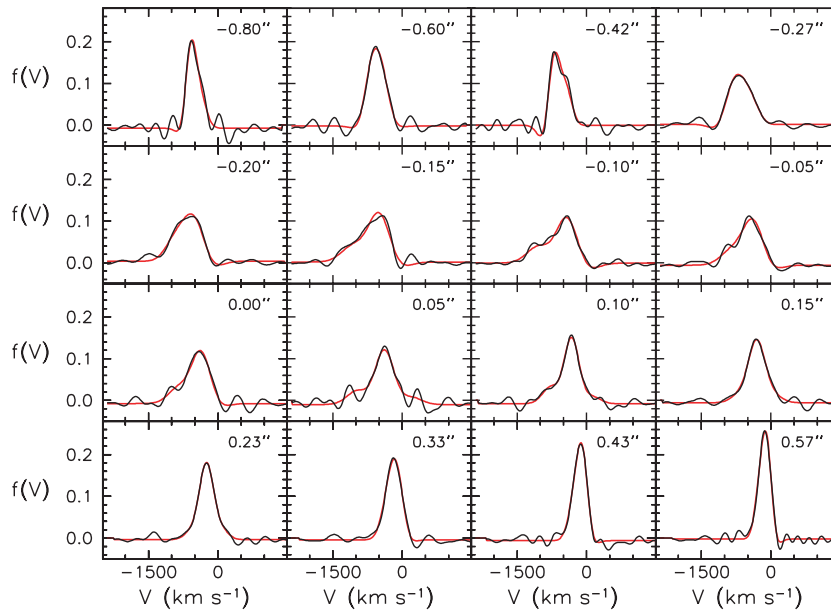


FIG. 20.—LOSVDs in the same radial bins that were used to derive the FCQ kinematic results shown in Fig. 19. The black lines are nonparametric LOSVDs; the red lines are the FCQ fits. The radius of the bin is given at upper right in each panel. At upper left, we tabulate the velocity dispersion and the Gauss-Hermite parameters h_3 and h_4 .

Our interpretation is the same as in KB99. The velocity dispersion is expected to look big near pericenter in the eccentric disk because the slit and PSF integrate over stars that are at different positions along orbits that are rapidly turning around the BH. A prograde LOSVD wing follows naturally if there are many stars still closer to the BH and if they also are in eccentric orbits with apocenters that point toward P1. In the almost Keplerian potential of the BH, these stars have larger pericenter velocities than the mean V farther out; in fact, their velocities should be larger than the local circular velocity. Consistent with this interpretation, the LOSVD asymmetry is most obvious at $r = -0''.05$ to $-0''.15$, i.e., at slightly more than one PSF radius on the anti-P1 side of P3. The highest velocities reach ~ 1000 km s $^{-1}$, indeed somewhat larger than what we measure at about the same location for the PSF-blurred velocities of the blue stars in P3. Of course, this explanation only works if the BH is embedded in P3.

The fact that we can understand naturally an observation not predicted by Tremaine (1995) increases our confidence in his model. With improved disk parameters, Peiris & Tremaine (2003, see Figs. 13 and 14) accurately predict the h_3 and h_4 profiles near the BH. At this point, there seems little doubt that the interpretation of the double nucleus as an eccentric disk is correct and that its main parameters have been determined. The important next step is self-consistent dynamical models to investigate whether the present configuration can be long lived (e.g., Statler et al. 1999; Statler 1999; Bacon et al. 2001; Salow & Statler 2004). A larger BH mass, as estimated here, will likely help to construct more long-lived models. Beyond that, the origin of the eccentric disk remains essentially unknown.

REFERENCES

- Aparicio, A., & Gallart, C. 2004, *AJ*, 128, 1465
 Bacon, R., Emsellem, E., Monnet, G., & Nieto, J.-L. 1994, *A&A*, 281, 691
 Bacon, R., et al. 2001, *A&A*, 371, 409
 Bender, R. 1990, *A&A*, 229, 441
 Bender, R., Saglia, R. P., & Gerhard, O. E. 1994, *MNRAS*, 269, 785
 Bertola, F., Bressan, A., Burstein, D., Buson, L. M., Chiosi, C., & di Serego Alighieri, S. 1995, *ApJ*, 438, 680
 Binney, J., & Tremaine, S. 1987, *Galactic Dynamics* (Princeton: Princeton Univ. Press)
 Bower, G. A., et al. 2001, *ApJ*, 550, 75
 Brown, G. E., & Bethe, H. A. 1994, *ApJ*, 423, 659
 Brown, T. M., Ferguson, H. C., Stanford, S. A., & Deharveng, J.-M. 1998, *ApJ*, 504, 113
 Bruzual, G., & Charlot, S. 2003, *MNRAS*, 344, 1000
 Corbin, M. R., O'Neil, E., & Rieke, M. J. 2001, *AJ*, 121, 2549
 Cox, A. N. 2000, *Allen's Astrophysical Quantities* (New York: Springer)
 Crane, P., et al. 1993a, *AJ*, 106, 1371
 Crane, P. C., Cowan, J. J., Dickel, J. R., & Roberts, D. A. 1993b, *ApJ*, 417, L61
 Crane, P. C., Dickel, J. R., & Cowan, J. J. 1992, *ApJ*, 390, L9
 Davidge, T. J., Rigaut, F., Doyon, R., & Crampton, D. 1997, *AJ*, 113, 2094
 Dressler, A. 1984, *ApJ*, 286, 97
 Dressler, A., & Richstone, D. O. 1988, *ApJ*, 324, 701
 Emsellem, E., & Combes, F. 1997, *A&A*, 323, 674
 Ferrarese, L., & Merritt, D. 2000, *ApJ*, 539, L9
 Finley, D. S., Koester, D., & Basri, G. 1997, *ApJ*, 488, 375
 Gebhardt, K., et al. 2000a, *AJ*, 119, 1157
 ———. 2000b, *ApJ*, 539, L13
 ———. 2003, *ApJ*, 583, 92

- Genzel, R., et al. 1998, *ApJ*, 498, 579
 ———. 2003, *ApJ*, 594, 812
- Ghez, A. M., Salim, S., Hornstein, S. D., Tanner, A., Lu, J. R., Morris, M., Becklin, E. E., & Duchêne, G. 2005, *ApJ*, 620, 744
- Ghez, A. M., et al. 2003, *ApJ*, 586, L127
- Goudfrooij, P., Baum, S. A., & Walsh, J. R. 1997, in *The 1997 HST Calibration Workshop*, ed. S. Casertano et al. (Baltimore: STScI), 100
- Iben, I., Tutukov, A. V., & Yungelson, L. R. 1996, *ApJ*, 456, 750
- Jacobs, V., & Sellwood, J. A. 2001, *ApJ*, 555, L25
- King, I. R., Stanford, S. A., & Crane, P. 1995, *AJ*, 109, 164
- King, I. R., et al. 1992, *ApJ*, 397, L35
- Kleinman, S. J., et al. 2004, *ApJ*, 607, 426
- Koester, D., et al. 2001, *A&A*, 378, 556
- Kormendy, J. 1987, in *IAU Symp. 127, Structure and Dynamics of Elliptical Galaxies*, ed. T. de Zeeuw (Dordrecht: Reidel), 17
 ———. 1988, *ApJ*, 325, 128
 ———. 2004, in *Coevolution of Black Holes and Galaxies*, ed. L. C. Ho (Cambridge: Cambridge Univ. Press), 1
- Kormendy, J., & Bender, R. 1999, *ApJ*, 522, 772 (KB99)
- Kormendy, J., Bender, R., & Bower, G. 2002, in *ASP Conf. Ser. 273, The Dynamics, Structure and History of Galaxies*, ed. G. S. Da Costa & H. Jerjen (San Francisco: ASP), 29
- Kormendy, J., & Gebhardt, K. 2001, in *AIP Conf. Proc. 586, 20th Texas Symposium on Relativistic Astrophysics*, ed. J. C. Wheeler & H. Martel (Melville: AIP), 363
- Kormendy, J., & Kennicutt, R. C., Jr. 2004, *ARA&A*, 42, 603
- Lauer, T. R., et al. 1993, *AJ*, 106, 1436
 ———. 1995, *AJ*, 110, 2622
 ———. 1998, *AJ*, 116, 2263
 ———. 2005, *AJ*, 129, 2138
- Le Borgne, J.-F., et al. 2003, *A&A*, 402, 433
- Light, E. S., Danielson, R. E., & Schwarzschild, M. 1974, *ApJ*, 194, 257
- Magorrian, J., et al. 1998, *AJ*, 115, 2285
- Maoz, E. 1995, *ApJ*, 447, L91
 ———. 1998, *ApJ*, 494, L181
- Morris, M. 1993, *ApJ*, 408, 496
- Mould, J., Graham, J., Matthews, K., Soifer, B. T., & Phinney, E. S. 1989, *ApJ*, 339, L21
- Nieto, J.-L., Macchetto, F. D., Perryman, M. A. C., di Serego Alighieri, S., & Lelièvre, G. 1986, *A&A*, 165, 189
- Peiris, H. V., & Tremaine, S. 2003, *ApJ*, 599, 237
- Pickles, A. J. 1998, *PASP*, 110, 863
- Rich, R. M., Mighell, K. J., Neill, J. D., & Freedman, W. L. 1996, in *New Extragalactic Perspectives in the New South Africa*, ed. D. L. Block & J. M. Greenberg (Dordrecht: Kluwer), 325
- Richstone, D., Bower, G., & Dressler, A. 1990, *ApJ*, 353, 118
- Salow, R. M., & Statler, T. S. 2001, *ApJ*, 551, L49
 ———. 2004, *ApJ*, 611, 245
- Salpeter, E. E. 1955, *ApJ*, 121, 161
- Sambhus, N., & Sridhar, S. 2002, *A&A*, 388, 766
- Sanders, R. H. 1998, *MNRAS*, 294, 35
- Schmidt, M. 1959, *ApJ*, 129, 243
- Schödel, R., Ott, T., Genzel, R., Eckart, A., Mouawad, N., & Alexander, T. 2003, *ApJ*, 596, 1015
- Schödel, R., et al. 2002, *Nature*, 419, 694
- Schwarzschild, M. 1979, *ApJ*, 232, 236
- Sérsic, J. L. 1968, *Atlas de Galaxias Australes* (Cordoba: Observatorio Astronomico)
- Statler, T. S. 1999, *ApJ*, 524, L87
- Statler, T. S., King, I. R., Crane, P., & Jedrzejewski, R. I. 1999, *AJ*, 117, 894
- Stevenson, D. J. 1991, *ARA&A*, 29, 163
- Thomas, J., Saglia, R. P., Bender, R., Thomas, D., Gebhardt, K., Magorrian, J., & Richstone, D. 2004, *MNRAS*, 353, 391
- Tonry, J. L. 1984, *ApJ*, 283, L27
 ———. 1987, *ApJ*, 322, 632
- Tonry, J. L., et al. 2001, *ApJ*, 546, 681
- Toomre, A. 1964, *ApJ*, 139, 1217
- Tremaine, S. 1995, *AJ*, 110, 628
 ———. 2001, *AJ*, 121, 1776
- Tremaine, S., et al. 2002, *ApJ*, 574, 740
- van der Marel, R. P., Cretton, N., de Zeeuw, T., & Rix, H.-W. 1998, *ApJ*, 493, 613
- van der Marel, R. P., Rix, H.-W., Carter, D., Franx, M., White, S. D. M., & de Zeeuw, T. 1994, *MNRAS*, 268, 521
- van der Marel, R. P., et al. 1997, *Nature*, 385, 610
- Verolme, E. K., et al. 2002, *MNRAS*, 335, 517
- Yu, Q. 2003, *MNRAS*, 339, 189
- Zapolsky, H. S., & Salpeter, E. E. 1969, *ApJ*, 158, 809

Bibliography

- Baes M., Buyle P., Hau G. K. T., Dejonghe H., 2003, MNRAS, 341, L44
- Baes M., Dejonghe H., Buyle P., 2003, A&A, 432, 411
- Bender R., Möllenhoff C., 1987, A&A, 177, 71
- Bender R., 1988a, A&A, 193, L7
- Bender R., 1988b, A&A, 202, L5
- Bender R., Surma P., Döbereiner S, Möllenhoff C., Madejsky R., 1989, A&A, 217, 35
- Bender R., Surma P., 1992, A&A, 258, 250
- Bender R., Saglia R. P., Gerhard O. E., 1994, MNRAS, 269, 785
- Bender R. et al., 2005, ApJ, 631, 280
- Bertola F., Galletta G., 1979, A&A, 77, 363
- Bertola F., Pizzella A., Persic M., Salucci P., 1993, ApJL, 416, 45
- Binney J., Mamon G. A., 1982, MNRAS, 200, 361
- Binney J., Gerhard O. E., Hut P., 1985, MNRAS, 215, 59
- Binney J., Tremaine S., 1987, Galactic Dynamics (princeton: Princeton University Press)
- Bissantz N., Debattista V. P., Gerhard O. E., ApJL, 601, 155
- Brainerd T. G., Blandford R. D., Smail I., 1996, ApJ, 466, 623
- Bureau M., Athanassoula E., 2005, ApJ, 626, 159
- Caon N., Capaccioli M., d'Onofrio M., 1993, MNRAS, 265, 1013
- Cappellari M., Verolme E. K., van der Marel R. P., Verdoes Kleijn G. A., Illingworth G. D., Franx M., Carollo C. M., de Zeeuw P. T., 2002, ApJ, 578, 787

- Cappellari M. et al., 2005, preprint (astro-ph/0509470)
- Cappellari M. et al., 2006, MNRAS, 366, 1126
- Carollo C. M., de Zeeuw P. T., van der Marel R. P., 1995, MNRAS, 276, 1131
- Carollo C. M., de Zeeuw P. T., van der Marel R. P., Danziger I. J., Qian E. E., 1995, ApJL, 441, 25
- Colin P., Avila-Reese V., Valenzuela O., 2000, ApJ, 542, 622
- Contopoulos G., 1963, AJ, 68, 1
- Copin Y., Cretton N., Emsellem E., 2004, A&A, 415, 889
- Cretton N., van den Bosch F. C., 1998, ApJ, 514, 704
- Cretton N., de Zeeuw P. T., van der Marel R. P., Rix H. W., 1999, ApJS, 124, 383
- Cretton N., Rix H. W., de Zeeuw P. T., 2000, ApJ, 536, 319
- Cretton N., Emsellem E., 2004, MNRAS 347, L31
- Davé R., Spergel D. N., Steinhardt P. J., Wandelt B. D., 2001, ApJ, 547, 574
- de Blok W. J. G., McGaugh S. S., Bosma A., Rubin V. C., 2001, ApJL, 552, 23
- de Bruyne V., de Rijcke S., Dejonghe H., Zeilinger W. W., 2004, MNRAS, 349, 440
- de Zeeuw P. T., Lynden-Bell D., 1985, MNRAS, 215, 713
- Dehnen W., Gerhard O. E., 1993, MNRAS, 261, 311
- Dehnen W., 1993, MNRAS, 265, 250
- Dehnen W., Gerhard O. E., 1994, MNRAS 268, 1019
- Dejonghe H., Merritt D. R., 1992, MNRAS, 391, 531
- Dejonghe H., de Bryne V., Vauterin P., Zeilinger W. W., 1996, A&A, 306, 363
- di Serego Alighieri S. et al., 2005, A&A, 442, 125
- Djorgovski S., Davies M., 1987, ApJ, 313, 59
- Dubinski J., 1998, ApJ, 502, 141
- Dressler A., Faber S. M., Burstein D., Davies R. L., Lynden-Bell D., Terlevich R. J., Wegner G., 1987, ApJ, 313, 37
- Efstathiou G., Ellis R. S., Carter D., 1982, MNRAS, 201, 975
- Eggen D. J., Lynden-Bell D., Sandage A. R., 1962, ApJ, 136, 748

- Emsellem E., Dejonghe H., Bacon R., 1999, MNRAS, 303, 495
- Faber S. M., 1973, ApJ, 179, 731
- Faber S. M., Jackson R. E., 1976, ApJ, 204, 668
- Faber S. M., Dressler A., Davies R. L., Burstein D., Lynden-Bell D., Terlevich R. J., Wegner G., 1987, in *Nearly Normal Galaxies*, ed. Faber S. M., Springer, New York, 175
- Ferrarese L., Merritt D., 2000, ApJL, 539, 9
- Ferrarese L., 2002, ApJ, 578, 90
- Franx M., Illingworth G., 1988, ApJL, 327, 55
- Fukazawa Y., Botoya-Noneso J. G., Pu J., Ohto A., Kawano N., 2006, ApJ, 636, 698
- Gebhardt K. et al., 2000, AJ, 119, 1157
- Gebhardt K. et al., 2000, ApJL, 539, 13
- Gebhardt K. et al., 2003, ApJ, 583, 92
- Gentile G., Salucci P., Klein U., Vergani D., Kalberla P., 2004, MNRAS, 351, 903
- Gerhard O. E., Saha P., 1991, MNRAS, 251, 449
- Gerhard O. E., 1993, MNRAS, 265, 213
- Gerhard O. E., Binney J., 1996, MNRAS, 279, 993
- Gerhard O. E., Jeske G., Saglia R. P., Bender R., 1998, MNRAS, 295, 197
- Gerhard O. E., Kronawitter A., Saglia R. P., Bender R., 2001, AJ, 121, 1936
- Godwin J. G., Metcalfe N., Peach J. V., 1983, MNRAS, 202, 113
- Graham A. W., Trujillo I., Caon N., 2001, AJ, 122, 1707
- Häfner R., Evans N. W., Dehnen W., Binney J., 2000, MNRAS, 314, 433
- Hernquist L., 1990, ApJ, 356, 359
- Hernquist L., 1992, ApJ, 409, 548
- Hernquist L., 1993, ApJ, 400, 460
- Hinz J. L., Rix H. W., Bernstein G. M., 2001, AJ, 121, 683
- Hinz J. L., Rieke G. H., Caldwell N., 2003, AJ, 126, 2622

- Houghton R. C. W., Magorrian J., Sarzi M., Thatte N., Davies R. L., Krajnović D., 2006, MNRAS in press
- Humphrey P. J., Buote, D. A., Gastaldello F., Zappacosta L., Bullock J. S., Brighenti F., Mathews W. G., 2006, preprint (astro-ph/0601301)
- Jedrzejewski R., Schechter P. S., 1989, AJ, 98, 147
- Jesseit R., Naab T., Burkert A., 2005, MNRAS, 360, 1185
- Jing Y. P., Suto Y., 2000, ApJ, 529, L69
- Jørgensen I., Franx M., 1994, ApJ, 433, 553
- Jørgensen I., Franx M., Kjaergard P., 1996, MNRAS, 280, 167
- Jørgensen I., Chiboucas K., Flint K., Bergmann M., Barr J., Davies R., 2006, ApJL, 639, 9
- Katz N., Richstone D. O., 1985, ApJ, 296, 331
- Keeton C. R., 2001, ApJ, 561, 46
- Knebe A., Devriendt J. E. G., Mahmood A., Silk J., 2002, MNRAS, 329, 813
- Kormendy J., Bender R., 1996, ApJ, 464, 119
- Krajnović D., Cappellari M., Emsellem E., McDermid R. M., de Zeeuw P. T., 2005, MNRAS, 357, 1113
- Kronawitter A., Saglia R. P., Gerhard O. E., Bender R., 2000, A&AS, 144, 53
- Larson R. B., 1974, MNRAS, 169, 229
- Levison H. F., Richstone D. O., 1984, ApJ, 295, 340
- Levison H. F., Richstone D. O., 1984, ApJ, 295, 349
- Loewenstein M., White R. E., 1999, ApJ 518, 50
- Lynden-Bell D., 1962, MNRAS, 123, 447
- Lynden-Bell D., 1962, MNRAS, 124, 1
- Lynden-Bell D., 1967, MNRAS, 136, 101
- Magorrian J., Binney J., 1994, MNRAS, 271, 949
- Magorrian J. et al., 1998, AJ, 115, 2285
- Magorrian J., 1999, MNRAS, 302, 530
- Magorrian J., Ballantyne D., 2001, MNRAS, 322, 702
- Maraston C., 1998, MNRAS, 300, 872

- Maraston C., 2004, preprint (astro-ph/0410207)
- Mathieu A., Merrifield M. R., Kuijken K., 2002, MNRAS, 330, 2002
- Matthias M., Gerhard O. E., 1999, MNRAS, 310, 879
- McGaugh S. S., 2005, ApJ, 632, 859
- Mehlert D., Saglia R. P., Bender R., Wegner G., 2000, A&AS, 141, 449
- Mehlert D., Thomas D., Saglia R. P., Bender R., Wegner G., 2003, A&A, 407, 423
- Merritt D. R., 1985a, AJ, 90, 1023
- Merritt D. R., 1985b, MNRAS, 214, 25
- Merritt D. R., Saha P., 1993, ApJ, 409, 75
- Merritt D. R., 1993, ApJ, 413, 79
- Merritt D. R., Fridman T., 1996, ApJ, 460, 136
- Merritt D. R., Valluri M., 1996, ApJ, 471, 82
- Miralda-Escudé J., Schwarzschild M., 1989, ApJ, 339, 752
- Moore B., Quinn T., Governato F., Stadel J., Lake G., 1999, MNRAS, 310, 1147
- Morelli L. et al., 2004, MNRAS, 354, 753
- Naab T., Burkert A., 2003, ApJ, 597, 893
- Navarro J. F., Frenk C. S., White S. D. M., 1996, ApJ, 462, 563
- Navarro J. F. et al., 2004, MNRAS, 349, 1039
- Neistein E., Maoz D., Rix H. W., Tonry J. L., 1999, AJ, 117, 2666
- Ollongren A., 1962, Bull. Astr. Inst. Netherlands, 16, 241
- Oosterloo T. A., Morganti R., Sadler E. M., Vergani D., Caldwell N., 2002, AJ, 123, 729
- Osipkov L. P., 1979, Pis'ma Astron. Zh., 55, 77
- Peng E. W., Ford H. C., Freeman K. C., 2004, ApJ, 602, 685
- Persic M., Salucci P., Stel F., 1996, MNRAS, 281, 27
- Persic M., Salucci P., Stel F., 1996, MNRAS, 283, 1102
- Press W. H., Teukosky S. A., Vetterling W. T., Flannery B. P., 1992, Numerical Recipes in FORTRAN 77, 2nd edn. Cambridge Univ. Press, Cambridge

- Qian E. E., de Zeeuw P. T., van der Marel R. P., Hunter C., 1995, MNRAS, 274, 602
- Renzini A., Ciotti L., 1993, ApJL, 416, 49
- Richstone D. O., 1980, ApJ, 238, 103
- Richstone D. O., 1982, ApJ, 252, 496
- Richstone D. O., 1984, ApJ, 281, 100
- Richstone D. O., Tremaine S., 1984, ApJ, 286, 27
- Richstone D. O., Tremaine S., 1988, ApJ, 327, 82
- Richstone D. O. et al, 2004, preprint, astro-ph/0403257
- Richstone D. O. et al., in preparation
- Rix H. W., White S. D. M., 1990, ApJ, 362, 52
- Rix H. W., de Zeeuw P. T., Cretton N., van der Marel R. P., Carollo C. M., 1997, ApJ, 488, 702
- Romanowsky A. J., Kochanek C. S., 2001, ApJ, 553, 722
- Romanowsky A. J., Douglas N. G., Arnaboldi M., Kuijken K., Merrifield M. R., Napolitano N. R., Capaccioli M., Freeman K. C., 2003, Sci, 301, 1696
- Rybicki G., 1987, in de Zeeuw T., ed., Proc. IAU Symp. 127, Structure and Dynamics of Elliptical Galaxies, Reidel, Dordrecht, p. 397
- Sakai S. et al., 2000, ApJ, 529, 698
- Saglia R. P., Bertin G., Stiavelli M., 1992, ApJ, 384, 433
- Saglia R. P., Bender R., Dressler A., 1993, A&A, 279, 75
- Saglia R. P., Kronawitter A., Gerhard O. E., Bender R., 2000, AJ, 119, 153
- Schwarzschild M., 1979, ApJ, 232, 236
- Schwarzschild M., 1982, ApJ, 263, 599
- Schwarzschild M., 1993, ApJ, 409, 563
- Schweizer F., 1982, ApJ, 252, 455
- Scorza C., Bender R., 1995, A&A, 293, 20
- Shewchuk J., 1996, in First Workshop on Applied Computational Geometry, ACM (<http://www.cs.cmu.edu/~quake/triangle.html>) 124
- Statler T. S., Dejonghe H., Smecker-Hane T., 1999, AJ, 117, 126

- Swaters R. A., Madore B. F., van den Bosch F. C., Balcells M., 2003, *ApJ*, 583, 732
- Syer D., Tremaine S., 1996, *MNRAS*, 282, 223
- Thomas D., Maraston C., Bender R., 2003, *MNRAS*, 339, 897
- Thomas D., Maraston C., Bender R., Mendes de Oliveira C., 2005, *ApJ*, 621, 673
- Thomas J., Saglia R. P., Bender R., Thomas D., Gebhardt K., Magorrian J., Richstone D., 2004, *MNRAS*, 353, 391
- Thomas J., Saglia R. P., Bender R., Thomas D., Gebhardt K., Magorrian J., Corsini E. M., Wegner G., 2005, *MNRAS*, 360, 1355
- Toomre A., Toomre J., 1972, *ApJ*, 178, 623
- Tremblay B., Merritt D., 1996, *AJ*, 111, 2243
- Treu T., Koopmans L. V. E., 2004, *ApJ*, 611, 739
- Tully R. B., Fisher J. R., 1977, *A&A*, 54, 661
- Valluri M., Merritt D., Emsellem E., 2004, *ApJ*, 602, 66
- van Albada T. S., 1982, *MNRAS*, 201, 939
- van de Ven G., Verolme E. K., Cappellari M., de Zeeuw P. T., 2003, in *Dark Matter in Galaxies*, IAU Symposium No. 220, eds. S. Ryder, D.J. Pisano, M. Walker and K. Freeman
- van den Bosch R., van de Ven G., Verolme E., Cappellari M., de Zeeuw P. T., in *Proc. of the 5th Marseille International Cosmology Conference: "The Fabulous Destiny of Galaxies: Bridging Past and Present"*, 2005 June 20-24, Marseille
- van der Marel R. P., 1991, *MNRAS*, 253, 710
- van der Marel R. P., Franx M., 1993, *ApJ*, 407, 525
- van der Marel R. P., Cretton N., de Zeeuw P. T., Rix H. W., 1998, *ApJ*, 493, 613
- Vandervoort P. O., 1984, *ApJ*, 287, 475
- Verolme E. K., de Zeeuw P. T., 2002, *MNRAS*, 331, 959
- Verolme E. K. et al., 2002, *MNRAS*, 335, 517
- Wechsler R. H., Bullock J. S., Primack J. R., Kravtsov A. V., Dekel A., 2002, *ApJ*, 568, 52

Wegner G., Corsini E. M., Saglia R. P., Bender R., Merkl D., Thomas D., Thomas J., Mehlert D., 2002, *A&A*, 395, 753

Weil M., Hernquist L., 1996, *ApJ*, 457, 51

Zhao H. S., 1996, *MNRAS*, 283, 149

Danksagung

Die vorliegenden Ergebnisse meiner mehrjährigen Arbeit an der Universitäts-Sternwarte München haben viele kleinere und grössere Einflüsse erfahren, die im Einzelnen aufzuzählen mir unmöglich ist.

Soviel ist klar, dass die Anfertigung dieser Arbeit ohne das Vertrauen und die umfassende Unterstützung von Ralf Bender nicht möglich gewesen wäre, für die ich mich herzlich bedanke.

Besonderer Dank gilt meinem Betreuer R. P. Saglia, der während der ganzen Arbeit aufmerksam und freundschaftlich mit Rat und Tat zur Seite stand. Viele Anregungen schulde ich seiner stets sicheren und zielgerichteten Kritik an meiner Arbeit.

Ferner danke ich D. Thomas für die Berechnung der SSP-Modelle sowie die Einführung in und die Unterstützung während dieser Doktorarbeit.

Ich danke vor allem auch K. Gebhardt und J. Magorrian, und weiter C. Botzler und J. Snigula, auf deren freigiebiger Weitergabe eigener Programme ein Teil dieser Arbeit aufbauen konnte.

Lebenslauf

Jens Thomas, geboren am 07.03.1974 in Essen-Werden, verheiratet, ein Kind

1980 - 1993 Besuch von Grundschule und Gymnasium
in Essen-Werden, Abitur

1993 - 2000 Physikstudium an der Ruhr-Universität Bochum und
der Universität Hamburg, Diplom

01.2001 - 06.2001 Mitglied im Graduiertenkolleg *Mathematik im Bereich
ihrer Wechselwirkung mit der Physik*,
Ludwig-Maximilians Universität München

seit 07.2001 Doktorarbeit an der Universitäts-Sternwarte München

Wissenschaftliche Veröffentlichungen:

- *Classification of multifluid CP world models*, **J. Thomas**, H. Schulz, 2001, A&A 366, 395
- *Incompatibility of a comoving Ly α forest with supernova-Ia luminosity distances*, **J. Thomas**, H. Schulz, 2001, A&A 371, 1
- *Spatially resolved spectroscopy of Coma cluster early-type galaxies. II. The minor axis dataset*, G. Wegner, E. M. Corsini, R. P. Saglia, R. Bender, D. Merkl, D. Thomas, **J. Thomas**, D. Mehlert, 2002, A&A, 395, 753
- *Mapping stationary axisymmetric phase-space distribution functions by orbit libraries*, **J. Thomas**, R. P. Saglia, R. Bender, D. Thomas, K. Gebhardt, J. Magorrian, D. Richstone, 2004, MNRAS, 353, 391
- *Regularized orbit models unveiling the stellar structure and dark matter halo of the Coma elliptical NGC 4807*, **J. Thomas**, R. P. Saglia, R. Bender, D. Thomas, K. Gebhardt, J. Magorrian, E. M. Corsini, G. Wegner, 2005, MNRAS, 360, 1355
- *HST STIS Spectroscopy of the Triple Nucleus of M31: Two Nested Disks in Keplerian Rotation around a Supermassive Black Hole*, R. Bender, J. Kormendy, G. Bower, R. Greene, **J. Thomas**, A. C. Danks, T. Gull, J. B. Hutchings, C. L. Joseph, M. E. Kaiser and 5 coauthors, 2005, ApJ, 631, 280

- *The Star-Forming Torus and Stellar Dynamical Black Hole Mass in the Seyfert 1 Nucleus of NGC 3227*, R. I. Davies, **J. Thomas**, R. Genzel, F. Mueller Sanchez, L. J. Tacconi, A. Sternberg, F. Eisenhauer, R. Abuter, R. Saglia, R. Bender, 2006, ApJ, 646, 754